Synthetic Aperture Radar TOPS-mode Interferometry for Ice Velocity Retrieval

Andersen, Jonas Kvist

Publication date:
2022

Document Version
Publisher's PDF, also known as Version of record

DTU Space
Microwaves & Remote Sensing

Synthetic Aperture Radar TOPS-mode Interferometry for Ice Velocity Retrieval

PhD thesis

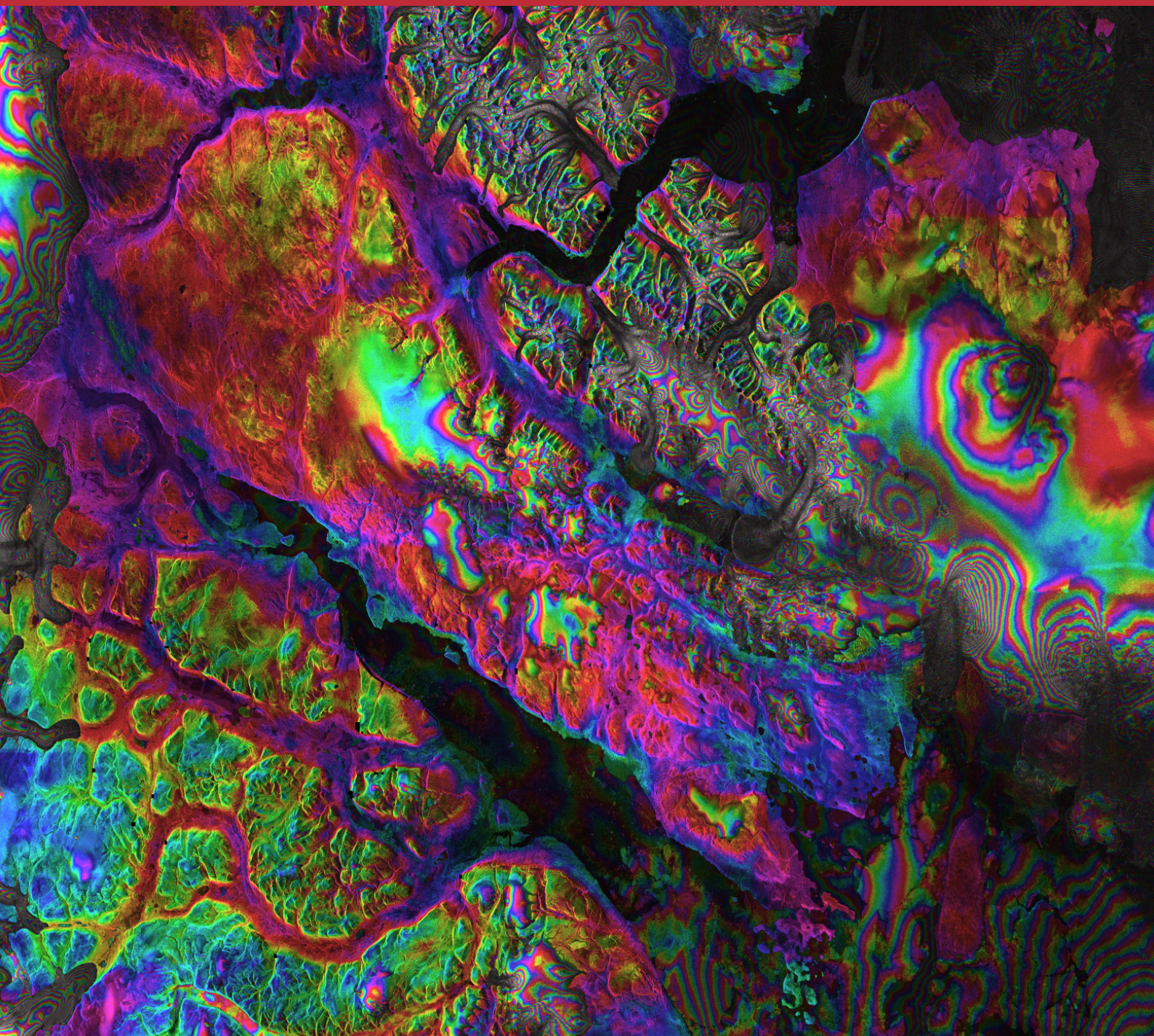

Synthetic Aperture Radar TOPS-mode Interferometry for Ice Velocity Retrieval

PhD thesis
August, 2022

By
Jonas Kvist Andersen

Cover picture: Contains modified EU Copernicus Sentinel-1 data, processed by J. K. Andersen

Published by: DTU Space, Microwaves & Remote Sensing, Ørsted Plads, Building 348, 2800 Kgs. Lyngby Denmark
www.space.dtu.dk

Preface

This PhD thesis was prepared at the Microwaves & Remote Sensing division at DTU Space, Technical University of Denmark. The PhD project was carried out from September 2019 to August 2022 and supervised by associate professor John Peter Merryman Boncori and research engineer Anders Kusk. An external research stay was spent at the Institut des Géosciences de l'Environnement, Université Grenoble-Alpes, under the supervision of associate professor Jérémie Mouginot.

The project was funded by DTU Space and by the European Space Agency (ESA) under Contract 4000129620/19/I-DT, awarded to the Phase-Based Sentinel-1 Ice Velocity (PHAB-IV) proposal under the ESA Earth Observation Science for Society Permanently Open Call.

Jonas Kvist Andersen

Signature

31st August 2022

Date

Abstract

Mass loss from the world's ice sheets and glaciers is one of the largest contributors to ongoing sea level rise. For both the Greenland and Antarctic ice sheets, a significant part of the mass loss stems from changes in ice dynamics, with many marine-terminating outlet glaciers consistently accelerating and retreating. Ice velocity is an essential variable in monitoring the state of ice sheets and glaciers. Over the past several decades, a revolution in the quality and availability of Synthetic Aperture Radar (SAR) satellite data has allowed frequent ice velocity retrievals to be carried out over major parts of the ice sheets. Particularly, the EU/ESA Sentinel-1 SAR satellites have been widely utilized in the generation of seasonal, annual, and multi-annual velocity retrievals, owing to their extensive coverage, facilitated by the Terrain Observation by Progressive Scans (TOPS) acquisition mode. So far, however, routine Sentinel-1 ice velocity measurements have relied solely on amplitude-based methods, which produce measurements of significantly lower accuracy and resolution than phase-based Differential SAR Interferometry (DInSAR). The main reason for this discrepancy is the added complexity introduced to interferometric processing by the TOPS acquisition mode, where along-track motion is coupled to the interferometric phase.

In this thesis, a refined image coregistration approach is developed, which alleviates the TOPS-related challenges and allows interferometric ice velocity retrieval from the extensive Sentinel-1 polar archive. A demonstration is provided of a combined DInSAR and amplitude offset tracking 2D velocity retrieval, which exploits the high accuracy and resolution of DInSAR in slower-moving inland regions and the ability of offset tracking to retrieve measurements from fast-flowing glacier outlets, highlighting the synergy between the two techniques. In the context of ice velocity retrieval, particularly in downstream regions, phase unwrapping errors is the most prominent error source in DInSAR measurements. Here, a method is designed to detect and discard measurements affected by unwrapping errors. The method is based on an estimate of pixel connectivity and is particularly effective at detecting high magnitude errors.

Finally, several demonstrations are provided of the capabilities of Sentinel-1 DInSAR time series measurements in monitoring changes in ice dynamics, with a focus on specific regions of the Greenland ice sheet. On longer time scales (multiple years), the high sensitivity of DInSAR allows for estimating trends in flow speed, even in slow-moving regions, where only subtle changes occur. On shorter time scales (months or even weeks), the DInSAR time series may reveal complex motion patterns and transient dynamic events. Multiple instances of hydrology-dynamic events, related to the drainage of both supraglacial and subglacial lakes, are documented in the thesis. Observations of such events are crucial for improving our understanding of hydrological processes in glaciers and ice sheets and the extent of their impact in the future. Collectively, these demonstrations highlight the potential of applying Sentinel-1 DInSAR measurements in investigating various types of ice dynamic changes on multiple time scales.

Resumé på dansk

Massetab fra verdens iskapper og gletsjere er en af de største bidragsydere til igangværende havniveaustigning. For både Grønlands og Antarktis iskapper stammer en betydelig del af massetabet fra ændringer i isdynamikken, hvor mange hav-terminerende udløbsgletsjere konsekvent accelererer og trækker sig tilbage. Isens hastighed er en essentiel variabel i overvågningen af indlandsisens og gletsjeres tilstand. I løbet af de sidste mange årtier har en revolution i kvaliteten og tilgængeligheden af Syntetisk Apertur Radar (SAR) satellitdata gjort det muligt at udføre hyppige ishastighedsmålinger over store dele af iskapperne. Især er EU/ESA Sentinel-1 SAR-satellitterne blevet brugt i vid udstrækning i genereringen af sæsonmæssige, årlige og flerårige hastighedsmålinger på grund af deres omfattende dækning, faciliteret af Terrain Observation by Progressive Scans (TOPS) optagelsesmetoden. Indtil videre har rutinemæssige Sentinel-1 ishastighedsmålinger udelukkende anvendt amplitudebaserede metoder, som producerer målinger med væsentligt lavere nøjagtighed og opløsning end fasebaseret Differential SAR Interferometry (DInSAR). Hovedårsagen til dette er den ekstra kompleksitet, der introduceres til interferometrisk behandling af TOPS-data, hvor azimuth bevægelse er koblet til den interferometriske fase.

I denne afhandling udvikles en raffineret billedkoregistreringstilgang, som afhjælper de TOPS-relaterede udfordringer og tillader interferometriske ishastighedsmålinger fra det omfattende Sentinel-1 arkiv i polare områder. Der gives en demonstration af en kombineret DInSAR og amplitude offset tracking 2D hastighedsmåling, som udnytter den høje nøjagtighed og opløsning af DInSAR i langsommere indlandsområder samt offset trackings evne til at optage målinger fra hurtigtflydende gletsjerudløb, hvilket fremhæver synergien mellem de to teknikker. I forbindelse med måling af ishastigheder, især i ablationszonen, er faseudpakningsfejl den mest fremtrædende fejlkilde i DInSAR-målinger. Her demonstreres en metode designet til at detektere og kassere målinger påvirket af udpakningsfejl. Metoden er baseret på et estimat af pixel-forbindelse og er særligt effektiv til at detektere fejl af høj størrelse.

Endeligt gives adskillige demonstrationer af Sentinel-1 DInSAR tidsseriemålinger til overvågning af ændringer i isdynamikken. På længere tidsskalaer (flere år) giver den høje følsomhed af DInSAR mulighed for at estimere tendenser i flowhastighed, selv i langsomt bevægende områder, hvor der typisk kun forekommer subtile ændringer. På kortere tidsskalaer (måneder eller endda uger) kan DInSAR-tidsserier afsløre komplekse bevægelsesmønstre og forbigående dynamiske hændelser. Flere forekomster af hydrologi-dynamiske hændelser, relateret til dræning af både supraglaciale og subglaciale søer, er dokumenteret i afhandlingen. Observationer af sådanne hændelser er afgørende for at forbedre vores forståelse af hydrologiske processer i gletsjere og iskapper samt omfanget af deres påvirkning i fremtiden. Tilsammen fremhæver disse demonstrationer potentialet af anvendelsen af Sentinel-1 DInSAR-målinger til undersøgelser af forskellige typer dynamiske ændringer på flere tidsskalaer.

Acknowledgements

I want to express a deep gratitude to my supervisors, John Peter Merryman Boncori and Anders Kusk, for their continued support, guidance, and motivation throughout the project.

The project builds on a long legacy of work in the field of cryospheric SAR applications at the Microwaves & Remote Sensing division. I thank everyone who has contributed to this legacy, which includes the inhouse SAR processing software, IPP, which was a vital tool in the project.

I thank Jérémie Mouginot for welcoming me to IGE in Grenoble, for his dedicated (ongoing) collaboration, which not only provided substantial contributions to the research output of this PhD project but also a great motivation, and for his continued support and friendship. I thank Nathan Maier for his hard work in an exciting collaboration and for his deep interest in my research and its potential future applications. I am also grateful to Marco Piantini and everyone else at IGE who provided a warm welcome, even during chaotic COVID times.

I thank Anne Solgaard at GEUS and Christine Hvidberg and Aslak Grinsted at NBI for helpful collaborations and discussions throughout the project.

Finally, I thank Jørgen Dall (DTU), Anders Bjørk (University of Copenhagen), and Adrian Luckman (Swansea University) for taking on the task of assessing and evaluating this PhD thesis.

To David

Contents

List of abbreviations

2D/3D	-	Two/three-dimensional
BO-MAI	-	Burst Overlap Multi-Aperture Interferometry
DEM	-	Digital Elevation Model
DInSAR	-	Differential Synthetic Aperture Radar Interferometry
ESA	-	European Space Agency
ESD	-	Extended Spectral Diversity
EU	-	European Union
FFT	-	Fast Fourier Transform
GCP	-	Ground Control Point
GPS	-	Global Positioning System
InSAR	-	Synthetic Aperture Radar Interferometry
IW	-	Interferometric Wide (Swath)
LoS	-	Line of Sight
LUT	-	Look-Up Table
MAI	-	Multi-Aperture Interferometry
m/y	-	Meters per year
NASA	-	National Aeronautics and Space Administration
NCC	-	Normalized Cross Correlation
NEGIS	-	Northeast Greenland Ice Stream
NG	-	Nioghalvfjerdsfjorden Glacier (79N Glacier)
OTR	-	Offset Tracking
POE	-	Precise Orbit Ephemerides
PROMICE	-	Programme for Monitoring of the Greenland Ice Sheet
S1(A/B)	-	Sentinel-1(A/B)
SAR	-	Synthetic Aperture Radar
SG	-	Storstrømmen Glacier
SLC	-	Single Look Complex
SLR	-	Sea Level Rise
SMB	-	Surface Mass Balance
TOPS	-	Terrain Observation by Progressive Scans
USGS	-	United States Geological Survey
ZI	-	Zachariae Isstrøm

List of figures

Chapter 1 | Introduction

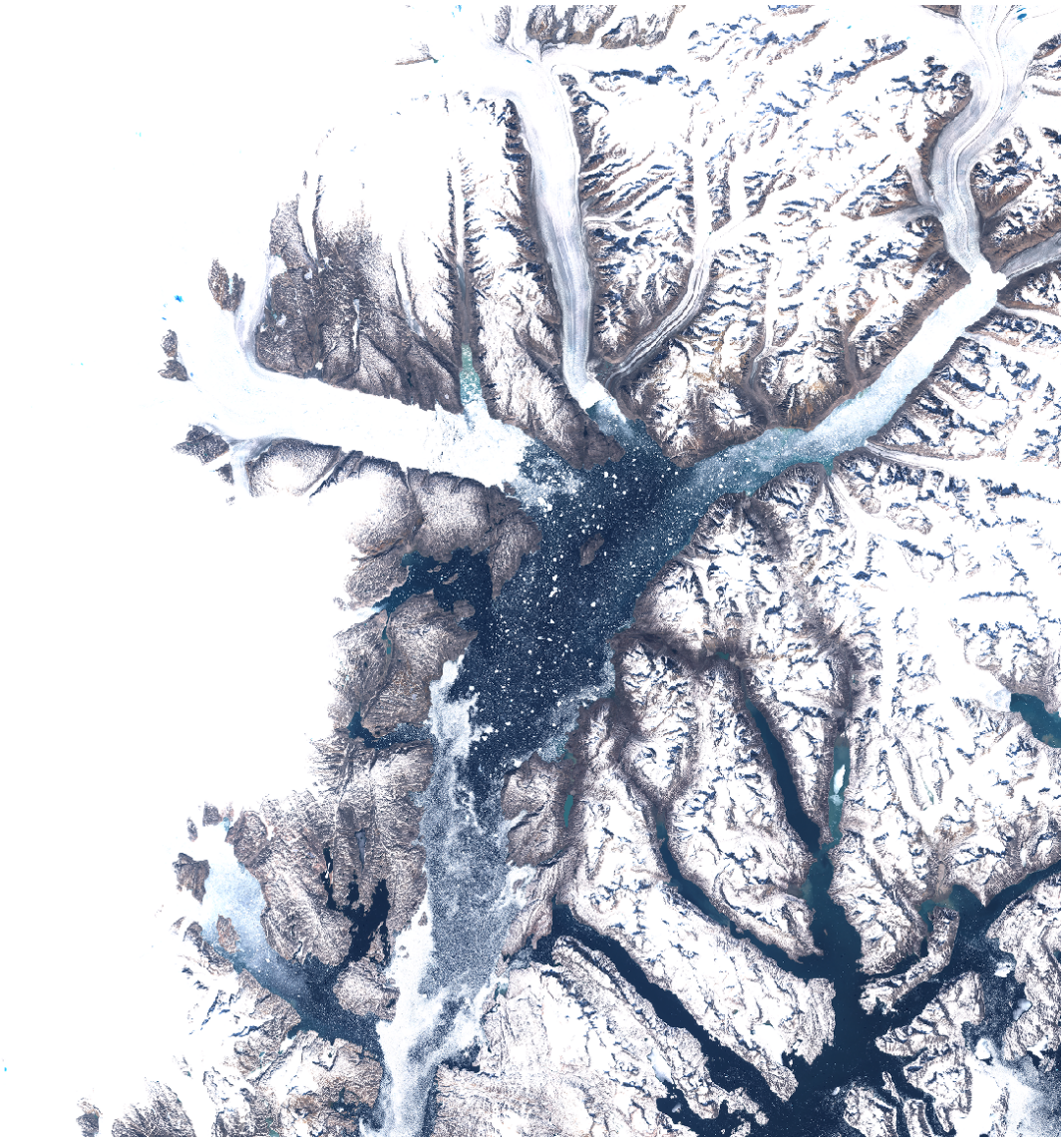

Sentinel-2 true color composite showing calving fronts of the Helheim, Fenris, and Midgård glaciers.

1.1 Importance of dynamic ice mass loss

For the past three decades, global sea level has been rising with an average rate of 3 mm per year, a rate which has been increasing in recent years (Nerem et al., 2018), fueled, in large part, by rising temperatures caused by anthropogenic greenhouse gas emissions (Marzeion et al., 2014; IPCC, 2021a). Future projections suggest that sea level rise (SLR) will continue throughout the century (IPCC, 2021b), leading to extensive socio-economic damage, due to floods and extreme weather events (Jevrejeva et al., 2018; Vousdoukas et al., 2017). Main contributors to SLR are thermal expansion of the ocean, also known as steric sea level rise (Church et al., 2011), and mass loss from ice sheets and glaciers around the world (WCRP Global Sea Level Budget Group, 2018). During the period 2006-2018, glacier and ice sheet mass loss was the largest contributor to SLR (IPCC, 2021b). Loss of mountain glaciers also threatens freshwater availability of local populations (McGranahan et al., 2007).

The ongoing mass loss from the world's ice sheets and glaciers is well documented (Box et al., 2022; IMBIE team, 2018, 2019; Slater et al., 2021; Hugonnet et al., 2021). For a given glacier or ice sheet, the net mass gain (or loss) is measured by the *mass balance*, computed as the net *accumulation* minus the net *ablation*. Accumulation occurs through snowfall, which eventually compacts into glacial ice, and through refreezing of glacial melt water. Ablation occurs through surface melt, basal melt occurring at the interface between the ice and the underlying bedrock (Karlsson et al., 2021), and through dynamic discharge of ice by marine-terminating outlet glaciers (also known as calving). The latter term is generally referred to as *dynamic mass loss*, while the balance between accumulation and surface melt is referred to as the *surface mass balance* (SMB). A glacier or ice sheet is generally partitioned in two zones: the upper zone (at higher elevation), known as the *accumulation zone*, where accumulation exceeds the melting rate, leading to a gain in mass, and the lower zone, known as the *ablation zone*, where the opposite is true. The *equilibrium line altitude* defines the surface elevation of the border where accumulation and ablation rates (on average) are in perfect balance. On a large scale, ice sheets are dome-shaped, and gravity causes ice to flow, such that ice may be transferred from the accumulation zone into the ablation zone. Acceleration in flow speed generally means an increase in mass loss, as more ice is transferred to lower elevation, where it may undergo melt or calving. In the interior ice sheet, at high elevations, ice flow is quite slow (on the order of a few meters per year (m/y) to a few tens of m/y). On outlet glaciers at the margin of the ice sheet, flow speeds may exceed several kilometers per year. As ice or melt water is discharged into the ocean, it directly contributes to sea level rise. The Greenland ice sheet holds a potential sea level equivalent of 7.4 m (Morlighem et al., 2017), while the Antarctic ice sheet holds a potential SLR of 57.9 m (Morlighem et al., 2020). The combination of all other glaciers (excluding the two ice sheets) are estimated to hold a sea level equivalent on the order of 0.3 m (Farinotti et al., 2019; Millan et al., 2022). Over the period 1992 to 2020, the largest SLR contributions stem from glaciers (globally, excluding the ice sheets) and the Greenland ice sheet (17.1 ± 4.4 mm and 13.5 ± 2.1 mm, respectively) while the

Antarctic ice sheet SLR contribution was 7.4 ± 2.4 mm (IPCC, 2021b). Throughout this thesis, the main focus is on dynamics of the Greenland ice sheet, and particular emphasis is put on the North East Greenland Ice Stream (NEGIS). However, the developed methods may just as well be applied to the Antarctic ice sheet or glaciers and ice caps elsewhere.

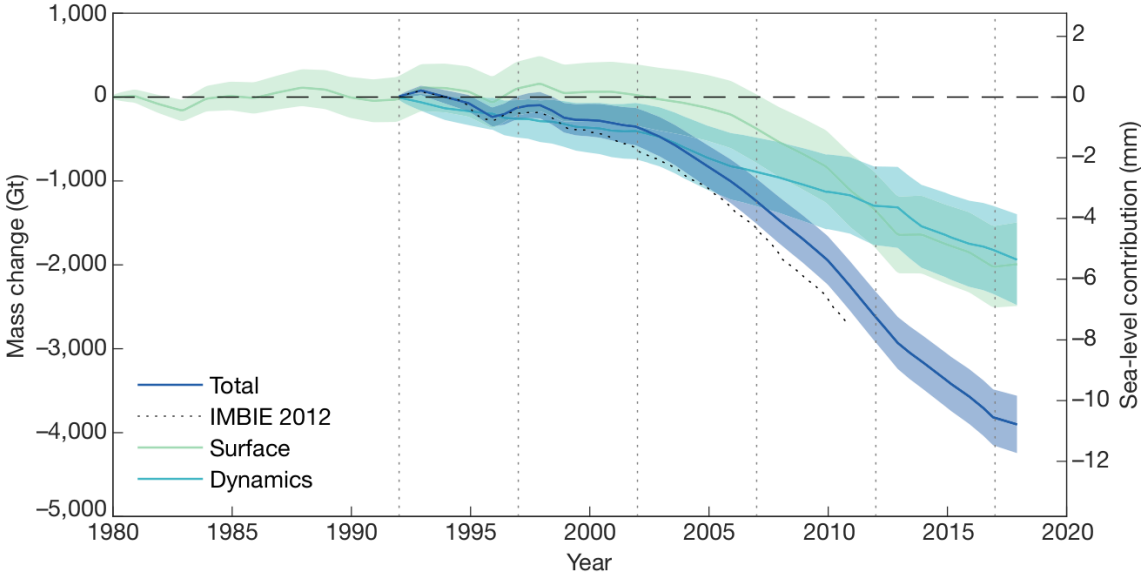

Figure 1.1: Mass loss of the Greenland ice sheet, estimated by the latest Ice Sheet Mass Balance Intercomparison Exercise (IMBIE), partitioned between surface mass balance and dynamic mass loss contributions. (Image source: IMBIE team, 2019).

In recent decades, mass loss of the Greenland ice sheet has consisted of roughly equal contributions in negative SMB and dynamic mass loss (IMBIE team, 2019), while mass loss of the Antarctic ice sheet stems primarily from increased dynamic mass loss (IMBIE team, 2018). Separation of the SMB and dynamic mass loss contributions relies on several techniques and measurements, including satellite altimetry (Sandberg Sørensen et al., 2018), satellite gravimetry (Velicogna et al., 2014), modeling of SMB (Fettweis et al., 2017), and estimation of ice discharge (Howat et al., 2007; Mankoff et al., 2020), which, in turn, relies on accurate measurements of ice flow velocity (Mouginot et al., 2017) and ice thickness (Morlighem et al., 2017). Fig 1.1 shows an estimated time series of mass change of the Greenland ice sheet, distinguishing between the SMB and dynamic components (IMBIE team, 2019). The partitioning between SMB and dynamic mass loss contributions (as well as their magnitudes) shows substantial variation across different geographical regions and different time periods (Mouginot et al., 2019b). Dynamic mass loss increases have been linked to the calving front retreat of outlet glaciers across the Greenland ice sheet (King et al., 2020). An example of such a retreat is shown in Fig. 1.2. Past studies point to links between ice dynamic changes, in the form of both calving front and ice flow variation, and various ocean and atmosphere processes (Howat et al., 2010; Khazendar et al., 2019; Luckman et al., 2015; Smith et al., 2020).

Monitoring ice flow velocity is essential for understanding the dynamic behaviour of a

glacier or ice sheet. Glacier flow has been observed to vary on time scales ranging from decadal, (multi-)annual, and seasonal (Joughin et al., 2018b; Luckman et al., 2006; Moon et al., 2014; Moon et al., 2020; Mouginot et al., 2015; Mouginot et al., 2018; Vijay et al., 2019) to sub-seasonal time scales, often associated with transient hydrological events (Andrews et al., 2018; Christoffersen et al., 2018; Bartholomew et al., 2010). Constraining current and projected mass loss estimates requires accurate measurements of ice velocity, preferably with high spatiotemporal resolution, such that processes responsible for both long-term and transient ice flow changes may be understood.

The Global Climate Observing System defines ice velocity as an Essential Climate Variable and specifies target requirements of 100 m resolution, 0.1 m/y accuracy, and 30 day measurement frequency (WMO, 2016). While the launch of the Sentinel-1 satellites (among other missions) enables velocity retrievals with a temporal resolution of 6 to 12 days, approaching the required accuracy and spatial resolution is infeasible with current tracking-based routine velocity retrievals. Instead, the requirements may be approached with interferometric processing, which is the main topic of this PhD project.

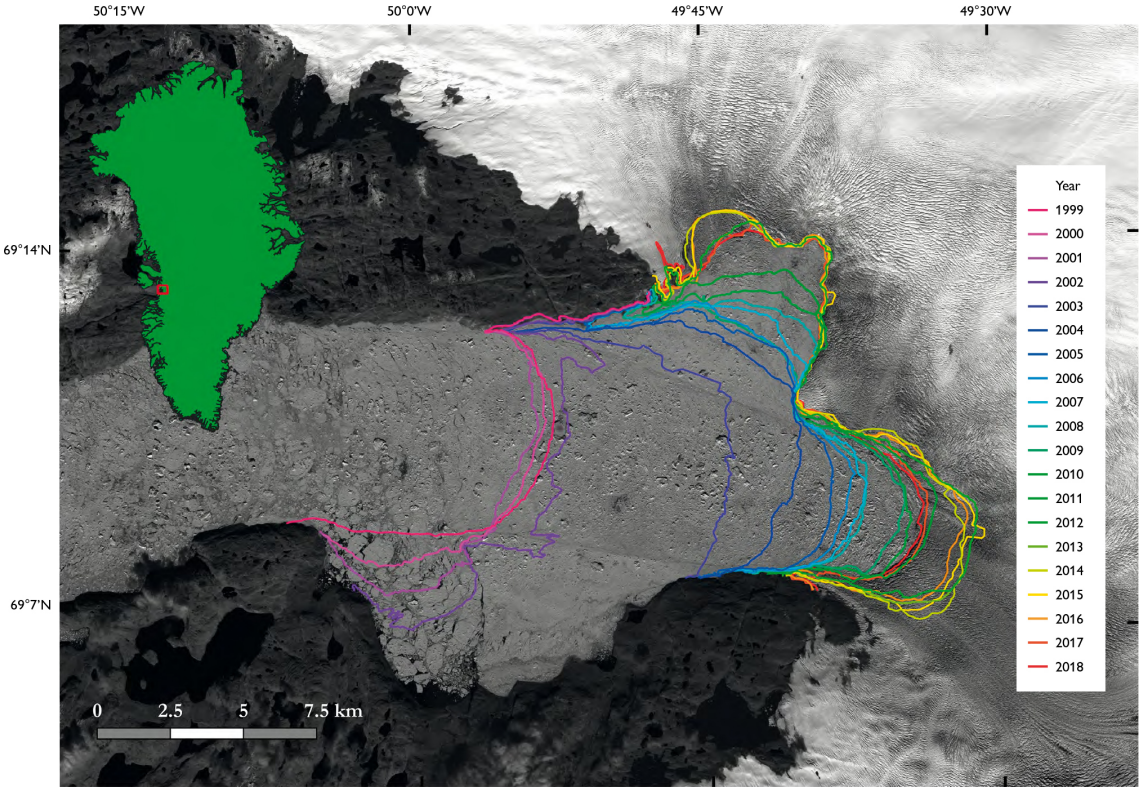

Figure 1.2: Evolution of the calving front location of Jakobshavn Isbræ (Sermeq Kujalleq), the fastest flowing glacier in Greenland. During 1999 to 2016, the calving front retreated more than 10 km, while flow speed and thinning rate of the glacier increased. From 2017, the calving front re-advanced, associated with decreases in glacier flow speed and thinning rate - a change that has been linked to anomalous cooling of nearby ocean water (Khazendar et al., 2019). (Image source: Andersen et al., 2019)

1.2 Remote sensing for ice flow mapping

Measurements of ice flow velocity have long been acquired through in-situ methods using, e.g., tellurometers (Dorrer et al., 1969), Transit (NAVSAT) satellite receivers (Mock, 1976), and later Global Positioning System (GPS) satellite receivers (Hvidberg et al., 1997; Thomas et al., 2000). While in-situ methods have produced, and continue to produce (Hvidberg et al., 2020; Maier et al., 2019; Sole et al., 2011), valuable results on individual areas of interest, they are naturally resource intensive and limited in spatial (and often temporal) coverage. Throughout the past ∼50 years, the rapid development in satellite remote sensing technology has allowed remote retrieval of ice velocity over glaciers and ice sheets worldwide, with increasingly improved data quality and spatiotemporal coverage. Two classes of imaging satellites have been extensively used in the retrieval of ice velocity, namely optical and Synthetic Aperture Radar (SAR) satellites. Both types of satellites are typically flown in near-polar, sun-synchronous orbits, meaning that measurements are acquired at the same local time on ground.

Optical satellites carry multi-spectral sensors, which record light at multiple wavelengths in the visible (and usually near-infrared) parts of the electromagnetic spectrum, similar to a modern camera. Through the comparison of images acquired with a certain time separation, the motion of features may be tracked and quantified, yielding an estimate of velocity when the temporal separation is taken into account. This method is typically denoted as feature tracking or offset tracking (Scambos et al., 1992), and it is also applicable to SAR measurements - it will be further described in section 2.2. A long archive of optical satellite images exists, provided in part by the NASA/USGS Landsat program and MODIS sensors and, more recently, the EU/ESA Sentinel-2 and -3 missions. Several commercial satellites exist, carrying high resolution (decimetric) optical sensors. Although such sensors typically have small swath sizes, which are less ideal for ice sheet mapping, they have proven valuable in retrieving surface properties and ice flow on mountain glaciers (Millan et al., 2019). Optical sensors rely on sun illumination of the imaged area, as they carry passive sensors, which implies that measurements in polar regions are not available during winter. Another limitation is cloud cover, which is opaque at optical wavelengths. In spite of these limitations, optical ice velocity measurements have been used extensively in mapping ice flow on the ice sheets of Greenland (Joughin et al., 2018b) and Antarctica (Mouginot et al., 2017), as well as glaciers worldwide (Millan et al., 2022). Furthermore, optical sensors have provided a valuable tool in generating surface elevation measurements for use in Digital Elevation Models (Howat et al., 2014; Porter et al., 2018). In the work related to this thesis, optical ice velocity retrievals were not carried out.

Conversely to optical sensors, a SAR is an active sensor, carrying a transmitting and receiving radar system. Consequently, SAR sensors do not rely on sun illumination, and as the radar transmits and receives electromagnetic waves at microwave frequencies (often in the L, C, or X frequency bands, corresponding to 1-12 GHz), SAR acquisitions are not limited by cloud cover. A SAR is an imaging radar, meaning that a two-dimensional image is acquired with each pass of the satellite. The image is complex, as it includes both

the amplitude and phase of the reflected radar signal. Analyzing images with a certain time separation, measurements of motion may be obtained through several methods. The amplitude signal allows for ice velocity measurement through tracking-based techniques (Gray et al., 1998; Strozzi et al., 2002), similar to those applied to optical data. The phase signal may be exploited through several techniques (Goldstein et al., 1993; Bechor & Zebker, 2006; Jiang et al., 2017a), collectively known as interferometric techniques. In general, phase-based techniques yield velocity measurements of significantly higher accuracy and spatial resolution, compared to amplitude-based measurements. Section 2.1 provides an introduction to the principles of SAR image acquisition and the relevant terminology, and section 2.2 describes the various methods that allow for retrieval of ice velocity from SAR measurements. In the following, a brief outline of some important past and current SAR satellite missions is provided.

The first scientific (non-military) spaceborne SAR system was carried on the NASA satellite Seasat (Born et al., 1979), launched in 1978. As implied by the mission name, Seasat's main focus area was the marine sector, particularly measuring surface wave fields and sea ice properties. Launch of satellite SAR sensors greatly accelerated from the 1990's, with the European Space Agency (ESA) launching the ERS-1 and ERS-2 satellites in 1991 and 1995, respectively, followed by the ENVISAT satellite in 2002, and the Canadian Space Agency (CSA) launching Radarsat-1 in 1995. All of these satellites carried C-band (5.4 GHz) SAR systems, which were used for ice velocity mapping (Goldstein et al., 1993; Joughin et al., 1996; Joughin, 2002; Mouginot et al., 2012; Rignot & MacAyeal, 1998; Thiel et al., 1996), among other applications. Of special note should be the ERS tandem operation, in which the orbits of ERS-1 and ERS-2 were reconfigured to yield a 24 hour repeat pass period, allowing for interferometric measurements that would be infeasible with the standard 35-day period (Cumming et al., 1997; Mohr et al., 1998). Meanwhile, the Japanese Aerospace Exploration Agency (JAXA) launched the JERS-1 and ALOS-1 satellites in 1992 and 2006, respectively, which both carried L-band (1.2 GHz) SAR systems, also used in ice flow mapping (Nakamura et al., 2007; Rignot, 2008). At the time of operation of all of these systems, the main limitation in ice velocity retrieval was the limited amount of data (Joughin et al., 2018a). The relatively small swath size and low duty cycle (the amount of time the SAR sensor can be operated during an orbit) of the SAR systems meant that mapping was only possible for select regions, with a relatively low revisit frequency, and ice sheet-wide velocity retrievals in Greenland or Antarctica were generally not feasible. The next generation of SAR satellites addressed this limitation through new acquisition modes. The Radarsat-2 and ALOS-2 satellites, launched by CSA and JAXA in 2007 and 2014, respectively, both employ the ScanSAR mode (Moore et al., 1981), which trades resolution in one of the image dimensions for a larger swath size. The TerraSAR-X and TanDEM-X satellites were launched by the German Aerospace Agency (DLR) along with EADS Astrium in 2007 and 2010, respectively, carrying X-band (9.6 GHz) SAR systems. The satellites have been frequently used in ice velocity retrievals (Floricioiu et al., 2008), but have also been extensively operated in a tandem orbit, allowing

for the generation of high quality DEMs of extensive coverage (Rizzoli et al., 2017). The Italian Space Agency (ASI) and Ministry of Defence launched the four COSMO-SkyMed satellites in 2007-2010, which, among other applications, have been used to map grounding lines of marine-terminating glaciers (Milillo et al., 2017). Fig. 1.3 shows two examples of ice sheet-wide ice velocity mosaics generated using data from several of the SAR satellite systems described above. The SAR images used to compile the mosaics span several decades, meaning that the resulting velocity field is an estimate of the long-term average field.

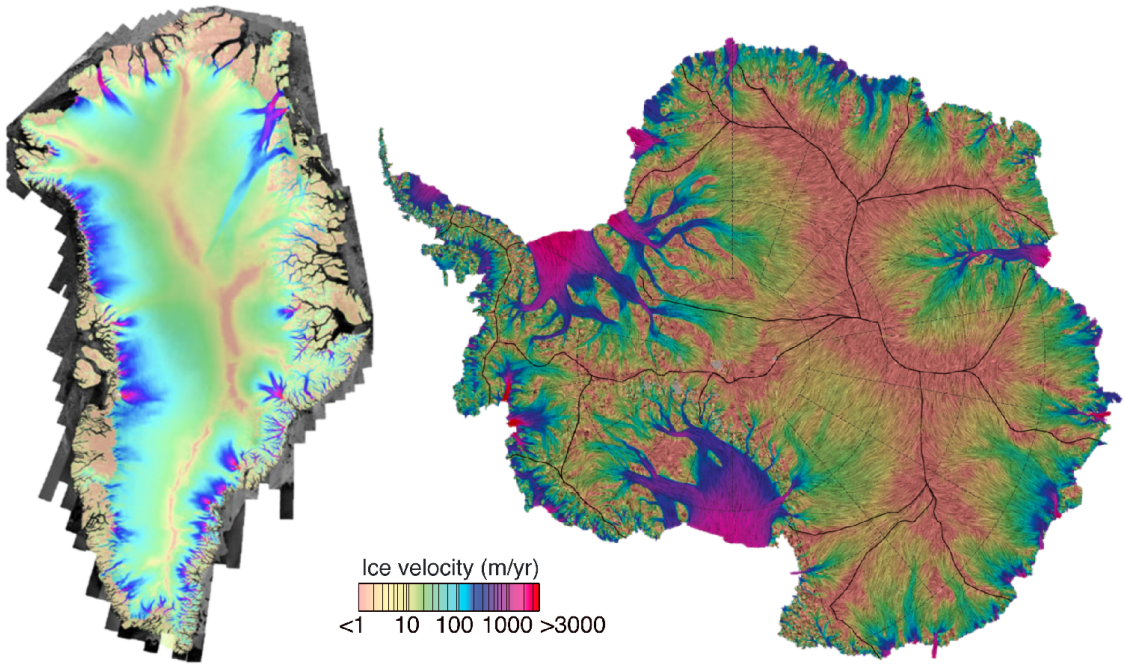

Figure 1.3: Ice velocity mosaics for the Greenland ice sheet (adapted from Joughin et al., 2018a) and Antarctic ice sheet (adapted from Mouginot et al., 2019a). The Greenland mosaic was generated using data from ERS-1/2, ALOS-1, Radarsat-1, TerraSAR-X, and Landsat-8. The Antarctic mosaic contains data from ERS-1/2, ENVISAT, ALOS-1/2, Radarsat-1/2, Landsat-8, and Sentinel-1.

Arguably, the most impactful SAR mission for consistent monitoring of ice dynamics has been the EU/ESA Sentinel-1 program. Since their launch in 2014 and 2016, respectively, the two Sentinel-1 satellites have gathered an extensive archive of polar measurements, with a particularly thorough spatiotemporal coverage of the Greenland ice sheet. The satellites employ the Terrain Observation by Progressive Scans (TOPS) acquisition mode (De Zan & Monti Guarnieri, 2006), which allows for a wide swath and hence comprehensive coverage in velocity retrievals (Nagler et al., 2015). The extensive coverage of Sentinel-1 combined with its open data policy (meaning that anyone is able to download the data) and the advancement of both processing techniques, computing power, and storage capacity has allowed for routine ice velocity retrieval over nearly the entire Greenland ice sheet, the majority of Antarctic outlet glaciers, and most other glaciers (Solgaard et al., 2021; Mouginot et al., 2017; Joughin et al., 2018b; Lei et al., 2021). Fig. 1.4 shows an example of

routinely generated Sentinel-1 ice velocity mosaics over Greenland. Such routine retrievals, however, have exploited only the amplitude signal of Sentinel-1, as the TOPS acquisition mode introduces specific challenges for interferometric processing (Mouginot et al., 2019a; Joughin et al., 2018a). Hence, a large archive of phase data over polar regions remains unexplored. The main goal of this PhD project is to unlock this archive and demonstrate its potential in monitoring ice dynamics.

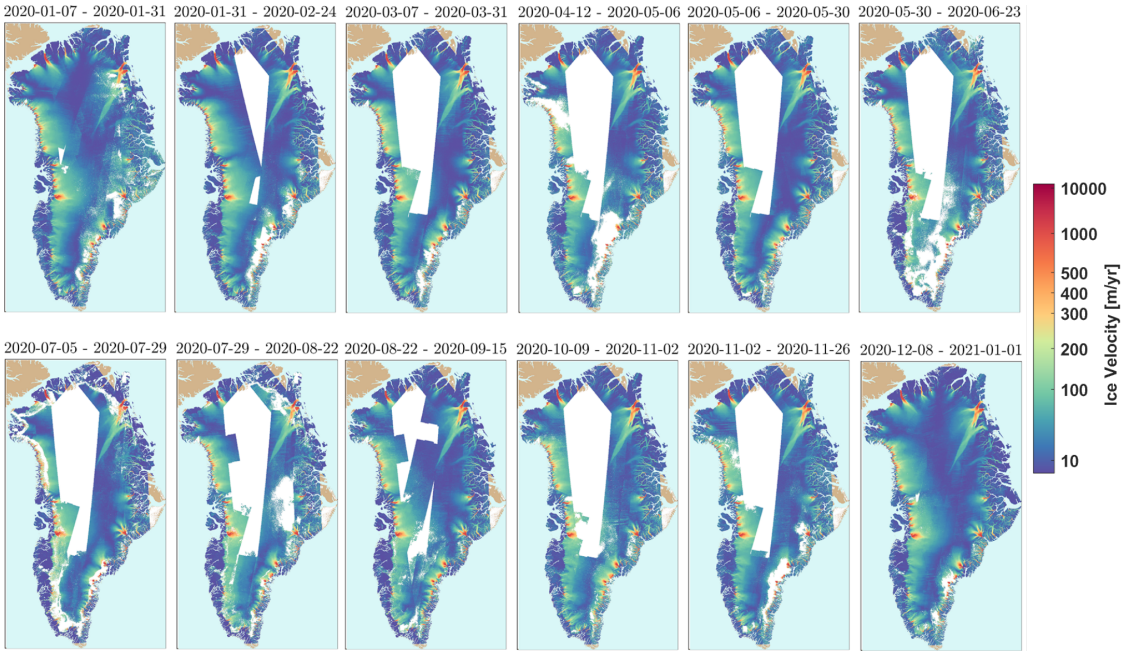

Figure 1.4: Examples of 24-day ice velocity mosaics generated with Sentinel-1 offset tracking measurements through the PROMICE program. (Image adapted from Solgaard et al., 2021).

1.3 Scope and outline of the thesis

The overall goal of the PhD project is to enable the exploitation of the vast archive of Sentinel-1 phase data in ice velocity retrieval. Aside from developing and implementing interferometric (DInSAR) routines for Sentinel-1 data, the aim is to demonstrate the value of DInSAR measurements in investigating changes in ice dynamics, particularly on short time scales and in slower-moving (inland) regions, where performance greatly exceeds that of tracking-based methods. The main research objectives of the PhD project can be summarized by the following three elements:

1. Design and implement methods allowing the interferometric retrieval of ice velocity from Sentinel-1 TOPS-mode measurements

2. Improve robustness of the Sentinel-1 interferometric algorithm for operational large-scale ice velocity retrieval

3. Demonstrate the potential of Sentinel-1 interferometry in studies of ice dynamic changes, exploiting the increased spatiotemporal resolution and accuracy

The thesis is comprised of six chapters, including the present introduction. **Chapter 2** provides relevant background knowledge on SAR image acquisition and methodologies related to ice velocity retrieval. **Chapter 3** addresses the first objective, documenting the work carried out to meet the coregistration requirements for applying Sentinel-1 TOPS interferometry over moderate and fast-flowing ice. **Chapter 4** documents efforts related to the second objective. Particularly, the work relates to the detection of phase unwrapping errors - the most prominent DInSAR error source in the context of ice velocity retrieval, which may yield errors of large magnitudes and extent. **Chapter 5** presents the work carried out under the third objective, providing demonstrations of Sentinel-1 DInSAR time series measurements. Specifically, the high accuracy and temporal resolution of the measurements are used to investigate both long-term (subtle) changes in flow speed and abrupt transient dynamic events. Finally, **Chapter 6** provides brief conclusions of the PhD project along with an outlook on potential future work. Chapters 3, 4, and 5 collectively include four journal manuscripts (three published and one currently in review). Each manuscript is introduced and briefly summarized in the main text, while the full manuscripts are provided in **Appendix A**. Supplementary materials are provided in **Appendix B**.

Chapter 2 | Background

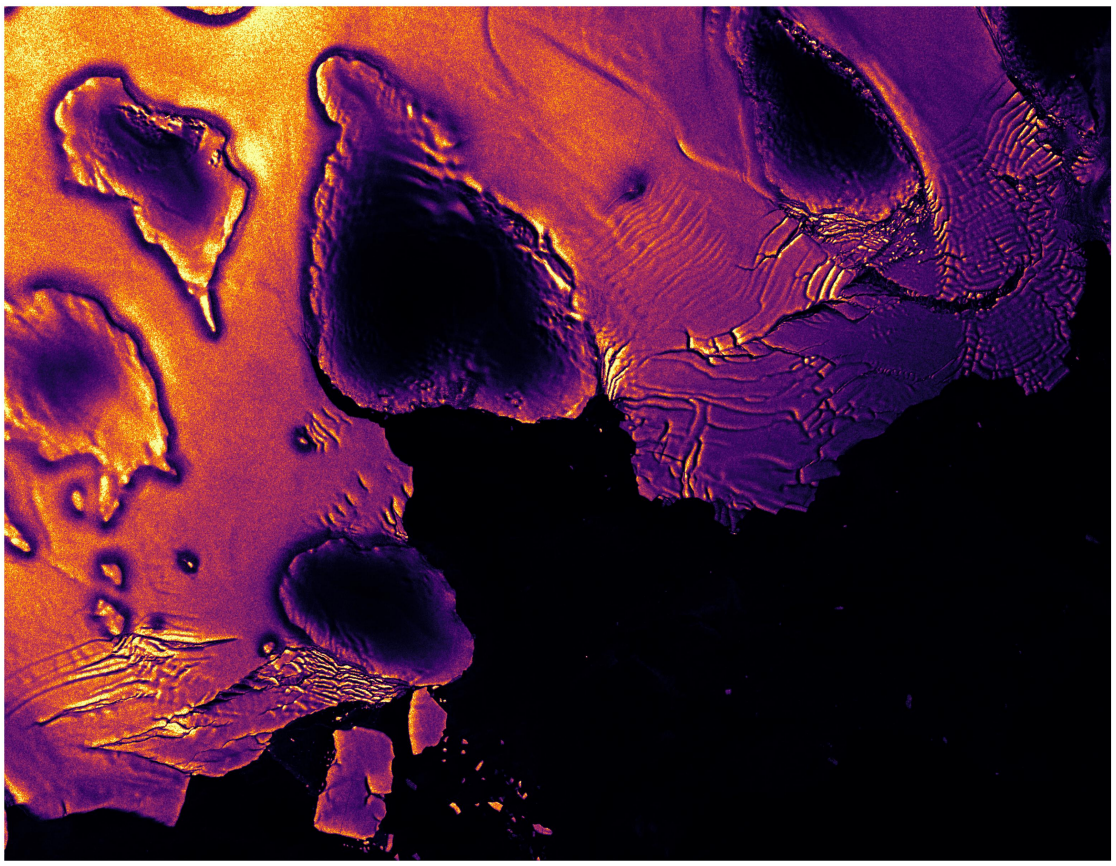

Sentinel-1 intensity image showing ice calving into the ocean in Sulzberger Bay, Antarctica.

2.1 SAR image acquisition - geometry and terminology

The goal of this section is to establish relevant terminology relating to the acquisition and processing of SAR images. The section is by no means a complete introduction to the concepts of SAR systems and processing, but aims to provide the reader with the background necessary to appreciate the results presented in the thesis. For a thorough introduction, the reader is referred to, e.g., Curlander and MacDonough, 1991 and Cumming and Wong, 2005. In the present section, an outline of the so-called Stripmap mode, which is the earliest and simplest SAR acquisition mode, is given. This is supplemented by a description of the Terrain Observation by Progressive Scans (TOPS) acquisition mode, employed by the Sentinel-1 satellites, in section 2.3. Section 2.2 introduces various methods for measuring motion with SAR images. Finally, sections 2.4-2.6 describe relevant error sources, the DInSAR calibration procedure, and the combination of multiple SAR velocity retrievals for inferring 3D motion, respectively.

A SAR system is, essentially, a radar mounted on a moving platform. The system may be airborne (mounted on airplanes, or even drones), however, throughout the thesis the focus lies on spaceborne, satellite SAR sensors. Conversely to optical sensors and radar/laser altimeters, which are generally pointed in the nadir direction, SAR sensors are side-looking. In the basic Stripmap acquisition mode (see Fig. 2.1), the sensor is pointed (approximately) perpendicular to the satellite flight path. The projection of the flight path to ground is known as the azimuth. As the satellite travels through orbit, the radar transmits and receives electromagnetic pulses of a certain microwave carrier frequency. In the case of Sentinel-1 the carrier frequency is 5.4 GHz, translating to a wavelength of 5.6 cm. The reader may be familiar with a simple stationary radar system, in which timing information of a received pulse is translated into a measure of distance, also known as range, to an object that reflected the transmitted pulse. With SAR, a given object (or *target*) on ground is illuminated by multiple pulses, as the satellite passes by and the target enters the antenna beam footprint. For each received pulse, reaching the antenna after being reflected and scattered by a target, a signal, or *echo*, is recorded. The echo consists of an amplitude (relating to the strength of the reflected wave) and a phase (relating to the scattering properties of the given target and, in principle, the distance to the target).

With this, we have established the two-dimensional nature of a SAR image, the dimensions being the sensor flight path, known as azimuth, and the sensor line-of-sight (LoS), also known as the slant range (i.e. the slanted line between the radar and target, sometimes abbreviated to just range). Simply arranging the recorded echoes line-by-line, however, would lead to an image of very poor resolution. This is because the azimuth antenna beam width and the length of the radar pulse, which collectively define the area within which targets contribute to the echo recorded at a given pixel, are both on the order of several kilometers. Instead, to achieve a much better resolution, on the order of a few meters, advanced signal processing techniques are applied to the received echoes. To improve the slant range resolution, a relatively common technique known as pulse compression is applied. The method involves transmission of a coded pulse, e.g. using linear frequency

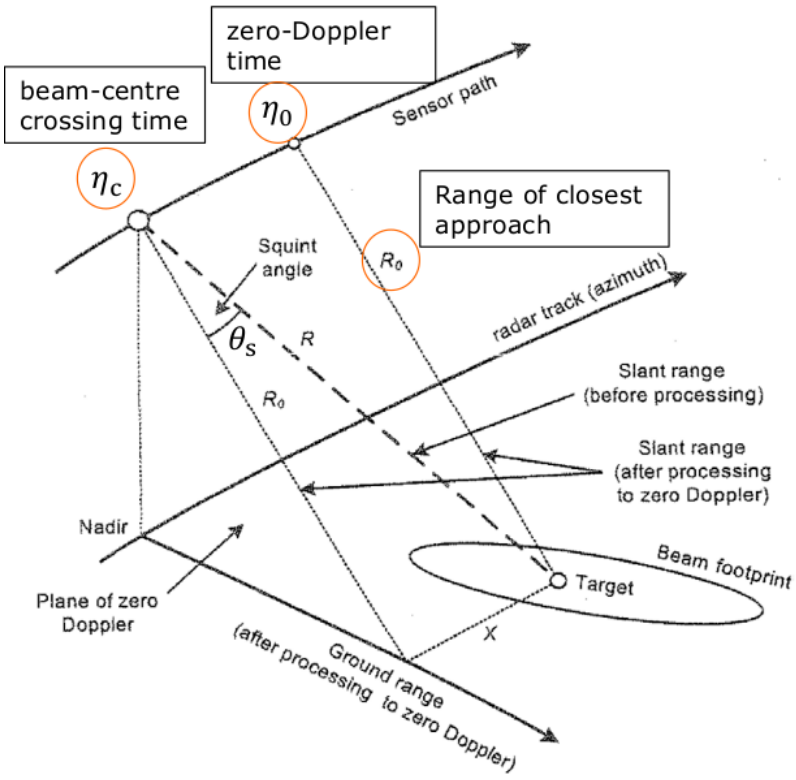

Figure 2.1: Sketch outlining the SAR acquisition geometry of the Stripmap mode. The various parameters are described in the text. (Adapted from Cumming and Wong, 2005)

modulation (FM), followed by correlation with the incoming echoes - a process known as matched filtering. The technique used to obtain high resolution in azimuth is what gives rise to the name *synthetic aperture radar*. In principle, the technique corresponds to pulse compression. It exploits the fact that echoes from a single target are received with a range of Doppler frequency shifts, which, through signal processing, yields a synthetic aperture (i.e. antenna) of several kilometers. As the antenna beam passes by a given target, the Doppler shift of the received echo varies with the sensor-to-target velocity, from positive values (when the sensor is approaching the target), to zero (when the sensor is exactly at the range of closest approach, also known as zero-Doppler time, see Fig. 2.1), and finally to negative values (as the sensor moves away from the target). With the antenna pointed roughly perpendicular to the azimuth, and under the assumption of a relatively narrow antenna beam in azimuth, the Doppler time series for the target will be linear, giving rise to a linear frequency modulation in the azimuth dimension (which in range was achieved through pulse coding). As the received echoes are recorded coherently (i.e. preserving the phase of the signal), the Doppler histories allow for compression in the azimuth dimension, which yields a resolution that is independent of range.

With the range and azimuth compression performed, the resulting SAR image is denoted as *focused*. The focused SAR image is also known as a *Single Look Complex* (SLC) image, where ”single look” refers to the fact that no spatial averaging has been performed and

"complex" refers to the fact that both an amplitude and a phase signal is recorded. For FM signals, the time-domain resolution is simply $1/B$, i.e. the inverse of the bandwidth, which in the slant range case is determined by the width of the transmitted chirp and in the azimuth case depends on the total range of measured Doppler shifts (which in turn is dependent on antenna properties). The digital sampling is controlled by the receiver electronics in the range case and by the pulse repetition frequency in the azimuth. Naturally, the sampling frequencies must be larger than the corresponding bandwidths, to comply with the Nyquist theorem and avoid undersampling. Hence, an image pixel is always smaller than the resolution cell. Several important trade-offs exist in the selection of all of these (and more) parameters (Curlander & MacDonough, 1991; Cumming & Wong, 2005), which we will not cover further in depth here. In the focused SAR image, each pixel is usually placed at the zero Doppler position, corresponding to the range and azimuth time of closest approach, such that the azimuth and LoS image dimensions are perpendicular, even if the sensor is not pointed perfectly perpendicular to the flight path (see Fig. 2.1, where the acquisition is squinted slightly forward by an angle, θ_s). Each pixel is represented by a complex number, corresponding to the amplitude and phase of the coherent sum of scattered signals returning from the area represented by the pixel. Note that the SAR image is actually slanted and hence does not align with the ground plane. Assuming horizontal (flat) terrain, a given slant range distance, R_0, is projected to ground range, R_g, as:

$$R_g = \frac{R_0}{\sin\theta_i} \tag{2.1}$$

where θ_i is the incidence angle of the radar look vector relative to a vertical line from the horizontal plane (see also Fig. 2.8). Assuming flat terrain, the ground range resolution increases with increasing distance from the radar, asymptotically approaching the slant range resolution. In order to accurately reference an image to ground (referred to here as geocoding) or to reference one SAR image to another (known as coregistration), a priori knowledge on the terrain height is required, typically provided in the form of a Digital Elevation Model (DEM).

A perfect point target, i.e. a target that perfectly reflects the transmitted pulse, would yield the following signal, which can be considered an approximation of the SAR impulse response:

$$s_1(\tau,\eta) = A_1 \exp(j\psi_1)\, p_r(\tau-\tau_0)\, p_a(\eta-\eta_0) \exp(-j2\pi f_c \tau_0) \exp(j2\pi f_{DC}(\eta-\eta_0)) \tag{2.2}$$

where (τ,η) are the range and azimuth time coordinates, respectively. Note that these time coordinates are associated with their corresponding spatial coordinates (slant range, R, and azimuth, x) as:

$$\tau = \frac{2R}{c} \tag{2.3}$$

$$\eta = \frac{x}{V_r} \tag{2.4}$$

where c is the speed of light, and V_r is the effective velocity of the satellite in a rectilinear coordinate system (Cumming & Wong, 2005). The factor two in eq. (2.3) accounts for the fact that τ measures the two-way travel time of the radar wave (i.e. from the sensor to the target and back again). Returning to eq. (2.2), R_0 and η_0 represent the range and azimuth time at closest approach, respectively. f_c is the radar carrier frequency, related to the radar wavelength, λ, through $\lambda = c/f_c$. A_1 and ψ_1 are amplitude and phase terms relating to the observed target and p_r and p_a are two sinc-like functions modulating the amplitude in the range and azimuth dimensions. Finally, f_{DC} is the so-called Doppler centroid frequency, which is the Doppler frequency of the target at the beam-center crossing time, η_c (see Fig. 2.1). If the sensor line-of-sight is perfectly perpendicular to the flight path, $\eta_c = \eta_0$, and the Doppler centroid is zero. If the line-of-sight is oriented backward or forward (as in Fig. 2.1) from the perpendicular, the Doppler centroid is negative or positive, respectively. Note that the phase of the measured signal consists of three contributions, one dependent on electromagnetic properties of the observed target, one dependent on the range to the target and the radar wavelength, and one dependent on the Doppler centroid and the azimuth time coordinate. The two latter phase terms allow for motion measurements, through methods outlined in the following section.

The first phase term depends on the scattering properties of the observed target, and hence also on the radar wavelength. In practice, the observed target is rarely a perfect point target. Instead, the received signal stems from the superposition of reflections from many scatterers distributed within the resolution cell, which is generally on the order of tens of m^2 in area. This gives rise to the phenomenon known as *speckle*. Two neighboring resolution cells, covering, for instance, a field of crops or a glacier, will consist of similar scattering elements (leaves or stems from the crops in the first case or ridges in the ice surface in the latter case, all of the same scale as the radar wavelength). However, the exact pattern of constructive and destructive interference arising from the coherent summation of reflections from the various scatterers is unlikely to be exactly the same between the two resolution cells. Consequently, speckle may lead to a substantial difference in the received amplitude and phase in neighboring pixels. Speckle is the cause of the grainy effect observed in the intensity image in Fig. 2.2 and the seemingly random pattern observed in the SLC phase images in Fig. 2.3. Speckle is often referred to as speckle noise, as it is an unwanted signal in many applications. Reduction of speckle is almost always performed in interferometric applications by performing so-called *multi-looking*, corresponding to a spatial averaging of measurements. Naturally, the speckle reduction obtained from spatial averaging comes at the cost of reduced resolution. Fig. 2.2 shows an example of the effects of multi-looking.

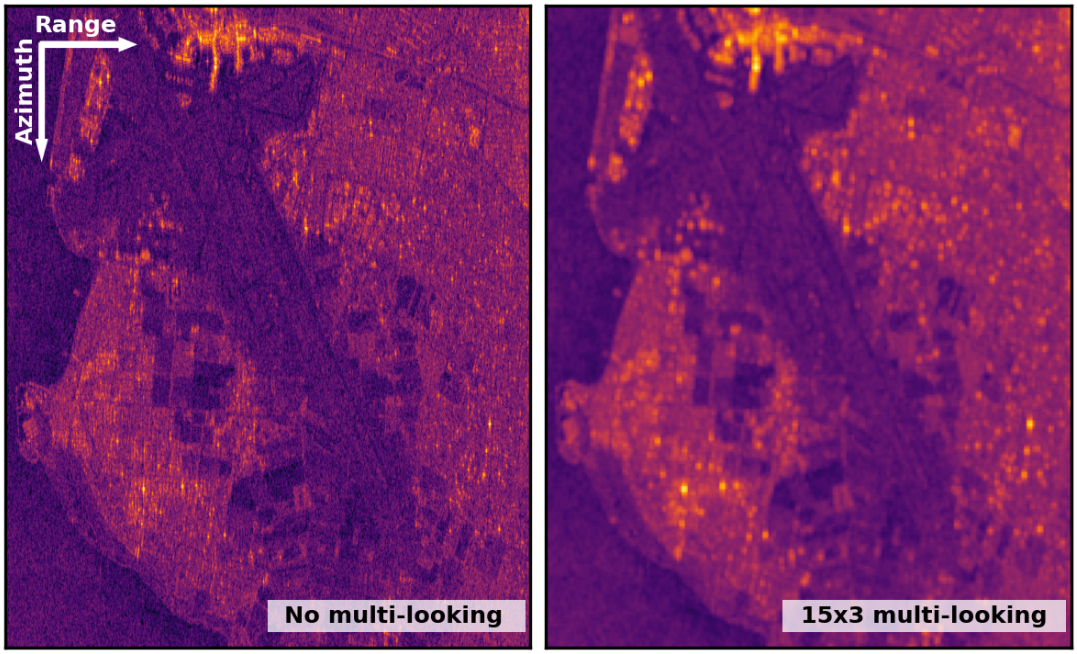

Figure 2.2: Sentinel-1 intensity image (i.e. amplitude squared) from an area around Copenhagen Airport before and after multi-looking. Speckle is clearly observed over fields, grass areas near the airport, and even over the ocean to the very left. Multi-looking substantially reduces speckle but leads to an image of coarser resolution.

2.2 SAR-based ice velocity retrieval

In this section, an outline of various methods for measuring displacements based on a pair of SAR images is provided. The methods are well established and have been applied to older SAR sensors (ERS, ALOS-1, Radarsat-1, etc.) as well as Sentinel-1 for various applications, e.g. seismic or volcanic activity, ground subsidence, or ice motion (Goldstein et al., 1993; Massonnet et al., 1994; Joughin, 2002; Jiang et al., 2017b; Mouginot et al., 2019a). Note that all of the methods measure *displacement* occurring in the time between the two SAR acquisitions, also known as the *temporal baseline*. Velocity measurements are simply computed as the measured displacement divided by the temporal baseline, which implicitly assumes that the observed displacements occur at a constant velocity. In the context of ice flow measured with temporal baselines of 6 or 12 days (the shortest possible with Sentinel-1), this assumption is generally assumed to be valid, although the presence of sudden transient flow changes could lead to a misinterpretation (as displacements occurring over times shorter than the temporal baseline of the SAR acquisitions will be averaged over the full temporal baseline).

For the phase-based motion retrieval methods, a prerequisite is that the two SAR acquisitions are coregistered, i.e. resampled to a common grid, such that the phase is compared at the same location in the two images. In practice, the *secondary* image (i.e. the second acquisition) is resampled to the geometry defined by the *reference* image (i.e. the first

acquisition). Although several approaches to coregistration exist, throughout the work presented here, coregistration is carried out through a back-projection approach, in which the geometry of the reference image is first referred to an Earth ellipsoid, then to the geometry of the secondary image, using FFT interpolation to allow sub-pixel precision. This allows for a resampling of the secondary image into the reference geometry. The process is known as *geometrical coregistration* and requires a DEM and precise orbit state vectors (Sansosti et al., 2006). Note that the exact correspondence between reference and secondary image pixels also depend on underlying motion within the imaged scene. This aspect is especially relevant in the case of Sentinel-1 TOPS measurements, and hence coregistration is a central element in Sentinel-1 interferometry. Refinements of the TOPS coregistration process is the topic of Chapter 3.

In the following, theoretical derivations assume the case of Stripmap acquisitions. Section 2.3 details important differences related to the TOPS mode, and hence to Sentinel-1 measurements, as well as an additional motion retrieval method unique to TOPS acquisitions. Table 2.1 gives a brief recap of the most important advantages and disadvantages of each of the described methods. Fig. 2.6 shows example ice velocity retrievals for the various methods.

Table 2.1: Overview of SAR motion retrieval methods described in sections 2.2-2.3.

Method	**Component**	**Advantages**	**Disadvantages**
DInSAR	LoS	Superior resolution and accuracy	Phase unwrapping needed, only LoS component, relative measurements
MAI	Azimuth	Measures all sources of azimuth misregistration, (generally) no unwrapping	Low resolution/accuracy (especially for TOPS mode)
BO-MAI	Azimuth	Measures all sources of azimuth misregistration, higher accuracy/resolution than MAI	Only applicable within TOPS/ScanSAR burst overlaps
Offset tracking	LoS + azimuth	2D motion, no unwrapping, applicable in fast flow	Low resolution and accuracy

2.2.1 Differential SAR interferometry

Differential SAR Interferometry (DInSAR) is a technique that estimates ground motion through the difference in phase signal between subsequently acquired SAR images, also known as repeat-pass interferometry. The received SAR signal of a point target, $s_1(\tau, \eta)$, was described by eq. (2.2) above. We now imagine a second SAR image, acquired a certain time Δt after the first, during which the target has moved a distance corresponding to $\Delta R = \Delta\tau c/2$ in slant range and $\Delta x = \Delta\eta V_r$ in azimuth:

$$s_2(\tau,\eta) \propto \exp(j\psi_2)\exp(-j2\pi f_c(\tau_0+\Delta\tau))\exp(j2\pi f_{DC}(\eta-(\eta_0+\Delta\eta))) \tag{2.5}$$

where amplitude terms have been omitted. Assuming coregistered images, an interferogram is simply formed as the multiplication of the first image with the complex conjugation of the second image:

$$I_D = s_1(\tau,\eta)\cdot s_2^*(\tau,\eta) = |s_1\cdot s_2^*|\exp(\phi_D) \tag{2.6}$$

where the interferogram phase, i.e. the phase difference between the two acquisitions, can be separated in the following contributions:

$$\phi_D = \Delta\psi + \frac{4\pi\Delta R}{\lambda} + 2\pi f_{DC}\Delta\eta + \Delta\phi_{topo} + \Delta\phi_{tropo} + \Delta\phi_{iono} \tag{2.7}$$

The first term is related to the difference in scattering properties of the given target between the two acquisitions, i.e. the speckle effect described in the previous section. If the scattering properties of the target (or resolution cell) are similar in the two acquisitions, then $\Delta\psi$ has a distribution that is closely centered around a mean value of zero (Bamler & Hartl, 1998). The statistical similarity of the scattering properties is defined as the *interferometric coherence*. As coherence decreases, the distribution of $\Delta\psi$ widens, and phase noise increases. A moderate level of coherence is a necessity for performing interferometric measurements. In the case of complete loss of coherence, also known as decorrelation, between the two acquisitions, $\Delta\psi$ will have a uniform distribution in the interval $[0;2\pi]$ and hence dominate the retrieved phase signal, making retrieval of ground motion impossible. In the context of ice velocity retrieval, loss of coherence may occur due to, e.g., surface melt, precipitation, rearrangement of snow layers due to winds, and shear stress caused by high velocity gradients. Such sources of coherence loss are typically denoted as *temporal decorrelation*, as their effect is increased with an increasing temporal baseline. Several other sources of decorrelation exist (see also section 2.4). Interferometric coherence is determined through the complex cross-correlation between the two SAR acquisitions:

$$\gamma = \frac{E(s_1\cdot s_2^*)}{\sqrt{E(|s_1|^2)}\sqrt{E(|s_2^*|^2)}} \simeq \frac{\Sigma_{i=1}^N s_1\cdot s_2^*}{\sqrt{\Sigma_{i=1}^N |s_1|^2}\sqrt{\Sigma_{i=1}^N |s_2^*|^2}} \tag{2.8}$$

where $E(\cdot)$ indicates the expected value, which in the final approximation is replaced by a summation over N image samples, assuming ergodicity. As previously mentioned, speckle noise may be reduced through multi-looking, which is usually done in DInSAR applications with window sizes of a few resolution cells in each dimension (resulting in a resolution on the order of 20-100 m for the final output measurements). In some applications, spectral filters, originally proposed by Goldstein and Werner, 1998, are used to further reduce phase noise.

The second term in eq. (2.7) is related to the difference in the sensor-to-target distance between the acquisitions, ΔR, i.e. the displacement of the target in the LoS direction, which is the desired signal in DInSAR. The third term is dependent on the Doppler centroid frequency and the displacement in the azimuth dimension. In general, this phase term is considered negligible for Stripmap acquisitions, where f_{DC} is typically close to zero and has a negligible variance across the scene. The fourth term, $\Delta\phi_{topo}$, relates to the difference in range caused by the sensor viewing the target from two different vantage points specifically in case of a non-zero distance in the plane perpendicular to the LoS, which is known as the *perpendicular baseline*. The phase term can be considered as two separate contributions: the phase that would be observed from a perfectly flat surface (referred to as the flat-earth phase) and the additional phase difference caused by local topography. In the case of DInSAR, where we wish to measure ground motion, these phase contributions can be estimated, and thus compensated for, through knowledge of the satellite orbit path and a DEM covering the scene. Alternatively, the sensitivity to topography can be used to generate DEMs, as has been done extensively (Rabus et al., 2003; Rizzoli et al., 2017). The final two terms in eq. (2.7) represent differences in propagation delay in the troposphere, $\Delta\phi_{tropo}$ (caused by differences in, e.g., water vapor levels), and in the ionosphere, $\Delta\phi_{iono}$ (caused by modulation of the radar signal by the electron content). Several past studies have investigated methods for estimating and compensating the tropospheric and ionospheric phase contributions (Bekaert et al., 2015; Brcic et al., 2010; Scott & Lohman, 2016; Yu et al., 2018). Such methods are not applied in the DInSAR processing presented in the thesis.

Fig. 2.3 shows an example of two Sentinel-1 SLC images, acquired 6 days apart near the ice front of Zachariae Isstrøm, Greenland. The phase images of the individual SLCs are seen to contain no interpretable information, however the interferometric phase contains a clear signal where coherence is retained.

Assuming all other phase contributions in eq. (2.7) can be eliminated or neglected, the measured interferometric phase is seen to be directly proportional to the LoS displacement, ΔR, and the radar wavelength, λ. Note that the radar wavelength is only a few centimeters (5.6 cm in the case of Sentinel-1), illustrating how DInSAR is sensitive to motion of very small scale, yielding high accuracy velocity retrievals. The process of computing displacement is, however, complicated by the fact that we are measuring a phase signal. The measured phase is obtained through the comparison of the received signal with a stable reference oscillator in the sensor. The phase measurement is constrained in the interval $[-\pi;\pi]$ (or -180 to 180 degrees) and is often denoted as the *wrapped phase*. However, the interferometric phase difference may easily exceed 2π, which corresponds to a displacement of just $\lambda/2$. In that case, the correct phase will consist of the measured ϕ_D plus/minus some integer multiple of 2π:

$$\phi_{unw} = \phi_D + 2\pi N \tag{2.9}$$

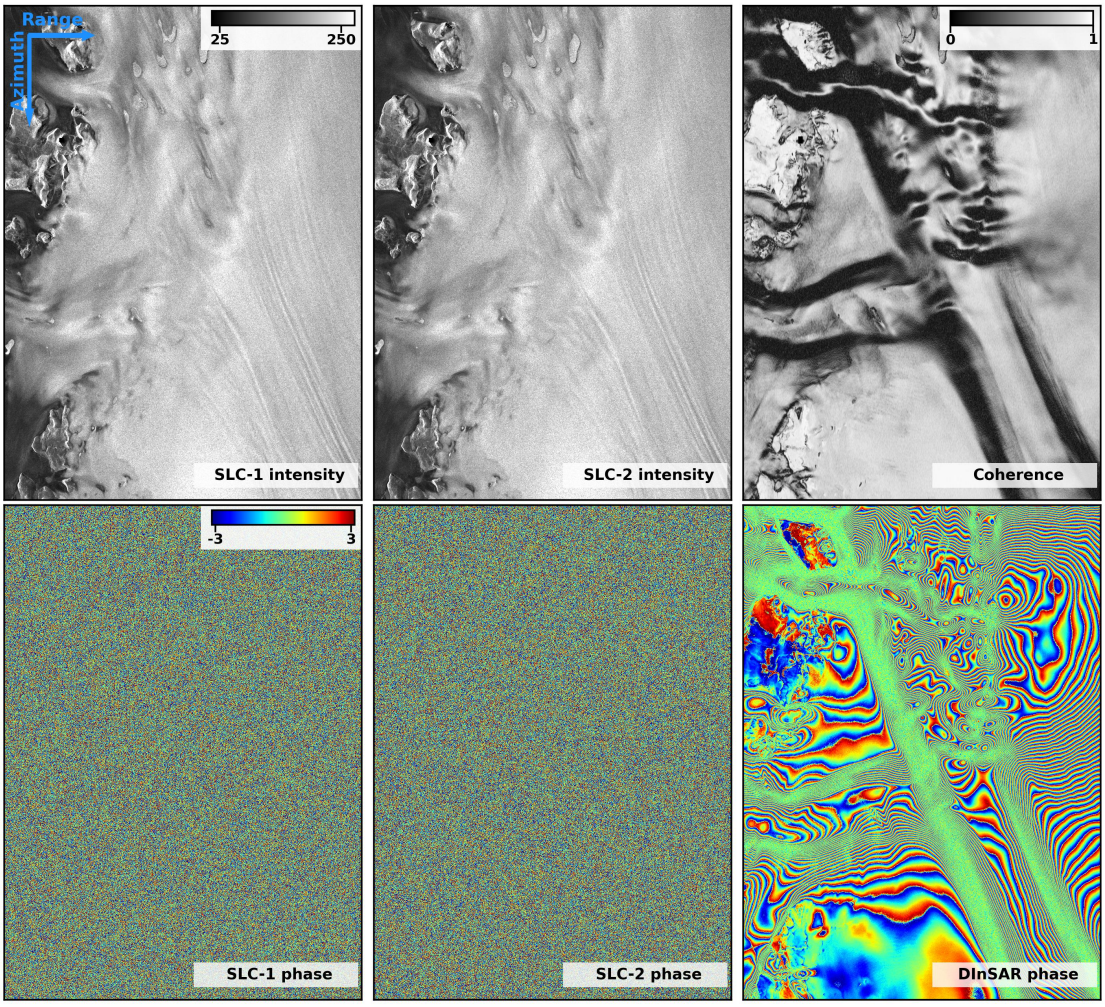

Figure 2.3: Example of an interferogram generated from a pair of Sentinel-1 SLC images near the outlet of Zachariae Isstrøm. The first two columns show the intensity (squared amplitude) and phase of the SLC images. Note how the SLC phase images show a uniform distribution, with seemingly no usable information. The third column shows the interferometric coherence and the differential phase obtained from DInSAR (after eliminating the topographic phase contribution). The dense fringe pattern indicates a high amount of motion. Coherence is lost in regions of high motion gradients, due to a change in orientation of the ice fabric caused by high shear stresses (Goldstein et al., 1993).

where N is an integer. The process of solving eq. (2.9) for all pixels in the scene is known as *phase unwrapping* and involves integration of the 2D wrapped phase image, resulting in the *unwrapped phase* image, ϕ_{unw}. Several approaches to phase unwrapping have been developed and extensively applied (Goldstein et al., 1988; Costantini, 1998; Chen & Zebker, 2000; Fornaro et al., 1996). A requirement for successful phase unwrapping is that the local phase gradient, i.e. the phase difference between neighboring pixels, does not exceed π radians, corresponding to a displacement difference of $\lambda/4$, as this would otherwise cause ambiguities. Fig. 2.4 shows an example of a wrapped and unwrapped phase image. From

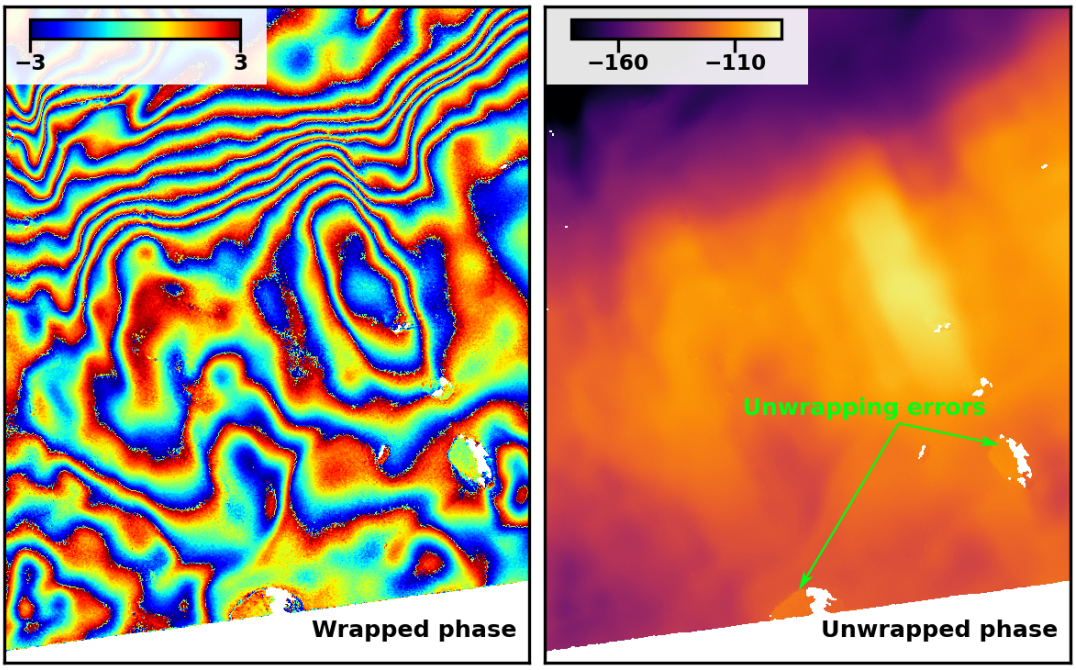

Figure 2.4: Subset of a Sentinel-1 interferogram near the southwest coast of Greenland. To the left, the wrapped differential phase is shown. The unwrapped phase is shown to the right. Both phase images are shown in units of radians. Pixels with a coherence level below 0.2 are discarded and are shown as transparent. Note how (presumed) phase unwrapping errors occur for two small regions, which show very steep gradients in the unwrapped phase. The errors occur near areas where coherence is partially lost, as shown by the transparent pixels.

the unwrapped phase, LoS velocity measurements are computed as:

$$v_{LoS} = \phi_{unw} \cdot \frac{\lambda}{4\pi T} + \epsilon \tag{2.10}$$

where T is the temporal baseline of the SAR image pair and ϵ represents all error terms, such as phase noise, inaccuracies of the DEM used to eliminated topographic signals, and tropospheric/ionospheric effects. In the derivations above, a perfect coregistration is assumed. Aside from the phase unwrapping process itself, which in many cases can be quite challenging, the problem of retrieving motion is further complicated by the fact that the unwrapped phase image provides measurements that are *relative*, i.e. referred to a seed point selected in the unwrapping process. In order to retrieve absolute displacements, one must refer the measurements to one (or more) point(s) of known displacement. This process is known as *calibration* and is described further in section 2.5. The calibration process may also mitigate large-scale errors caused by orbital uncertainties and/or atmospheric error contributions, which may also be relevant in offset tracking and Multi-Aperture Interferometry measurements.

2.2.2 Multi-aperture interferometry

One of the main limitations of the DInSAR technique is that only one component of the three-dimensional motion vector is measured, namely the component in the sensor LoS direction. Multi-Aperture Interferometry (MAI) is a phase-based technique that is sensitive to motion in the azimuth direction, making a 2D velocity retrieval from a single SAR image pair possible by combining both methods. The MAI method involves the generation of interferograms generated with upper and lower spectral sub-bands of the two SAR acquisitions followed by the computation of a so-called *double difference interferogram*. The first proposal for such a method used sub-bands in the range dimension in order to estimate absolute phase (Madsen & Zebker, 1992). A similar method was proposed with the objective of refining image coregistration using both range and azimuth sub-bands (Moreira & Scheiber, 1998; Scheiber & Moreira, 2000) and was given the name Spectral Diversity. Finally, the azimuth Spectral Diversity method was reformulated with an emphasis on measuring physical motion, rather than misregistration. This method was named MAI (Bechor & Zebker, 2006) and is the one presented here.

The MAI principle can be understood through the following relation between the Doppler centroid frequency, f_{DC}, and the sensor squint angle, θ_s (recall Fig. 2.1), (Cumming & Wong, 2005):

$$f_{DC} = \frac{2V_s \sin\theta_s}{\lambda} \simeq \frac{2V_s\theta_s}{\lambda} \tag{2.11}$$

where the second equality, and hence the proportionality between Doppler centroid and squint angle, holds for small angles. The relation above confirms the intuitive idea that a forward-squinted acquisition leads to a positive Doppler shift, while the opposite is true for the backward-squinted case. The relation also suggests that extracting part of the Doppler spectrum (i.e. band-pass filtering the azimuth spectrum) effectively generates a squinted acquisition. Hence, an interferogram may be formed by the (synthetically) forward-squinted acquisitions, which are centered on the higher Doppler centroid frequency f_{DC}^u:

$$I_u \propto \exp\left(j\Delta\psi_u\right) \exp\left(j2\pi f_c \Delta\tau\right) \exp\left(j2\pi f_{DC}^u \Delta\eta\right) \tag{2.12}$$

and similarly, a backward-squinted interferogram, centered on the lower Doppler centroid f_{DC}^l becomes:

$$I_l \propto \exp\left(j\Delta\psi_l\right) \exp\left(j2\pi f_c \Delta\tau\right) \exp\left(j2\pi f_{DC}^l \Delta\eta\right) \tag{2.13}$$

A double difference interferogram can now be formed by interfering the two squinted interferograms (showing only phase terms):

$$I_{MAI} = I_u \cdot I_l^* \propto \exp\left(j\Delta\psi\right) \exp\left(j2\pi \left(f_{DC}^u - f_{DC}^l\right) \Delta\eta\right) \tag{2.14}$$

and it is noted that the phase term related to LoS displacement cancels out in the MAI interferogram, leaving behind only a term related to phase noise, $\Delta\psi$, and a term related to azimuth displacement, $\Delta\eta$. In section 2.2.1, it was stated that, for Stripmap acquisitions, the azimuth displacement term in the interferometric phase of eq. (2.7) is often neglected, as the Doppler centroid frequency is close to zero. In the MAI phase, however, the azimuth displacement is proportional not to the original Doppler centroid, but to the difference in Doppler centroids between the upper and lower sub-bands, $\Delta f_{DC} = f_{DC}^{u} - f_{DC}^{l}$. Hence, ignoring error terms, azimuth displacement can be retrieved from the MAI interferogram phase as:

$$\Delta x = \Delta\eta V_r = \phi_{MAI} \cdot \frac{V_r}{2\pi \left(f_{DC}^{u} - f_{DC}^{l}\right)} \tag{2.15}$$

Azimuth velocity is then obtained simply as Δx divided by the temporal baseline of the image pair. Note that, similarly to DInSAR, MAI measures a timing difference, $\Delta\eta$, which in practice relates not only to displacement. In the MAI case, the measured phase, and hence timing difference, contains the following additional contributions:

$$\Delta\eta = \Delta\eta_{motion} + \Delta\eta_{orb} + \Delta\eta_{coreg} + \Delta\eta_{iono} \tag{2.16}$$

where the first component relates to the physical displacement, i.e. the signal of interest. The remaining components are related to uncertainties in the orbit state vectors, coregistration errors, and ionospheric propagation, respectively. From eq. (2.15) it is seen that the sensitivity to azimuth displacement is determined by the Doppler frequency separation, Δf_{DC}, motivating a large separation between the two sub-bands. On the other hand, as the total available bandwidth is finite, increasing the frequency separation means that the bandwidth of each sub-band must be decreased (see Fig. 2.5). The bandwidth determines the azimuth resolution and hence a trade-off exists between maximizing the frequency separation and maximizing the sub-band width. Previous studies derive an optimal frequency band separation as 2/3 of the azimuth bandwidth (Bamler & Eineder, 2005).

Just as DInSAR, the MAI method relies on interferometric coherence being retained. Due to the limited bandwidth (and the relatively low sensitivity, compared to DInSAR), a high amount of multi-looking is typically necessary in order to generate displacement measurements with an acceptable noise level. Consequently, MAI measurements usually have lower resolution than those obtained with DInSAR (see Fig. 2.6). An advantage of the relatively low sensitivity, however, is that phase unwrapping is often not required, as the azimuth motion that would be required to exceed a phase of 2π is generally high enough to cause complete loss of coherence (particularly for Sentinel-1). In some cases, this may mean an improvement in coverage, compared to DInSAR.

2.2.3 Amplitude-based offset tracking

Offset tracking techniques allow for the measurement of motion in both the LoS and azimuth directions. For a given image pair, the amplitude terms, defined in eq. (2.2), are

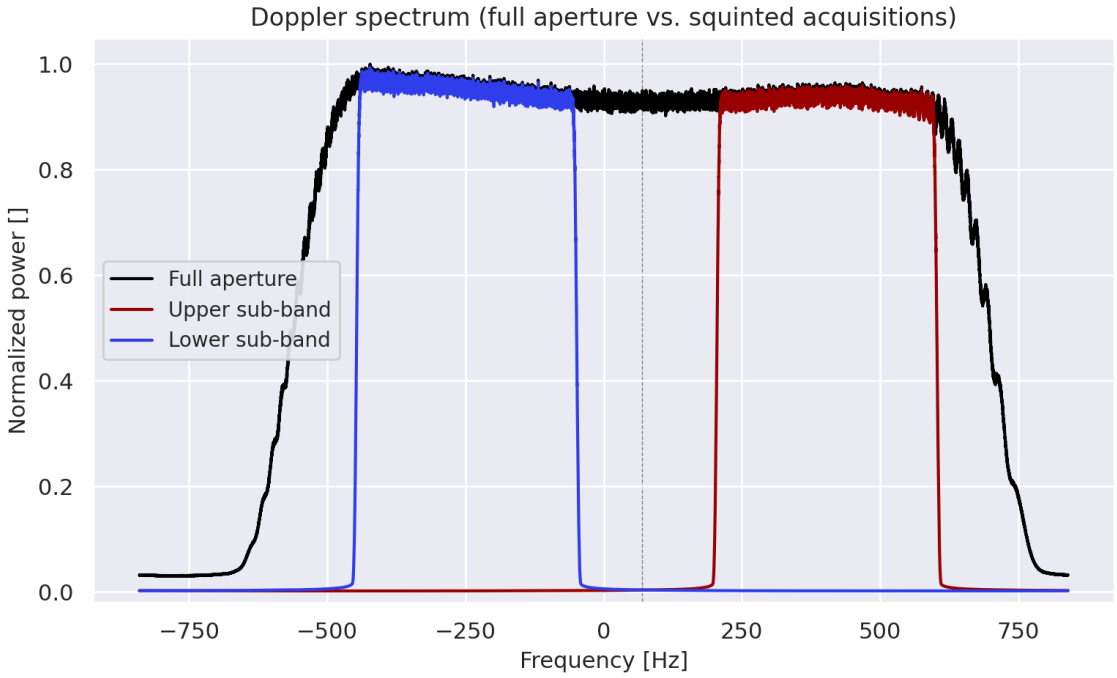

Figure 2.5: Example of azimuth (i.e. Doppler) band-pass filtering required for MAI measurements. The upper and lower sub-bands (corresponding to a forward- and backward-squinted acquisition, respectively) are generated from the full spectrum. Note that the original spectrum is centered around 70 Hz, indicating that the image was acquired with a slightly forward-squinted geometry. The data stems from an ERS-2 image.

used to track the misregistration between the two acquisitions in each dimension (Scambos et al., 1992; Gray et al., 1998). Although several types of tracking techniques exist, the most widely applied method, and the one used for offset tracking measurements presented in this thesis (Solgaard et al., 2021), is based on a two-dimensional Normalized Cross Correlation (NCC) between the two amplitude (or intensity, i.e. amplitude squared) images (Strozzi et al., 2002; De Lange et al., 2007). Image patches of a certain size (generally tens of resolution cells in each dimension, corresponding to >500 m for satellite SAR sensors) are extracted from the reference image and used to generate the NCC field by correlating with patches of the same size in the secondary image. To reduce the computational workload, a search window is defined, in which the correlation is computed with a certain posting, which is typically some fraction of the patch size. For each patch, a 2D displacement estimate is obtained by determining the distance from the patch location in the reference image to the maximum of the NCC field. Sub-pixel displacement measurements are achieved through FFT interpolation. Note that the two images do not need to be resampled to the same grid (i.e. coregistered), although misregistrations caused by the difference in acquisition geometry must still be estimated, in order to separate them from shifts due to physical motion.

Surface features such as cracks and crevasses in the ice may be observed, and hence tracked, in SAR amplitude images, similar to optical images. Conversely to the optical case, how-

ever, SAR offset tracking may also be carried out in areas that do not contain visible features. This is because of the speckle noise inherent in SAR images. A given patch in the reference image will show a certain distribution of speckle in the amplitude signal and assuming no major changes happen to the surface scattering properties, i.e. assuming a relatively high coherence level, this speckle distribution may be tracked to its new location in the secondary image. In that case, the process is usually referred to as speckle tracking (Strozzi et al., 2002), although the method implementation is no different from the feature tracking case. The fact that the same method can be used to simultaneously track velocities over fast-flowing glacier fronts, where coherence is often lost but visible features may be abundant, and over the slower-moving ice sheet interior, where coherence is often high but few visible features are present, is one of the advantages of SAR offset tracking. Another advantage is that motion can be measured in two dimensions, meaning that the three-dimensional velocity vector may be retrieved by combining measurements acquired from two satellite tracks with different look angles (Joughin et al., 1998). Finally, while the offset tracking algorithm is more computationally intensive than DInSAR, it does not include the often delicate phase unwrapping procedure. A disadvantage of tracking-based measurements is that their accuracy is limited by the resolution cell size (several meters) as opposed to the radar wavelength (few centimeters) in the DInSAR case. Estimates of offset tracking displacement errors are on the order of 1/100th to a few tenths of the resolution cell size in each dimension (Bamler & Eineder, 2005; De Lange et al., 2007), which is about an order of magnitude worse than the accuracy expected with DInSAR, dependent on the signal-to-clutter ratio when tracking features and the coherence level when tracking speckle. As for the resolution of the output measurements, in the worst case it will be equal to the size of the image patch used for matching (tens of resolution cells in each direction), while in the best case it will be equal to the posting distance (a fraction of the matching patch) (Pritchard et al., 2005), meaning that also the resolution is about an order of magnitude poorer than for DInSAR (compare Fig. 2.6a-b with Fig. 2.6c).

2.3 Sentinel-1 and the TOPS acquisition mode

In the description of SAR acquisitions and motion retrieval above, the simple Stripmap mode has been assumed. The focus of this thesis, however, is interferometric measurements generated with acquisitions from the Sentinel-1 satellites, which apply the Terrain Observation by Progressive Scans (TOPS) mode. This section provides a description of the Sentinel-1 satellites, the TOPS acquisition mode and its consequences in relation to the discussed motion retrieval methods, and finally an additional motion retrieval technique, which exploits the MAI principle and is unique to the TOPS (and ScanSAR) mode.

The Sentinel-1 satellite constellation is part of the EU's Copernicus program, managed by the European Space Agency. The constellation consists of two satellites, Sentinel-1A and -1B, launched in April of 2014 and 2016, respectively. The satellites carry a C-band (5.4 GHz, corresponding to a wavelength of 5.6 cm) SAR system and travel in a polar sun-synchronous orbit with a repeat-pass period of 12 days. The orbits of the two satellites

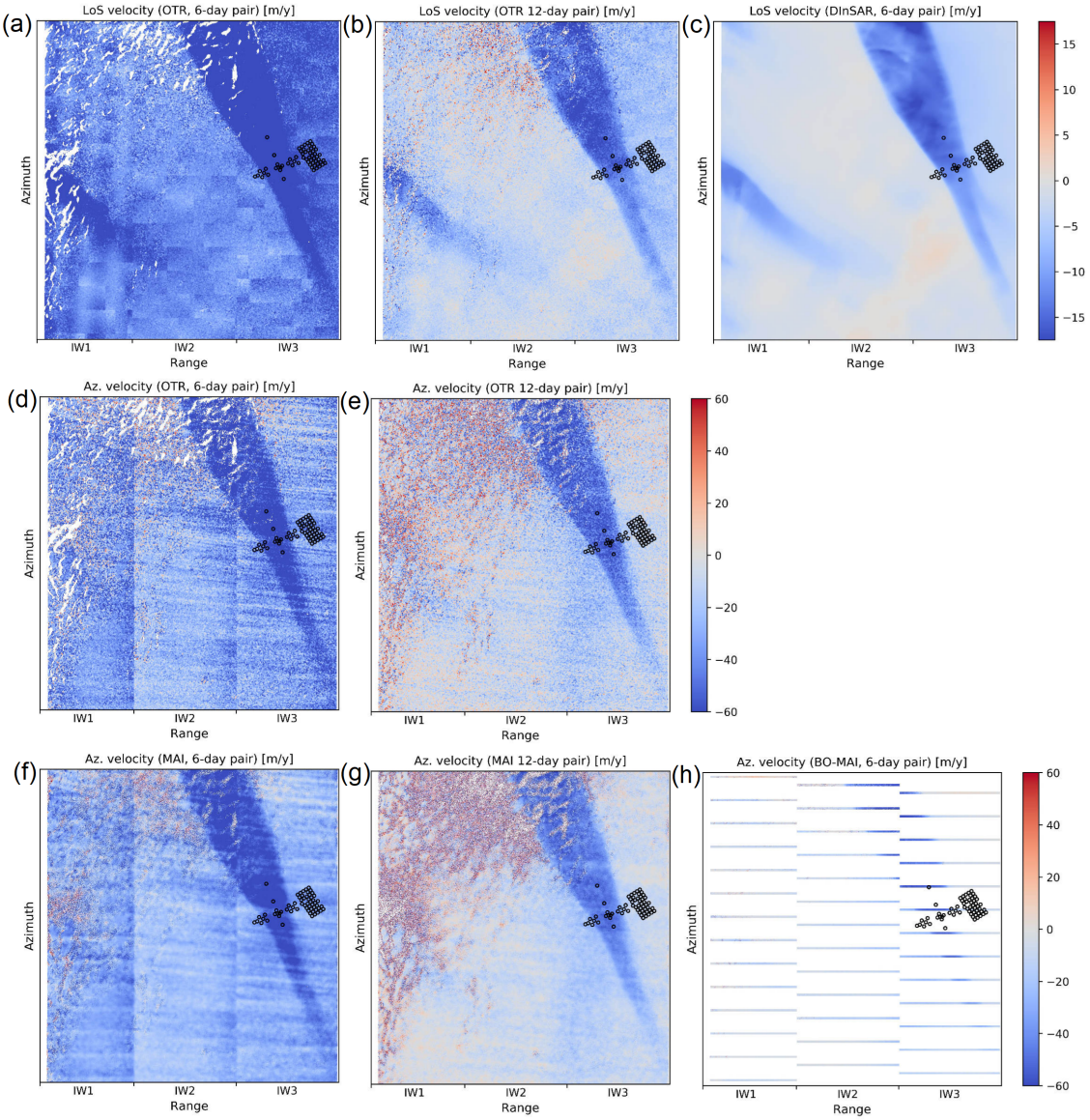

Figure 2.6: Line-of-sight and azimuth ice velocity measurements from various SAR motion retrieval methods for Sentinel-1 data in the vicinity of the Northeast Greenland Ice Stream. (a)-(b) LoS offset tracking for 6- and 12-day image pairs, (c) DInSAR LoS velocity for a 6-day pair, (d)-(e) azimuth offset tracking for 6- and 12-day pairs, (f)-(g) azimuth velocity from MAI for 6- and 12-day pairs, (h) BO-MAI azimuth velocity measurements for a 6-day pair. Note that certain biases/artefacts impact the Sentinel-1 offset tracking and MAI measurements. These are further discussed in Chapter 3. (Figure adapted from supplementary material of Andersen et al., 2020 - see also Appendix B.1).

are separated by 180° in phase, such that the repeat-pass period of the constellation becomes 6 days. Since December 23rd 2021, however, Sentinel-1B has been unavailable due to a power failure, and in August 2022 efforts to restore the SAR system were halted.[1]

[1] https://www.esa.int/Applications/Observing_the_Earth/Copernicus/Sentinel-1/Mission_ends_for_Copernicus_Sentinel-1B_satellite

Two additional satellites, Sentinel-1C and 1-D, have been planned to replace the 1A/1B satellites at the end of their lifespan, with the Sentinel-1C launch moved forward to the first half of 2023 as a response to the outage of Sentinel-1B.[2]

Fig. 2.7 illustrates the Sentinel-1 Interferometric Wide (IW) TOPS acquisition mode, which is the standard mode of operation over land.[3] Conversely to the Stripmap case, where the antenna squint angle is kept constant and measurements are recorded within a single swath, the TOPS mode involves scanning of the antenna within individual *bursts* in three neighboring *sub-swaths*. Within each burst, the antenna scans in the azimuth direction, moving from the aft (backward-looking) to fore (forward-looking). The steering is done electronically with a phased-array antenna. The sub-swaths are recorded sequentially, switching the elevation angle of the antenna every time a burst has been completed. The total swath width (combining all sub-swaths) is 250 km and the length of each burst is 20 km. As indicated in Fig. 2.7, there is an azimuth overlap region between neighboring bursts roughly 2 km in length (and an overlap between sub-swaths, also of 2 km width). In the generation of contiguous IW image mosaics, bursts are usually stitched together such that the overlap region consists of half of the first-acquired burst and half of the latter-acquired burst (the same goes for neighboring sub-swaths).

The scanning of the antenna has several consequences for the acquired data. First, the image resolution is roughly 5 m $\times$ 20 m in ground range/azimuth (with the ground range resolution varying with range, cf. eq. (2.1)), i.e. the azimuth resolution is about 4-5 times lower than the range. Consequently, multi-looking is typically applied with an uneven number of range and azimuth pixels, such that the resulting ground resolution cell is roughly square. The low azimuth resolution is a consequence of the decreased observation time, caused by scanning the antenna across each burst, which in turn allows for recording a very wide swath (De Zan & Monti Guarnieri, 2006). The trading of azimuth resolution for a wider swath is the aim of the TOPS mode. Other SAR satellites have applied the similar ScanSAR mode, in which several sub-swaths are also recorded in bursts, but without azimuth scanning of the antenna. An advantage of the TOPS mode, however, is that the antenna steering leads to a nearly uniform signal-to-noise ratio in azimuth, which is not the case for ScanSAR (De Zan & Monti Guarnieri, 2006).

The antenna steering causes a significant Doppler frequency variation across each burst. For sub-swath IW1, the Doppler frequency varies from -2.6 kHz at the burst start to $+2.6$ kHz at the burst end (Yague-Martinez et al., 2016). Referring back to eq. (2.7), it is seen how even a small, constant azimuth misregistration, $\Delta\eta$, will lead to an azimuth phase ramp in the interferometric phase of each burst (while a varying misregistration pattern will cause a more complex phase contribution). Consequently, accuracy requirements of the image coregistration are substantially stricter for DInSAR in the TOPS case,

[2] https://www.esa.int/Applications/Observing_the_Earth/Copernicus/Sentinel-1/Ride_into_orbit_secured_for_Sentinel-1C

[3] https://sentinels.copernicus.eu/web/sentinel/user-guides/sentinel-1-sar/acquisition-modes/interferometric-wide-swath

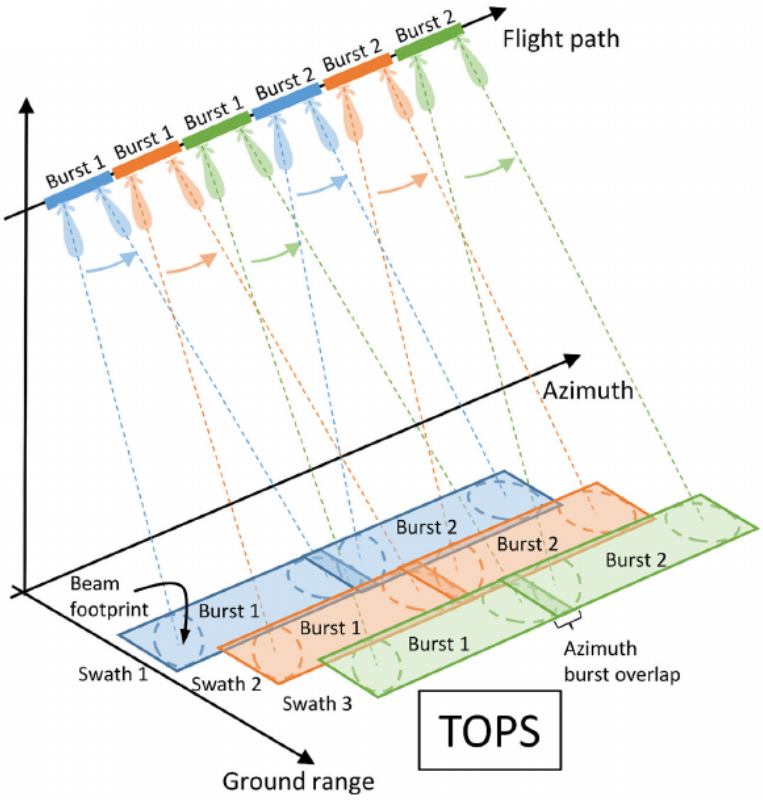

Figure 2.7: Sketch showing the geometry of the Terrain Observation by Progressive Scans (TOPS) acquisition mode, specifically the Interferometric Wide (IW) mode of Sentinel-1, with three sub-swaths in range. The antenna is electronically steered from aft to fore, which leads to azimuth burst overlaps that are measured with two different look vectors. (Figure adapted from Merryman Boncori, 2019).

compared to the Stripmap case. In applications measuring (small-scale) displacements over solid earth, the coregistration accuracy requirements have been met through the use of precise orbit data, high quality DEMs, and data-dependent methods that seek to estimate misregistrations using offset tracking (Scheiber et al., 2014) or the Extended Spectral Diversity technique (Prats-Iraola et al., 2012; Yague-Martinez et al., 2016). In the case of glaciers or ice sheets, however, ice motion may cause a large (non-uniform) contribution to $\Delta\eta$, which may lead to biased measurements and substantial issues in the phase unwrapping process. Resolving this challenge is the topic of Chapter 3.

Another consequence of the Doppler centroid variation is that a deramping (Miranda, 2017), i.e. a basebanding of the signal, must be performed prior to any interpolation or filtering of a TOPS image. Deramping is thus required during, e.g., image coregistration and MAI processing.

2.3.1 Burst overlap multi-aperture interferometry with TOPS mode

As indicated by Fig. 2.7, each of the burst overlap regions are observed twice by the sensor. First, the overlap is measured by the forward-looking antenna (with a Doppler centroid on the order of +2.6 kHz), then, the overlap is observed with the backward-looking antenna

(with a Doppler centroid on the order of −2.6 kHz). With the MAI principle, described in section 2.2.2, azimuth displacement information was extracted by synthetically generating forward- and backward-squinted acquisitions through band-pass filtering. In the TOPS burst overlaps, however, the squinted acquisitions are carried out separately, and the MAI interferogram may be generated simply as the double-difference interferogram between the forward- and backward-looking interferograms, without the need for band-pass filtering. This method was first used in the formulation of the Extended Spectral Diversity coregistration refinement technique (Prats-Iraola et al., 2012), which seeks to estimate a constant misregistration, however in this thesis, we refer to the method as Burst Overlap Multi-Aperture Interferometry (BO-MAI), as the aim is generally to utilize the spatially varying measurements to estimate collectively motion and misregistration terms. A further description of the BO-MAI method and how it was used in aiding TOPS coregistration for DInSAR ice velocity retrievals is presented in Chapter 3.

An advantage of BO-MAI measurements, compared to the MAI case, is that band-pass filtering of the images is not required. Consequently, the BO-MAI measurements utilize the full azimuth bandwidth and a smaller amount of spatial averaging is required to lower the noise floor in the azimuth motion measurements (see Fig. 2.6h for an example BO-MAI retrieval). Additionally, recall from eq. (2.15) that the sensitivity of the MAI phase to azimuth displacement is governed by the difference in Doppler centroid, $\Delta f_{DC} = f_{DC}^{u} - f_{DC}^{l}$. In the MAI case, the frequency separation will be some fraction of the azimuth bandwidth, which is on the order of 320 Hz, while in the BO-MAI case, the frequency separation is on the order of 4-5 kHz. While this means a substantially higher sensitivity of BO-MAI measurements, it also carries the consequence that phase ambiguities may arise in the presence of large azimuth motion. This point is further addressed in section 3.4. Note that the BO-MAI measurements may be used both for coregistration refinement purposes and as estimates of azimuth motion within the burst overlaps (Jiang et al., 2017a; Li et al., 2021).

2.4 Error sources in SAR-based velocity measurements

In the following, a brief description of various error sources related to SAR motion retrieval methods is provided. Emphasis is put on error sources pertaining to (Sentinel-1) DInSAR, as this method is the main focus of the thesis. In the case of DInSAR, any error contributions in the interferometric phase, δ_ϕ, translates to a LoS velocity error following eq. (2.10), that is:

$$\delta_{v_{LoS}} = \delta_\phi \frac{\lambda}{4\pi T} \tag{2.17}$$

where T is the temporal baseline.

Decorrelation

In section 2.2.1, the phenomenon of temporal decorrelation was introduced, which arises from differences in the scattering properties within a resolution cell in the time between

two subsequent acquisitions. Another contribution of decorrelation is *spatial decorrelation*, which arises from viewing the given resolution cell from two (slightly) different look angles. Hence, this contribution increases with increasing perpendicular baseline. The orbital tube of Sentinel-1 is relatively small, meaning that perpendicular baselines tend to be small. Consequently, in our application domain, spatial decorrelation is generally assumed to comprise a smaller (though non-negligible) contribution, compared to temporal decorrelation caused by surface melt or precipitation. Spatial decorrelation is usually separated in a contribution due to horizontal spread of scattering elements (sometimes denoted as baseline decorrelation) and a contribution due to vertical spread of scatterers, denoted as volume scattering, which is indeed relevant over ice and snow, where the penetration of microwaves is generally non-zero (Weber Hoen & Zebker, 2000).

Coregistration errors lead to a misalignment in the phase centers between the two acquisitions, which may also cause decorrelation. Finally, decorrelation may also arise from thermal noise in the radar receiver system. Thus, in practice, the interferometric coherence γ can be divided into the following components:

$$\gamma = \gamma_{spatial} \cdot \gamma_{temporal} \cdot \gamma_{coreg} \cdot \gamma_{thermal} \tag{2.18}$$

The DInSAR phase error standard deviation associated with decorrelation can be approximated as (Rodriguez & Martin, 1992):

$$\sigma_{\phi_n} = \frac{1}{\sqrt{2N_L}} \cdot \frac{\sqrt{1-\gamma^2}}{\gamma} \tag{2.19}$$

where γ is the interferometric coherence and N_L is the *equivalent number of looks* (i.e. the number of independent samples, which depends on the level of multi-looking). Hence, phase noise is lower for higher amounts of multi-looking and for regions of higher coherence, which is also true for amplitude offset tracking.

In the context of ice velocity retrieval, complete decorrelation (i.e. a coherence level close to zero) tends to limit coverage, particularly in regions where large amounts of surface melt or precipitation occur. Assuming a moderate level of coherence (higher than $\sim$0.3), on a pixel level, decorrelation phase noise is generally not a source of substantial error. However, as will be demonstrated in Chapter 4, phase unwrapping errors, which are typically associated with areas of low coherence, may propagate into high coherence areas. Hence, the distribution of coherence across the scene may greatly affect the occurrence of medium- and large-scale unwrapping errors.

Topographic estimation errors

For DInSAR, errors in the estimated topography, i.e. deviations of the surface elevation from the applied DEM, lead to a phase contribution of:

$$\delta_{\phi_z} = \Delta z \frac{4\pi}{\lambda} \cdot \frac{B_\perp}{R_0 \sin(\theta_l)} \tag{2.20}$$

where $B_\perp$ is the perpendicular baseline between the vantage points of the two satellite acquisitions and θ_l is the angle between nadir and the radar LoS. Hence, there is a direct proportionality between perpendicular baseline and topographic phase error. As Sentinel-1 was designed primarily for differential interferometry, the orbital tube is narrow, meaning that perpendicular baselines are generally small, with $B_\perp < 150$ m for the majority of image pairs (Barat et al., 2015). Furthermore, high quality DEMs of extensive polar coverage are widely available (Rizzoli et al., 2017; Porter et al., 2018). Consequently, errors related to the topographic phase contribution are assumed to have a minor influence on Sentinel-1 DInSAR measurements.

Tropospheric effects

As SAR satellites orbit the Earth at a distance on the order of 700 km, the transmitted and received radar waves must propagate through the entirety of the Earth's atmosphere. In the troposphere (the bottom ∼15 km of the atmosphere), the refractive index, and hence the velocity of the radar wave, may vary depending on the temperature, air pressure, and the amount of water vapor and liquid water content. In the DInSAR derivations presented so far, the wave speed was assumed to be constant. In that case, the refraction of the radar waves may be interpreted as an additional phase delay, τ_{tropo}, or equivalently an additional path (in range) traveled by the wave, ΔR_{tropo}. Consequently, differences in the refractive index caused by, e.g., an increase in the tropospheric water vapor content between the two SAR acquisitions will contribute directly a phase term:

$$\delta_{\phi_{tropo}} = 2\pi f_c \Delta\tau_{tropo} \tag{2.21}$$

Tropospheric phase errors may arise from differences in stratified delay or turbulent delay. Stratified delay relates to the vertical distribution of the refractive index. A difference in tropospheric stratification between image acquisitions leads to a phase contribution that varies with topography. In some cases, data from numerical weather prediction may be used to compensate for the stratified delay error (Doin et al., 2009). Turbulent delay arises from horizontal mixing in the troposphere, often related to thunderstorms or other weather events (although a difference in turbulent delay may also exist under clear sky conditions). The phase errors caused by turbulent effects are generally not possible to accurately model. The errors will typically lead to spatially correlated patterns.

Ionospheric effects

The radar waves also travel through the ionosphere, which spans from about 50 km altitude to the exosphere (beyond the satellite orbit). In the ionosphere, solar radiation leads to free electrons, which may impact the propagating radar wave. The amount of free electrons between the sensor and target, denoted the Total Electron Count (TEC), may differ between subsequent SAR acquisitions due to, for instance, changes in solar wind. In that case, a phase contribution due to ionospheric propagation delay will arise:

$$\delta_{\phi_{iono}} = 2\pi f_c \Delta\tau_{iono} \tag{2.22}$$

The ionospheric delay has the following relation to the change in TEC and the radar carrier frequency (Brcic et al., 2010):

$$\Delta\tau_{iono} \propto \frac{\Delta TEC}{f_c^2} \tag{2.23}$$

meaning that lower frequency SAR systems (e.g. L-band) are substantially more affected. Although C-band SAR systems often show negligible ionospheric phase errors at low or mid latitudes, in polar regions, where TEC variations are generally much larger, this is not always the case. Generally, ionospheric effects occur on large spatial scales (Brcic et al., 2010). For azimuth shift measurements, such as the ones carried out with MAI and offset tracking, ionospheric delay may lead to *streaks* of high magnitude errors in the azimuth dimension (Gray et al., 2000). Examples of this are seen in the azimuth velocity measurements in Fig. 2.6.

Phase unwrapping errors

In the absence of various phase error sources and decorrelation, phase unwrapping is, in principle, a trivial process. In practice, however, coherence loss occurs to some extent in every application of DInSAR. Consequently, the unwrapping process is, generally speaking, an ill-posed problem that is far from trivial. As previously mentioned, ambiguities arise if local phase gradients exceed π radians, which may happen due to, for instance, physical motion exceeding $\lambda/4$ or decorrelation leading to excessive phase noise. In such regions, the true unwrapped phase cannot be unambiguously recovered. However, the presence of such ambiguities may also complicate the unwrapping of the surrounding regions (see Fig. 2.4). Ultimately, the unwrapping algorithm must decide on some integer multiple of phase cycles (i.e. 2π radians) to add/subtract from each pixel (recall eq. (2.9)). Alternatively, the pixel should be masked out. Most phase unwrapping algorithms utilize a pixel-wise quality estimate such as the coherence image to mask out areas where an unambiguous phase signal is not expected. Still, local inconsistencies often occur, and in some cases, these may propagate into regions where unwrapping errors would otherwise not be expected (i.e. regions of high coherence). Consequently, phase unwrapping errors may yield errors of a large spatial extent and as the algorithm seeks to resolve integer multiples of 2π radians, errors may also be of significant magnitudes. For Sentinel-1 interferograms with a 6-day temporal baseline, a phase unwrapping error of just a single phase cycle corresponds to an error in estimated LoS velocity of 1.7 m/y, which is already much greater than the expected DInSAR accuracy (Andersen et al., 2020). Dependent on the scene specifics (and the unwrapping algorithm) errors may reach many phase cycles, far exceeding other DInSAR error sources. Phase unwrapping errors and their detection is the topic of Chapter 4.

2.5 Calibration of DInSAR measurements

In order to retrieve displacement (or velocity) measurements from the relative phase differences obtained after unwrapping, calibration is required. The unwrapped phase measure-

ments are referred to some arbitrarily selected seed point. The goal of the calibration is to estimate an absolute (global) phase offset, corresponding to a constant offset in range, and refer the relative measurements to the true displacement field. Aside from the error contributions described in the previous section, uncertainties of the baseline between the two acquisitions (in the form of orbit and timing errors) may lead to an error contribution that varies across the scene. In practice, the absolute phase error may be modeled as a constant baseline error. Hence, one approach is to consider all slow-varying (and constant) errors as baseline uncertainties. Calibration is then performed by selecting a series of so-called Ground Control Points (GCPs), where elevation and motion is known, and estimate a correction, following the approach described by Mohr and Boncori, 2008. We consider only linear baseline errors (in azimuth and range). Accurately estimating a varying baseline error requires a series of GCPs that are distributed across the full scene. In some cases, this may not be practical, and we instead estimate a constant (global) offset, neglecting the linearly varying errors. For DInSAR retrievals covering large regions, however, the linear baseline model was generally found to outperform the constant error estimation, when a reasonable GCP coverage is possible, as it may also account for large-scale atmospheric error contributions.

A common approach is to select GCPs in stationary regions (e.g. bedrock near the margin, nunataks, etc.), where motion can be assumed to be zero over the temporal baselines of DInSAR retrievals. However, this approach may be problematic, as the combination of steep terrain and high motion gradients at the ice/bedrock transitions sometimes lead to phase unwrapping errors. If such GCPs are used for calibration, those unwrapping errors may propagate to the rest of the scene. Therefore, our approach has generally been to select GCPs in slow-moving parts of the glacier/ice sheet under investigation (velocity magnitudes lower than a few tens of m/y), where motion is assumed to show little variation over the relatively short time scales considered. The velocity at each GCP is then estimated from a multi-year average map (projected to the SAR LoS), while the elevation may be obtained from a DEM.

2.6 Combining measurements for 3D velocity retrieval

Many glaciological applications require two- or three-dimensional ice velocity measurements, preferably in a local Cartesian coordinate system, i.e. the velocity vector, $\boldsymbol{v} = [v_x, v_y, v_z]^T$ (where (x, y) refer to the horizontal surface and z is the vertical dimension). The methods described in this chapter all measure motion in the SAR image dimensions, line-of-sight and azimuth, and all, except for offset tracking, measure only one of these motion components. Consequently, measurements from multiple motion retrieval methods and/or multiple satellite tracks are required to resolve the 2D/3D velocity field. Tracks are divided in the categories of ascending and descending, in which the satellite passes from south to north or from north to south, respectively. As most SAR senors, including Sentinel-1, are permanently right-looking, tracks in each category have similar look angles and thus measure roughly the same motion components. Hence, a combination of ascending and descending tracks are required if only a single measurement type is used.

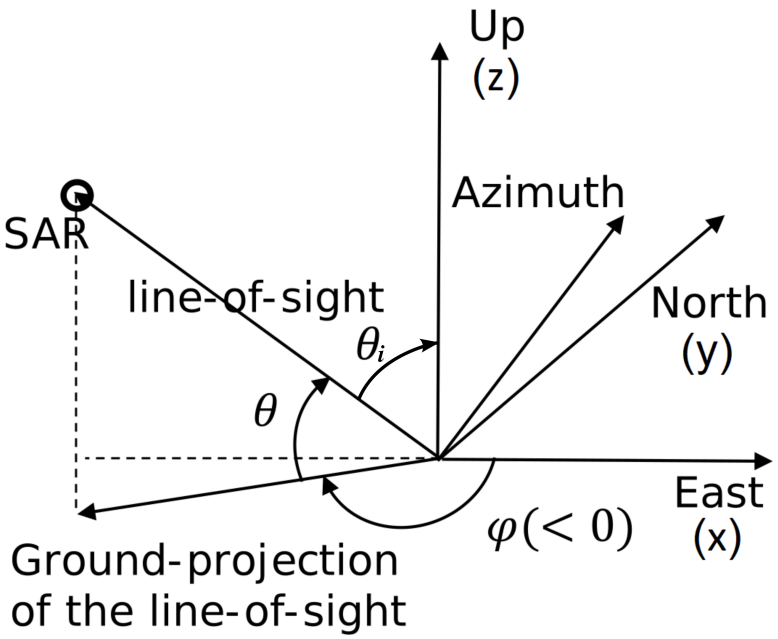

Figure 2.8: Sketch showing the SAR look vector elevation angle (also known as grazing angle), θ, and orientation angle, ϕ, as well as the incidence angle, θ_i, in relation to a local (x, y, z) or $(east, north, up)$ Cartesian coordinate system. The angle θ_i is known as the local incidence angle.

It is often assumed that ice flow follows the slope of the surface, which can be formulated as:

$$v_z = \frac{dz}{dx} v_x + \frac{dz}{dy} v_y \tag{2.24}$$

where the surface gradients can be determined from a DEM. This assumption is known as the surface-parallel flow assumption (Joughin et al., 1998; Mohr et al., 1998). It should be noted that the assumption is less valid in areas of non-zero surface mass balance, i.e. areas of high accumulation or ablation, where there is a non-zero velocity contribution due to ice submergence/emergence (Joughin et al., 1998). With this, the following inverse problem of the form $\boldsymbol{u} = \boldsymbol{H}\boldsymbol{v} + \boldsymbol{\epsilon}$ can be formulated:

$$\begin{bmatrix} v_{r1} \\ v_{a1} \\ \vdots \\ v_{rN} \\ v_{aN} \end{bmatrix} = \begin{bmatrix} \cos\theta_1 \cos\phi_1 + \sin\theta_1 \frac{\partial z}{\partial x} & \cos\theta_1 \sin\phi_1 + \sin\theta_1 \frac{\partial z}{\partial y} \\ -\sin\phi_1 & \cos\phi_1 \\ \vdots & \vdots \\ \cos\theta_N \cos\phi_N + \sin\theta_N \frac{\partial z}{\partial x} & \cos\theta_N \sin\phi_N + \sin\theta_N \frac{\partial z}{\partial y} \\ -\sin\phi_N & \cos\phi_N \end{bmatrix} \begin{bmatrix} v_x \\ v_y \end{bmatrix} + \boldsymbol{\epsilon} \tag{2.25}$$

where v_{rn} and v_{an} represent LoS and azimuth velocity measurements from the nth image pair, θ_n is the look vector elevation angle for pair n (i.e. the angle from ground level to the LoS) and ϕ_n is the horizontal orientation angle for pair n (see Fig. 2.8, which shows the

relation between SAR geometry and a local Cartesian coordinate system). $\boldsymbol{\epsilon}$ represents error terms. Assuming independent, normally distributed and zero-mean noise for each retrieval, the following diagonal covariance matrix can be assumed:

$$\boldsymbol{\Sigma} = \begin{bmatrix} \sigma_{r1}^2 & 0 & \cdots & 0 \\ 0 & \sigma_{a1}^2 & \cdots & 0 \\ \vdots & \vdots & \ddots & \vdots \\ 0 & 0 & \cdots & \sigma_{aN}^2 \end{bmatrix} \tag{2.26}$$

where σ_{rn} and σ_{an} are the estimated standard deviations of the LoS and azimuth velocity measurements, respectively, for the nth image pair. The system can then be solved through weighted least squares, with the solution:

$$\hat{\boldsymbol{v}} = (\boldsymbol{H}^T \boldsymbol{\Sigma}^{-1} \boldsymbol{H}) \boldsymbol{H}^T \boldsymbol{\Sigma}^{-1} \boldsymbol{u} \tag{2.27}$$

The system may be solved using only DInSAR measurements, which generally have the highest accuracy, however in that case, both ascending and descending measurements are needed. Alternatively, azimuth measurements from either MAI or offset tracking (or BO-MAI) are required. Note that the inversion of measurements from N image pairs implicitly assumes that the velocity field is unchanged through the span of the image acquisition times. If a series of image pairs spanning long periods are combined, the result may be considered a (pseudo)-average velocity, where the sampling may be irregular due to, e.g., loss of interferometric coherence.

Chapter 3 | Meeting coregistration requirements of TOPS interferometry on ice

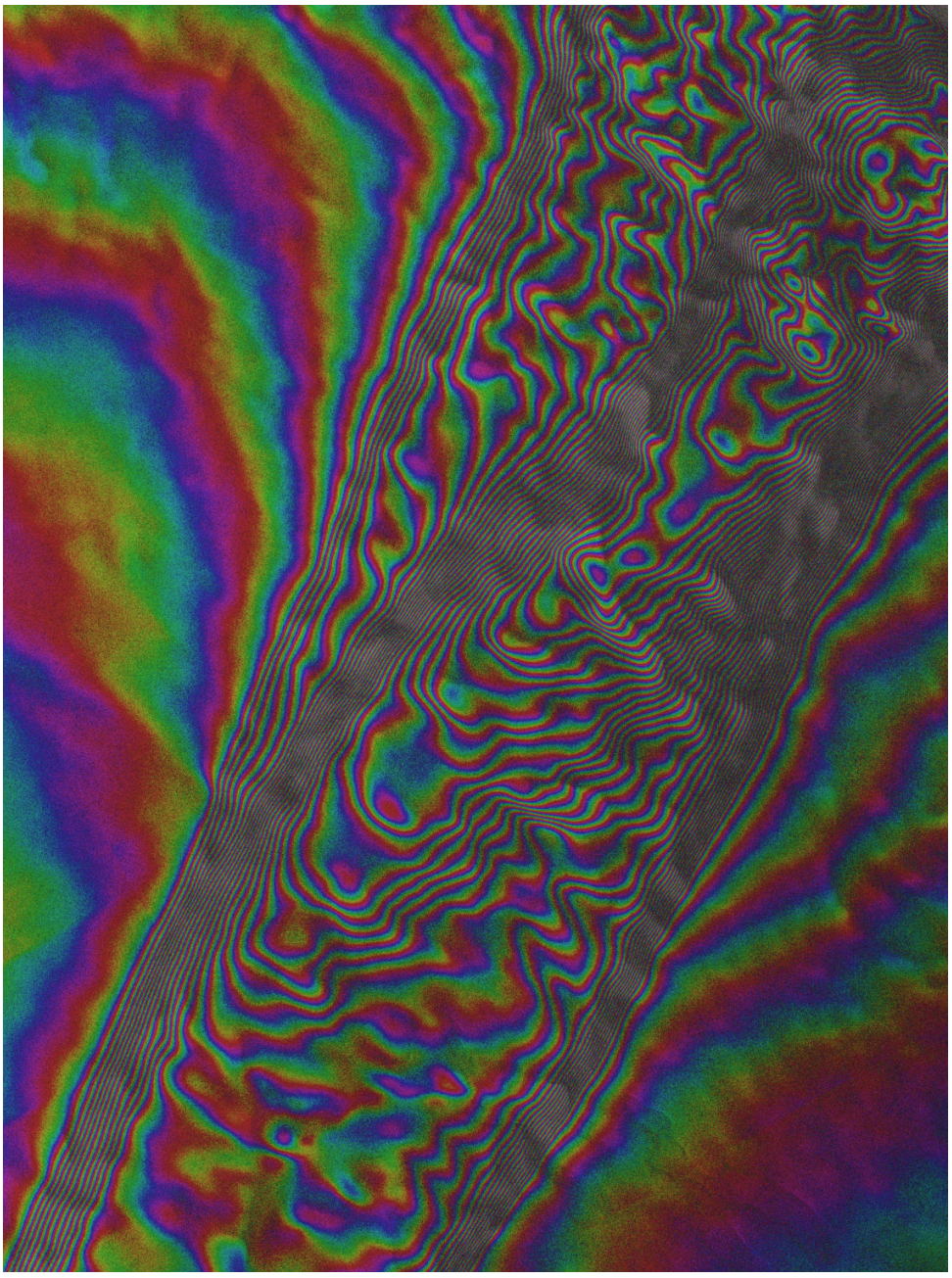

Interferometric phase of a Sentinel-1 differential interferogram covering part of the Northeast Greenland Ice Stream.

3.1 TOPS mode interferometry in the presence of fast motion

The TOPS acquisition mode inherently leads to a coupling between the interferometric (i.e. DInSAR) phase and azimuth misregistrations, $\Delta\eta$, as shown by eq. (2.7). As indicated by eq. (2.16), the azimuth misregistration may be separated in terms involving limitations of the geometric coregistration and orbit uncertainties ($\Delta\eta_{coreg}$ and $\Delta\eta_{orb}$), a term related to ionospheric effects ($\Delta\eta_{iono}$), and finally a term related to physical motion in the azimuth direction ($\Delta\eta_{motion}$). In some applications, a sufficiently accurate geometric coregistration may be achieved and the ionospheric and azimuth motion terms may be considered negligible. In the case of glaciers and ice sheets, large displacements are often present over most of the imaged scene, generally with a spatially varying magnitude and direction. Hence, the azimuth motion term cannot be neglected. While it is true that the coupling between azimuth motion and interferometric phase is simply a characteristic of the TOPS acquisition mode (De Zan et al., 2014), and not strictly speaking an error term, the phase unwrapping process may be significantly complicated by the occurrence of phase discontinuities at burst boundaries. The phase discontinuities, or *phase jumps*, occur in the burst overlap region, where the Doppler centroid makes a sudden change from positive to negative values. Fig. 3.1a shows an example of a Sentinel-1 TOPS interferogram over a region in northeast Greenland with a purely geometric coregistration (i.e. based only on a DEM and orbit data). Phase jumps are clearly observed at nearly all burst boundaries. As demonstrated in section 3.3, the phase ramps caused by unaccounted azimuth motion may lead not only to ramps and discontinuities in the resulting velocity measurements, but also to phase unwrapping errors, which may result in velocity errors of tens (or even hundreds) of m/y.

This chapter documents the work carried out to resolve the challenges related to coregistration of Sentinel-1 TOPS images for DInSAR processing. The remaining three sections focus on different approaches to refining image coregistration. Section 3.2 outlines methods previously published on the topic and discuss their merits in the case of Sentinel-1 interferometric ice velocity retrieval. Section 3.3 presents a coregistration refinement based on an external, average velocity estimate as well as BO-MAI measurements. Finally, section 3.4 provides a more thorough description of the BO-MAI coregistration refinement.

3.2 Data-dependent coregistration refinement approaches

Common to all the coregistration refinement methods presented in this chapter is the goal of estimating some (or all) of the contributions to azimuth misregistration (i.e. coregistration errors, ionospheric effects, azimuth motion, or some combination of these) and subsequently account for the azimuth shifts caused by these contributions in the image coregistration. Then, the DInSAR phase is interpreted as purely arising from motion in the zero-Doppler LoS direction, as in the Stripmap case. Scheiber et al., 2014 evaluated the performance of using offset tracking and MAI to estimate the spatially varying pattern of azimuth misregistration and tested the approach on TerraSAR-X TOPS acquisitions. An advantage of this and other data-dependent approaches is that the offset tracking and

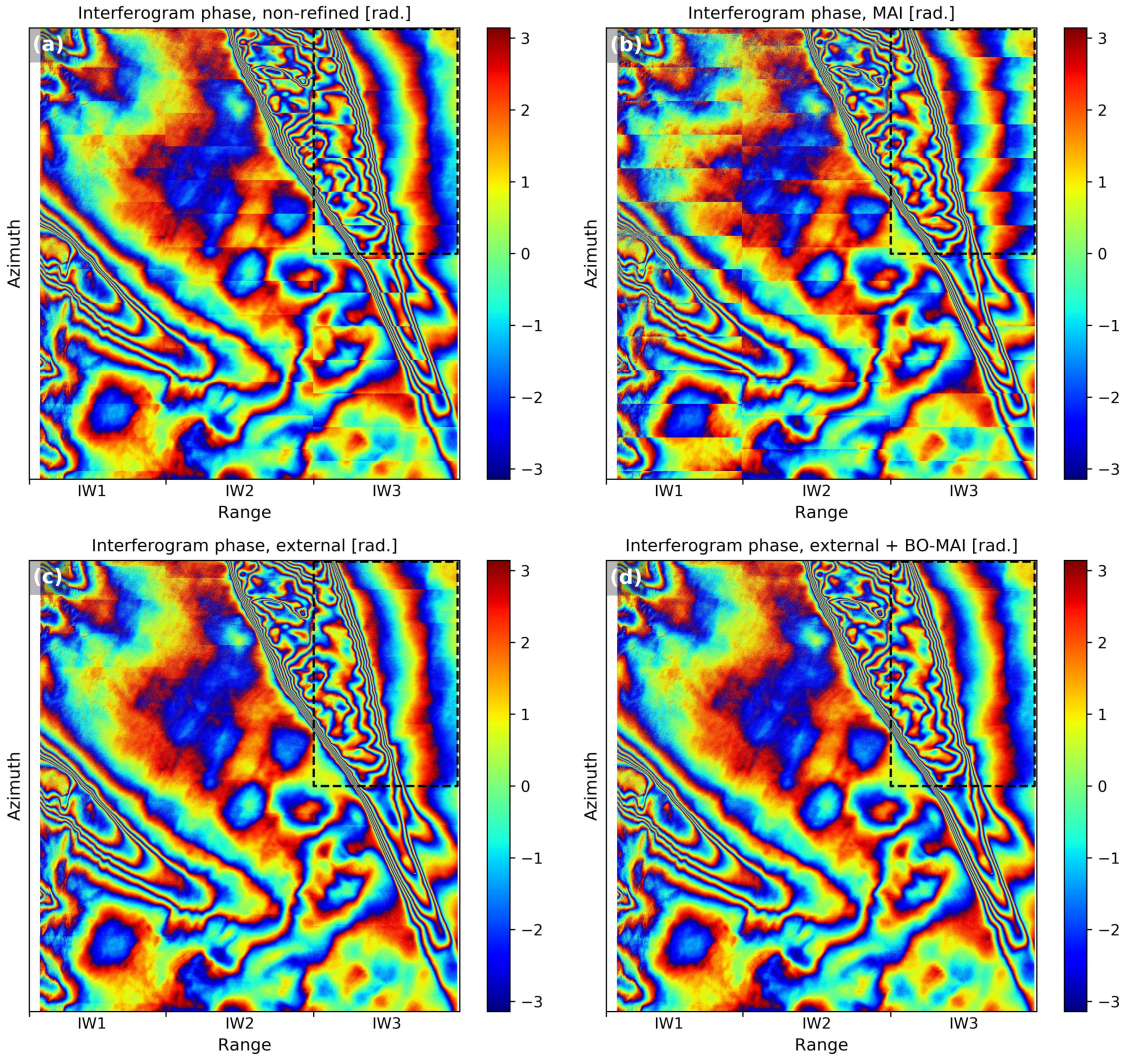

Figure 3.1: Sentinel-1 TOPS interferogram obtained from a 6-day image pair using various coregistration strategies. (a) Geometric coregistration with no refinements, (b) with a refinement based on MAI measurements, (c) with a refinement based on an external multi-year average velocity map, and (d) with a refinement based on the external average velocity map and an additional refinement based on BO-MAI measurements. (Figure adapted from Andersen et al., 2020).

MAI measurements are sensitive not just to azimuth motion, but to all sources of azimuth misregistration. For Sentinel-1, however, two issues arise in the application of such a coregistration refinement. First, due to the limited azimuth bandwidth, the multi-looking window size required to achieve an acceptable noise level of the MAI or offset tracking measurements means that spatial variability of the azimuth motion pattern cannot be captured (see also section 3.4 and the associated manuscript). Additionally, for image pairs consisting of one acquisition from each satellite (i.e. S1A/S1B or S1B/S1A pairs), a swath-dependent azimuth bias exists, which affects both offset tracking and MAI measurements. Recent studies suggest that the bias may be related to an S1A antenna anomaly

occurring in summer 2016 (Gisinger et al., 2021). Both satellites are required to generate image pairs with the lowest possible temporal baseline of 6 days, which is favorable for DInSAR processing. The bias does not affect same-satellite image pairs, however, in that case, the minimum temporal baseline is 12 days, which leads to a substantial increase in phase noise, due to increased temporal decorrelation. Fig. 3.1b shows an example interferogram obtained after applying the coregistration refinement based on MAI measurements. Evidently, the phase jumps have only increased in magnitude, compared to the case of no coregistration refinements, which is a result of the swath-dependent azimuth bias. Offset tracking measurements contain a similar noise level as MAI and are also affected by the bias. Note that an additional artefact impacts the LoS offset tracking measurements, seen as patches that roughly align with burst edges in Fig. 2.6a. The MAI and offset tracking coregistration refinement approach is further documented in section 3.3 and the associated manuscript.

Another approach for coregistration refinement, which was briefly mentioned in the previous chapter, is the Extended Spectral Diversity (ESD) method (Prats-Iraola et al., 2012; Yague-Martinez et al., 2016). The ESD approach involves the measurement of azimuth misregistration within TOPS burst overlaps via the BO-MAI method. With ESD, however, instead of providing spatially varying measurements within each burst overlap, a uniform scene-wide azimuth shift is assumed, which is then estimated using available measurements from all burst overlaps. This method has been successfully applied in DInSAR applications where the majority of the imaged scene is nearly stationary, such that ESD may estimate the shift caused by a (presumably) uniform azimuth coregistration error, $\Delta\eta_{coreg}$ (Cigna & Tapete, 2021; Yague-Martinez et al., 2016). In the case of ice velocity retrieval, azimuth misregistration will, generally, contain a major contribution from ice motion in the azimuth dimension, which is unlikely to be perfectly uniform. Hence, there is a need for estimating a spatially variable coregistration refinement. To this end, we applied the BO-MAI measurements directly, after some spatial averaging via multi-looking, to refine the azimuth coregistration within burst overlaps. Similar to the MAI and offset tracking measurements, the BO-MAI measurements are sensitive also to other sources of misregistration, such as ionospheric effects, which may then be corrected for. The obvious downside to the BO-MAI refinement is that it is only applicable within burst overlaps. The BO-MAI coregistration refinement is further documented in sections 3.3 and 3.4 and the associated manuscripts.

3.3 Using average velocity estimates for coregistration refinement

Barring major ionospheric effects, the main contributor to azimuth misregistration on glaciers and ice sheets is the azimuth component of ice motion. While several methods are available, which directly estimate the azimuth misregistration term, as described in the previous section, none of these were found to provide a reliable coregistration refinement. Aside from the (presumably) antenna-related bias, the azimuth bandwidth of Sentinel-

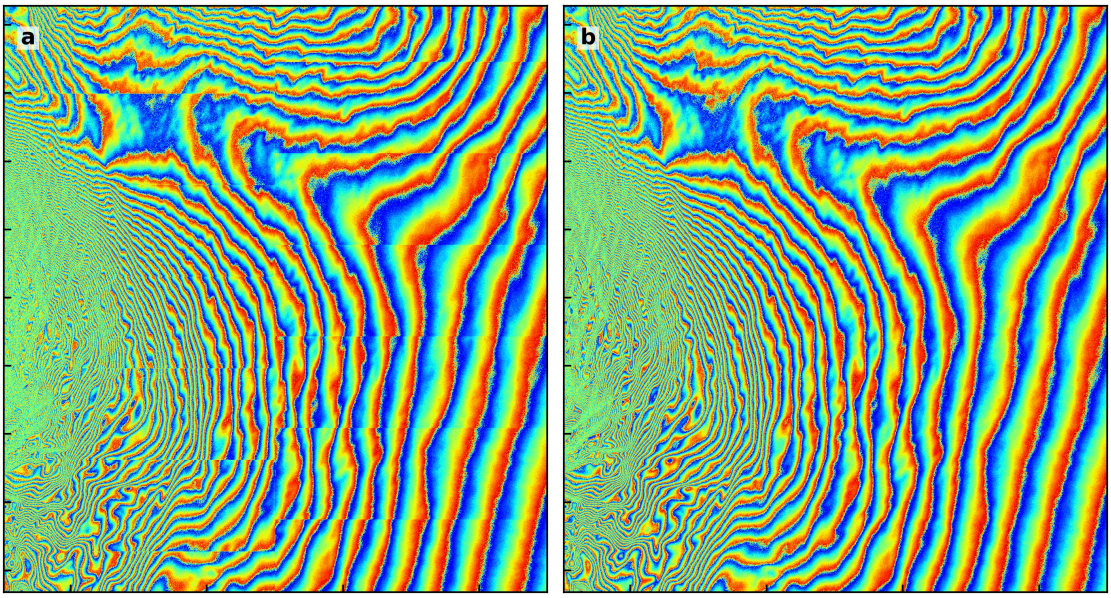

Figure 3.2: Sentinel-1 TOPS interferogram from a 6-day image pair in the upstream parts of Helheim glacier. Panel (a) shows the interferogram obtained with a geometric coregistration with no refinements, while panel (b) shows the result of applying the coregistration refinement based on both an external average velocity map and BO-MAI measurements.

1 leads to MAI and offset tracking measurements of relatively low accuracy. Instead, we sought to refine image coregistration through an external estimate of ice velocity within the scene. As previously described, routine measurements are carried out using offset tracking methods on data from Sentinel-1 (and other sensors) (Solgaard et al., 2021; Joughin et al., 2018a). Combining range and azimuth measurements from several tracks allows for the estimation of the three-dimensional velocity field (assuming surface-parallel flow), as described in section 2.6. Using data from several months, or even years, an average velocity field may be computed, where the noise level is substantially reduced by the temporal averaging. In the manuscript described below, we demonstrate a TOPS image coregistration refinement based on a multi-year average velocity estimate and a second refinement based on the BO-MAI method. An additional example of the effects of the coregistration refinements, from a different region of the Greenland ice sheet, is given in Fig. 3.2.

In the following, a brief summary and outline of the main results is provided for the manuscript:

J. K. Andersen, A. Kusk, J. P. M. Boncori, C. S. Hvidberg, and A. Grinsted, Improved ice velocity measurements with Sentinel-1 TOPS interferometry, *Remote Sensing*, vol. 12, no. 12, p. 2014, doi:10.3390/rs12122014 (2020)

The full manuscript is provided in Appendix A.1 and supplementary material is provided in Appendix B.1.

3.3.1 Summary of Andersen et al. (Remote Sensing, 2020)

A Sentinel-1 TOPS interferometric processing chain is presented, which uses an external velocity estimate, in this case a 2016-2019 average velocity mosaic generated through PROMICE (Solgaard et al., 2021), to correct for the bulk of azimuth motion in the image coregistration. While the average velocity mosaic naturally does not capture other misregistration sources (such as ionospheric contributions) or local deviations from the average velocity pattern, we find that the external velocity estimate provides a substantial improvement in the form of significant reduction in phase jumps at burst boundaries, as seen in Fig. 3.1c and Fig. 4 in the manuscript. For some burst boundaries, the external velocity refinement does not quite resolve the phase discontinuities, presumably because of local velocity variations or ionospheric effects. To further improve the coregistration, particularly within the burst overlaps, in which the interferometric phase is especially sensitive to azimuth misregistration, we define an additional coregistration refinement, using multi-looked BO-MAI measurements. An example is seen in the top right of Fig. 3.1d and Fig. 4 in the manuscript. It is noted that the BO-MAI measurements may also serve as azimuth velocity measurements (although these are affected by other sources of misregistration, such as ionospheric effects). With the refined image coregistration carried out, the velocity extracted from the interferometric phase is assumed to be related only to motion in the line-of-sight direction, similarly to the Stripmap case. The manuscript also documents the previously described issues with MAI and offset tracking-based azimuth coregistration refinements (see the Appendix and supplementary material of the manuscript).

The TOPS DInSAR processing chain is demonstrated for a large drainage basin in Northeast Greenland, using three ascending and four descending Sentinel-1 tracks. The region is chosen for two main reasons: 1) the basin includes the Northeast Greenland Ice Stream (NEGIS), which is a unique dynamic feature of high scientific interest, extending more than 600 km inland, and 2) velocity measurements from GPS stakes are available, courtesy of the EastGRIP (East Greenland Ice-core Project) team (Hvidberg et al., 2020). The availability of GPS retrievals allows for a validation of the TOPS DInSAR measurements. Additionally, we carry out offset tracking processing for the same Sentinel-1 data set. The range offset tracking measurements allow for a comparison with the DInSAR measurements, as they measure the same motion component. Furthermore, we demonstrate a combined DInSAR and offset tracking 2D velocity product, through a weighted inversion as described in section 2.6 as well as in the manuscript, which exploits the advantages of both methods: DInSAR measurements are the dominant contributor where they are available, while offset tracking measurements are needed to capture fast-flowing regions near marine-terminating glacier outlets.

The GPS stakes are situated far upstream on the NEGIS, where only minor velocity change is expected. Hence, even though the temporal alignment of the SAR and GPS measurements is not perfect, a valid comparison is expected. The GPS validation shows a standard deviation of 0.18 m/y in the x-direction and 0.44 m/y in the y-direction for the

DInSAR measurements, which is a factor five lower than the offset tracking measurements alone and even a factor two lower than the multi-year average offset tracking mosaic. In the generation of the combined velocity product, several phase unwrapping errors were identified in the DInSAR measurements, leading to substantial velocity errors near the glacier outlets. In this case, the unwrapping error-prone regions were manually masked out in the DInSAR measurements (such that only offset tracking measurements contribute to the velocity inversion in these regions). Chapter 4 documents work that was carried out to address this issue.

3.4 Exploiting burst overlaps for additional refinement

In the manuscript presented in the previous section, a coregistration refinement based on BO-MAI was introduced. This method was further elaborated upon in a separate publication:

A. Kusk, J. K. Andersen, and J. P. M. Boncori, Burst overlap coregistration for Sentinel-1 TOPS DInSAR ice velocity measurements, *IEEE Geoscience and Remote Sensing Letters*, vol. 19, pp. 1–5, 2021, doi:10.1109/LGRS.2021.3062905 (2021)

The section below provides a brief summary of the manuscript, which is provided in full in Appendix A.2.

3.4.1 Summary of Kusk et al. (IEEE GRSL, 2021)

This paper provides a more thorough description of the BO-MAI coregistration refinement method introduced in (Andersen et al., 2020). Note that, in this manuscript, the MAI and BO-MAI methods are referred to as SD and BO-SD (where SD stands for Spectral Diversity), respectively, which is more in line with past nomenclature (where split-bandwidth techniques have usually been referred to as Spectral Diversity when pertaining to coregistration refinements).

We first provide formal expressions on the interferometric phase uncertainties associated with the SD and BO-SD methods, as well as the error in line-of-sight velocity that would result from interpreting those phase uncertainties as motion (eqs. (4)-(6) in the manuscript). It is noted that, at the burst boundaries, the BO-SD technique provides a phase uncertainty that is 40 times smaller than that of the SD method. Fig. 2 in the manuscript shows the uncertainty in LoS velocity resulting from the SD and BO-SD refinements as a function of coherence level for different multi-looking (i.e. spatial averaging) window sizes. For comparison, the estimated LoS velocity uncertainty associated with speckle noise in the interferogram, using a multi-looking window on the order of 60 m $\times$ 60 m, is also shown. Here, it is seen that the SD measurements would require multi-looking with a window size exceeding 700 m to reach a noise level that is comparable with the interferogram phase noise. Conversely, BO-SD measurements lead to a LoS velocity uncertainty of less than 0.1 m/y even with a modest multi-looking window size of about 85 m $\times$ 85 m and moderately low coherence values. The higher spatial resolution of BO-SD means that

local variations of the azimuth ice velocity or ionospheric errors may be captured.

As the BO-SD technique is only applicable within the burst overlaps, in some cases, residual phase discontinuities may occur at the overlap edges (for instance, see Fig. S3 in Appendix B.1). In order to diminish such residual phase jumps, we introduce an azimuth tapering function to the BO-SD measurements, before applying them in the coregistration. In principle, this introduces a small error in the BO-SD correction term near the burst overlap edges, however, the residual phase jumps are generally well suppressed, lowering the risk of phase unwrapping errors.

As the sensitivity of BO-SD measurements to azimuth misregistration is high, compared to SD, wrapping of the BO-SD phase may occur if azimuth motion exceeds 40 m/y (assuming a 6-day interferogram), which is not uncommon even in far upstream parts of glaciers. For the ESD method, a periodogram estimation method was suggested (Yague-Martinez et al., 2016), which is, however, not applicable in the present case, where local estimates must be carried out (as opposed to an image-wide estimate). Instead, we seek to account for the bulk of azimuth motion through the external multi-year average velocity map, such that the remaining BO-SD phase contribution is restricted to an interval of 2π radians and thus does not require unwrapping. Naturally, this approach would fail in regions that show local velocity variations (in azimuth) larger than 40 m/y, however such regions are likely to be fast-flowing glacier outlets, where interferometric coherence is lost anyways, preventing DInSAR retrievals entirely.

Chapter 4 | Towards reliable DInSAR ice velocity retrievals

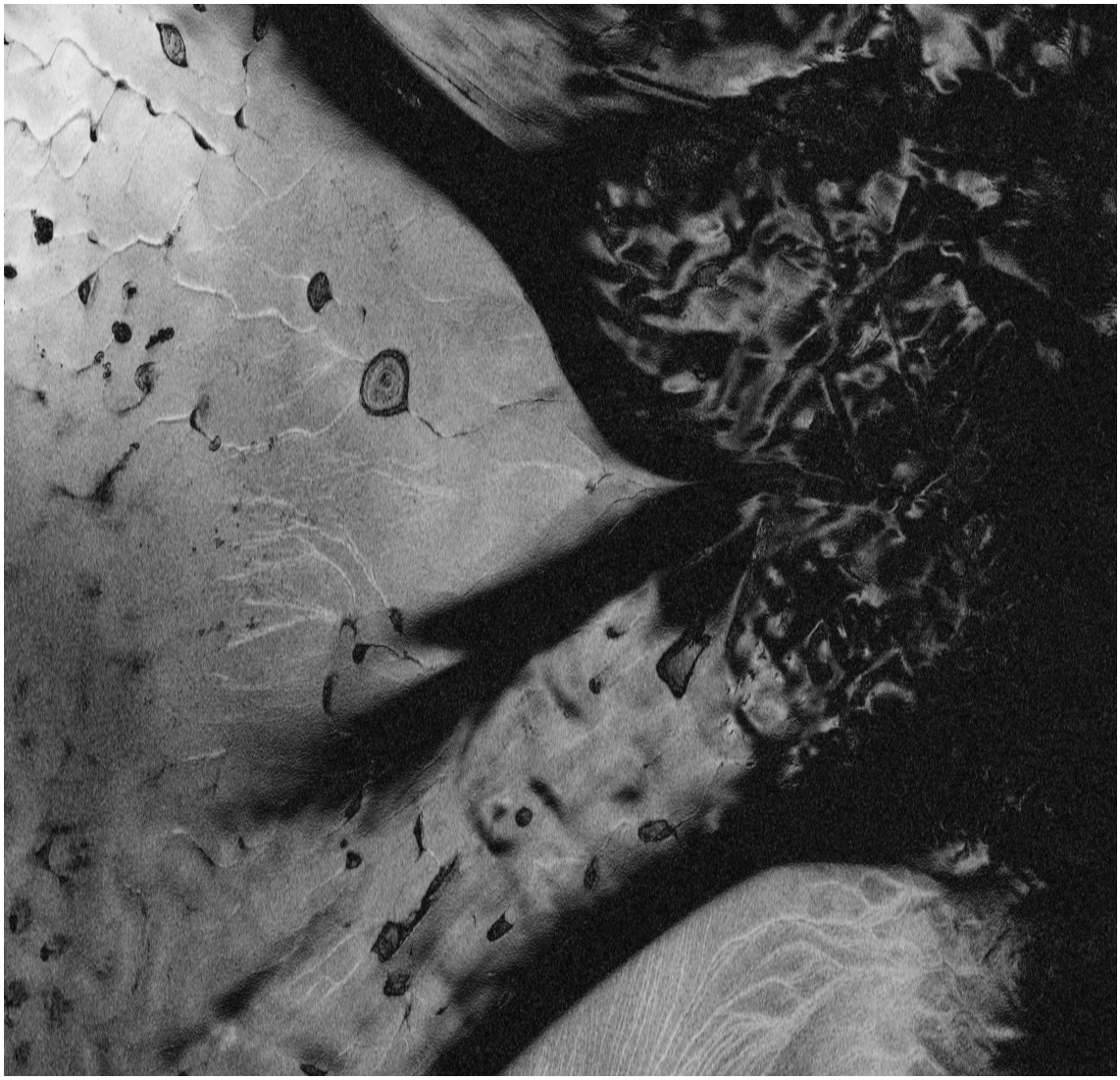

Sentinel-1 coherence image in a region with fast flow, supraglacial lakes, and crevasses.

4.1 Phase unwrapping errors in DInSAR ice velocity retrievals

In Andersen et al., 2020 (section 3.3), we showed the potential of a combined DInSAR and offset tracking velocity retrieval. The implemented coregistration refinements resolve the TOPS-related DInSAR challenges, namely the coupling between azimuth misregistration and differential phase, meaning that remaining limitations are similar to those associated with Stripmap imagery. The comparison with GPS indicated an accuracy of the DInSAR measurements far exceeding offset tracking capabilities, however, one issue was that even with the measures for phase unwrapping error mitigation implemented in the inhouse DInSAR processing chain, unwrapping errors were observed in parts of the downstream region. Hence, this observation motivated efforts to further detect and mitigate phase unwrapping errors, with the goal of achieving a more reliable operational DInSAR processing scheme.

As previously mentioned, unwrapping errors may have a large spatial extent as well as magnitudes of a nearly arbitrary number of phase cycles, leading to potential ice velocity errors of tens or even hundreds of meters per year. As such an error magnitude far exceeds other DInSAR error sources, and in some cases even the noise level in offset tracking measurements, detection of unwrapping errors is important for DInSAR applicability. Because unwrapping errors are spatially correlated, they are generally not reduced by multi-looking. Their spatial correlation, however, means that unwrapping errors may often be recognized by visual inspection of the unwrapped interferogram (or velocity measurements) as patches surrounded by unrealistically high gradients - an approach that is often used in practice (Mouginot et al., 2019a). For large scale, routine ice velocity retrievals, however, visual inspection of individual measurements becomes a cumbersome task. Another common practice approach is to manually determine a border, beyond which unwrapping errors are deemed likely and hence DInSAR is not carried out (Joughin et al., 2018a). Such a border is often based on an a priori velocity field, as unwrapping errors are typically associated with high motion gradients (a finding that is further documented in section 4.2). An obvious downside to this approach is that no DInSAR ice velocity measurements are acquired beyond the selected border, even if error-free retrieval is possible for some image pairs.

In other applications, unwrapping error detection (and correction) has been based on the principle of phase closure of interferogram triplets (Yunjun et al., 2019; Pinel-Puyssegur et al., 2018). For applications on glaciers, however, such an approach is not straightforward. First, coherence may vary substantially between neighboring 6- and 12-day image pairs, meaning that, for many regions, it may not be possible to retrieve measurements across the triplet pairs. Furthermore, as demonstrated in section 4.2, it is often the same areas that are prone to unwrapping errors across subsequent interferograms, meaning that the risk of an unwrapping error occurring in two, or even three, of the triplet interferograms is non-negligible. In that case, it is not straightforward to determine which of the interferograms contain errors and which do not.

In the context of ice velocity retrieval, unwrapping errors are often related to shear margins,

i.e. transition areas from slow-moving ice to the fast-flowing part of a glacier or ice stream, where coherence loss may occur due to rotation of the ice fabric. In one of the first demonstrations of DInSAR ice velocity measurements, Goldstein et al., 1993 proposed an adaptive multi-looking strategy, where the multi-looking window size is reduced within shear margins. Fig 4.1 shows a portion of a shear margin as seen in the same Sentinel-1 interferogram (6-day baseline) with different levels of multi-looking. The reduction in spatial averaging means an increase in phase noise, but also an increase in resolution, which makes it possible to unambiguously resolve the phase signal in the region where the motion gradient is highest. Hence, with the lowest amount of multi-looking (right-most column in Fig. 4.1), velocity may be retrieved over the full extent of the shear margin, as seen in the unwrapped phase images. Aside from being an advantage in terms of diminishing some instances of unwrapping errors, high resolution measurements of dynamics across shear margins are of high interest to glaciologists. One disadvantage of this approach is that computing time drastically increases as multi-looking is decreased. Additionally, areas where phase noise is high (and motion gradients are relatively low) may benefit from higher levels of spatial averaging. Hence, the multi-looking should be decreased mainly in areas such as shear margins, where the benefits outweigh the disadvantages. Such an adaptive multi-looking approach was not implemented in the course of this project, but could be further investigated in the future.

The following section presents the design, implementation, and performance of an interferogram masking approach, which aims to detect and mask out phase unwrapping errors.

4.2 Connectivity approach for phase unwrapping error detection

As demonstrated in the manuscript presented shortly, regions that are separated by low coherence pixels (e.g. due to fast flow, surface melt, and ice/bedrock transitions) are more likely to contain phase unwrapping errors. As these sources of coherence loss are often associated with regions near outlet glacier fronts, this motivates the approach of manually defining a boundary, beyond which DInSAR is avoided. However, such an approach implies that no DInSAR velocity measurements will be available for regions beyond the boundary, meaning that the substantial accuracy and resolution improvements offered by DInSAR are not realized. Hence, the ideal solution would involve detection of unwrapping errors on an image pair level, i.e. depending on characteristics of the image pair at hand.

Some unwrapping algorithms, including the algorithm of the DTU IPP software (Kusk et al., 2018) applied in the generation of all interferograms in this chapter and the associated manuscript, apply a segmentation approach (Mohr & Boncori, 2008; Hubig et al., 2000), which aims to reduce unwrapping error occurrence. The first step is the generation of a mask based on the coherence estimate. Pixels below a certain coherence threshold are masked, followed by a morphological erosion of the valid pixels, which serves to mask out areas bordering low coherence pixels. A segmentation is then performed, separating valid pixels into a collection of connected segments (shown as the different colored segments

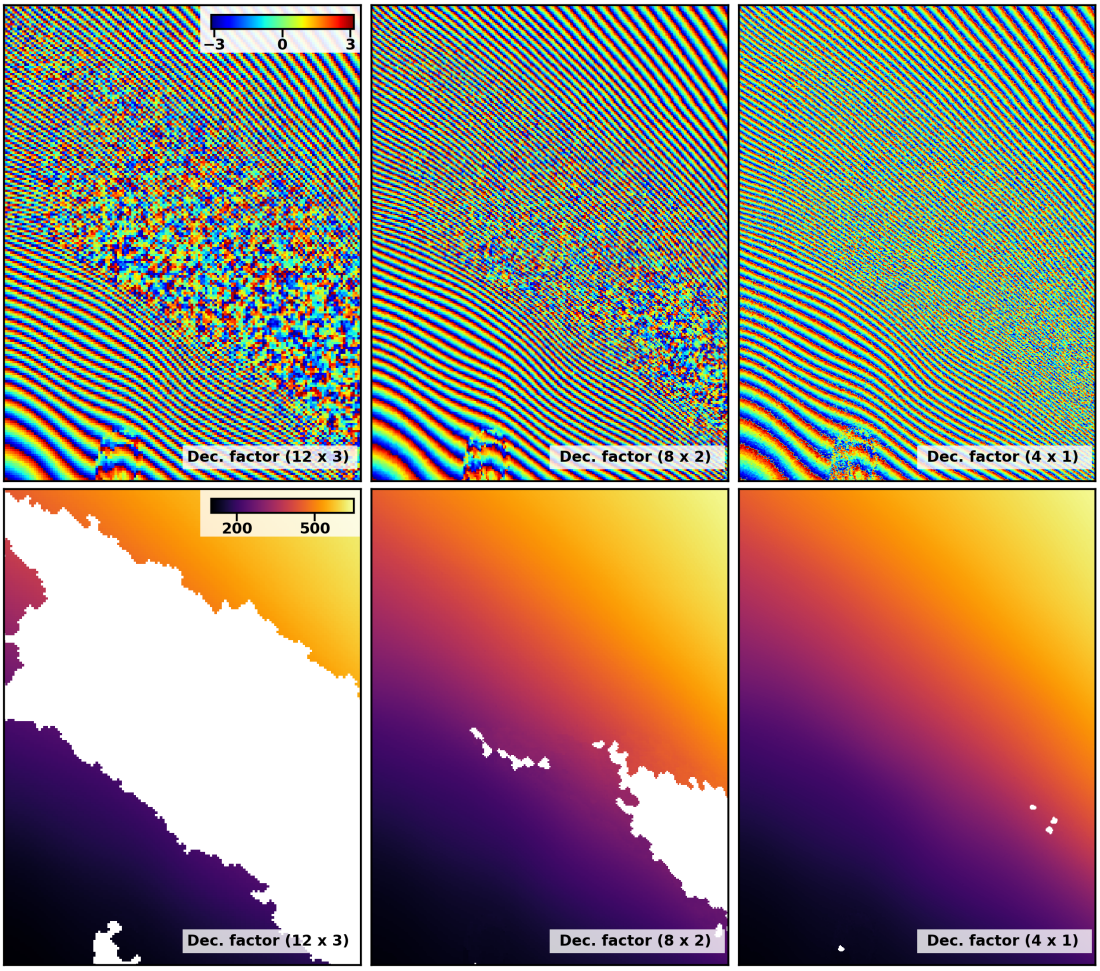

Figure 4.1: Example of a 6-day Sentinel-1 interferogram subset covering parts of a shear margin. From left to right, the applied multi-looking window size is decreased. The plot labels show the decimation factor in range × azimuth - the multi-looking factor is about 1.5 times these numbers. The top row shows the wrapped interferogram phase, while the bottom row shows the unwrapped phase image, both in radians. Transparent pixels indicate areas where the unwrapping algorithm could not determine a solution.

in Fig. 4.2b). If GCPs with accurately known velocity values are available within each segment, a segment-wise calibration can be performed, effectively correcting for unwrapping inconsistencies across different segments. Alternatively, small disconnected segments may be discarded. The approach is relatively effective at preventing unwrapping error occurrence in scenes with highly varying coherence patterns, such as glaciers and ice sheets. However, as shown in Fig 4.2c, some unwrapping errors may persist even with the application of the segmentation method. In this case, an unwrapping error of large scale and magnitude occurs in a region that is almost, but not quite, disconnected from the largest segment of the scene.

To combat such instances of unwrapping errors, an approach was defined, which seeks to mask pixels based on their *connectivity* to the rest of the scene. The approach, along with

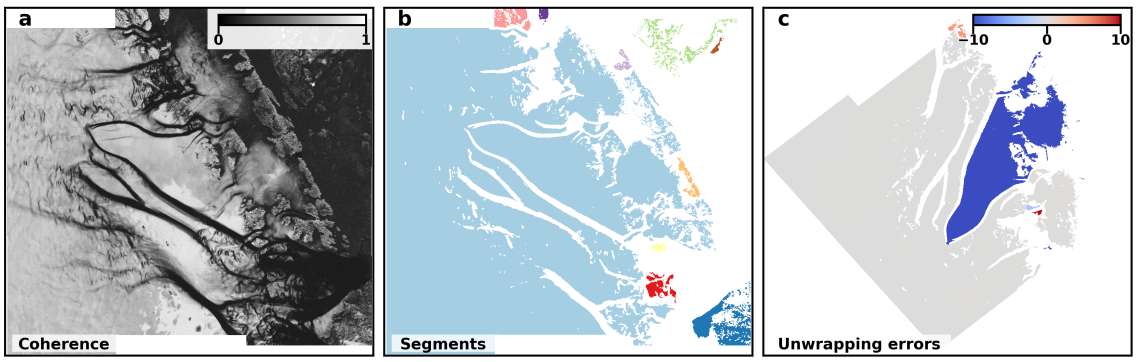

Figure 4.2: Example of the coherence segmentation approach used to reduce phase unwrapping error occurrence. Panel (a) shows the coherence, while panel (b) shows the result of the segmentation of the masked coherence image (with transparent pixels indicating masked data). The data shown here stems from a simulation, and hence the true distribution of unwrapping errors is known (and shown as number of phase cycles in panel (c) in geocoded geometry). In this example, both small- and large-scale unwrapping errors remain even after applying the masking and segmentation method.

an investigation of its performance, was documented in the manuscript:

J. K. Andersen, J. P. M. Boncori, and A. Kusk, Connectivity approach for detecting unreliable DInSAR ice velocity measurements, *IEEE Transactions on Geoscience and Remote Sensing*, vol. 60, pp. 1–12, 2022, doi:10.1109/TGRS.2022.3169722 (2022)

The full manuscript is provided in Appendix A.3 and supplementary material is found in Appendix B.2. In the following, a brief summary of the paper is provided.

4.2.1 Summary of Andersen et al. (IEEE TGRS, 2022)

The unwrapping error detection method presented in this paper builds on a definition of pixel connectivity. There are many possible approaches to defining such a parameter - in this case, we base our method on the connectivity measure first defined in Galli, 2001. The pixel connectivity estimation is based on a *confidence* measure, i.e. a measure of quality of each pixel, for which the coherence is an obvious choice. Section II-B of the paper provides a concise description of the connectivity measure. As a side note, experiments were conducted to test the effects of various weighting functions applied to the confidence map prior to estimating the pixel connectivity (some examples are shown in Fig. 4.3). None of the weighting functions, however, appeared to significantly improve the performance of the connectivity masking method. The connectivity is computed for each pixel with respect to a certain reference pixel. In the examples shown in the main text, the reference pixel is manually selected in a region of consistently high coherence, in the inland portion of the imaged scene. The reference point selection may be automated by selecting a point of maximum coherence in the largest image segment, based on the segmentation approach described in the previous section (see also the supplementary material in Appendix B.2).

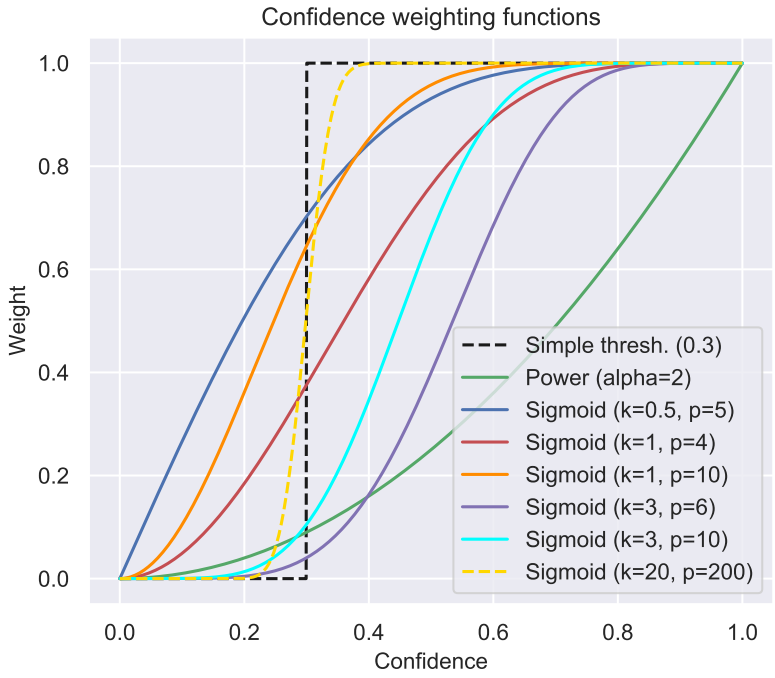

Figure 4.3: Various weight functions applied to the confidence (i.e. coherence) map prior to estimating pixel connectivity.

With the connectivity measure computed for each pixel, a mask is generated by a simple thresholding of the connectivity map. The rationale is that low connectivity values are strongly related to unwrapping error occurrence (see Fig. 5 in the manuscript). Essential to the performance evaluation of the connectivity-based masking approach is the generation of a data set of simulated interferograms. The simulation approach is described in the paper's appendix. For the performance evaluation, the downstream part of NEGIS was selected, as this constitutes a particularly challenging region for phase unwrapping, with high velocity gradients and frequent coherence loss. As the true velocity field is known for the simulated image pairs, the distribution of unwrapping errors can be accurately determined as pixels where the deviation between the DInSAR output LoS velocity field and the input field exceeds the levels that are expected due to phase noise (see Fig. 4.2c in the previous section and Fig. S2 in Appendix B.2).

With the simulated data set, consisting of 60 interferograms covering drastically different coherence scenarios, the best-performing connectivity threshold, ϵ_c, is determined. There is a certain class imbalance between the pixels with unwrapping errors and the valid (i.e. error-free) pixels. The number of valid pixels far exceeds the number of error pixels, however, we argue that masking of an unwrapping error pixel is more important than the erroneous masking of a valid pixel. Consequently, the performance of the masking algorithm is evaluated through the *recall* and *precision* estimates, which, in the context of a detection algorithm, place more emphasis on the positive class (i.e. the unwrapping error pixels). In the present case, recall can be considered the estimated probability that an error pixel is detected, while precision is the estimated probability that a pixel drawn

from the pool of all masked pixels is actually an error pixel. It is the goal of the masking algorithm to maximize both of these measures, however, to reflect the added importance of masking error pixels (compared to the erroneous masking of the same amount of valid pixels), we argue that maximizing the recall should be prioritized over maximizing the precision. This prioritization can be formalized through the F_β-score:

$$F_\beta = (1 + \beta^2)\frac{precision \cdot recall}{\beta^2 \cdot precision + recall} \tag{4.1}$$

which is a measure of performance of a detection algorithm, where recall is considered β times as important as precision. In this case, we opt to use $\beta = 2$, and thus use the F_2-score as a performance parameter to be maximized (see Fig. 4.4 for a visualization of the relationship between recall, precision, and F_2-score). Connectivity thresholds are evaluated in increments of 0.05, and a maximum F_2-score is found for the threshold $\epsilon_c = 0.30$ (see Table 1 in the paper). With this threshold, the majority of unwrapping errors are detected (recall of 0.86), although a substantial amount of valid data is also masked (precision of 0.52). Importantly, the results also show a relation between connectivity and unwrapping error magnitude, where lower connectivity values are associated with higher error magnitudes (see Fig. 5 and Table 1 in the paper). Thus, although the optimum connectivity threshold of 0.30 does not detect all unwrapping errors, remaining errors have a median magnitude of 1.7 m/y (i.e. one phase cycle).

The connectivity masking method is also demonstrated for a set of real image pairs from several Sentinel-1 ascending and descending tracks (section IV). Although the true distribution of unwrapping errors is of course unknown for these image pairs, some errors may be identified purely from visual inspection. On a qualitative level, a threshold of 0.30 also appears reasonable for the real image pairs. The paper is rounded off by a discussion of the advantages and further challenges of the connectivity masking method.

4.3 Simplistic machine learning approaches for phase unwrapping error detection

The manuscript presented above demonstrated a clear linkage between low connectivity and unwrapping error occurrence. As evidenced by the mediocre precision of the connectivity masking method, however, not all low-connectivity regions lead to unwrapping errors. In an effort to exploit the detection power of the connectivity measure, while limiting the amount of valid data discarded, a small study was conducted with a focus on utilizing simple machine learning methods for improving the pixel-wise masking approach.

Three different supervised binary classification algorithms were applied along with the simulated data set presented in the previous section. The classification algorithms are logistic regression as well as two ensemble methods using the Decision Tree method, namely AdaBoost and Random Forest. Aside from the pixel connectivity measure, a total of four other input features are provided to the algorithms: interferogram coherence, intensity

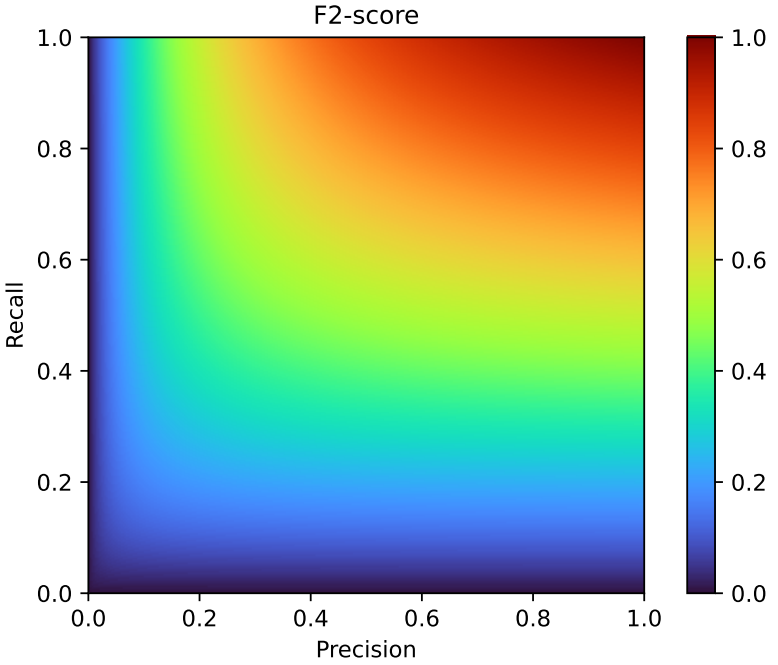

Figure 4.4: F2-score as a function of precision and recall, used in assessing the performance of a detection algorithm where recall is weighed higher than precision.

of the reference SLC image, the surface topography, and the multi-year average velocity (projected to the radar line-of-sight). The inclusion of multiple input features allows the algorithms to determine more complex patterns that lead to unwrapping errors, as opposed to simply thresholding on one feature. The classification models are trained on a subset of the simulated data set, where the output feature is simply the binary unwrapping error mask (0: valid pixel, 1: unwrapping error). Hence, the unwrapping error magnitude is not considered.

Each of the classification models are trained on a randomly selected subset of the simulated data set, as the full data set consists of $>10^9$ pixels, which would require excessive computation times. Furthermore, it is interesting to see how well the models perform when trained on a limited amount of data. Before sampling the data, four interferograms are reserved, allowing for an evaluation of the models' predictive performance on full interferograms where no samples have been used in model training. A relatively small subset is then sampled from the remaining data set. This sampling process is also used to resolve the inherent class imbalance, by randomly sampling an equal amount of valid pixels and error pixels from the data. The data subset is then used for determining the best-performing hyper-parameters for the various classification models. This is done through a 5-fold cross-validation setup using 80% of the data, while the remaining 20% is used for assessing performance of the final models. The methodology is further elaborated along with a presentation of the results, and a discussion of these, in a short unpublished manuscript in Appendix A.4.

The results of the study indicate a good performance of the classification models, which achieve both a higher recall than the connectivity masking approach described in the previous section and a substantially higher precision. As discussed in the manuscript, however, the study does have certain limitations, and it is unclear exactly how well the results generalize to other data sets. Further investigation on this topic could be carried out as future work. Concerning other possible approaches related to unwrapping error detection, whether applying the connectivity measure or not, an obvious direction would be to try to capture the spatial correlation of unwrapping errors. As seen through multiple examples in the previous sections, unwrapping errors tend to form contiguous regions, typically containing roughly the same magnitude error, surrounded by a high gradient to the neighboring areas. Some attempts were made to identify zones of unwrapping errors through the difference in output LoS velocity measurements with respect to a multi-year average velocity mosaic. While such an approach may allow for detecting obvious errors of high magnitudes, it is not obvious how to reliably separate low/moderate magnitude unwrapping errors from real velocity variations (e.g. due to seasonal effects or transient dynamic events). Hence, a simple masking of the velocity deviation, based on some threshold, will run the risk of biasing measurements towards the a priori velocity field and discard dynamic fluctuations that are actually of great interest.

Chapter 5 | Investigating ice flow changes with Sentinel-1 DInSAR time series

Land-terminating glacier in South Greenland. (Photo courtesy of Marie B. Jensen).

5.1 Sentinel-1 time series processing over the NEGIS region

One of the main goals of the PhD project was to exploit the frequent revisit time of Sentinel-1 (6 days for much of the Greenland ice sheet) and the high accuracy of the DInSAR technique to demonstrate the value of dense ice velocity time series. The Northeast Greenland Ice Stream (NEGIS) was, once again, selected as an area of interest.

The work presented in this section was carried out in collaboration with Jérémie Mouginot (IGE, Université Grenoble-Alpes). Additionally, the majority of the presented offset tracking measurements (from September 2016 onwards) were processed by Anne Solgaard (GEUS). Finalization of the analyses and documentation of the results in a journal manuscript or letter is ongoing work. In this section, we present some of the obtained results along with (preliminary) analyses and conclusions.

Introduction

The NEGIS is a unique feature of the Greenland ice sheet, being the only ice stream with enhanced ice flow 600 km inland from the margin. It is drained by three marine-terminating outlet glaciers: Zachariae Isstrøm (ZI), Nioghalvfjerdsfjorden (NG), and Storstrømmen Glacier (SG), collectively draining an area of more than 16% of the Greenland ice sheet and holding a 142 cm sea level equivalent (Mouginot et al., 2019b). While NG and SG have been close to mass balance in recent decades, ZI detached from a stabilizing sill during the 1990s. Beginning in 2012, ZI experienced a period of greatly accelerated retreat and thinning, leading to the melting of its remaining ice shelf and a significant mass loss (Mouginot et al., 2015). Previous studies have examined how changes in stress balance at the ice margin, influenced by warmer air and ocean temperatures, impact ice dynamics and mass distribution in the downstream regions (Khan et al., 2014; Mouginot et al., 2015), however it remains to be established how the interior ice sheet has responded to such changes. In other words, the extent to which inter-annual and/or seasonal changes in ice motion, caused by variations in the grounding and calving line positions, as well as other forcings, propagate upstream of the glaciers is still unclear.

In this study, we investigate recent evolution in ice dynamics on NEGIS and its surroundings by generating a time series of ice velocity using Sentinel-1 acquisitions from the past 6 years (2015-2021). We use DInSAR to retrieve high accuracy measurements of a high temporal resolution (with sampling frequency down to 6 days, when both satellites are active and interferometric coherence is retained) and a high spatial resolution (on the order of 50 m $\times$ 50 m). Amplitude-based offset tracking is also applied, allowing for a comparison between the time series obtained with the two methods. The measurements allow for examining changes in ice flow on both long and short time scales - from multiple years to seasonal, monthly, or, in some cases, even weekly changes. Particularly, we wish to investigate the spatial extent in which long-term dynamic changes are observed with each of the two methods. Additionally, we wish to determine whether sudden speed-ups observed near the ZI and NG glacier fronts during summer are also visible further upstream. Finally, in an exploratory manner, we are looking for any signs of transient

dynamic events, without a preconceived idea of exactly what type of dynamic responses to expect.

Data and methods

We processed Sentinel-1 Interferometric Wide swath images from an ascending track (T074), covering the outlets of ZI/NG/SG as well as the slower-moving upstream parts of NEGIS (see Fig. 5.1). We utilize all available images since the launch of Sentinel-1A (although the earliest available acquisitions in this region are from 2015) to generate densely sampled velocity time series. DInSAR velocity measurements are generated with all possible 6-day image pairs, i.e. the minimum temporal baseline, as loss of coherence and phase aliasing increase significantly for higher baselines. When no measurements are available from Sentinel-1B (prior to September 2016) 12-day interferograms are generated. Offset tracking velocity measurements are generated for 12-day image pairs. Although tracking-based measurements also suffer from coherence loss, feature tracking may still be possible in some regions and the increased motion observed with a longer baseline effectively increases the SNR. Additionally, using 12-day image pairs avoids the sensor-specific biases affecting tracking retrievals with one acquisition from each of the S1A/S1B satellites (Gisinger et al., 2021; Solgaard et al., 2021).

Interferometric measurements are carried out following the approach described in (Andersen et al., 2020; Kusk et al., 2021) (see also sections 3.3-3.4), using a 2016-2019 multi-year average velocity mosaic generated through PROMICE (Solgaard et al., 2021) and the 90 m TanDEM-X Digital Elevation Model (Rizzoli et al., 2017) in the coregistration and phase flattening steps. Multi-looking is performed with a factor of 15×3 in range/azimuth for each interferogram and velocity measurements are resampled to the same polar stereographic grid with a 50 m $\times$ 50 m pixel spacing. Offset tracking measurements follow the approach from Solgaard et al., 2021. Note that we exclusively use LoS offsets, which for Sentinel-1 are of a much higher quality than azimuth offsets and allow for a direct comparison with DInSAR. The offset tracking measurements are resampled to a 500 m $\times$ 500 m grid covering the same region as the DInSAR measurements. The DTU IPP software (Kusk et al., 2018) is used in the generation of both types of measurements.

Previous studies on Sentinel-1 ice velocity provide accuracy estimates of LoS measurements from individual image pairs on the order of tens of m/y for offset tracking (Solgaard et al., 2021) and $\sim$0.5 m/y for DInSAR (Andersen et al., 2020) in regions where phase unwrapping errors are not expected. Individual measurements may be affected by multiple error sources (cf. section 2.4). Both techniques are affected by spatial and temporal decorrelation, although offset tracking, in some cases, may still be able to track features. Atmospheric effects may also occur, in the form of variations in ionospheric electron count and tropospheric water content. In the case of DInSAR, a calibration is performed with a linear baseline model (cf. section 2.5), which may partially mitigate long-wavelength error effects. Note, however, that an ideal distribution of GCPs across the extent of the scene is not possible in the present case, as we wish to avoid having GCPs in areas that are either prone to unwrapping errors or may be expected to show variation in velocity across

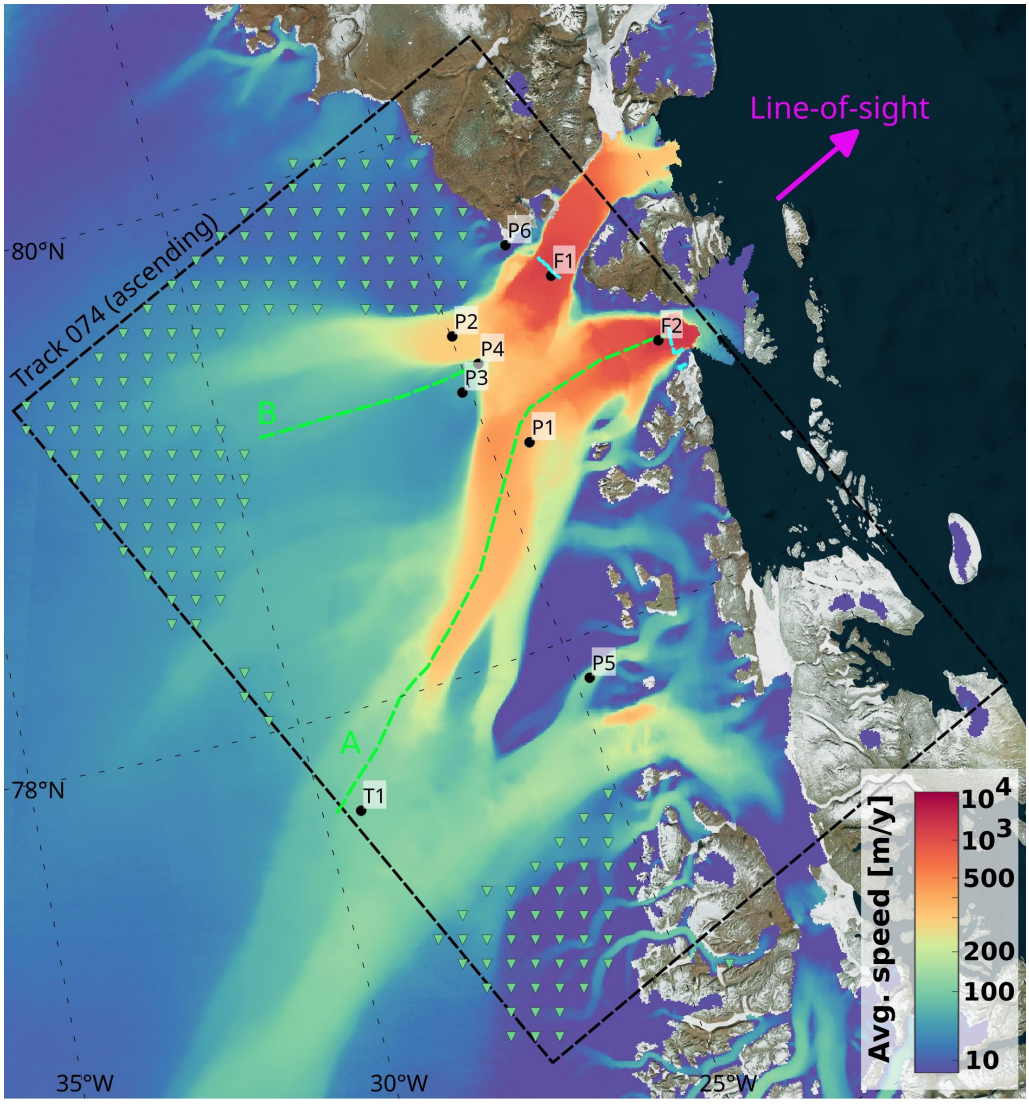

Figure 5.1: Overview of the NEGIS area studied with DInSAR and offset tracking time series. The black rectangle shows the extent of the ascending Sentinel-1 track, T074, with the magenta arrow indicating the (ground-projected) LoS, green triangles represent Ground Control Points used for DInSAR calibration, and black dots indicate various points of interest that are further investigated throughout the section. Teal lines indicate grounding lines for ZI and NG (i.e. the transition zone from grounded to floating ice, which for ZI is close to the glacier front) (Mouginot et al., 2015), and dashed green lines show transects used in Fig. 5.9. The underlying color scale shows 2016-2019 average speed (from PROMICE).

the span of the time series. The latter condition particularly limits the GCP coverage, as preliminary investigations suggested that long-term velocity changes may occur even in relatively slow-moving regions. For offset tracking, calibration is not performed (Solgaard et al., 2021).

Arguably, the most important DInSAR error source is phase unwrapping errors, which

may reach magnitudes far exceeding all other error sources. Unwrapping errors tend to occur in and around regions of high decorrelation, meaning that in the context of ice velocity retrieval, they are more likely further toward the ice sheet margin where surface melt and shear zones associated with high motion gradients are prevalent (cf. Chapter 4). Although a method was developed to reduce the occurrence of such errors (presented in section 4.2), this method was, as a starting point, not applied to the measurements here. The reason is that a main focus of the present time series analysis is to reveal brief summertime accelerations and other transient changes in ice dynamics. With the relatively low precision of the connectivity-based detection algorithm, there is a risk that some of these transient events get masked out and go unnoticed. Hence, the produced time series will inevitably contain some unwrapping errors. A mitigating factor is that once a long time series is generated, large magnitude unwrapping errors will often stand out as obvious outliers when plotting the LoS velocity time series for a given point of interest. Such outliers can then be manually inspected to determine whether they are likely caused by unwrapping errors or by actual dynamic changes.

Preliminary inspections of the obtained velocity time series suggested a roughly linear trend in velocity over a large part of the NEGIS region. In order to investigate the magnitude and extent of acceleration/deceleration, we perform a linear regression over the full time series for each pixel. As described above, outliers of large magnitudes may occur in the DInSAR time series, due to the phase unwrapping process. With an Ordinary Least Squares (OLS) regression approach, a few large magnitude outliers may heavily influence the estimated trend. Therefore, we opt to use the Theil-Sen estimator to estimate the trend in the DInSAR velocity time series. The Theil-Sen estimator is a non-parametric method, in which the slope of a data set is computed as the median of the slopes between all individual pairs of measurement points (Sen, 1968). The method is unbiased, has low sensitivity to outliers, and competes well with OLS even in cases where the normality assumption is valid (in fact, the standard error of the Theil-Sen estimator may be substantially lower than that obtained with OLS, even under normality, as long as there is heteroscedasticity (Wilcox, 2001)). A confidence interval for the estimated Theil-Sen slope is computed from the collection of slopes between pairs of measurements. Hence, a 95% confidence interval is determined as the interval containing the middle 95% of the slopes between measurement pairs. The confidence interval allows for testing the significance of the estimated trend - that is, if the confidence interval contains zero, the trend is assumed to be insignificant, and vice versa. For offset tracking measurements, the error distribution is closer to a Gaussian and the difference between results obtained with OLS and Theil-Sen is generally smaller than for DInSAR. For consistency, and because the offset tracking retrievals do contain a scarce amount of large-magnitude outliers, all the regression results shown here are based on the Theil-Sen estimator. Regression is only performed for pixels where a minimum of 50 observations are available.

Results

Fig. 5.2 shows, for each pixel in the track T074 time series, the relative annual acceleration, computed as the LoS velocity Theil-Sen slope divided by the intercept of the fit, as obtained with DInSAR and offset tracking measurements, respectively. Note that if the flow direction vector is assumed to be constant over the measurement period, the relative acceleration computed from the LoS measurements is equivalent to the absolute change in speed. A linear trend is only shown for pixels where a significant trend is observed, meaning pixels for which the 95% confidence interval does not overlap zero. Note that some areas, in which meaningful results were not obtained, are masked. These are areas of bedrock, areas of very low LoS velocities ($v_{LoS} < 15$ m/y average speed) and areas where the LoS and flow direction are nearly perpendicular. Additionally, the shear margins in the fast-flowing parts of NEGIS do not contain data (as coherence is lost in every retrieval).

Both methods observe a similar pattern within the bulk of the faster-flowing ice stream, i.e. a significant acceleration in the range 0.2-1.5%/y, increasing to >2%/y close to the ice front (where only offset tracking measurements are available). With DInSAR, however, significant acceleration is observed until roughly 230 km upstream of the ZI ice front, the corresponding distance being 190 km for offset tracking. The DInSAR measurements also indicate acceleration in a large region between the ZI and NG branches of the ice stream. For the northern stream leading to NG, only a small acceleration is observed with DInSAR (on the order of 0.2%/y), which is not observed with offset tracking. Both methods show a general deceleration of the NEGIS branch leading to SG (less than 0.5%/y) and a large relative deceleration for the smaller sub-stream emerging from the northern part of this branch (reaching nearly 5%/y). Finally, both methods detect a large relative acceleration in a sub-stream extending east of the main ZI branch.

Fig. 5.3 shows velocity time series plots for three points: one within the NEGIS branch leading to ZI, one in the branch leading to NG, and one in the slow-moving region in between these two branches. Looking first at the time series from the ZI branch (point P1), we observe that the data, particularly the DInSAR measurements, conform fairly well to the linear model, with an acceleration of about 1%/y. DInSAR measurements are scarce prior to September 2016, as coherence is often lost in this fast-flowing region for 12-day pairs. Unwrapping errors are also prevalent in this region, as evidenced by the relatively large amount of outliers. Note, however, that the outliers in September 2020 and November 2021 are actually not caused by unwrapping errors, but by an extensive dynamic response, which will be further investigated in section 5.2. Finally, a slight deceleration is observed in late summer in 2019. The time series from the NG branch (point P2) shows a much more modest acceleration of about 0.2%/y. Interestingly, a slow-down appears at the end of summer in both 2019 and 2020, similar to the slow-down of the ZI branch in late August 2019. Unfortunately, the dynamic pattern leading up to this slow-down is not captured, due to lack of coherence (a general issue of both the DInSAR and offset tracking techniques in summer for this region). In the summer of 2018, decent coverage is available,

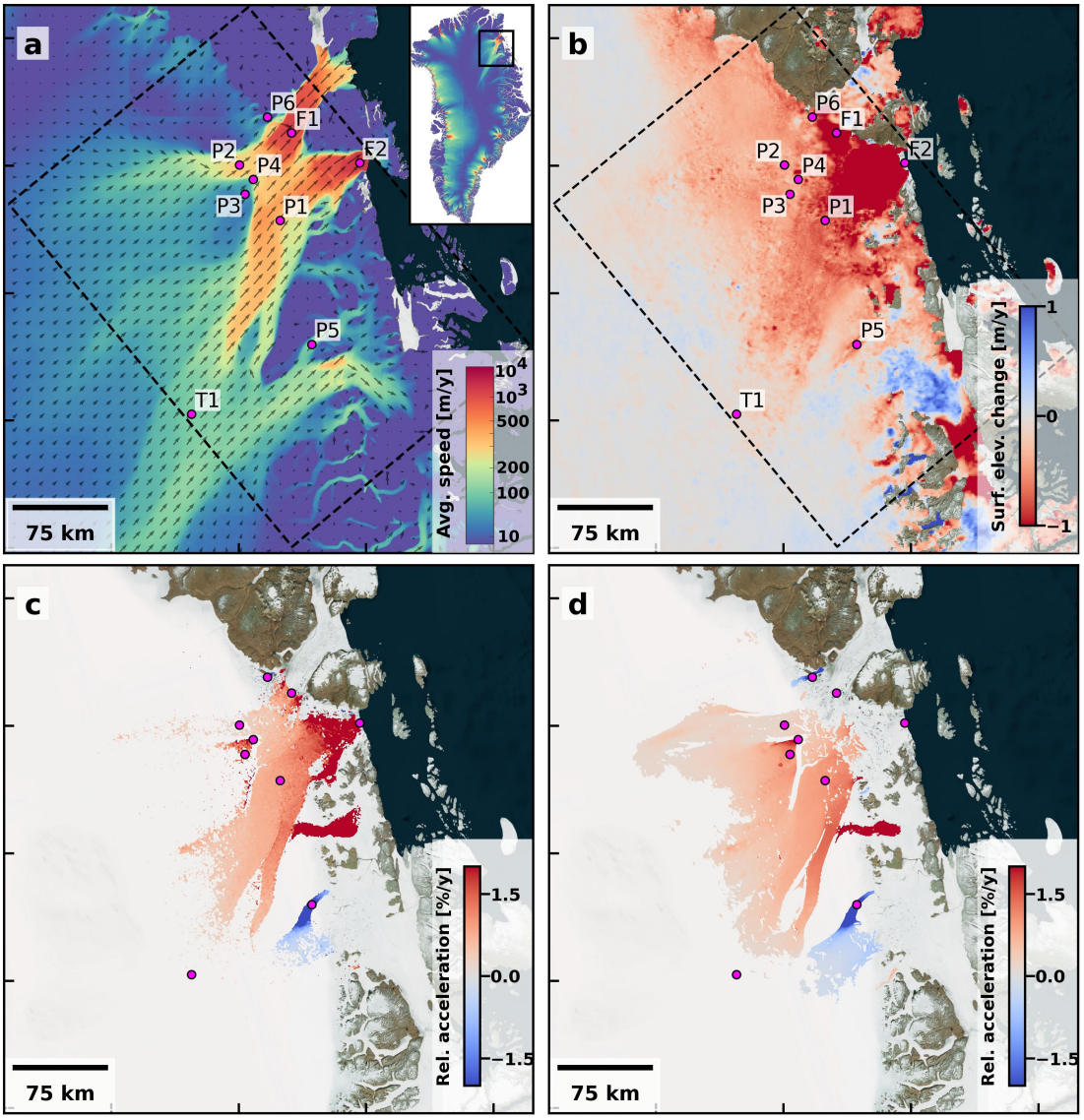

Figure 5.2: Results of linear regression (using the Theil-Sen estimator) applied to the full Sentinel-1 track T074 time series of LoS velocity measurements from DInSAR and offset tracking. Panels (c) and (d) show the estimated relative acceleration (i.e. the trend relative to the intercept of the fit, expressed in %/y), where significant at the 95% confidence level, for offset tracking and DInSAR, respectively. Panel (a) shows 2016-2019 average speed (from PROMICE) and panel (b) shows 2018-2021 surface elevation change from the ICESat-2 L3B/ATL15 product at 1 km resolution (Smith et al., 2021).

and a relatively stable velocity is observed. Finally, for the slow-moving area between the NG and ZI branches (P3), no discernible short-term patterns are observed. A relative acceleration of more than 1%/y is observed with DInSAR (which is barely significant with the offset tracking measurements). Again, coherence is mostly lost during summer.

The results in Fig. 5.2 indicates areas where a significant trend is observed in the generated time series, suggesting that these areas are unlikely to have zero trend. However,

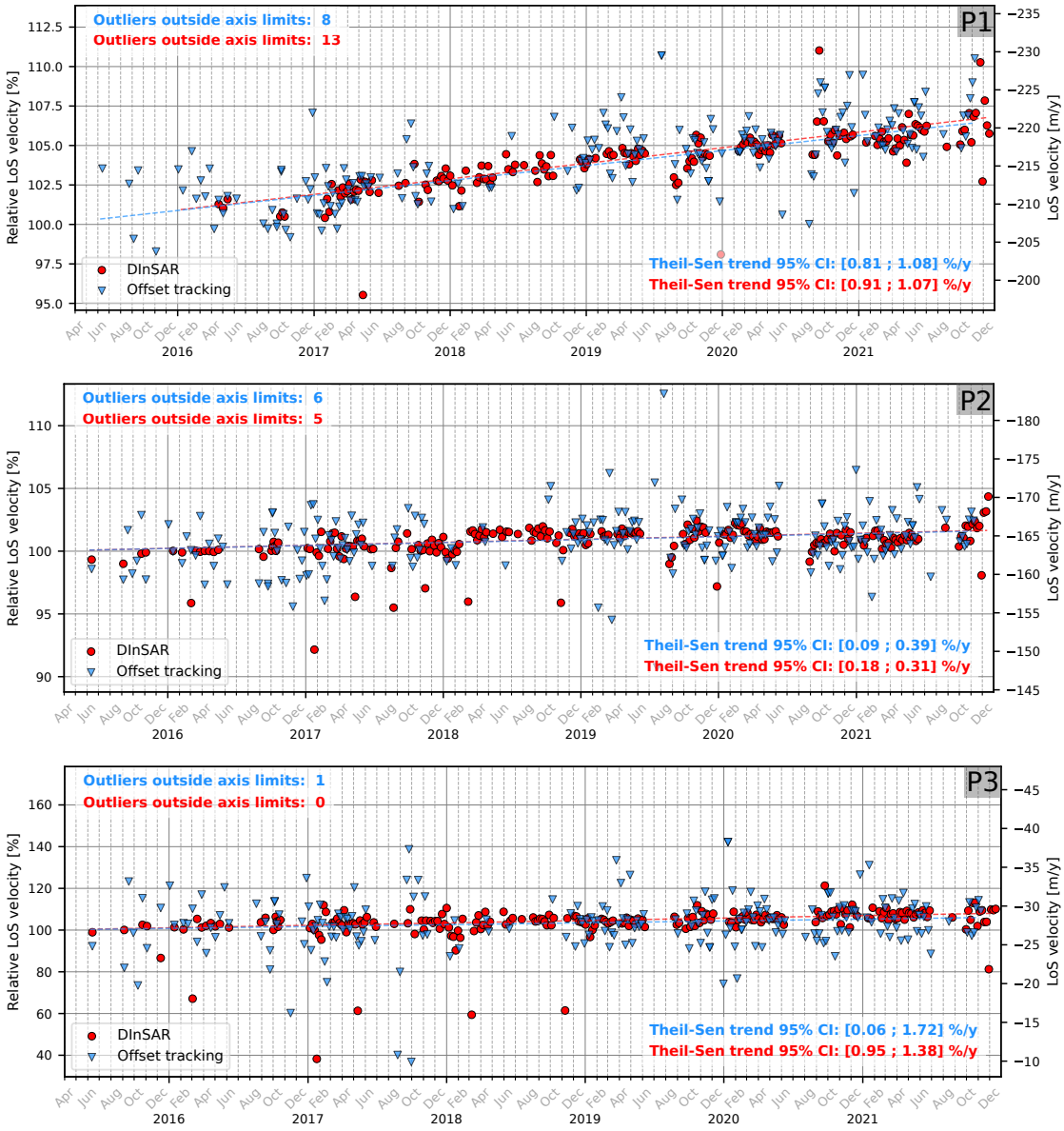

Figure 5.3: Time series plots showing relative (left y-axis) and absolute (right y-axis) LoS velocity from track T074 DInSAR (red) and offset tracking (blue) measurements for the points P1-P3 (shown in Fig. 5.1). Dashed lines show the Theil-Sen linear regression fit. Relative LoS velocity measurements are referred to the intercept of the Theil-Sen fit. Note that some large magnitude outliers exist outside of the axis limits, to allow a zoomed in view of the bulk of the data set.

based on these results, one cannot directly infer that areas where a significant trend is *not* observed actually have zero acceleration. Within the main branch of NEGIS, the DInSAR measurements indicate a significant trend until about 230 km upstream from the ZI grounding line. To determine how small of a trend would be detectable in the area further upstream (around point T1 in Fig. 5.2), given the noise parameters of our DInSAR time series, a sensitivity test was carried out in the form of a Monte Carlo simulation. An

estimate of the (pseudo)-Gaussian noise in the LoS velocity (i.e. the uncertainty caused by phase noise, not unwrapping errors) was obtained by computing the standard deviation of the time series from a representative point in the region, discarding the few obvious unwrapping errors that were present. This provided an estimate of the LoS velocity standard deviation of $\sigma_{LoS} = 0.8$ m/y. The intercept of the Theil-Sen fit, i.e. the LoS velocity at the start of the time series, is about -60 m/y (in this case we simply use the absolute value). Inspecting individual time series in the region, we estimate that roughly 5% of measurements are affected by an unwrapping error, while about 20% of measurements are missing, due to either loss of coherence or lack of Sentinel-1 acquisitions (relevant for parts of 2015 and 2016). Using these parameters, we generate synthetic time series of 6 years in length, a sampling frequency of 6 days, Gaussian noise determined by σ_{LoS}, 20% missing data (removing measurements at random), 5% outliers in the form of unwrapping errors with random magnitudes in the interval 15 m/y to 150 m/y, and a known (true) trend. We then perform a Theil-Sen regression on the synthetic time series and determine whether or not a significant trend is observed (given a 95% confidence level). This experiment is repeated for a range of (true) trends. For each trend value, a total of $N = 1000$ realizations are carried out, each time estimating whether or not a significant trend is obtained. This allows for the computation of a significant trend *detection rate* for each trend. For a given true trend, this detection rate can be interpreted as the probability of actually observing a significant trend.

The result of the Monte Carlo sensitivity analysis for the far upstream region (point T1) is shown in Fig. 5.4. Note that the true trend is given as a relative trend (in units of percent of the intercept velocity per year, as in Fig. 5.2). Fig. 5.4 indicates that, given a trend of 0.2 %/y, a significant trend would be observed more than 95% of the time. Conversely, for a trend of 0.1 %/y, significance would be concluded only 50% of the time. Hence, for this region, we find that a relative acceleration of a magnitude around 0.1 %/y or smaller could exist in this far upstream region. Note that the estimated relative sensitivity corresponds to an absolute LoS velocity trend sensitivity of $(0.1\ \%/\text{y})/100\% \cdot 60\ \text{m/y} = 0.06\ \text{m/y}^2$. This estimate, however, is only accurate for the parameters above, which were defined for the specific region in upstream NEGIS. The level of phase noise, coherence loss, and unwrapping errors may all be different in other regions.

While estimating accurate long-term trends in ice velocity is valuable in itself, the main value in obtaining a densely sampled velocity time series is, arguably, the possibility of observing dynamic changes that occur on time scales shorter than multiple years. In the following, we present time series measurements from a few different locations, which demonstrate interesting (non-linear) dynamic behaviour and highlight the added value of monitoring changes in ice flow speed at a high temporal resolution. Fig. 5.5 shows DInSAR and offset tracking LoS velocity time series for each of the locations.

Inspecting first the velocity time series for P4 in Fig. 5.5, which is located right at the intersection of the shear margins of the NG and ZI branches, reveals that the relatively large observed acceleration in this area is highly non-uniform. In fact, the acceleration

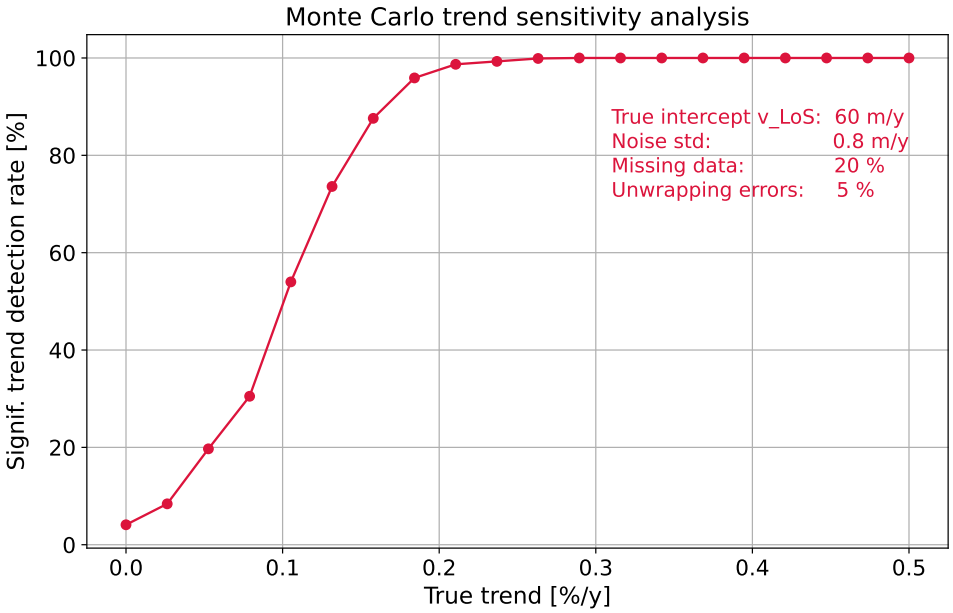

Figure 5.4: Monte Carlo sensitivity analysis estimating minimum detectable (relative) trend in velocity using the Theil-Sen estimator, given characteristics of the DInSAR data in the vicinity of point T1 in Figs 5.1/5.2. The plot shows the rate of detection of a significant trend (y-axis), given a true relative velocity trend (x-axis, expressed in percent of the intercept velocity per year) and a starting velocity of 60 m/y. For each true velocity trend sampled, a total of $N = 1000$ experiments is conducted. In each realization, a 6 year time series (sampled with a frequency of 6 days) is generated, adding Gaussian noise with a standard deviation $\sigma_{LoS} = 0.8$ m/y. Additionally, 20% of the data is discarded (simulating loss of coherence) and an additional 5% of the data are converted to unwrapping errors by adding a random outlier magnitude in the interval 15 m/y to 150 m/y.

appears to occur at two distinct points in time, namely the summers of 2019 and 2020, where accelerations of nearly 10% and 5%, respectively, occur. Surface melt in northeast Greenland was high for the 2019 and 2020 summers, compared to previous summers (see Fig. 5.6), and inspection of the interferometric coherence reveals a much larger presence of melt ponds and crevasses in early September 2019 and 2020, compared to the previous summers (2017 and 2018) and to the period right before the speed-ups are observed (May-June 2019/2020). Fig. 5.7 shows a comparison between early and late summer coherence retrievals for the years 2018 and 2019. Interestingly, following each of the two summer speed-ups is a period of gradual slow-down. This could, perhaps, be caused by a decrease in available melt water in the subglacial system (after a sudden influx of water, which could explain the summer speed-up), or through the transition into a more efficient drainage system, i.e. the evolution of efficient drainage channels in the ice and/or underlying sediments. This interpretation would be consistent with the conceptual model of the dynamic response caused by a subglacial drainage event suggested by Livingstone et al., 2022. It is not quite obvious, however, whether or not the observed dynamic response is indeed related to surface melt and subsequent subglacial water routing, and the exact

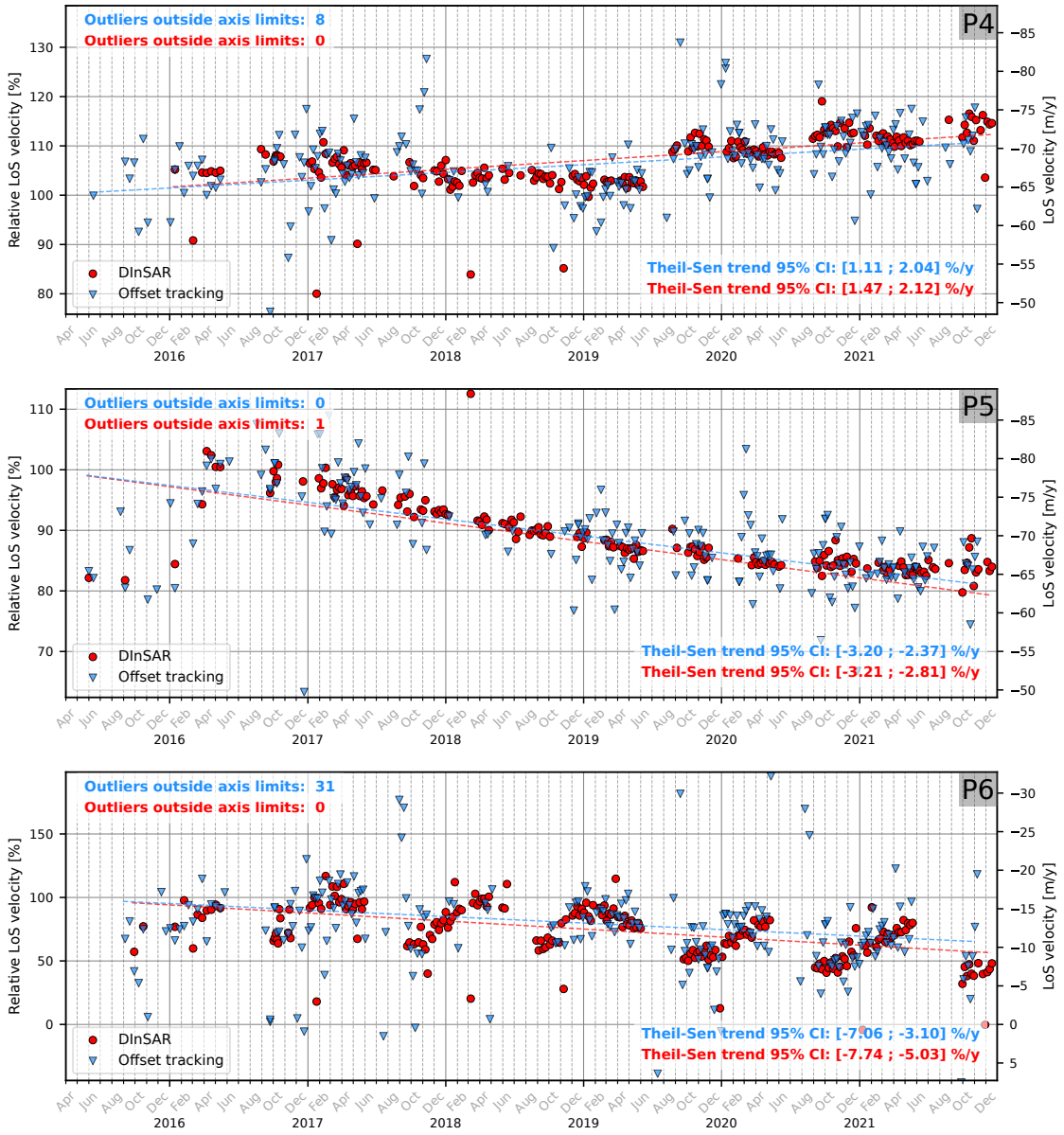

Figure 5.5: Time series plots showing relative (left y-axis) and absolute (right y-axis) LoS velocity from track T074 DInSAR (red) and offset tracking (blue) measurements for the points P4-P6 (shown in Fig. 5.1). Dashed lines show the Theil-Sen linear regression fit. Relative LoS velocity measurements are referred to the intercept of the Theil-Sen fit. Note that some large magnitude outliers exist outside of the axis limits, to allow a zoomed in view of the bulk of the data set.

cause of the speed-ups remains a point of further research. It should be noted that the speed-up in 2020 coincides with a (presumed) subglacial drainage event propagating far along the ZI branch (documented in section 5.2) and a slight deceleration within the NG branch, as shown in Fig. 5.3.

Similarly, inspecting the time series for point P5 in Fig. 5.5, located in a sub-stream in the northern part of the SG branch, reveals a velocity history which does not conform

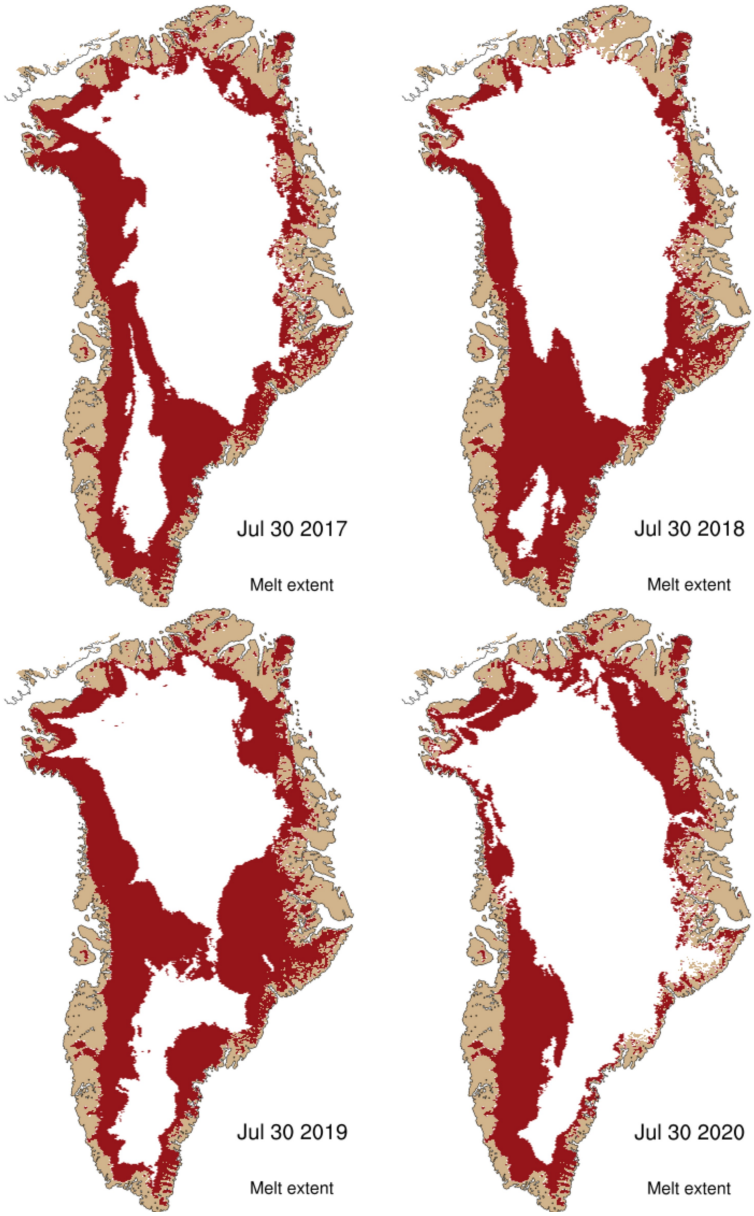

Figure 5.6: Extent of surface melt over the Greenland ice sheet in late July 2017-2020. The melt extent, indicated in red, is identified as areas where a minimum of 1 mm surface melt is predicted by an SMB model (Langen et al., 2017). Data was acquired from DMI/PolarPortal: http://polarportal.dk/en/greenland/ (accessed on 16th August 2022).

to a simple linear model. A substantial increase in speed (about 20%) occurs between late 2015 and April 2016. Note that only a few data points are available during this time (partially due to a lack of Sentinel-1 acquisitions and partially due to increased decorrelation in 12-day image pairs) and one might reasonably assume that unwrapping errors affect the earliest measurements. Visual inspections of the wrapped and unwrapped interferograms from before and after the speed-up, however, suggest that this is not the case. Additionally, there is a reasonable agreement between offset tracking and DInSAR measurements, which can be considered (mostly) independent retrievals. From May 2016

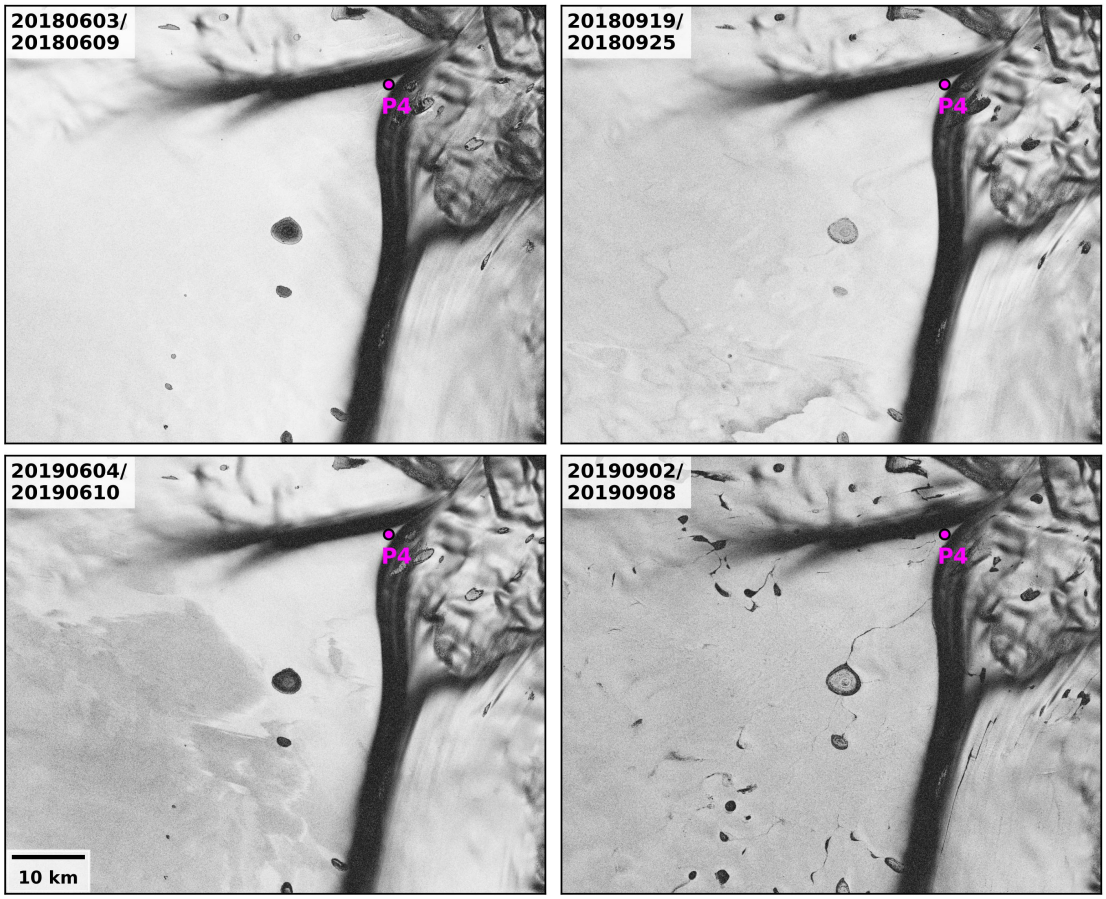

Figure 5.7: Interferometric coherence for Sentinel-1 interferograms (track T074) acquired in early June and September 2018 (top) and 2019 (bottom). Note that the presence of crevasses and surface lakes/ponds, seen as cracks and small polygons of lost coherence, is substantially increased in summer 2019, coinciding with a speed-up of the region bordering the intersection of the ZI/NG shear margins (which are seen as black bands, due to coherence loss). The point P4 refers to the same point indicated in Fig. 5.1 and for which the velocity time series was shown in 5.5.

onward, the speed gradually decreases, at a varying rate, until reaching roughly the same velocity as in 2015. SG has long been known as a surge-type glacier (Mouginot et al., 2018), although previous studies (to my knowledge) has not investigated the behaviour of this particular sub-stream. The downstream parts of SG do not contain a meaningful time series as the flow direction is nearly perpendicular to the LoS. The onset of the observed early-2016 speed-up is a point of further investigation.

P6 in Fig. 5.5 shows the observed time series for a small slow-moving glacier just west of the NG outlet. Here, we observe a long-term deceleration, on the order of 5%/y, but also a seemingly seasonal pattern. In this region, DInSAR coverage is consistently lacking in summer (presumably due to extensive surface melt), making it harder to interpret the seasonal signal. It appears that velocity is consistently highest during early summer, i.e.

the onset of the melt season (with the exception of 2019). Such a dynamic response would be consistent with the model proposed by Davison et al., 2019 for a glacier on a hard bed. In this context, a hard bed refers to a surface consisting of non-deformable bedrock, as opposed to a soft bed, which contains deformable sediments and till. As an efficient drainage system has not yet been established at the onset of the melt season, surface melt water from crevasses and moulins may cause a decrease in basal friction, and hence a higher degree of basal sliding (Davison et al., 2019). Note that the offset tracking measurements struggle to map the seasonal pattern, as the signal-to-noise ratio becomes small in this slow-moving region.

Near the glacier fronts of ZI and NG, velocity peaks of high magnitudes occur during all summers since 2015, as shown by the offset tracking measurements in Fig. 5.8. These downstream summer speed-ups have also been documented with in-situ GPS measurements (personal communication, Abbas Khan). While oceanic warming of the ice, which affects glacier calving processes (Straneo & Heimbach, 2013), has been observed to cause long-term changes in the dynamics of ZI and NG (An et al., 2021; Mouginot et al., 2015), the summer speed-ups have previously been associated with surface melt water infiltrating the subglacial system, causing increased sliding speeds through bed lubrication (Vijay et al., 2019). One of the objectives of this study was to investigate whether a corresponding speed-up is observed in the upstream parts of those glaciers. In the DInSAR measurements, however, similar velocity peaks are not apparent (see Fig. 5.3). It should be noted, again, that observational gaps are present for most summers (particularly during 2019-2021), as coherence loss tends to be more pronounced during melt season. The accelerations at the fronts occur relatively briefly, beginning sometime in June, peaking in July, and returning to pre-event speeds during August. This is exactly the period in which coherence is often completely lost, meaning that a potential dynamic response in the upstream regions may simply be missed due to observational gaps. Measurements over the 2018 summer, where DInSAR coverage is better, do not suggest a summer speed-up (Fig. 5.3), however, the summer speed-up was also much smaller at the glacier outlets, likely due to a smaller amount of surface melt that year. For NG (point P2 in Fig. 5.3), a slight deceleration was observed in late August/September for multiple summers. Such a deceleration is also observed at the ZI front (and in the upstream parts for the year 2019), however it is not readily apparent at the NG front.

The region in which we observe significant flow acceleration through the DInSAR LoS velocity measurements coincides well with the region in which ice thinning (i.e. negative surface elevation change) is observed by ICESat-2 laser altimetry, as seen in Fig. 5.2. Ice thinning may be caused both by increased surface melting and by flow acceleration (that is, ice is transported downstream faster than new ice, transported from upstream or generated through snowfall, can replace it). The latter term is often referred to as dynamic thinning. As seen in Fig. 5.2, the thinning rates on ZI and NG are comparable (although ZI shows high thinning rates further upstream from its grounding line, compared to NG). A recent study (An et al., 2021) concluded that, during the last four decades, thinning

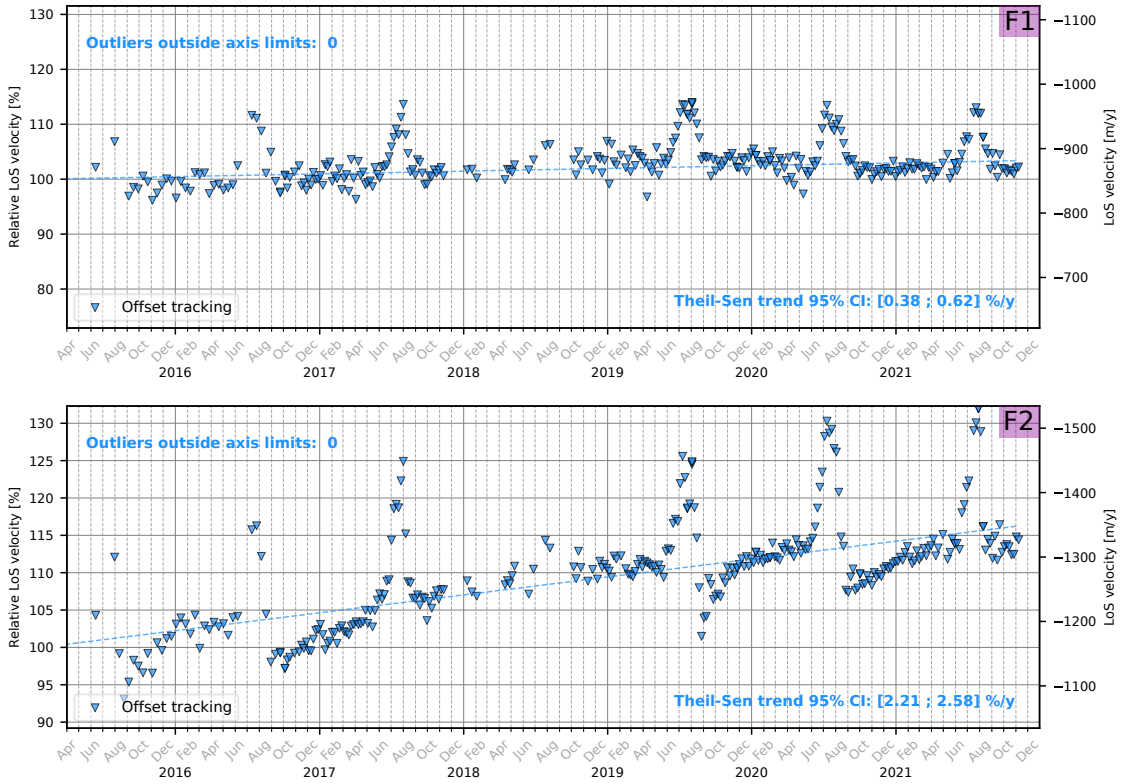

Figure 5.8: Sentinel-1 offset tracking LoS velocity time series for two points near the NG (top) and ZI (bottom) grounding line, respectively. Locations of the two points, F1 and F2, are shown in Figs. 5.1 and 5.2.

induced by surface melt has been small, relative to the total thinning observed on ZI, suggesting that dynamic thinning is the dominant contributor for this glacier (along with thinning due to oceanic warming close to the grounding line). Conversely, for NG, the surface melt contribution is close to the observed thinning rate, indicating that dynamic thinning plays a smaller role. These observations are well in line with our results, where ZI is observed to show a substantially higher flow acceleration than NG.

Fig. 5.9 presents transect plots showing relative acceleration (from DInSAR and offset tracking) along with surface elevation change from ICESat-2 altimetry for transects A and B, indicated in Fig. 5.1. For transect A, which follows the ice stream towards the ZI grounding line, thinning is observed at a roughly constant rate from about 180 km to 50 km upstream, where DInSAR and offset tracking also measure a moderate (relative) acceleration. Then, as we approach the ZI grounding line, both thinning and relative acceleration drastically increase. For transect B, which traverses through the slow-moving region between the NG and ZI branches, ending at the intersection of the shear margins, a small relative acceleration is observed across the transect with DInSAR, whereas offset tracking only finds significant acceleration in the last stretch of the transect, closer to the shear margins, where relative acceleration increases to around 2%/y. The surface elevation data set shows increasing thinning (although of a relatively low magnitude) across most

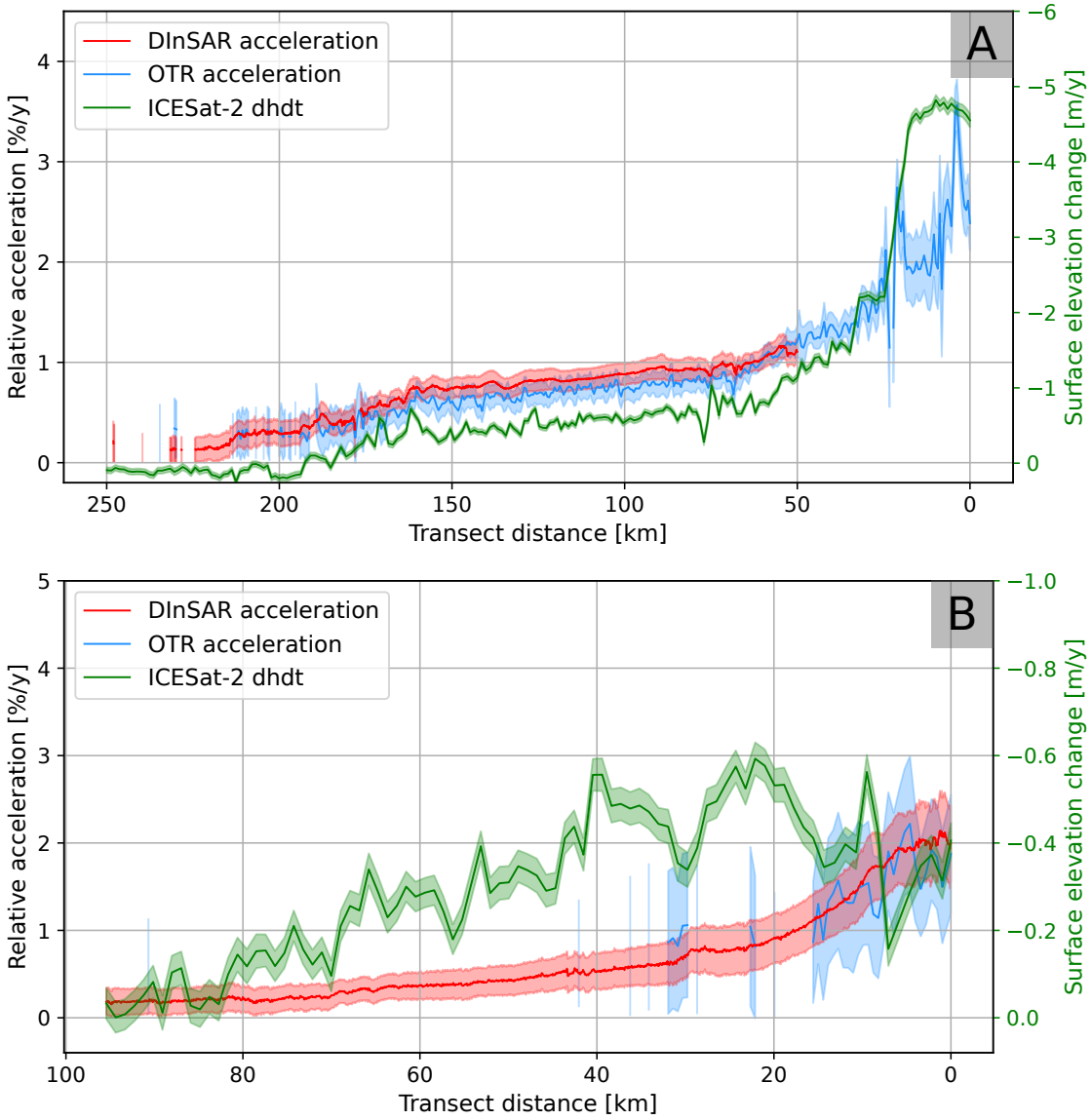

Figure 5.9: Transect plots showing estimated relative ice flow acceleration from DInSAR (red line) and offset tracking (blue line) along with 2018-2021 surface elevation change from ICESat-2 data (green line, values shown on y-axis to the right). The top and bottom panels show results along transects A (ZI branch) and B (slower-moving region between the ZI and NG branches), respectively. The transects are indicated in Fig. 5.1. Transparent bands indicate the 95% confidence interval for the DInSAR and offset tracking measurements, and ± 3 times the estimated standard error for the ICESat-2 product. Note that acceleration values are only plotted where significance is found. The x-axis shows distance along the transect, with 0 representing the lowest elevation - for transect A, this is near the ZI grounding line, while for transect B, this is near the intersection of the ZI/NG shear margins.

of the transect, trailing off as we approach the shear margin intersection.

Discussion and conclusion

A limitation of the DInSAR method is that only motion in the radar LoS direction (i.e. a combination of horizontal and vertical contributions) can be measured. For areas where the ice flow vector is perpendicular to the LoS, horizontal motion sensitivity is lost. Although a single satellite track yields only 1-dimensional measurements, assuming a constant flow direction, relative change in speed may still be estimated, as demonstrated here. A common approach for obtaining the full ice flow vector with DInSAR is to combine measurements from an ascending and descending track with the assumption of surface-parallel flow (Joughin et al., 1998). A disadvantage of this approach is that image pairs from the ascending and descending tracks available over this region only have a 50% temporal overlap, which may introduce inaccuracies when short-term flow changes occur. Furthermore, in our experience, interferometric coherence may vary substantially in the span of just a few days and retrieval of the velocity vector is, of course, limited to areas where coherence is retained for both tracks. Consequently, we opt to analyze the LoS velocity measurements from a single track directly. Under the assumption of a constant flow direction, the relative change in LoS velocity from a single track was interpreted as the relative change in absolute speed. Note, however, that this assumption breaks down in some cases, for instance in areas near (and beyond) glacier grounding lines or where local dynamic effects lead to vertical motion (as presented in section 5.2).

The availability of several years of observations allows the estimation of a multi-year trend in ice velocity (see Fig. 5.2). As exemplified in Fig. 5.5, however, the motion history does not conform to a simple linear model for all locations, highlighting the added value of DInSAR in generating time series of high temporal resolution and high accuracy, and the importance of analyzing full time series. Naturally, observations of transient ice flow changes are limited by the satellite repeat period (which is currently 12 days, after the failure of S1B in December 2021), and further limitations may be imposed in the case of coherence loss, which, in the context of the Greenland ice sheet, increases rapidly with increasing temporal baseline. Even with 6-day image pairs available, coherence loss is a significant obstacle in summer (at least for the region investigated here), as for instance seen in P6 in Fig. 5.5. It should be noted that this obstacle is also present for offset tracking. Although offset tracking is often advertised as not relying on retained coherence as heavily as DInSAR, this is only true in the presence of trackable features, which is far from always the case, particularly in upstream regions.

We presented a densely sampled time series of velocity measurements in the NEGIS region using both tracking- and phase-based techniques on Sentinel-1 data. We demonstrated how phase-based measurements provides improved accuracy and resolution, increasing the sensitivity to changes in ice motion on both long and short time scales. A roughly constant acceleration of the ice stream is observed far inland, more than 200 km from the Zachariae Isstrøm ice front with a magnitude up to about 1%/y, increasing to several percent per year towards the grounding line. The upstream parts of Nioghalvfjerdsfjorden Glacier appear to be more stable, showing little to no acceleration, which is in line with

previous studies investigating changes closer to the ice front. Additionally, acceleration is observed in the slow-moving region outside of the ice stream. Close to the shear margins, a sudden speed up occurs during two consecutive summers, suggesting a possible relation to surface melt conditions. In a small sub-stream near Storstrømmen Glacier, a sudden speed-up was observed over the course of a few months, followed by a long-term return to pre-event speeds. Finally, we demonstrated the ability of DInSAR to capture a consistent seasonal pattern over a small, relatively slow-moving glacier, which was not apparent in tracking-based measurements. The findings illustrate how regions far inland are impacted by various forcings, be it warmer air temperatures or dynamic changes occurring near the ice front of the large outlet glaciers. The exact forcings relevant in each of the observed cases remain to be fully established. This study demonstrates a so far under-utilized potential for measuring changes in ice motion with high accuracy and temporal resolution by applying interferometric techniques to the Sentinel-1 archive.

The remaining two sections of this chapter investigate two cases of a transient dynamic response, both related to hydrological events.

5.2 Subglacial hydrology-dynamic effects observed on NEGIS

In analyzing time series of DInSAR measurements, a standard approach within the PhD project has been to inspect, for each image pair, a map of the difference between the output LoS velocity and some reference LoS velocity field, for instance the pixel-wise median LoS velocity over the full time series, or a certain representative retrieval. In regions where DInSAR retrieval is possible, velocity variations are often of a relatively small magnitude (<10%). Hence, visualizing velocity anomalies, with respect to some reference field, provides a clearer picture of potential dynamic changes, rather than simply inspecting the LoS velocity retrievals. The reference field could also be taken as the LoS-projection of a multi-year and multi-sensor average velocity map, however, as these are typically at a substantially lower resolution than the DInSAR measurements, there is a risk of interpolation artefacts being disguised as small-scale velocity changes. Consequently, the reference field is instead taken as the pixel-wise median DInSAR LoS velocity. The median is preferred over the mean, as a few unwrapping errors of large magnitude may (locally) cause a substantial bias in the mean. In many cases, the velocity anomaly maps simply show negligible deviations from the reference field or patterns that may be inferred to arise from residual unwrapping errors or atmospheric effects. However, some cases show distinct features that are clearly unrelated to the known error sources and can (with high confidence) be interpreted as dynamic effects. In this section, a presentation is provided of an apparent hydrology-dynamic event (meaning a dynamic response associated with subglacial and/or supraglacial hydrology), extending far along the NEGIS, revealed by DInSAR time series measurements. It should be stressed that the work presented in this section is recent and unfinished. Hence, in-depth analyses and interpretations of the DInSAR measurements (in combination with other data sources), preferably in collaboration with experts in subglacial hydrology, is work to be carried out beyond the PhD project. This is further addressed at the end of the section.

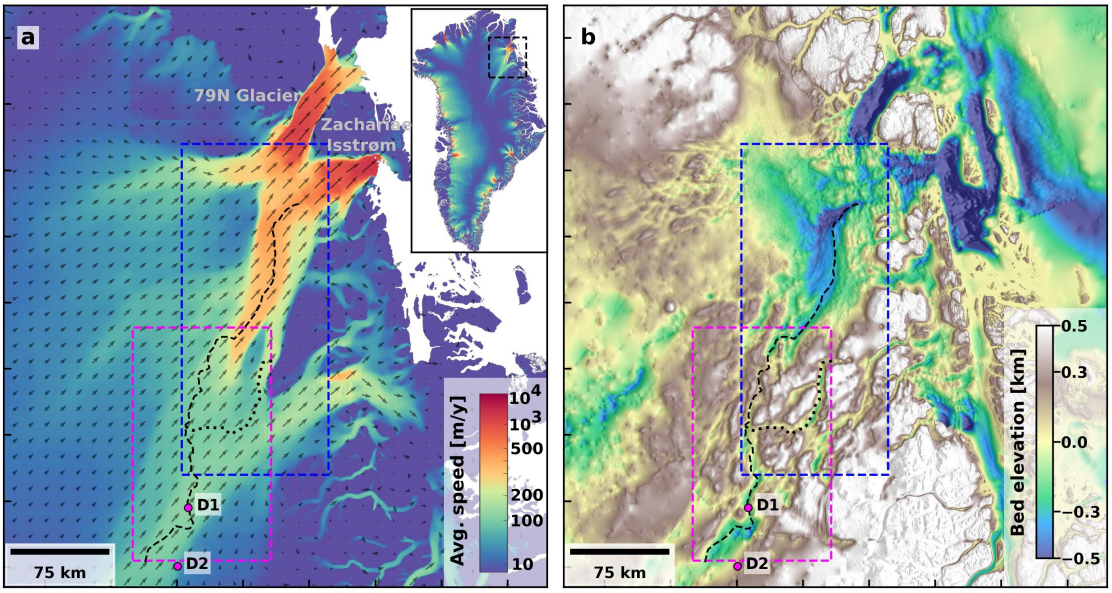

Figure 5.10: Overview of the NEGIS study area showing 2016-2019 average velocity magnitude from PROMICE (Solgaard et al., 2021) (a) and bed elevation from BedMachine v4 (Morlighem, 2021) (b). The blue and magenta rectangles indicate the outlines of Figs. 5.11-5.12 and Fig. 5.13, respectively. The black dashed line indicates the drainage pathway inferred from propagation of the observed uplift wave (with the dotted line indicating a secondary branch-off), further described in the text. Magenta dots indicate points of interest further analyzed in Figs. 5.15 and 5.16.

An overview of the study region is provided in Fig. 5.10, which shows the average velocity magnitude (Solgaard et al., 2021) and bed elevation (Morlighem, 2021), along with outlines showing the locations of the presented DInSAR measurements. Note that bed elevation varies substantially along the ice stream, with a complicated pattern of cavities and protrusions further upstream, and a deep (but locally relatively smooth) basin further downstream.

Fig. 5.11 shows Sentinel-1 DInSAR measurements from one ascending track (T074) and one descending track (T112) in the downstream portion of NEGIS (blue rectangle in Fig. 5.10). The plots show anomalies in LoS velocity, i.e. the deviation of the given DInSAR retrieval from the median over the full 2016-2021 DInSAR time series. Note that the T074 measurements stem from the time series presented in section 5.1. For the descending track, the same processing parameters are used. Looking first at the T074 measurements in the bottom panels of Fig. 5.11, a negative LoS velocity anomaly is observed in a large-scale wave propagating downstream of Zachariae Isstrøm through late August and September. Within this wave, however, ”bead-like” patterns are observed, which show a LoS velocity anomaly that changes from positive to negative values in subsequent acquisitions. In the T112 measurements (top panels of Fig. 5.11), the same bead-like pattern is observed, while the large-scale wave of uniform anomaly values that was observed in the T074 data

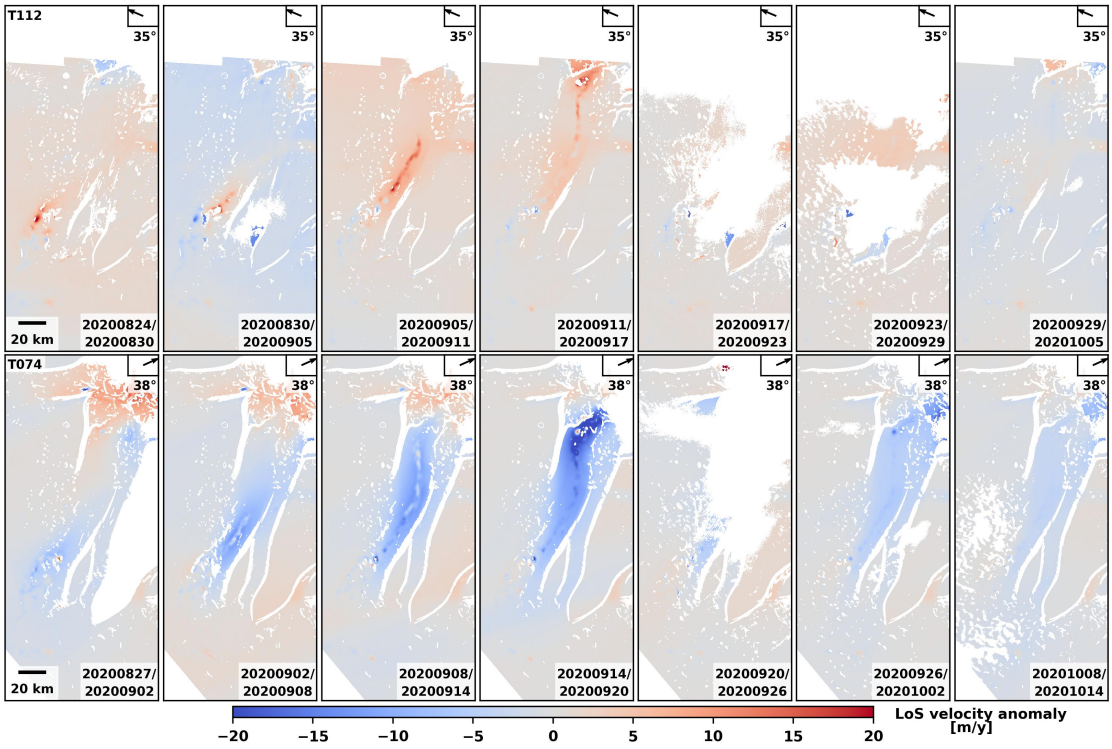

Figure 5.11: Sentinel-1 DInSAR LoS velocity anomalies (with respect to median) in the downstream NEGIS region (indicated by the blue rectangle in Fig. 5.10). Measurements are shown for both a descending track (top row) and an ascending track (bottom row). The ground-projected LoS vector and incidence angle are indicated in the top right corner of each panel.

is much less pronounced. Considering the LoS vectors, which are indicated by a horizontal arrow and an average incidence angle in Fig. 5.11, and the convention that positive motion is considered *towards* the radar, a qualitative interpretation of the dynamic response is given in the following.

For T074, the ground-projected LoS is almost parallel to the horizontal ice flow direction (which is shown as quivers in Fig. 5.10) within most of the ice stream. Consequently, the large-scale negative LoS velocity anomaly would be consistent with a speed up of the ice stream towards the margin. Conversely, the ground-projected LoS of T112 is nearly perpendicular to the horizontal flow direction in the majority of the ice stream, meaning that a general speed up in the horizontal flow would lead to only a minor (positive) signal in the LoS velocity anomaly for this track. Hence, the large-scale smooth anomaly field that spans the full ice stream is consistent with a speed up in the horizontal flow direction. Instead, the more intricate and small-scale bead-like signal is consistent with vertical motion. As both tracks feature a similar incidence angle, the sensitivity to vertical motion is roughly the same, and uplift causes a positive LoS velocity anomaly in both tracks (while subsidence causes a negative signal). From Fig. 5.11, it is seen that the bead-like structures show anomalies of matching signs between the two tracks for the image pairs

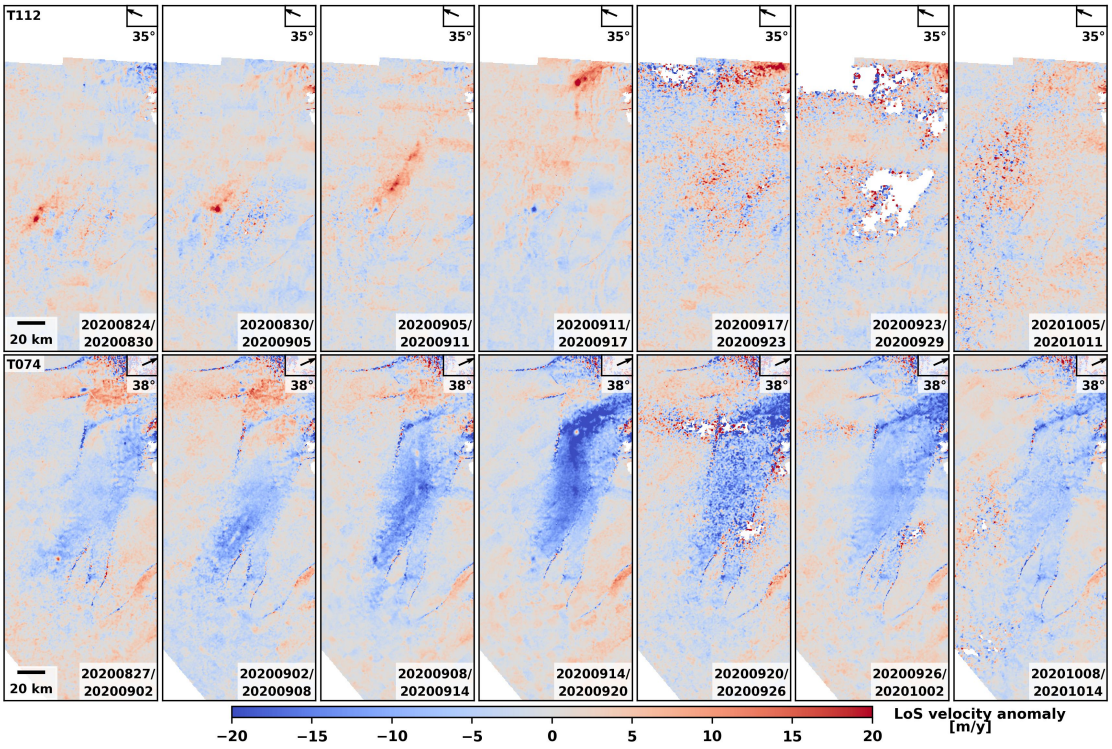

Figure 5.12: Sentinel-1 offset tracking LoS velocity anomalies (with respect to the 2016-2019 PROMICE average velocity map) in the downstream NEGIS region (indicated by the blue rectangle in Fig. 5.10). The acquisitions correspond to the DInSAR measurements shown in Fig. 5.11. Note that an ad-hoc calibration of the measurements was performed by subtracting the mean difference with respect to the average 2016-2019 velocity map, as measured outside of fast-flowing regions, in order to mitigate the S1A/S1B bias (described in section 3.2).

that have the closest temporal overlaps. These observations, in combination with the fact that variations in horizontal velocity does not seem likely to generate the bead-like signatures, leads to the likely conclusion that these local anomalies are caused by vertical motion. With this interpretation, it is observed that each of the bead-like structures first exhibits uplift (positive anomalies), followed by subsidence (negative anomalies), as the wave propagates downstream. A quantitative separation of the horizontal and vertical motion components would require acquisitions from a third LoS, which is not available. In section 5.3, a case is presented in which the inversion is performed using only two different LoS (and some assumptions on the ice flow), however, in the present case the temporal overlap between the ascending and descending acquisitions is deemed too small (compared to the propagation speed of the dynamic response) for this method to be viable, and we stick to a more qualitative analysis.

Fig. 5.12 shows the same LoS velocity anomaly time series as in Fig. 5.11, but captured instead with Sentinel-1 offset tracking. Note that a calibration of the measurements was performed by estimating a swath-wide constant bias, in order to account for the S1A/S1B

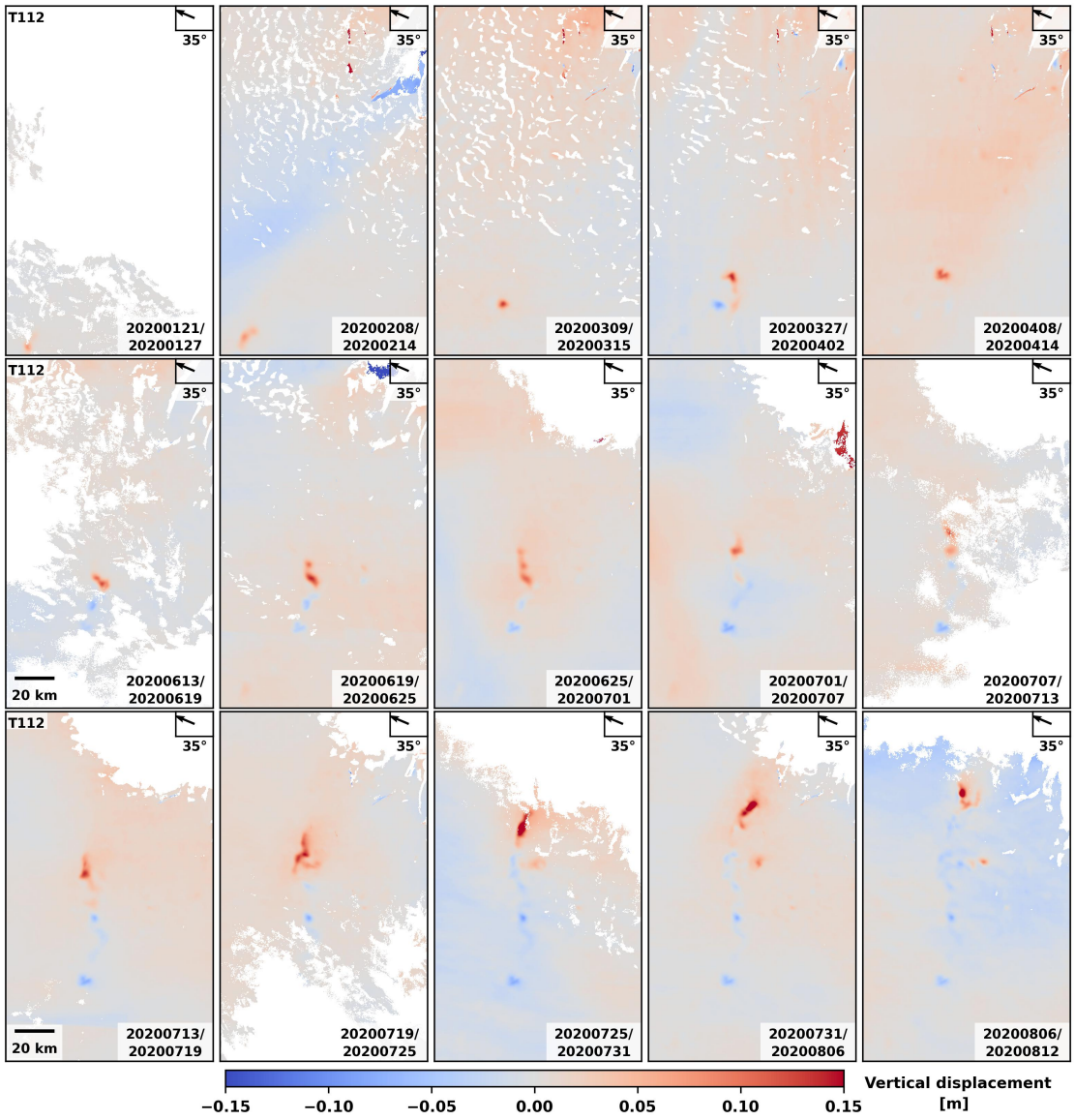

Figure 5.13: Vertical displacement anomalies inferred from Sentinel-1 DInSAR measurements in the downstream NEGIS region (indicated by the magenta rectangle in Fig. 5.10). All measurements are from the descending track (T112). The ground-projected LoS vector and incidence angle are indicated in the top right corner of each panel.

bias (as discussed in section 3.2). While the smooth velocity wave, which we attribute to a horizontal speed up, is indeed visible in the T074 measurements, the bead-like structures associated with vertical motion are less clear in the offset tracking measurements. Close comparison between the offset tracking and DInSAR measurements do show similarities at some of the areas of suspected vertical motion, however, without the DInSAR measurements available for comparison, it is difficult to confidently separate these areas from noise.

Fig 5.13 shows a DInSAR motion anomaly time series obtained for the upstream portion of NEGIS (magenta rectangle in Fig. 5.10) in the months leading up to the time series

shown in Fig. 5.11. Note that all panels of the figure show measurements from the descending track, as the ascending track does not cover the upstream parts. In this case, a qualitative inspection of the measurements does not suggest a wave of horizontal speed-up, as was observed further downstream. Instead, the observed anomalies show only the bead-like pattern, which is assumed to stem from vertical motion (and some long wavelength deviations, which are assumed to arise from, e.g., atmospheric error contributions and imperfect calibration). Consequently, the measurements in Fig. 5.13 have been projected from the LoS to vertical, simply by dividing by the cosine of the incidence angle, θ_i, and scaled to displacement anomalies (over the course of the 6-day baseline) instead of velocity anomalies - that is:

$$\Delta d_{vertical} = \frac{\Delta v_{LoS}}{\cos \theta_i} \cdot \frac{6}{365.25} \tag{5.1}$$

assuming a LoS velocity given in meters per year. Arguably, interpreting these measurements as displacements instead of velocities is more meaningful, as they likely occur at non-uniform rates, in some cases at timespans shorter than the 6-day temporal baseline. Similarly to the measurements in the downstream portion, the upstream measurements show the propagation of bead-like features, appearing first as uplift, followed by subsidence after one or more weeks. Note that many of the bead-like structures show subsidence of relatively low magnitudes long after the uplift wave has propagated further downstream. The uplift generally appears at shorter time intervals and higher magnitudes, suggesting that the uplift occurs at a high rate, while the following subsidence takes longer. The measured uplift events are mostly on the order of 5 to 15 cm (over the 6-day temporal baseline) or smaller, but for the events during July 25th to August 6th uplift exceeding 30 cm (over 6 days) is measured.

By manually tracking the occurrences of uplift, the propagation path of the uplift wave was mapped. It is shown as the black dashed line in Fig. 5.10. Note how the propagation of the uplift wave closely follows features in the bed elevation, and not the ice flow direction. The uplift wave appears to propagate towards the local (downstream) bed elevation minimum, suggesting that the observed dynamic response is strongly linked to subglacial conditions. From July 25th, the uplift wave branches off into two components: one moving further downstream, towards the Zachariae Isstrøm outlet, and a component propagating east (showing somewhat lower uplift magnitudes), which is indicated by the dotted line in Fig. 5.10. In total, propagation of the main component of the uplift wave can be tracked for more than 350 km, from the far upstream parts of NEGIS (where flow speed is less than 100 m/y) to the downstream region about 60 km from the Zachariae grounding line (where flow speed exceeds 500 m/y). The propagation of the main uplift wave component occurs over almost a full year (January to October 2020), while the secondary branch is tracked through about 6 months (from July to December 2020).

Seemingly, the only physical process that is consistent with the dynamic response observed in the DInSAR measurements is the movement of subglacial water, i.e. transport of

water beneath the ice. Preliminary inspections of the Sentinel-1 intensity and coherence images in the upstream regions do not indicate the presence of supraglacial lakes (that is, lakes formed on top of the ice sheet) or collapse basins, suggesting that the water does not stem from an abrupt drainage of melt water lakes on the surface (such an event is instead documented in section 5.3, in a different region). Dynamic activity, in the form of vertical surface displacement, related to the drainage and filling of subglacial lakes has previously been measured using DInSAR (Gray, 2005; Palmer et al., 2015), altimetry (Fricker et al., 2007) and DEM differencing (Willis et al., 2015). Compared to the latter two methods, DInSAR has rarely been applied in mapping subglacial activity, likely due to the limited coverage over Antarctica, where most subglacial lakes have been observed. A very recent study utilized Sentinel-1 DInSAR to measure uplift from subglacial water flow under an Antarctic glacier in Dronning Maud Land (Neckel et al., 2021), and found results that are in many ways similar to the ones shown here. Subglacial lakes have also been detected using radar-echo sounding measurements (Palmer et al., 2013; Ashmore & Bingham, 2014), which may reveal lakes that are inactive (that is, lakes that do not undergo volume change and hence do not cause surface displacements). Subglacial lake drainages have been observed to initiate transient ice flow accelerations on the Antarctic ice sheet, through lubrication of the bed beneath the ice, thereby affecting the total ice sheet mass balance (Stearns et al., 2008; Siegfried et al., 2016; Das et al., 2008). Hence, understanding the interplay between subglacial hydrology and ice dynamics is important to accurately model the evolution of ice sheets both on short and long time scales.

Transport of subglacial water has long been observed to occur on large scales in Antarctica, where pooling of water into subglacial lakes and drainage of said lakes through interconnected drainage pathways has been documented (Wingham et al., 2006; Fricker et al., 2007). Analyses based on hydrological potential estimates and radar-echo soundings suggest that basal water and subglacial lakes are likely prevalent under much of the Greenland ice sheet as well, particularly under fast-flowing regions such as NEGIS (Livingstone et al., 2013; Oswald et al., 2018; Jordan et al., 2018). So far, however, substantially fewer observations have been made of subglacial lake activity on the Greenland ice sheet, compared to its Antarctic counterpart, and no observations have been made of lakes beneath fast-flowing glaciers. A recent mapping of subglacial lakes under the Greenland ice sheet, using airborne radar-echo sounding and measurements of surface elevation change, found no indication of lakes in the NEGIS region, although it is stressed that the radar sounding-based method may have difficulties in separating subglacial lakes from saturated sediments, that are expected to be present at the uniformly thawed bed under NEGIS (Bowling et al., 2019; MacGregor et al., 2022).

Tracking the propagation of the uplift wave, along the path indicated by the dashed black line in Fig. 5.10, it is noted that the propagation speed of the wave strongly varies. From late January (first panel in Fig. 5.13) to mid July (where the propagation path starts to branch off into a main and secondary branch) the wave covers a distance of 130 km, corresponding to a speed of about 750 m/day. From here, along the main path, the wave

propagates 95 km until August 24th (first panel of Fig. 5.11), corresponding to a wave speed of about 2.3 km/day. Finally, the wave propagates 135 km through the fast-flowing portion of the ice stream leading to the Zachariae Isstrøm outlet from August 24th to (about) September 20th, corresponding to a speed of 5 km/day. In the latter of those sectors, the DInSAR measurements also indicate a widespread increase in horizontal ice flow speed. Fig. 5.14 shows the BedMachine v4 bed elevation (Morlighem, 2021) along the main component of the uplift wave propagation path. The plot indicates the extent and timing of the propagation through the three sectors described above (with sector 1 indicating the most upstream sector and sector 3 indicating the downstream sector). Also shown is the extent and timing of the most prominent uplift events. Note that most, but not all, of the observed uplift events coincide with a depression at the bed. Aside from the local depressions and protrusions, the bed elevation is observed to actually increase in sector 1 and most of sector 2. From about 190 km along the transect, bed elevation decreases and becomes locally smooth in the majority of sector 3, aside from the very beginning and end of the sector. This could explain the relatively slow propagation of the uplift wave through sectors 1 and 2, compared to the fast propagation through sector 3. The increase in propagation speed coincides with the late melt season, where it is believed that efficient drainage systems may have developed (Bartholomew et al., 2010). The transition to a more efficient drainage system is, however, often associated with a decrease in ice flow velocity (Bartholomew et al., 2010), conversely to the horizontal ice flow speed-up interpreted from the DInSAR observations in Fig. 5.11.

A hypothesis on the mechanism behind the observed uplift wave is that water is transported downstream, filling up bedrock cavities along the way. The water alters effective pressure at the ice/bedrock transition, leading to uplift of the ice. Once a given cavity is filled, additional supply of basal water causes runoff further downstream and eventually a drainage of the cavity (Livingstone et al., 2016). Once water has migrated downstream, the ice surface (slowly) subsides, presumably back to its original elevation. Naturally, the time required to fill a given cavity depends both on the cavity size and on the supply of melt water. Both of these factors may vary, which likely contributes to the large variation in propagation speed of the observed uplift wave. This interpretation is also presented in previous studies (Gray, 2005; Neckel et al., 2021), where similar characteristics in the dynamic response of subglacial hydrological activity is observed for two slow-moving Antarctic glaciers. In those studies, however, the authors find no evidence of an increase in ice flow speed (although in the latter study, this could be due to geometry of the DInSAR acquisitions, as the LoS is nearly perpendicular to the flow direction). Based on the lack of flow acceleration, Neckel et al., 2021 suggest that the subglacial water is transported through efficient transient channels, either through the ice or through canals in the subglacial sediments. Whether this deviation from the NEGIS event presented here (where horizontal flow acceleration *is* inferred) is due to differences in the underlying mechanism of the routing of subglacial water, or simply due to a difference in the DInSAR sensitivity to horizontal motion, remains uncertain.

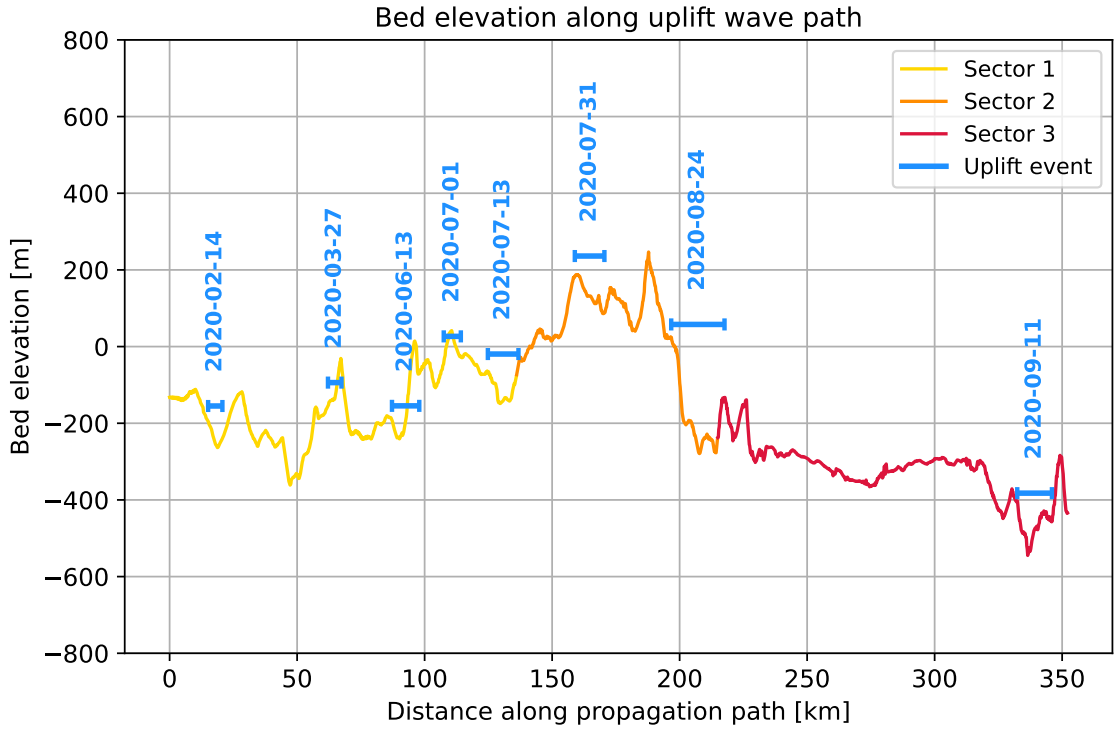

Figure 5.14: Interpolated bed elevation from BedMachine v4 (Morlighem, 2021) along the main propagation path of the uplift wave (shown by the dashed line in Fig. 5.10), divided into three sectors, as described in the text. Blue lines show the extent (along the propagation path) of the most prominent observed uplift events, with the date indicating the onset of uplift, taken as the earliest date of the DInSAR image pair in which uplift was first observed. Note that the x-axis indicates distance from the first observed uplift event (i.e. furthest upstream).

A natural point of interest is to determine the origin of the melt water transported during the event. In a recent study, Karlsson et al., 2021 presented estimates of basal melt water contributions for the full Greenland ice sheet from three main sources: geothermal heat (assumed to cause a roughly constant melt rate at the bedrock), frictional heat (arising from sliding of the ice across the bed), and surface melt heat (i.e. heat transferred from surface melt water as it penetrates to the subglacial domain). In the northeast region, where NEGIS is situated, Karlsson et al., 2021 estimate relative contributions of each of these sources to be 46%, 36%, and 18%, respectively. For NEGIS, however, it is noted that a suspected ”hot spot” beneath the ice stream likely exists (Smith-Johnsen et al., 2020), meaning that the geothermal heat contribution may be underestimated. Additionally, the frictional heat contribution is significantly higher within NEGIS than in most of the surrounding regions (see also Fig. 1 in Karlsson et al., 2021). Finally, the surface melt contribution seems unlikely to have a meaningful contribution for the present event, at least in the first 80 km of the event propagation path, where surface elevation is above 2000 m and the dynamic response is observed during winter.

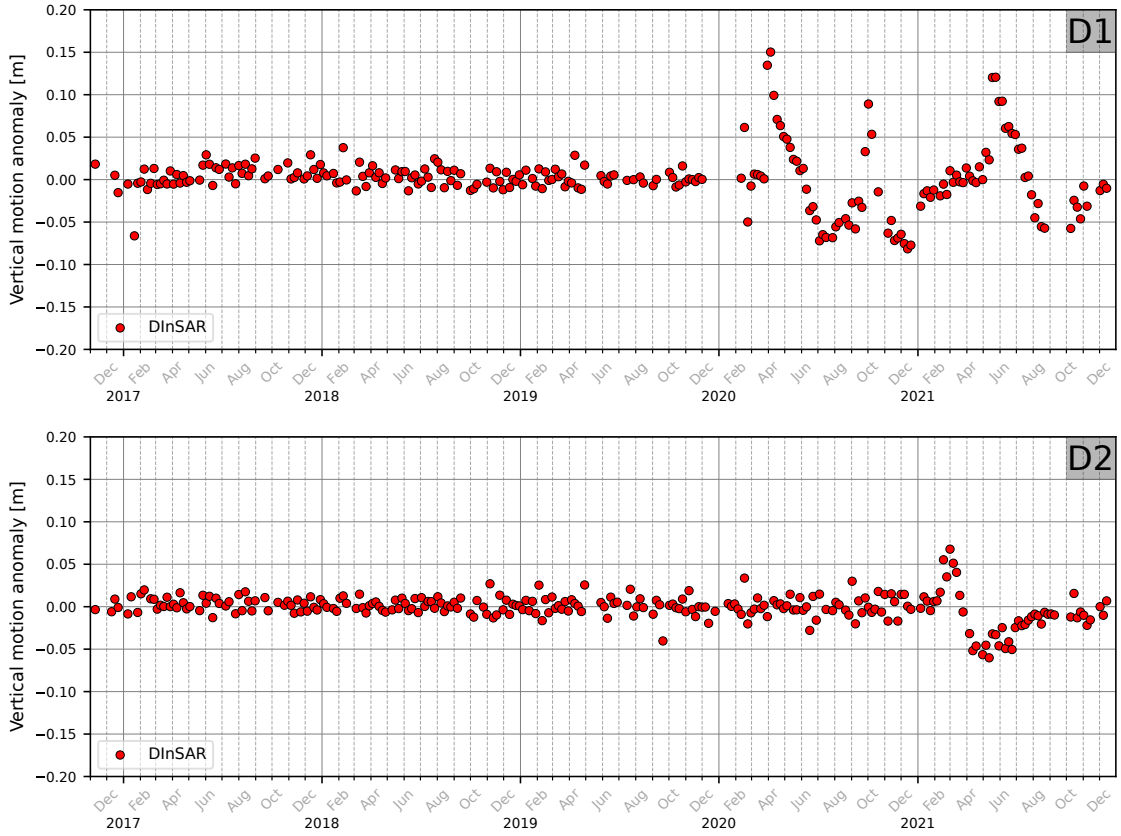

Figure 5.15: Vertical displacement anomaly time series inferred from Sentinel-1 DInSAR measurements at points D1 (top) and D2 (bottom), the locations of which are indicated in Fig. 5.10. Measurements stem from the descending track T112 and all measurements points are from 6-day image pairs.

Finally, the event presented here is by no means unique. In fact, similar events, in which a bead-like pattern of uplift and subsequent subsidence propagates downstream, were observed for every year of the processed time series. The extent and magnitude of the (inferred) uplift waves vary across the span of the time series, with some events being more thoroughly documented than others, depending on whether coherence is retained. While the various events do not all propagate along the same pathway, several events are observed to propagate (at least partially) along the main pathway outlined in Fig. 5.10. In Fig. 5.15, the DInSAR time series of vertical displacement anomaly, computed via eq. (5.1), is shown for points D1 and D2 (indicated in Fig. 5.10). For point D1, which is located on the propagation path of the original event, uplift signals are observed for three separate events: in April 2020 (corresponding to the event shown in Fig. 5.13), in September-October 2020, and in May-June 2021. Note that the uplift in September 2020 occurs just as the original early-2020 uplift wave has passed through the furthest downstream point in the propagation pathway. Although coherence loss is more frequent in the following months, available measurements suggest that the late 2020 uplift wave traverses roughly the same pathway as the early 2020 event. Fig. 5.15 also shows the vertical displacement anomaly

time series for point D2, which is located outside the original propagation pathway. Here, an uplift event is observed in February 2021, after which an uplift wave propagates from D2 to D1 (where uplift is then observed in May-June 2021). For the 2020 events, however, no dynamic response was observed at D2, exemplifying the differences in drainage pathways for the various events. Fig. 5.16 shows the corresponding time series as inferred from offset tracking measurements, including measurements from both 6-day and 12-day image pairs. Comparing these measurements to Fig. 5.15 demonstrates how DInSAR is essential in analyzing dynamic changes at this scale.

As mentioned at the beginning of this section, further analysis of the acquired DInSAR time series, including a comprehensive mapping of all inferred uplift/subsidence signals and a comparison with other available data sources, will be the topic of work beyond the present PhD project. Particularly, a mapping of local hydropotential should be carried out, allowing a comparison between the observed dynamic response and expected drainage pathways. It is worth noting that the main propagation path of the observed uplift wave actually coincides roughly with a drainage pathway simulated based on hydropotential mapping in a previous study (Livingstone et al., 2013). Additionally, it is of interest to compare the DInSAR measurements to those of ICESat-2, similar to Neckel et al., 2021. One limitation with ICESat-2 is that measurements are acquired in narrow tracks with a 91-day repeat period. As shown here, the dynamic response of subglacial water movement may unfold on time scales down to 6 days (or less) and individual uplift events may be limited in spatial extent. Combining the vast and frequent coverage provided by Sentinel-1 and the high sensitivity to vertical motion, DInSAR measurements may provide a highly valuable method for mapping the dynamic response of changes in subglacial hydrology. One of the main limitations of DInSAR measurements is the quantitative separation of vertical and horizontal motion components, which is not straightforward. Still, depending on the available satellite tracks and their orientation with the ice flow direction, the measurements may provide constraints that are crucial in understanding the dynamic response and its extent, as well as the frequency at which hydrology-dynamic events occur.

Figure 5.16: Vertical displacement anomaly time series inferred from Sentinel-1 offset tracking measurements at points D1 (top) and D2 (bottom), the locations of which are indicated in Fig. 5.10. Measurements stem from the descending track T112, with purple markers indicating measurements from 6-day image pairs and blue markers indicating 12-day pairs.

5.3 Wintertime lake drainage cascade observed with DInSAR

This section documents a study, in which Sentinel-1 DInSAR measurements were used to capture the dynamic response of a series of supraglacial lake drainages, occurring in western Greenland in the winter of 2018, with extraordinary detail. The full study is presented in the following manuscript:

N. Maier, J. K. Andersen, J. Mouginot, F. Gimbert, and O. Gagliardini, Wintertime lake drainage cascade triggers large-scale ice flow response in Greenland, *Science*, [in review] (2022)

which is provided in Appendix A.5, with supplementary material found in Appendix B.3. Note that the supplementary material also includes the section *Materials and Methods*, which documents the methodologies used. In the following, some introductory comments concerning the investigations are given, followed by a brief summary of the main findings of the paper.

A dynamic response, in the form of an ice speed-up, was first observed in routinely gen-

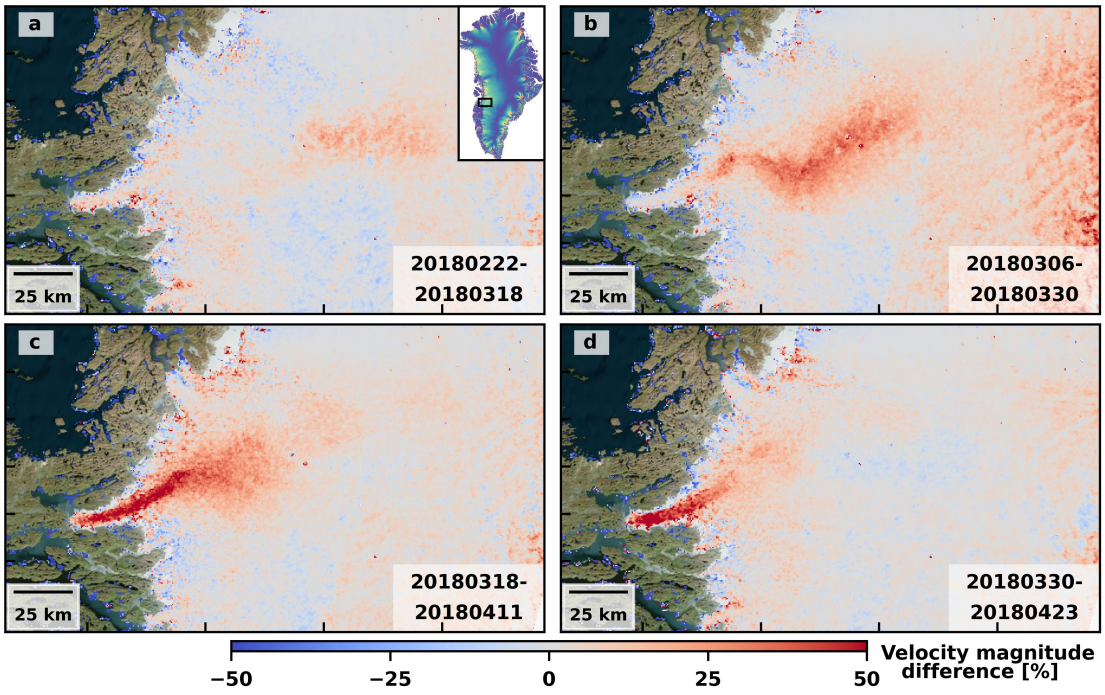

Figure 5.17: 24-day horizontal velocity magnitude mosaics from PROMICE Sentinel-1 offset tracking (Solgaard & Kusk, 2021; Solgaard et al., 2021), showing the dynamic response of the lake drainage cascade in the vicinity of Nordenskiöld glacier (the inset in panel (a) shows the extent of the imaged region). The measurements show relative change in velocity magnitude, with respect to the PROMICE product spanning 20180117 - 20180210.

erated Sentinel-1 offset tracking measurements. An example is shown in Fig. 5.17, which shows measurements from 24-day PROMICE mosaics. Optical satellite imagery from Landsat 8 and Sentinel-2 was used to identify lake drainages in the time before, during, and right after the observed dynamic response. In optical images, lake drainages are observed as an abrupt change from the smooth surface of the ice "lid" (a relatively thin layer of ice that is usually generated when a surface lake freezes over winter) to a collapse basin, which shows a rugged, fractured surface in the depression left by the drained lake. The change in ice flow following a lake drainage is caused by the influx of water to the ice-bed interface, causing increased sliding due to the added lubrication. A total of 15 supraglacial lakes were observed to drain over the course of March 2018. This observation is unusual, as such drainage events are generally believed to occur only during the melt season in summer. The offset tracking measurements do indeed reveal a general speed-up in ice flow following the identified drainages. With the limited accuracy and spatial resolution, however, these measurements do not reveal distinct patterns in the flow response, and the horizontal velocity measurements do not indicate whether or not a vertical motion component exists. With DInSAR measurements, intricate details in the dynamic response are observed (cf. Fig. 1 in Appendix A.5).

A time series of Sentinel-1 DInSAR velocity retrievals from multiple tracks (yielding multiple lines-of-sight) spanning the drainage event was acquired. These measurements reveal a wave of accelerating ice flow, propagating from the initially draining lakes towards the margin. The DInSAR time series allows for monitoring the evolution of the dynamic response, as it propagates, triggering other supraglacial lake drainages, which in turn impact the dynamic response. Because of the high spatiotemporal resolution, it is possible to interpret the changes in ice flow in relation to the subglacial conditions and infer details about the drainage pathways. Additionally, exploiting the sensitivity of DInSAR measurements to both vertical and horizontal motion, we decompose the velocity contributions into a horizontal component and a vertical component. While this is not strictly possible without three different lines-of-sight, acquired simultaneously, we make the assumption that the horizontal flow-direction remains unchanged and use measurements from one ascending and one descending track, each with a 6-day temporal baseline, which have a temporal overlap of 4.5 days, to make the decomposition possible. The horizontal flow-direction is estimated from a multi-year average velocity map. The approach is further described in the *Materials and Methods* section in Appendix B.3. Estimating the vertical motion component is of great importance, as the measurements provide valuable knowledge on the drainage characteristics, specifically revealing a bead-and-thread structure that is similar to that observed during some subglacial lake drainages (including the dynamic response documented in section 5.2).

5.3.1 Summary of Maier et al. (Science, 2022)

According to current understanding of the coupling between hydrology and dynamics on the Greenland ice sheet, ice flow acceleration caused by the drainage of supraglacial lakes, which store melt water, commonly occur in summertime when melt conditions prevail. In winter, where there is an absence of surface melt, drainage events leading to a large-scale dynamic response have been assumed improbable. Hence, the hydrology-dynamic coupling is generally considered on a seasonal time scale. Our observations show an expansive dynamic response, forced by the cascading drainage of a series of supraglacial lakes in wintertime. The dynamic response lasted more than 30 days, propagating more than 160 km from the highest lakes to the margin and affected an area of 5200 km^2. The earliest draining lake, which triggered the cascade, is located at high elevation (>1600 m), above the time-averaged snow line, and an analysis of historical satellite data revealed that this lake had been accumulating melt water without draining for nearly five decades (see Appendix B.3). Several other lakes also stored melt water for years before being drained by the cascade event. Hence, not only do the results suggest that this type of transient drainage event may occur in wintertime, they also suggest that melt-forcing may affect ice dynamics long after the melt is produced, meaning that the hydrology-dynamic coupling spans time scales much longer than a single season.

Because the drainage event occurs during winter, where external forcing due to surface melt is absent, it provides an opportunity to investigate the properties of the drainage system as the event unfolds. Using high resolution DInSAR measurements, decomposed

into a horizontal and vertical motion component, we can carefully track the velocity wave as it travels towards the margin underneath the ice, mapping the multi-threaded drainage pathways and estimating the drainage velocity through these pathways. The vertical motion estimates reveal details about changes in flow pathways and bed separation. All of these findings provide important constraints for hydrology-dynamic models, which are needed to predict the response of ice sheets to rising temperatures.

A precursory search using DInSAR processing in the region near the observed event revealed two additional winter lake drainage events (in 2019 and 2021, see Fig. S9 in Appendix B.3). Although these events are of a smaller scale, the observations suggest that winter drainage events are likely a relatively common phenomenon. For the cascading drainage event, we estimate a $1 - 4\%$ increase in marginal ice discharge over the affected area. Coupled with the fact that climate warming is expected to increase both melt production and the capacity of melt water storage, these findings suggest that melt-forced winter drainage events may increase in frequency in the future and play an important role in the evolution of the ice sheet.

Chapter 6 | Conclusions and outlook

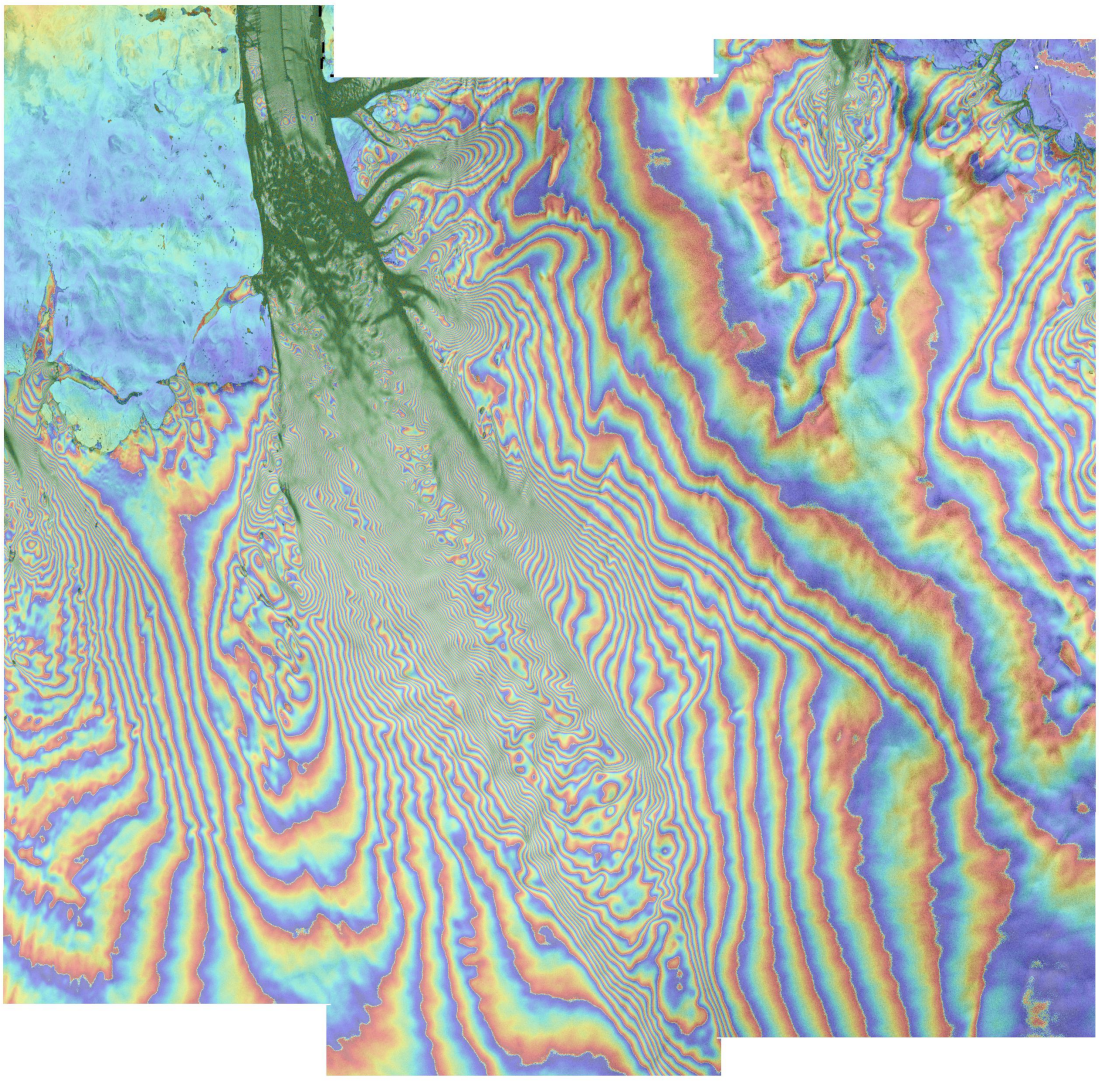

Sentinel-1 differential interferogram phase over Petermann glacier in north Greenland.

The overall goal of this PhD project has been to enable the exploitation of the vast archive of Sentinel-1 phase data for ice velocity retrieval and to demonstrate the value of interferometric (DInSAR) measurements in investigating changes in ice dynamics. In Chapter 1, the research objectives of the PhD project were condensed into three key elements, which are repeated here:

1. Design and implement methods allowing the interferometric retrieval of ice velocity from Sentinel-1 TOPS-mode measurements

2. Improve robustness of the Sentinel-1 interferometric algorithm for operational large-scale ice velocity retrieval

3. Demonstrate the potential of Sentinel-1 interferometry in studies of ice dynamic changes, exploiting the increased spatiotemporal resolution and accuracy

Chapter 3 addressed the first objective. Here, several approaches to meeting the strict requirements on azimuth coregistration for TOPS-mode DInSAR, in the presence of substantial scene-wide motion, were investigated. The combination of two separate coregistration refinement methods was found to perform the best. The first refinement method utilizes an estimate of 2D average velocity and accounts for the bulk of azimuth motion within the scene, while the second method is based on the principles of multi-aperture interferometry and provides an additional refinement near TOPS burst boundaries, where sensitivity to registration errors is the highest. The chapter included a demonstration of the Sentinel-1 DInSAR processing chain, in combination with offset tracking measurements, for a large drainage basin northeast Greenland, including a validation with GPS velocity retrievals. Throughout the project, the refined coregistration procedure has been used on an extensive amount of Sentinel-1 image pairs, performing quite consistently in eliminating inter-burst phase discontinuities. In some instances, residual discontinuities may remain, particularly in the presence of ionosphere-induced phase errors. Recently, an auxiliary timing annotation data set was developed (Gisinger et al., 2022), which seeks to improve Sentinel-1 geolocation accuracy, taking into account both atmospheric effects as well as effects from solid Earth tides. The data set was demonstrated for use in offset tracking ice velocity retrieval (Gisinger et al., 2022). In the future, it would be interesting to investigate the potential improvements for DInSAR.

Chapter 4 addressed the second objective. After developing a robust method for TOPS coregistration on ice, we found that the main obstacle in applying Sentinel-1 DInSAR measurements at an operational (i.e. fully automated) level is the occurrence of phase unwrapping errors, particularly in regions near the ice sheet margin. Therefore, the main focus in efforts to improve the robustness of the DInSAR algorithm was on the detection of unwrapping errors. A masking algorithm was designed, based on a measure of pixel connectivity, and validated using a simulated data set. The algorithm effectively detects unwrapping errors, particularly those of high magnitudes, although with a mediocre precision, meaning that some valid data is discarded along with the errors. In campaign-style

ice velocity retrievals over large regions, where multiple satellite tracks are combined to infer a single seasonal/annual 2D velocity map, the connectivity-based masking method is effective at discarding errors that might otherwise drastically impact the results through the inversion process and lead to unrealistic velocity fields. However, in cases where one seeks to map a transient dynamic response, the duration of which spans only a few satellite acquisitions, the risk of discarding valid data may outweigh the benefits of detecting potential unwrapping errors. Hence, increasing the precision of the algorithm would be a crucial improvement to its applicability. Chapter 4 also documented a preliminary investigation into applying simple machine learning methods to generate a more reliable unwrapping error mask, with increased recall and precision, based on pixel connectivity as well as other parameters. Improved unwrapping error detection algorithms might also seek to better exploit the spatial correlation in phase unwrapping errors. Ultimately, the goal is for the DInSAR processing chain to reach the same level of robustness and automation as that implemented for offset tracking. While the connectivity-based masking approach provides a major step towards that goal, future work should seek to further refine the method, with the objective of minimizing the need for user input and manual inspection in large-scale (ice sheet-wide) processing scenarios.

Finally, addressing the third research objective, Chapter 5 provided several demonstrations of the capabilities of Sentinel-1 DInSAR in investigating dynamic changes in ice flow. The high spatiotemporal resolution of Sentinel-1 DInSAR measurements allow for dense ice velocity time series. As an example, a 2015-2021 time series was generated for the Northeast Greenland Ice Stream and its surroundings. The time series was used both for mapping the extent of long-term (i.e. multi-year) acceleration/deceleration and for studying more complex (local) dynamic changes. Time series were generated using both DInSAR and offset tracking, allowing a comparison between the methods. In the estimation of long-term velocity trends, the lower noise level in DInSAR leads to an improvement in motion sensitivity, revealing acceleration also in slow-moving regions, where the high relative noise level of offset tracking makes the method insensitive to low-magnitude changes. When investigating short-term dynamic changes, the higher accuracy of DInSAR effectively allows for a better temporal resolution of investigated events. This is demonstrated for several areas, in which distinct changes in the velocity field occur over just a few months, which are not readily apparent in offset tracking retrievals. The yet expanding extensive Sentinel-1 polar archive allows for similar investigations to be carried out in other sectors of both Greenland and Antarctica, however, the loss of Sentinel-1B has a substantial impact on the retrieved DInSAR time series, as the 12-day temporal baseline available with one satellite yields significantly poorer coherence, particularly in the ablation zone. Fortunately, current plans see Sentinel-1C in orbit in the first half of 2023.

Future efforts should seek to exploit Sentinel-1 DInSAR measurements to investigate acceleration (or deceleration) in other regions of the Greenland ice sheet as well as the Antarctic ice sheet, particularly within inland parts of major glaciers, where tracking-based measurements may not capture the relatively subtle changes. For Antarctica, Sentinel-1 coverage

is not as extensive as it is for Greenland, providing images mainly over the ice sheet margin. This situation will improve with the launch of the NISAR (NASA-ISRO Synthetic Aperture Radar) satellite in 2024, which prioritizes Antarctic coverage (Rosen et al., 2016). Studying the inland response to recent calving and thinning of major Antarctic ice shelves (Greene et al., 2022) would be valuable for future efforts in monitoring and predicting ice dynamics in Antarctica. Furthermore, as glaciers and ice caps outside of the polar ice sheets (in areas such as High-mountain Asia, the Canadian Arctic, Patagonia, etc.) collectively comprise the largest contributor to current sea level rise, future efforts may also seek to generate Sentinel-1 DInSAR time series in these regions, potentially aiding in monitoring the acceleration in mass loss that has recently been observed (Hugonnet et al., 2021). Challenges in these regions could be the occurrence of radar shadowing effects, due to steep slopes, and a lack of reference velocity maps (for use in the coregistration refinement processing step) with sufficient accuracy, although availability of global ice velocity mosaics has recently improved (Millan et al., 2022; Scambos & Fahnestock, 2016).

Chapter 5 also presented two investigations on transient dynamic events related to subglacial and supraglacial hydrology - one on NEGIS and one in the vicinity of Nordenskjold Glacier in the southwest of Greenland. These investigations exploit the sensitivity of DInSAR measurements to both horizontal and vertical motion, in order to interpret the dynamic response caused by the transport of water through the subglacial hydrological system. For the NEGIS event, indications of uplift and subsequent subsidence are observed in a bead-and-thread structure extending more than 400 km from the Zachariae Isstrøm ice front. Further downstream, DInSAR measurements indicate a horizontal flow speed up superimposed on the bead-like uplift pattern. A preliminary analysis of the observations is provided in the thesis, while a more thorough investigation, incorporating also additional data sources, will be a topic of future work.

In the case of the Nordenskjold event, the combination of DInSAR measurements and optical satellite data revealed an expansive cascade of supraglacial lake drainages occurring in wintertime. The drainage cascade was associated with both a significant horizontal flow speed up (locally exceeding 200% of pre-event measurements) and a bead-and-thread structure showing uplift and subsidence. As coverage from multiple Sentinel-1 tracks is available, and coherence is generally well retained due to the absence of surface melt, a detailed characterization of the dynamic response was possible, including a decomposition of the observed motion into a horizontal (flow-directed) and vertical component. Historic analysis of optical satellite imagery revealed that the lake at highest elevation, which triggered the drainage cascade, had been increasing in area for almost half a century without draining. The findings redefine the timescales on which melt forcing is considered to affect ice dynamics and allow for detailed insight in the dynamic response of supraglacial drainage events.

Finally, for both of the transient hydrology-dynamic events presented in Chapter 5, precursory searches indicated similar events occurring nearby in the years up to or after the original observations, suggesting that neither of the observed events are unique, but occur

with some frequency in various regions of the ice sheet. So far, Sentinel-1 data has not been heavily utilized in investigating hydrology-dynamic events. We show that, using interferometric techniques and the broad coverage provided by Sentinel-1, these measurements may be highly valuable in constraining such events. Future work will include further analysis of the observed hydrology-dynamic events on NEGIS, as well as searches for similar events in other regions of the Greenland (and Antarctic) ice sheet.

Bibliography

An, L., Rignot, E., Wood, M., Willis, J. K., Mouginot, J., and Khan, S. A. (2021). "Ocean melting of the Zachariae Isstrøm and Nioghalvfjerdsfjorden glaciers, northeast Greenland". *Proceedings of the National Academy of Sciences* 118.2, e2015483118. DOI: 10.1073/pnas.2015483118.

Andersen, J. K. et al. (2019). "Update of annual calving front lines for 47 marine terminating outlet glaciers in Greenland (1999–2018)". *Geological Survey of Denmark and Greenland Bulletin* 43. DOI: 10.34194/GEUSB-201943-02-02.

Andersen, J. K., Kusk, A., Boncori, J. P. M., Hvidberg, C. S., and Grinsted, A. (2020). "Improved Ice Velocity Measurements with Sentinel-1 TOPS Interferometry". *Remote Sensing* 12.12, p. 2014. DOI: 10.3390/rs12122014.

Andrews, L. C., Hoffman, M. J., Neumann, T. A., Catania, G. A., Lüthi, M. P., Hawley, R. L., Schild, K. M., Ryser, C., and Morriss, B. F. (2018). "Seasonal Evolution of the Subglacial Hydrologic System Modified by Supraglacial Lake Drainage in Western Greenland". *Journal of Geophysical Research: Earth Surface* 123.6, pp. 1479–1496. DOI: 10.1029/2017JF004585.

Ashmore, D. W. and Bingham, R. G. (2014). "Antarctic subglacial hydrology: current knowledge and future challenges". *Antarctic Science* 26.6, pp. 758–773. DOI: 10.1017/S0954102014000546.

Bamler, R. and Hartl, P. (1998). "Synthetic aperture radar interferometry". *Inverse Problems* 14.4, R1–R54. DOI: 10.1088/0266-5611/14/4/001.

Bamler, R. and Eineder, M. (2005). "Accuracy of Differential Shift Estimation by Correlation and Split-Bandwidth Interferometry for Wideband and Delta-k SAR Systems". *IEEE Geoscience and Remote Sensing Letters* 2.2, pp. 151–155. DOI: 10.1109/LGRS.2004.843203.

Barat, I., Prats-Iraola, P., Duesmann, B., and Geudtner, D. (2015). "Sentinel-1: link between orbit control and interferometric SAR baselines performance". 25th International Symposium on Space Flight Dynamics. Munich, Germany, pp. 1–11.

Bartholomew, I., Nienow, P., Mair, D., Hubbard, A., King, M. A., and Sole, A. (2010). "Seasonal evolution of subglacial drainage and acceleration in a Greenland outlet glacier". *Nature Geoscience* 3.6, pp. 408–411. DOI: 10.1038/ngeo863.

Bechor, N. B. D. and Zebker, H. A. (2006). "Measuring two-dimensional movements using a single InSAR pair". *Geophysical Research Letters* 33.16, p. L16311. DOI: 10.1029/2006GL026883.

Bekaert, D., Walters, R., Wright, T., Hooper, A., and Parker, D. (2015). "Statistical comparison of InSAR tropospheric correction techniques". *Remote Sensing of Environment* 170, pp. 40–47. DOI: 10.1016/j.rse.2015.08.035.

Born, G. H., Dunne, J. A., and Lame, D. B. (1979). "Seasat Mission Overview". *Science* 204.4400, pp. 1405–1406. DOI: 10.1126/science.204.4400.1405.

Bowling, J. S., Livingstone, S. J., Sole, A. J., and Chu, W. (2019). "Distribution and dynamics of Greenland subglacial lakes". *Nature Communications* 10.1, p. 2810. DOI: 10.1038/s41467-019-10821-w.

Box, J. E. et al. (2022). "Greenland ice sheet climate disequilibrium and committed sea-level rise". *Nature Climate Change*. DOI: 10.1038/s41558-022-01441-2.

Brcic, R., Parizzi, A., Eineder, M., Bamler, R., and Meyer, F. (2010). "Estimation and compensation of ionospheric delay for SAR interferometry". *IEEE International Geoscience and Remote Sensing Symposium (IGARSS) 2010*. Honolulu, HI, USA: IEEE, pp. 2908–2911. DOI: 10.1109/IGARSS.2010.5652231.

Chen, C. W. and Zebker, H. A. (2000). "Network approaches to two-dimensional phase unwrapping: intractability and two new algorithms". *Journal of the Optical Society of America A* 17.3, p. 401. DOI: 10.1364/JOSAA.17.000401.

Christoffersen, P., Bougamont, M., Hubbard, A., Doyle, S. H., Grigsby, S., and Pettersson, R. (2018). "Cascading lake drainage on the Greenland Ice Sheet triggered by tensile shock and fracture". *Nature Communications* 9.1, p. 1064. DOI: 10.1038/s41467-018-03420-8.

Church, J. A. et al. (2011). "Revisiting the Earth's sea-level and energy budgets from 1961 to 2008". *Geophysical Research Letters* 38.18. DOI: 10.1029/2011GL048794.

Cigna, F. and Tapete, D. (2021). "Present-day land subsidence rates, surface faulting hazard and risk in Mexico City with 2014–2020 Sentinel-1 IW InSAR". *Remote Sensing of Environment* 253, p. 112161. DOI: 10.1016/j.rse.2020.112161.

Costantini, M. (1998). "A novel phase unwrapping method based on network programming". *IEEE Transactions on Geoscience and Remote Sensing* 36.3, pp. 813–821. DOI: 10.1109/36.673674.

Cumming, I., Valero, J., Vachon, P., and Mattar, K. (1997). "Glacier flow measurements with ERS tandem mission data". *European Space Agency, (Special Publication)* 406, pp. 353–362.

Cumming, I. G. and Wong, F. H. (2005). *Digital processing of synthetic aperture radar data: algorithms and implementation*. Artech House remote sensing library. Boston: Artech House. 625 pp. ISBN: 978-1-58053-058-3.

Curlander, J. C. and MacDonough, R. N. (1991). *Synthetic aperture radar: systems and signal processing*. Wiley series in remote sensing. New York, NY: Wiley. 647 pp. ISBN: 978-0-471-85770-9.

Das, S. B., Joughin, I., Behn, M. D., Howat, I. M., King, M. A., Lizarralde, D., and Bhatia, M. P. (2008). "Fracture Propagation to the Base of the Greenland Ice Sheet During Supraglacial Lake Drainage". *Science* 320.5877, pp. 778–781. DOI: 10.1126/science.1153360.

Davison, B. J., Sole, A. J., Livingstone, S. J., Cowton, T. R., and Nienow, P. W. (2019). "The Influence of Hydrology on the Dynamics of Land-Terminating Sectors of the Greenland Ice Sheet". *Frontiers in Earth Science* 7, p. 10. DOI: 10.3389/feart.2019.00010.

De Lange, R., Luckman, A., and Murray, T. (2007). "Improvement of Satellite Radar Feature Tracking for Ice Velocity Derivation by Spatial Frequency Filtering". *IEEE Transactions on Geoscience and Remote Sensing* 45.7, pp. 2309–2318. DOI: 10.1109/TGRS.2007.896615.

De Zan, F. and Monti Guarnieri, A. (2006). "TOPSAR: Terrain Observation by Progressive Scans". *IEEE Transactions on Geoscience and Remote Sensing* 44.9, pp. 2352–2360. DOI: 10.1109/TGRS.2006.873853.

De Zan, F., Prats-Iraola, P., Scheiber, R., and Rucci, A. (2014). "Interferometry with TOPS: Coregistration and azimuth shifts". *Proceedings of the European Conference on Synthetic Aperture Radar, EUSAR*, pp. 949–952.

Doin, M., Lasserre, C., Peltzer, G., Cavalié, O., and Doubre, C. (2009). "Corrections of stratified tropospheric delays in SAR interferometry: Validation with global atmospheric models". *Journal of Applied Geophysics* 69.1, pp. 35–50.

Dorrer, E., Hofmann, W., and Seufert, W. (1969). "Geodetic Results of the Ross Ice Shelf Survey Expeditions, 1962–63 and 1965–66". *Journal of Glaciology* 8.52, pp. 67–90. DOI: 10.3189/S0022143000020773.

Farinotti, D., Huss, M., Fürst, J. J., Landmann, J., Machguth, H., Maussion, F., and Pandit, A. (2019). "A consensus estimate for the ice thickness distribution of all glaciers on Earth". *Nature Geoscience* 12.3, pp. 168–173. DOI: 10.1038/s41561-019-0300-3.

Fettweis, X., Box, J. E., Agosta, C., Amory, C., Kittel, C., Lang, C., As, D. van, Machguth, H., and Gallée, H. (2017). "Reconstructions of the 1900–2015 Greenland ice sheet surface mass

balance using the regional climate MAR model". *The Cryosphere* 11.2, pp. 1015–1033. DOI: 10.5194/tc-11-1015-2017.

Floricioiu, D., Eineder, M., Rott, H., and Nagler, T. (2008). "Velocities of Major Outlet Glaciers of the Patagonia Icefield Observed by TerraSAR-X". *IEEE International Geoscience and Remote Sensing Symposium (IGARSS) 2008*. Boston, MA, USA: IEEE, pp. 347–350. DOI: 10.1109/IGARSS.2008.4779729.

Fornaro, G., Franceschetti, G., and Lanari, R. (1996). "Interferometric SAR phase unwrapping using Green's formulation". *IEEE Transactions on Geoscience and Remote Sensing* 34.3, pp. 720–727. DOI: 10.1109/36.499751.

Fricker, H. A., Scambos, T., Bindschadler, R., and Padman, L. (2007). "An Active Subglacial Water System in West Antarctica Mapped from Space". *Science* 315.5818, pp. 1544–1548. DOI: 10.1126/science.1136897.

Galli, L. (2001). "A new approach based on network theory to locate phase unwrapping unreliable results". *IEEE International Geoscience and Remote Sensing Symposium (IGARSS) 2001*. IEEE, 118–120.

Gisinger, C., Schubert, A., Breit, H., Garthwaite, M., Balss, U., Willberg, M., Small, D., Eineder, M., and Miranda, N. (2021). "In-Depth Verification of Sentinel-1 and TerraSAR-X Geolocation Accuracy Using the Australian Corner Reflector Array". *IEEE Transactions on Geoscience and Remote Sensing* 59.2, pp. 1154–1181.

Gisinger, C. et al. (2022). "The Extended Timing Annotation Dataset for Sentinel-1—Product Description and First Evaluation Results". *IEEE Transactions on Geoscience and Remote Sensing* 60, pp. 1–22. DOI: 10.1109/TGRS.2022.3194216.

Goldstein, R. M., Zebker, H. A., and Werner, C. L. (1988). "Satellite radar interferometry: Two-dimensional phase unwrapping". *Radio Science* 23.4, pp. 713–720. DOI: 10.1029/RS023i004p00713.

Goldstein, R. M., Engelhardt, H., Kamb, B., and Frolich, R. M. (1993). "Satellite Radar Interferometry for Monitoring Ice Sheet Motion: Application to an Antarctic Ice Stream". *Science* 262.5139, pp. 1525–1530. DOI: 10.1126/science.262.5139.1525.

Goldstein, R. M. and Werner, C. L. (1998). "Radar interferogram filtering for geophysical applications". *Geophysical Research Letters* 25.21, pp. 4035–4038. DOI: 10.1029/1998GL900033.

Gray, A. L., Mattar, K. E., and Sofko, G. (2000). "Influence of Ionospheric Electron Density Fluctuations on Satellite Radar Interferometry". *Geophysical Research Letters* 27.10, pp. 1451–1454.

Gray, A., Mattar, K., Vachon, P., Bindschadler, R., Jezek, K., Forster, R., and Crawford, J. (1998). "InSAR results from the RADARSAT Antarctic Mapping Mission data: estimation of glacier motion using a simple registration procedure". *IEEE International Geoscience and Remote Sensing Symposium (IGARSS) 1998*. Seattle, WA, USA: IEEE, 1638–1640 vol.3. DOI: 10.1109/IGARSS.1998.691662.

Gray, L. (2005). "Evidence for subglacial water transport in the West Antarctic Ice Sheet through three-dimensional satellite radar interferometry". *Geophysical Research Letters* 32.3, p. L03501. DOI: 10.1029/2004GL021387.

Greene, C. A., Gardner, A. S., Schlegel, N.-J., and Fraser, A. D. (2022). "Antarctic calving loss rivals ice-shelf thinning". *Nature*. DOI: 10.1038/s41586-022-05037-w.

Howat, I. M., Negrete, A., and Smith, B. E. (2014). "The Greenland Ice Mapping Project (GIMP) land classification and surface elevation data sets". *The Cryosphere* 8.4, pp. 1509–1518. DOI: 10.5194/tc-8-1509-2014.

Howat, I. M., Joughin, I., and Scambos, T. A. (2007). "Rapid Changes in Ice Discharge from Greenland Outlet Glaciers". *Science* 315.5818, pp. 1559–1561. DOI: 10.1126/science.1138478.

Howat, I. M., Box, J. E., Ahn, Y., Herrington, A., and McFadden, E. M. (2010). "Seasonal variability in the dynamics of marine-terminating outlet glaciers in Greenland". *Journal of Glaciology* 56.198, pp. 601–613. DOI: 10.3189/002214310793146232.

Hubig, M., Suchandt, S., and Eineder, M. (2000). "Automatic Correction of Baseline and Phase Unwrapping Errors in SAR Interferograms". Proceedings of the European Conference on Synthetic Aperture Radar (EUSAR 2000). VDE Verlag, pp. 131–134.

Hugonnet, R. et al. (2021). "Accelerated global glacier mass loss in the early twenty-first century". *Nature* 592.7856, pp. 726–731. DOI: 10.1038/s41586-021-03436-z.

Hvidberg, C. S., Keller, K., Gundestrup, N. S., Tscherning, C. C., and Forsberg, R. (1997). "Mass balance and surface movement of the Greenland Ice Sheet at Summit, central Greenland". *Geophysical Research Letters* 24.18, pp. 2307–2310. DOI: 10.1029/97GL02280.

Hvidberg, C. S. et al. (2020). "Surface velocity of the Northeast Greenland Ice Stream (NEGIS): Assessment of interior velocities derived from satellite data by GPS". *Cryosphere* 14.10, pp. 3487–3502.

IMBIE team (2018). "Mass balance of the Antarctic Ice Sheet from 1992 to 2017". *Nature* 558.7709, pp. 219–222. DOI: 10.1038/s41586-018-0179-y.

IMBIE team (2019). "Mass balance of the Greenland Ice Sheet from 1992 to 2018". *Nature* 579, pp. 233–239. DOI: 10.1038/s41586-019-1855-2.

Intergovernmental Panel on Climate Change (IPCC), ed. (2021a). *Climate Change 2021: The Physical Science Basis. Contribution of Working Group I to the Sixth Assessment Report of the Intergovernmental Panel on Climate Change (Human Influence on the Climate System)*. Cambridge University Press. DOI: 10.1017/9781009157896.005.

Intergovernmental Panel on Climate Change (IPCC), ed. (2021b). *Climate Change 2021: The Physical Science Basis. Contribution of Working Group I to the Sixth Assessment Report of the Intergovernmental Panel on Climate Change (Ocean, Cryosphere and Sea Level Change)*. Cambridge University Press. DOI: 10.1017/9781009157896.011.

Jevrejeva, S., Jackson, L. P., Grinsted, A., Lincke, D., and Marzeion, B. (2018). "Flood damage costs under the sea level rise with warming of 1.5 °C and 2 °C". *Environmental Research Letters* 13.7, p. 074014. DOI: 10.1088/1748-9326/aacc76.

Jiang, H. J., Pei, Y. Y., and Li, J. (2017a). "Sentinel-1 TOPS interferometry for along-track displacement measurement". *IOP Conference Series: Earth and Environmental Science* 57, p. 012019. DOI: 10.1088/1755-1315/57/1/012019.

Jiang, H., Feng, G., Wang, T., and Bürgmann, R. (2017b). "Toward full exploitation of coherent and incoherent information in Sentinel-1 TOPS data for retrieving surface displacement: Application to the 2016 Kumamoto (Japan) earthquake". *Geophysical Research Letters*. DOI: 10.1002/2016GL072253.

Jordan, T. M., Williams, C. N., Schroeder, D. M., Martos, Y. M., Cooper, M. A., Siegert, M. J., Paden, J. D., Huybrechts, P., and Bamber, J. L. (2018). "A constraint upon the basal water distribution and thermal state of the Greenland Ice Sheet from radar bed echoes". *The Cryosphere* 12.9, pp. 2831–2854. DOI: 10.5194/tc-12-2831-2018.

Joughin, I. (2002). "Ice-sheet velocity mapping: a combined interferometric and speckle-tracking approach". *Annals of Glaciology* 34, pp. 195–201. DOI: 10.3189/172756402781817978.

Joughin, I., Kwok, R., and Fahnestock, M. (1996). "Estimation of ice-sheet motion using satellite radar interferometry: method and error analysis with application to Humboldt Glacier, Greenland". *Journal of Glaciology* 42.142, pp. 564–575. DOI: 10.3189/S0022143000003543.

Joughin, I., Kwok, R., and Fahnestock, M. (1998). "Interferometric estimation of three-dimensional ice-flow using ascending and descending passes". *IEEE Transactions on Geoscience and Remote Sensing* 36.1, pp. 25–37. DOI: 10.1109/36.655315.

Joughin, I., Smith, B. E., and Howat, I. M. (2018a). "A complete map of Greenland ice velocity derived from satellite data collected over 20 years". *Journal of Glaciology* 64.243, pp. 1–11. DOI: 10.1017/jog.2017.73.

Joughin, I., Smith, B. E., and Howat, I. (2018b). "Greenland Ice Mapping Project: ice flow velocity variation at sub-monthly to decadal timescales". *The Cryosphere* 12.7, pp. 2211–2227. DOI: 10.5194/tc-12-2211-2018.

Karlsson, N. B. et al. (2021). "A first constraint on basal melt-water production of the Greenland ice sheet". *Nature Communications* 12.1, p. 3461. DOI: 10.1038/s41467-021-23739-z.

Khan, S. A. et al. (2014). "Sustained mass loss of the northeast Greenland ice sheet triggered by regional warming". *Nature Climate Change* 4.4, pp. 292–299. DOI: 10.1038/NCLIMATE2161.

Khazendar, A. et al. (2019). "Interruption of two decades of Jakobshavn Isbrae acceleration and thinning as regional ocean cools". *Nature Geoscience* 12.4, pp. 277–283. DOI: 10.1038/s41561-019-0329-3.

King, M. D., Howat, I. M., Candela, S. G., Noh, M. J., Jeong, S., Noël, B. P. Y., Broeke, M. R. van den, Wouters, B., and Negrete, A. (2020). "Dynamic ice loss from the Greenland Ice Sheet driven by sustained glacier retreat". *Communications Earth & Environment* 1.1, p. 1. DOI: 10.1038/s43247-020-0001-2.

Kusk, A., Boncori, J., and Dall, J. (2018). "An automated system for ice velocity measurement from SAR". Proceedings of the 12th European Conference on Synthetic Aperture Radar (EUSAR 2018). VDE Verlag, pp. 929–932.

Kusk, A., Andersen, J. K., and Boncori, J. P. M. (2021). "Burst Overlap Coregistration for Sentinel-1 TOPS DInSAR Ice Velocity Measurements". *IEEE Geoscience and Remote Sensing Letters* 19, pp. 1–5. DOI: 10.1109/LGRS.2021.3062905.

Langen, P. L., Fausto, R. S., Vandecrux, B., Mottram, R. H., and Box, J. E. (2017). "Liquid Water Flow and Retention on the Greenland Ice Sheet in the Regional Climate Model HIRHAM5: Local and Large-Scale Impacts". *Frontiers in Earth Science* 4. DOI: 10.3389/feart.2016.00110.

Lei, Y., Gardner, A. S., and Agram, P. (2021). "Processing methodology for the ITS_LIVE Sentinel-1 ice velocity product". DOI: 10.5194/essd-2021-393. URL: https://essd.copernicus.org/preprints/essd-2021-393/.

Li, X., Jónsson, S., and Cao, Y. (2021). "Interseismic Deformation From Sentinel-1 Burst-Overlap Interferometry: Application to the Southern Dead Sea Fault". *Geophysical Research Letters* 48.16. DOI: 10.1029/2021GL093481.

Livingstone, S. J., Clark, C. D., Woodward, J., and Kingslake, J. (2013). "Potential subglacial lake locations and meltwater drainage pathways beneath the Antarctic and Greenland ice sheets". *The Cryosphere* 7.6, pp. 1721–1740. DOI: 10.5194/tc-7-1721-2013.

Livingstone, S. J., Utting, D. J., Ruffell, A., Clark, C. D., Pawley, S., Atkinson, N., and Fowler, A. C. (2016). "Discovery of relict subglacial lakes and their geometry and mechanism of drainage". *Nature Communications* 7.1, ncomms11767. DOI: 10.1038/ncomms11767.

Livingstone, S. J. et al. (2022). "Subglacial lakes and their changing role in a warming climate". *Nature Reviews Earth & Environment* 3.2, pp. 106–124. DOI: 10.1038/s43017-021-00246-9.

Luckman, A., Murray, T., Lange, R. de, and Hanna, E. (2006). "Rapid and synchronous ice-dynamic changes in East Greenland". *Geophysical Research Letters* 33.3, p. L03503. DOI: 10.1029/2005GL025428.

Luckman, A., Benn, D. I., Cottier, F., Bevan, S., Nilsen, F., and Inall, M. (2015). "Calving rates at tidewater glaciers vary strongly with ocean temperature". *Nature Communications* 6.1, p. 8566. DOI: 10.1038/ncomms9566.

MacGregor, J. A., Chu, W., Colgan, W. T., Fahnestock, M. A., Felikson, D., Karlsson, N. B., Nowicki, S. M. J., and Studinger, M. (2022). "GBaTSv2: a revised synthesis of the likely basal thermal state of the Greenland Ice Sheet". *The Cryosphere* 16.8, pp. 3033–3049. DOI: 10.5194/tc-16-3033-2022.

Madsen, S. and Zebker, H. (1992). "Automated Absolute Phase Retrieval in Across-Track Interferometry". *IEEE International Geoscience and Remote Sensing Symposium (IGARSS) 1992*. Vol. 2. Houston, TX: IEEE, pp. 1582–1584. DOI: 10.1109/IGARSS.1992.578639.

Maier, N., Humphrey, N., Harper, J., and Meierbachtol, T. (2019). "Sliding dominates slow-flowing margin regions, Greenland Ice Sheet". *Science Advances* 5.7. DOI: 10.1126/sciadv.aaw5406.

Mankoff, K. D., Solgaard, A., Colgan, W., Ahlstrøm, A. P., Khan, S. A., and Fausto, R. S. (2020). "Greenland Ice Sheet solid ice discharge from 1986 through March 2020". *Earth System Science Data* 12.2, pp. 1367–1383. DOI: 10.5194/essd-12-1367-2020.

Marzeion, B., Cogley, J. G., Richter, K., and Parkes, D. (2014). "Attribution of global glacier mass loss to anthropogenic and natural causes". *Science* 345.6199, pp. 919–921. DOI: 10.1126/science.1254702.

Massonnet, D., Feigl, K., Rossi, M., and Adragna, F. (1994). "Radar interferometric mapping of deformation in the year after the Landers earthquake". *Nature* 369.6477, pp. 227–230. DOI: 10.1038/369227a0.

McGranahan, G., Balk, D., and Anderson, B. (2007). "The rising tide: assessing the risks of climate change and human settlements in low elevation coastal zones". *Environment and Urbanization* 19.1, pp. 17–37. DOI: 10.1177/0956247807076960.

Merryman Boncori, J. P. (2019). "Measuring Coseismic Deformation With Spaceborne Synthetic Aperture Radar: A Review". *Frontiers in Earth Science* 7, p. 16. DOI: 10.3389/feart.2019.00016.

Milillo, P., Rignot, E., Mouginot, J., Scheuchl, B., Morlighem, M., Li, X., and Salzer, J. T. (2017). "On the Short-term Grounding Zone Dynamics of Pine Island Glacier, West Antarctica, Observed With COSMO-SkyMed Interferometric Data: PIG Grounding Line Dynamics". *Geophysical Research Letters* 44.20, pp. 10, 436–10, 444. DOI: 10.1002/2017GL074320.

Millan, R., Mouginot, J., Rabatel, A., Jeong, S., Cusicanqui, D., Derkacheva, A., and Chekki, M. (2019). "Mapping Surface Flow Velocity of Glaciers at Regional Scale Using a Multiple Sensors Approach". *Remote Sensing* 11.21, p. 2498. DOI: 10.3390/rs11212498.

Millan, R., Mouginot, J., Rabatel, A., and Morlighem, M. (2022). "Ice velocity and thickness of the world's glaciers". *Nature Geoscience* 15.2, pp. 124–129. DOI: 10.1038/s41561-021-00885-z.

Miranda, N. (2017). *Definition of the TOPS SLC deramping function for products generated by the S-1 IPF*. Tech. rep. COPE-GSEG-EOPG-TN-14-0025. Paris, France: European Space Agency.

Mock, S. J. (1976). *Geodetic Positions of Borehole Sites of the Greenland Ice Sheet Program*. CRREL Report. U.S. Army Cold Regions Research and Engineering Laboratory.

Mohr, J. and Boncori, J. (2008). "An error prediction framework for interferometric SAR data". *IEEE Transactions on Geoscience and Remote Sensing* 46.6, pp. 1600–1613. DOI: 10.1109/TGRS.2008.916213.

Mohr, J. J., Reeh, N., and Madsen, S. N. (1998). "Three-dimensional glacial flow and surface elevation measured with radar interferometry". *Nature* 391.6664, pp. 273–276. DOI: 10.1038/34635.

Moon, T., Joughin, I., Smith, B., Broeke, M. R. van den, Berg, W. J. van de, Noël, B., and Usher, M. (2014). "Distinct patterns of seasonal Greenland glacier velocity". *Geophysical Research Letters* 41.20, pp. 7209–7216. DOI: 10.1002/2014GL061836.

Moon, T. A., Gardner, A. S., Csatho, B., Parmuzin, I., and Fahnestock, M. A. (2020). "Rapid Reconfiguration of the Greenland Ice Sheet Coastal Margin". *Journal of Geophysical Research: Earth Surface* 125.11. DOI: 10.1029/2020JF005585.

Moore, R., Claassen, J., and Lin, Y. (1981). "Scanning Spaceborne Synthetic Aperture Radar with Integrated Radiometer". *IEEE Transactions on Aerospace and Electronic Systems* AES-17.3, pp. 410–421. DOI: 10.1109/TAES.1981.309069.

Moreira, A. and Scheiber, R. (1998). "A new method for accurate co-registration of interferometric SAR images". *International Geoscience and Remote Sensing Symposium Proceedings (IGARSS) 1998*. Seattle, WA, USA, pp. 1091–1093. DOI: 10.1109/IGARSS.1998.699682.

Morlighem, M. et al. (2017). "BedMachine v3: Complete Bed Topography and Ocean Bathymetry Mapping of Greenland From Multibeam Echo Sounding Combined With Mass Conservation". *Geophysical Research Letters* 44.21. DOI: 10.1002/2017GL074954.

Morlighem, M. (2021). *IceBridge BedMachine Greenland, Version 4*. Type: dataset. DOI: 10.5067/VLJ5YXKCNGXO. URL: https://nsidc.org/data/IDBMG4/versions/4 (visited on 07/29/2022).

Morlighem, M. et al. (2020). "Deep glacial troughs and stabilizing ridges unveiled beneath the margins of the Antarctic ice sheet". *Nature Geoscience* 13.2, pp. 132–137. DOI: 10.1038/s41561-019-0510-8.

Mouginot, J., Rignot, E., Scheuchl, B., Fenty, I., Khazendar, A., Morlighem, M., Buzzi, A., and Paden, J. (2015). "Fast retreat of Zachariae Isstrom, northeast Greenland". *Science* 350.6266, pp. 1357–1361. DOI: 10.1126/science.aac7111.

Mouginot, J., Bjørk, A. A., Millan, R., Scheuchl, B., and Rignot, E. (2018). "Insights on the Surge Behavior of Storstrømmen and L. Bistrup Bræ, Northeast Greenland, Over the Last Century". *Geophysical Research Letters* 45.20. DOI: 10.1029/2018GL079052.

Mouginot, J., Rignot, E., and Scheuchl, B. (2019a). "Continent-Wide, Interferometric SAR Phase, Mapping of Antarctic Ice Velocity". *Geophysical Research Letters* 46.16, pp. 9710–9718. DOI: 10.1029/2019GL083826.

Mouginot, J., Scheuchl, B., and Rignot, E. (2012). "Mapping of Ice Motion in Antarctica Using Synthetic-Aperture Radar Data". *Remote Sensing* 4.9, pp. 2753–2767. DOI: 10.3390/rs4092753.

Mouginot, J., Rignot, E., Scheuchl, B., and Millan, R. (2017). "Comprehensive Annual Ice Sheet Velocity Mapping Using Landsat-8, Sentinel-1, and RADARSAT-2 Data". *Remote Sensing* 9.4, p. 364. DOI: 10.3390/rs9040364.

Mouginot, J., Rignot, E., Bjørk, A. A., Broeke, M. van den, Millan, R., Morlighem, M., Noël, B., Scheuchl, B., and Wood, M. (2019b). "Forty-six years of Greenland Ice Sheet mass balance from 1972 to 2018". *Proceedings of the National Academy of Sciences* 116.19, pp. 9239–9244. DOI: 10.1073/pnas.1904242116.

Nagler, T., Rott, H., Hetzenecker, M., Wuite, J., and Potin, P. (2015). "The Sentinel-1 Mission: New Opportunities for Ice Sheet Observations". *Remote Sensing* 7.7, pp. 9371–9389. DOI: 10.3390/rs70709371.

Nakamura, K., Doi, K., and Shibuya, K. (2007). "Estimation of seasonal changes in the flow of Shirase Glacier using JERS-1/SAR image correlation". *Polar Science* 1.2, pp. 73–83. DOI: 10.1016/j.polar.2007.09.002.

Neckel, N., Franke, S., Helm, V., Drews, R., and Jansen, D. (2021). "Evidence of Cascading Subglacial Water Flow at Jutulstraumen Glacier (Antarctica) Derived From Sentinel-1 and ICESat-2 Measurements". *Geophysical Research Letters* 48.20. DOI: 10.1029/2021GL094472.

Nerem, R. S., Beckley, B. D., Fasullo, J. T., Hamlington, B. D., Masters, D., and Mitchum, G. T. (2018). "Climate-change–driven accelerated sea-level rise detected in the altimeter era". *Proceedings of the National Academy of Sciences* 115.9, pp. 2022–2025. DOI: 10.1073/pnas.1717312115.

Oswald, G. K. A., Rezvanbehbahani, S., and Stearns, L. A. (2018). "Radar evidence of ponded subglacial water in Greenland". *Journal of Glaciology* 64.247, pp. 711–729. DOI: 10.1017/jog.2018.60.

Palmer, S., McMillan, M., and Morlighem, M. (2015). "Subglacial lake drainage detected beneath the Greenland ice sheet". *Nature Communications* 6.1, p. 8408. DOI: 10.1038/ncomms9408.

Palmer, S. J., Dowdeswell, J. A., Christoffersen, P., Young, D. A., Blankenship, D. D., Greenbaum, J. S., Benham, T., Bamber, J., and Siegert, M. J. (2013). "Greenland subglacial lakes detected by radar". *Geophysical Research Letters* 40.23, pp. 6154–6159. DOI: 10.1002/2013GL058383.

Pinel-Puyssegur, B., Lasserre, C., Benoit, A., Jolivet, R., Doin, M.-P., and Champenois, J. (2018). "A Simple Phase Unwrapping Errors Correction Algorithm Based on Phase Closure Analysis". *IEEE International Geoscience and Remote Sensing Symposium (IGARSS) 2018*. Valencia, Spain, pp. 2212–2215. DOI: 10.1109/IGARSS.2018.8518050.

Porter, C. et al. (2018). *ArcticDEM*. DOI: 10.7910/DVN/OHHUKH. URL: https://dataverse.harvard.edu/citation?persistentId=doi:10.7910/DVN/OHHUKH (visited on 06/27/2022).

Prats-Iraola, P., Scheiber, R., Marotti, L., Wollstadt, S., and Reigber, A. (2012). "TOPS interferometry with terraSAR-X". *IEEE Transactions on Geoscience and Remote Sensing* 50.8, pp. 3179–3188.

Pritchard, H., Murray, T., Luckman, A., Strozzi, T., and Barr, S. (2005). "Glacier surge dynamics of Sortebræ, east Greenland, from synthetic aperture radar feature tracking". *Journal of Geophysical Research: Earth Surface* 110.3.

Rabus, B., Eineder, M., Roth, A., and Bamler, R. (2003). "The shuttle radar topography mission—a new class of digital elevation models acquired by spaceborne radar". *ISPRS Journal of Photogrammetry and Remote Sensing* 57.4, pp. 241–262. DOI: 10.1016/S0924-2716(02)00124-7.

Rignot, E. (2008). "Changes in West Antarctic ice stream dynamics observed with ALOS PALSAR data: ALOS PALSAR ANTARCTICA". *Geophysical Research Letters* 35.12. DOI: 10.1029/2008GL033365.

Rignot, E. and MacAyeal, D. R. (1998). "Ice-shelf dynamics near the front of the Filchner—Ronne Ice Shelf, Antarctica, revealed by SAR interferometry". *Journal of Glaciology* 44.147, pp. 405–418. DOI: 10.1017/S0022143000002732.

Rizzoli, P. et al. (2017). "Generation and performance assessment of the global TanDEM-X digital elevation model". *ISPRS Journal of Photogrammetry and Remote Sensing* 132, pp. 119–139. DOI: 10.1016/j.isprsjprs.2017.08.008.

Rodriguez, E. and Martin, J. (1992). "Theory and design of interferometric synthetic aperture radars". *IEE Proceedings F (Radar and Signal Processing)* 139 (2), 147–159(12). ISSN: 0956-375X.

Rosen, P. et al. (2016). "An update on the NASA-ISRO dual-frequency DBF SAR (NISAR) mission". *IEEE International Geoscience and Remote Sensing Symposium (IGARSS) 2016*. Beijing, China: IEEE, pp. 2106–2108. DOI: 10.1109/IGARSS.2016.7729543.

Sandberg Sørensen, L., Simonsen, S. B., Forsberg, R., Khvorostovsky, K., Meister, R., and Engdahl, M. E. (2018). "25 years of elevation changes of the Greenland Ice Sheet from ERS, Envisat, and CryoSat-2 radar altimetry". *Earth and Planetary Science Letters* 495, pp. 234–241. DOI: 10.1016/j.epsl.2018.05.015.

Sansosti, E., Berardino, P., Manunta, M., Serafino, F., and Fornaro, G. (2006). "Geometrical SAR image registration". *IEEE Transactions on Geoscience and Remote Sensing* 44.10, pp. 2861–2870. DOI: 10.1109/TGRS.2006.875787.

Scambos, T. and Fahnestock, M. (2016). *Global Land Ice Velocity Extraction from Landsat 8 (GoLIVE)*. Type: dataset. DOI: 10.7265/N5ZP442B. URL: https://nsidc.org/data/nsidc-0710 (visited on 08/26/2022).

Scambos, T. A., Dutkiewicz, M. J., Wilson, J. C., and Bindschadler, R. A. (1992). "Application of image cross-correlation to the measurement of glacier velocity using satellite image data". *Remote Sensing of Environment* 42.3, pp. 177–186. DOI: 10.1016/0034-4257(92)90101-O.

Scheiber, R. and Moreira, A. (2000). "Coregistration of interferometric SAR images using spectral diversity". *IEEE Transactions on Geoscience and Remote Sensing* 38.5, pp. 2179–2191. DOI: 10.1109/36.868876.

Scheiber, R., Jager, M., Prats-Iraola, P., De Zan, F., and Geudtner, D. (2014). "Speckle tracking and interferometric processing of TerraSAR-X TOPS sata for mapping nonstationary scenarios". *IEEE Journal of Selected Topics in Applied Earth Observations and Remote Sensing* 8.4, pp. 1709–1720.

Scott, C. P. and Lohman, R. B. (2016). "Sensitivity of earthquake source inversions to atmospheric noise and corrections of InSAR data". *Journal of Geophysical Research: Solid Earth* 121.5, pp. 4031–4044. DOI: 10.1002/2016JB012969.

Sen, P. K. (1968). "Estimates of the Regression Coefficient Based on Kendall's Tau". *Journal of the American Statistical Association* 63.324, pp. 1379–1389. DOI: 10.1080/01621459.1968.10480934.

Siegfried, M. R., Fricker, H. A., Carter, S. P., and Tulaczyk, S. (2016). "Episodic ice velocity fluctuations triggered by a subglacial flood in West Antarctica". *Geophysical Research Letters* 43.6, pp. 2640–2648. DOI: 10.1002/2016GL067758.

Slater, T., Lawrence, I. R., Otosaka, I. N., Shepherd, A., Gourmelen, N., Jakob, L., Tepes, P., Gilbert, L., and Nienow, P. (2021). "Review article: Earth's ice imbalance". *The Cryosphere* 15.1, pp. 233–246. DOI: 10.5194/tc-15-233-2021.

Smith, B., Jelley, B. P., Dickinson, S., Sutterley, T., Neumann, T. A., and Harbeck, K. (2021). *ATLAS/ICESat-2 L3B Gridded Antarctic and Arctic Land Ice Height Change, Version 1*. Type: dataset. URL: https://doi.org/10.5067/ATLAS/ATL15.001 (visited on 08/11/2022).

Smith, B. et al. (2020). "Pervasive ice sheet mass loss reflects competing ocean and atmosphere processes". *Science* 368.6496, pp. 1239–1242. DOI: 10.1126/science.aaz5845.

Smith-Johnsen, S., Schlegel, N.-J., Fleurian, B., and Nisancioglu, K. H. (2020). "Sensitivity of the Northeast Greenland Ice Stream to Geothermal Heat". *Journal of Geophysical Research: Earth Surface* 125.1. DOI: 10.1029/2019JF005252.

Sole, A. J., Mair, D. W. F., Nienow, P. W., Bartholomew, I. D., King, M. A., Burke, M. J., and Joughin, I. (2011). "Seasonal speedup of a Greenland marine-terminating outlet glacier forced by surface melt–induced changes in subglacial hydrology". *Journal of Geophysical Research* 116 (F3). DOI: 10.1029/2010JF001948.

Solgaard, A. and Kusk, A. (2021). *Greenland Ice Velocity from Sentinel-1 Edition 2*. Type: dataset. DOI: 10.22008/promice/data/sentinel1icevelocity/greenlandicesheet. URL: https://doi.org/10.22008/promice/data/sentinel1icevelocity/greenlandicesheet (visited on 08/20/2022).

Solgaard, A. et al. (2021). "Greenland ice velocity maps from the PROMICE project". *Earth System Science Data* 13.7, pp. 3491–3512. DOI: 10.5194/essd-13-3491-2021.

Stearns, L. A., Smith, B. E., and Hamilton, G. S. (2008). "Increased flow speed on a large East Antarctic outlet glacier caused by subglacial floods". *Nature Geoscience* 1.12, pp. 827–831. DOI: 10.1038/ngeo356.

Straneo, F. and Heimbach, P. (2013). "North Atlantic warming and the retreat of Greenland's outlet glaciers". *Nature* 504.7478, pp. 36–43. DOI: 10.1038/nature12854.

Strozzi, T., Luckman, A., Murray, T., Wegmuller, U., and Werner, C. (2002). "Glacier motion estimation using SAR offset-tracking procedures". *IEEE Transactions on Geoscience and Remote Sensing* 40.11, pp. 2384–2391. DOI: 10.1109/TGRS.2002.805079.

Thiel, K.-H., Hartl, P., and Wu, X. (1996). "Monitoring the ice movements with ERS SAR interferometry in the Antarctic region". 383, pp. 219–223.

Thomas, R., Akins, T., Csatho, B., Fahnestock, M., Gogineni, P., Kim, C., and Sonntag, J. (2000). "Mass Balance of the Greenland Ice Sheet at High Elevations". *Science* 289.5478, pp. 426–428. DOI: 10.1126/science.289.5478.426.

Velicogna, I., Sutterley, T. C., and Broeke, M. R. van den (2014). "Regional acceleration in ice mass loss from Greenland and Antarctica using GRACE time-variable gravity data". *Geophysical Research Letters* 41.22, pp. 8130–8137. DOI: 10.1002/2014GL061052.

Vijay, S., Khan, S. A., Kusk, A., Solgaard, A. M., Moon, T., and Bjørk, A. A. (2019). "Resolving Seasonal Ice Velocity of 45 Greenlandic Glaciers With Very High Temporal Details". *Geophysical Research Letters* 46.3, pp. 1485–1495. DOI: 10.1029/2018GL081503.

Vousdoukas, M. I., Mentaschi, L., Voukouvalas, E., Verlaan, M., and Feyen, L. (2017). "Extreme sea levels on the rise along Europe's coasts". *Earth's Future* 5.3, pp. 304–323. DOI: 10.1002/2016EF000505.

WCRP Global Sea Level Budget Group (2018). "Global sea-level budget 1993–present". *Earth System Science Data* 10.3, pp. 1551–1590. DOI: 10.5194/essd-10-1551-2018.

Weber Hoen, E. and Zebker, H. (2000). "Penetration depths inferred from interferometric volume decorrelation observed over the Greenland Ice Sheet". *IEEE Transactions on Geoscience and Remote Sensing* 38.6, pp. 2571–2583. DOI: 10.1109/36.885204.

Wilcox, R. R. (2001). *Fundamentals of modern statistical methods: substantially improving power and accuracy*. New York: Springer. ISBN: 978-0-387-95157-7.

Willis, M. J., Herried, B. G., Bevis, M. G., and Bell, R. E. (2015). "Recharge of a subglacial lake by surface meltwater in northeast Greenland". *Nature* 518.7538, pp. 223–227. DOI: 10.1038/nature14116.

Wingham, D. J., Siegert, M. J., Shepherd, A., and Muir, A. S. (2006). "Rapid discharge connects Antarctic subglacial lakes". *Nature* 440.7087, pp. 1033–1036. DOI: 10.1038/nature04660.

World Meteorological Organization (WMO), ed. (2016). *GCOS-200: The Global Observing System for Climate: Implementation Needs*. URL: https://library.wmo.int/doc_num.php?explnum_id=3417.

Yague-Martinez, N., Prats-Iraola, P., Gonzalez, F. R., Brcic, R., Shau, R., Geudtner, D., Eineder, M., and Bamler, R. (2016). "Interferometric Processing of Sentinel-1 TOPS Data". *IEEE Transactions on Geoscience and Remote Sensing* 54.4, pp. 2220–2234. DOI: 10.1109/TGRS.2015.2497902.

Yu, C., Li, Z., Chen, J., and Hu, J.-C. (2018). "Small Magnitude Co-Seismic Deformation of the 2017 Mw 6.4 Nyingchi Earthquake Revealed by InSAR Measurements with Atmospheric Correction". *Remote Sensing* 10.5, p. 684. DOI: 10.3390/rs10050684.

Yunjun, Z., Fattahi, H., and Amelung, F. (2019). "Small baseline InSAR time series analysis: Unwrapping error correction and noise reduction". *Computers & Geosciences* 133, p. 104331. DOI: 10.1016/j.cageo.2019.104331.

Chapter A | Manuscripts

A.1 Improved ice velocity measurements with Sentinel-1 TOPS interferometry

This appendix provides the full manuscript:

J. K. Andersen, A. Kusk, J. P. M. Boncori, C. S. Hvidberg, and A. Grinsted, Improved ice velocity measurements with Sentinel-1 TOPS interferometry, *Remote Sensing*, vol. 12, no. 12, p. 2014, doi:10.3390/rs12122014 (2020)

Supplementary material for the manuscript is provided in Appendix B.1.

remote sensing

MDPI

Article

Improved Ice Velocity Measurements with Sentinel-1 TOPS Interferometry

Jonas Kvist Andersen [1,*], Anders Kusk [1], John Peter Merryman Boncori [1], Christine Schøtt Hvidberg [2] and Aslak Grinsted [2]

[1] DTU Space Institute, Technical University of Denmark (DTU), DK-2800 Kongens Lyngby, Denmark; ak@space.dtu.dk (A.K.); jme@space.dtu.dk (J.P.M.B.)

[2] Niels Bohr Institute, University of Copenhagen, DK-2100 Copenhagen, Denmark; ch@nbi.ku.dk (C.S.H.); aslak@nbi.ku.dk (A.G.)

* Correspondence: jkvand@space.dtu.dk

Received: 13 May 2020; Accepted: 19 June 2020; Published: 23 June 2020

Abstract: In recent years, the Sentinel-1 satellites have provided a data archive of unprecedented volume, delivering C-band Synthetic Aperture Radar (SAR) acquisitions over most of the polar ice sheets with a repeat-pass period of 6-12 days using Interferometric Wide swath (IW) imagery acquired in Terrain Observation by Progressive Scans (TOPS) mode. Due to the added complexity of TOPS-mode interferometric processing, however, Sentinel-1 ice velocity measurements currently rely exclusively on amplitude offset tracking, which generates measurements of substantially lower accuracy and spatial resolution than would be possible with Differential SAR Interferometry (DInSAR). The main difficulty associated with TOPS interferometry lies in the spatially variable azimuth phase contribution arising from along-track motion within the scene. We present a Sentinel-1 interferometric processing chain, which reduces the azimuth coupling to the line-of-sight phase signal through a spatially adaptive coregistration refinement incorporating azimuth velocity measurements. The latter are based on available ice velocity mosaics, optionally supplemented by Burst-Overlap Multi-Aperture Interferometry. The DInSAR processing chain is demonstrated for a large drainage basin in Northeast Greenland, encompassing the Northeast Greenland Ice Stream (NEGIS), and integrated with state-of-the-art offset tracking measurements. In the ice sheet interior, the combined DInSAR and offset tracking ice velocity product provides a spatial resolution of 50 × 50 m and 1-sigma accuracies of 0.18 and 0.44 m/y in the x and y components respectively, compared to GPS.

Keywords: ice velocity; Greenland ice sheet; Sentinel-1; TOPS; DInSAR

1. Introduction

Ice velocity is an essential parameter in the study of ice sheet and glacier dynamics. It governs the discharge of ice from the accumulation zone to the edges of outlet glaciers and hence influences estimates of ice sheet mass balance and sea level rise [1,2]. Furthermore, ice velocity measurements constitute valuable input for constraining and validating numerical ice sheet models and for inversions seeking to infer, for example, basal sliding patterns and ice thickness.

Application of Synthetic Aperture Radar (SAR) satellites to ice motion monitoring has long been established. SAR-based measurements are currently obtained either through amplitude-based feature and speckle tracking (collectively referred to as offset tracking) [3,4] or through Differential SAR interferometry (DInSAR), a technique exploiting the radar phase [5]. Offset tracking has the advantage of producing two-dimensional velocity measurements, namely along the range (satellite line-of-sight) and azimuth (flight path) dimensions, and is applicable even on fast-flowing outlet glaciers, which may reach velocities as high as several km/year. The accuracy and resolution of the amplitude-based

offset tracking velocity retrievals, however, are generally substantially poorer than those obtained with DInSAR [6], although the latter technique provides only measurements of the range motion component. A comprehensive review of SAR-based ice velocity measurement techniques applicable to Stripmap imagery is provided in [6].

In recent years, the European Space Agency (ESA) Sentinel-1A (S1A) and Sentinel-1B (S1B) SAR missions have been generating an unprecedented archive of regularly acquired free and open access data. Its main acquisition mode over land, namely Terrain Observation by Progressive Scans (TOPS) [7], trades off azimuth spatial resolution for wide swath coverage, allowing full coverage of the Greenland ice sheet to be achieved every 6–12 days. Concerning ice motion, however, such an archive is not being exploited to its full extent. Sentinel-1-based ice velocity products are in fact exclusively based on SAR offset tracking [8–11], whereas DInSAR is applied solely to Stripmap-mode imagery from other SAR missions [10,12]. This is a limitation particularly for the ice sheet interior regions, where the velocity magnitudes are often below the measurement accuracy provided by offset tracking. Even though interior velocities are slow, it is of high interest to monitor dynamical changes related to fast-flowing ice streams in order to detect how marginal acceleration and thinning spread inland [13], or to infer knowledge of basal hydrology from ice velocity patterns [14].

TOPS interferometry on ice sheets is complicated by the azimuth antenna steering of this acquisition mode, which significantly increases the sensitivity of the interferometric phase to azimuth misregistration compared to the Stripmap and ScanSAR case. For scenes covering near-stationary areas, Extended Spectral Diversity (ESD) was proposed in [15,16] to estimate a constant (i.e., scene-wide) azimuth offset to refine the results of geometric coregistration based on precise orbits and a Digital Elevation Model (DEM). Ice motion applications provide an additional challenge, however, since the projection of the underlying horizontal surface motion causes the azimuth misregistration to be spatially varying. In [17], a TOPS DInSAR approach based on adaptive azimuth coregistration and Multi-Aperture Interferometry (MAI) azimuth motion measurements was presented and demonstrated on TerraSAR-X TOPS acquisitions. However, this method was never applied to Sentinel-1 data. Sentinel-1 TOPS DInSAR was used in [18] to measure ice velocity on glaciers in the Canadian Arctic using the approach mentioned above for stationary scenes, which was justified for an area of interest in which motion was confined to glacier tongues with velocity magnitudes within $\sim$ 35 m/y. In [19], Sentinel-1 TOPS DInSAR was used to measure ice velocity and grounding line location for a set of glaciers in West Antarctica, using offset tracking to estimate and remove the phase contribution due to azimuth misregistration.

In this paper, we demonstrate the feasibility of generating Sentinel-1 TOPS DInSAR ice velocity measurements in the interior of the Greenland ice sheet using a DInSAR processing approach based on an azimuth coregistration refinement, as in [17]. However, after investigating different approaches, we select a different method to generate such a refinement. We assess the performance of our algorithm for the full Zwally 2.1 drainage basin [20], containing the North East Greenland Ice Stream (NEGIS), using both ascending and descending tracks from the Sentinel-1 winter campaign 2019–2020 and the surface parallel flow assumption [21] to generate 3D DInSAR velocity measurements. These are compared to GPS velocity retrievals as well as to 3D ice velocity mosaics based on amplitude offset tracking alone.

Section 2 outlines the data utilized in this study and describes the SAR data processing methods. Section 3 presents the ice velocity maps obtained for the Zwally 2.1 drainage basin using both offset tracking and DInSAR and their comparison with GPS measurements. Section 4 provides a discussion on the performance of Sentinel-1 TOPS DInSAR and on the requirements to include this processing algorithm in the routine generation of Greenland-wide ice velocity products. Conclusions are drawn in Section 5.

2. Data and Methods

2.1. Data

We utilized Sentinel-1A/B IW SLC images from the 2019–2020 Greenland winter campaign, during which the acquisition plan prioritized a frequent, comprehensive coverage of the Greenland ice sheet. We processed 3 acquisition cycles for 4 descending and 3 ascending passes, meaning that for each track, a total of five 6-day image pairs and three 12-day pairs could be formed. An overview of the processed Sentinel-1 images is found in Table 1. Figure 1 shows the coverage of the processed Sentinel-1 tracks along with an outline of the region of interest, i.e., the Zwally 2.1 drainage basin, containing the NEGIS.

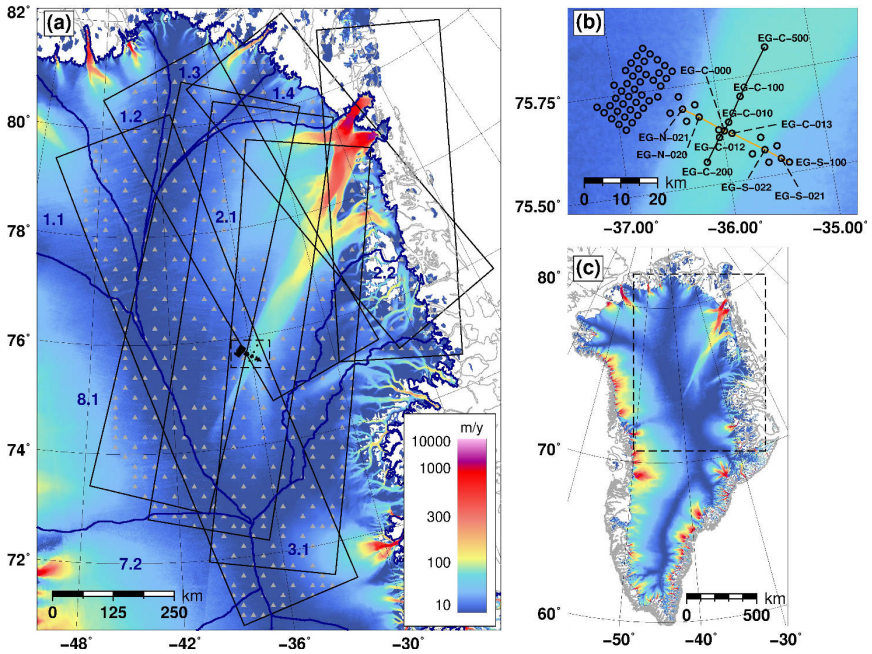

Figure 1. (**a**) Sentinel-1 tracks processed in this study (black rectangles), Zwally drainage basins [20] (dark blue polygons and numbers), GPS measurements used for validation (black dots), and Ground Control Points used for the calibration described in Section 2.4 (gray triangles). (**b**) Zoom of the area located within the dashed rectangle in panel a, containing the EastGRIP GPS measurements (circles). (**c**) Area of interest for this study, shown in panel a. In all panels the color scale represents the Programme for Monitoring of the Greenland Ice Sheet (PROMICE) multi-year velocity mosaic described in Section 2.1.

External datasets used for the SAR data processing include the 90 m Tandem-X DEM [22], Sentinel-1 Precise Orbit Ephimeredes files downloaded from: https://qc.sentinel1.eo.esa.int/aux_poeorb/, and a Greenland-wide multi-year average (2016–2019) ice velocity mosaic, based on the monthly ice velocity products distributed by the Geological Survey of Denmark and Greenland (GEUS) within the Danish Programme for Monitoring of the Greenland Ice Sheet (PROMICE) [9]. These measurements were carried out with Sentinel-1 intensity offset tracking (cfr. Section 2.2), exploiting all available observations from 14 September 2016 to 17 June 2019, and are referred to as the PROMICE multi-year velocity mosaic throughout the remainder of this paper.

Validation of the core measurement techniques and of the final ice velocity mosaics was carried out using GPS measurements provided by the East Greenland Ice-core Project (EastGRIP). These cover transects both across and along the upstream part of NEGIS, as shown in Figure 1b. Additionally, measurements were collected for a 5×9 grid of stakes (spaced 2.5 km apart) just outside of the shear

margin. The GPS measurements provide a range of velocities for validation between approximately 10–60 m/y and strain rates (i.e., velocity gradients) in the order of 10^{-3} y^{-1} near the NEGIS shear margin [23].

Table 1. Overview of Sentinel-1 image pairs processed for the Zwally 2.1 drainage basin test case. In the case of DInSAR, every available 6-day pair from the listed cycles (i.e., 5 image pairs per track) was used, while all available 12-day pairs were used in offset tracking processing (3 image pairs per track).

Track	Orbit	Cycles	Acquisition Dates
31	Ascending	A: 188, 189, 190/B: 118, 119, 120	16 December 2019–15 January 2020
54	Descending	A: 188, 189, 190/B: 118, 119, 120	18 December 2019–17 January 2020
74	Ascending	A: 188, 189, 190/B: 118, 119, 120	19 December 2019–18 January 2020
83	Descending	A: 188, 189, 190/B: 118, 119, 120	20 December 2019–19 January 2020
89	Ascending	A: 188, 189, 190/B: 118, 119, 120	20 December 2019–19 January 2020
112	Descending	A: 188, 189, 190/B: 118, 119, 120	22 December 2019–21 January 2020
170	Descending	A: 188, 189, 190/B: 118, 119, 120	26 December 2019–25 January 2020

2.2. Intensity Offset Tracking

A reference offset tracking processing was carried out using the IPP processing software developed at the Technical University of Denmark [24]. Intensity data patches of size 256 × 64 (range × azimuth), corresponding to about 900 × 900 m on the ground, are selected on a regular grid of 40 × 10 pixels in the master SLC, corresponding to 560 × 560 m on the ground, and the corresponding patches in the slave SLC are located using the satellite orbits and a DEM. For each patch pair, the normalized 2D cross-correlation surface is calculated, and the position of the correlation peak is estimated with sub-pixel accuracy using FFT oversampling and a parabolic fit on a region surrounding the peak. Displacement estimates are accepted based on thresholds for the correlation (>0.05) and the signal-to-noise ratio (>7), i.e., the ratio of the peak to the surrounding correlation surface. These thresholds are the same used for the offset tracking processing within PROMICE and hence are not fine-tuned for this specific data set. The output is two offset maps (i.e., range and azimuth offsets), from which outliers are removed based on local medians using the approach described in [25]. Error estimates are generated by calculating the local standard deviation for each pixel in the displacement maps in a 5 × 5 neighborhood. Finally, the displacements and error estimates are scaled to velocity and geocoded to form slant range/azimuth velocity maps on a polar stereographic grid with 250 m spacing. The calculation of Cartesian velocity components is deferred to a later stage, as described in Section 2.5, since this allows to "fuse" measurements generated using different techniques and acquisition geometries.

2.3. Sentinel-1 TOPS Interferometry

2.3.1. Theoretical Background

Regardless of the SAR acquisition mode, for example, Stripmap or TOPS, the phase of a differential interferogram pixel $\Delta\phi$ contains the following range- and azimuth-dependent contributions, respectively $\Delta\phi_r$ and $\Delta\phi_a$:

$$\Delta\phi = \Delta\phi_r + \Delta\phi_a = -\frac{4\pi}{\lambda} v_r \Delta T + 2\pi f_{DC} \Delta\eta \quad (1)$$

where λ is the radar wavelength, v_r represents the range velocity component due to surface motion (positive towards the satellite), ΔT represents the time difference (temporal baseline) between acquisitions, f_{DC} is the pixel's Doppler centroid frequency, and $\Delta\eta$ represents the azimuth position difference (misregistration) expressed in time units, which is in turn given by:

$$\Delta\eta = \Delta\eta_{motion} + \Delta\eta_{orb} + \Delta\eta_{iono} \quad (2)$$

where $\Delta\eta_{motion}$ is due to the underlying horizontal surface motion, and $\Delta\eta_{orb}$ and $\Delta\eta_{iono}$ represent respectively the contributions of orbital uncertainties and ionospheric propagation. The azimuth motion contribution is related to the azimuth velocity component v_a in an equivalent rectilinear geometry as follows:

$$\Delta\eta_{motion} = \frac{v_a \Delta T}{V_r} \tag{3}$$

where V_r is an effective velocity [26], which is in the order of 7100 m/s for remote sensing satellites in near-polar orbit. Range and azimuth velocities are related to the 3D ice velocity vector, $\mathbf{v} = \left[v_x, v_y, v_z\right]^T$ as follows:

$$\begin{bmatrix} v_r \\ v_a \end{bmatrix} = \begin{bmatrix} \cos\theta\cos\phi & \cos\theta\sin\phi & \sin\theta \\ -\sin\phi & \cos\phi & 0 \end{bmatrix} \begin{bmatrix} v_x \\ v_y \\ v_z \end{bmatrix} \tag{4}$$

where angles ϕ and θ describe the orientation of the line-of-sight (LoS) vector pointing from the pixel under consideration to the sensor, with the horizontal angle ϕ measured counter-clockwise from the y-axis of the map projection and the elevation angle θ measured from the ground to the LoS vector.

In the Stripmap case, f_{DC} in Equation (1) is at most a few hundred Hz for current yaw-steered SARs, and its variations between adjacent pixels amount to a small fraction of a Hz, causing $\Delta\phi_a$ and its spatial gradient to be negligible compared to $\Delta\phi_r$. However, for the TOPS acquisition mode, due to the azimuth antenna steering, the instantaneous Doppler centroid magnitude varies from Stripmap-like values at the burst center to as much as 2.6 kHz at the burst edges [16], where more importantly also a variation of up to 5.2 kHz occurs within one azimuth pixel. For a 6-day Sentinel-1 image pair, based on Equations (1)–(3), an azimuth motion v_a of 10 m/y will cause a maximum intra-burst $\Delta\phi_a$ variation from -0.12π rad at burst start to 0.12π rad at burst end, as well as a phase jump of 0.24π rad at the azimuth burst boundaries. If such a phase contribution were erroneously interpreted as being due to $\Delta\phi_r$ in Equation (1), this would lead to a maximum v_r error of 0.2 m/y. Furthermore, as pixel phase differences approach $+/-\pi$, errors amounting to integer multiples of 2π rad will arise in the unwrapped DInSAR phase, corresponding to integer multiples of 1.67 m/y in terms of v_r. This example shows that even for slow moving ice sheet areas, with horizontal ice motion magnitudes in the order of a few tens of m/y, the contribution of the azimuth phase term in Equation (1) should not be neglected.

The rationale of the algorithm we describe in Section 2.3.2 is to estimate the misregistration due to $\Delta\eta_{motion}$ in Equation (3) to reduce its contribution to Equation (1). The residual DInSAR phase can then be interpreted as being due to the range term $\Delta\phi_r$ alone, as for the Stripmap case, and scaled to yield the LoS velocity v_r. As a by-product, azimuth velocity v_a can also be accurately retrieved in the burst overlap regions.

2.3.2. Processing Algorithm

Our TOPS DInSAR algorithm is shown in Figure 2. Most steps are identical to those of a Stripmap DInSAR processor, albeit for a more complex coregistration approach detailed below. After image coregistration, the interferogram is formed from the mosaicked SLCs. We applied multilooking with a 15×3 averaging factor in range/azimuth (about 50×50 m on the ground) and a 10×2 decimation. Phase unwrapping is carried out using a Minimum Cost Flow algorithm with coherence-based weights [27], masking out results for areas with a coherence below 0.2. Finally, the unwrapped interferogram is scaled to yield a line-of-sight displacement map. A calibration is performed for each displacement map using the procedure described in Section 2.4 and Ground Control Points (GCPs) extracted from the PROMICE multi-year velocity mosaic (cfr. Section 2.1).

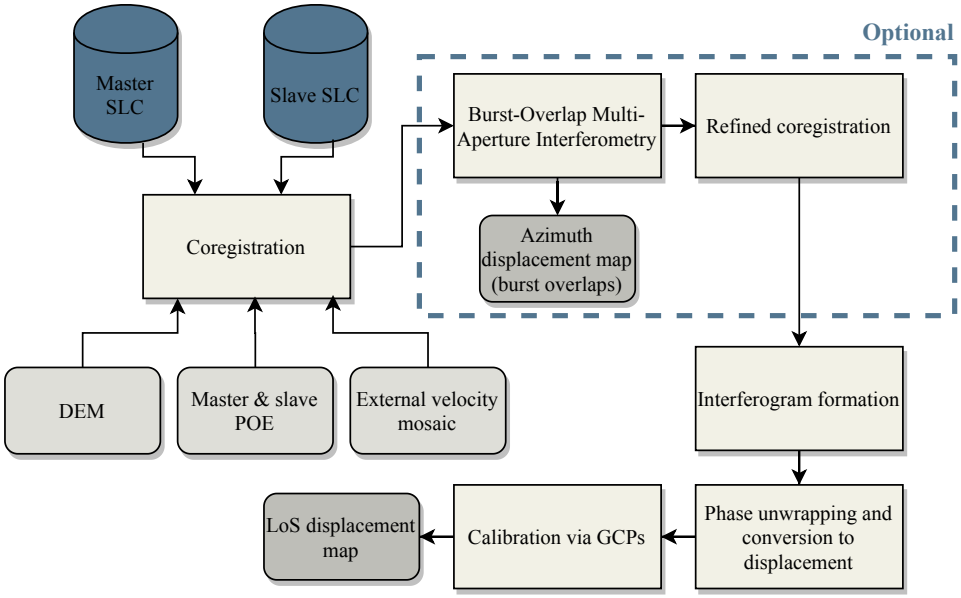

Figure 2. Block diagram showing the interferometric processing chain for a single Sentinel-1 Terrain Observation by Progressive Scans (TOPS) image pair.

Coregistration is based on a resampling lookup table containing the range and azimuth slave SLC coordinates corresponding to each master SLC pixel. The lookup table is computed using precise orbits and a DEM, as in the Stripmap case [28], but also an external ice velocity mosaic, consisting of maps of the horizontal ice velocity components v_x and v_y. Within the processor, the latter are scaled to obtain the displacement between the master and slave acquisitions, and projected onto the azimuth dimension of the master SLC image using the second line in Equation (4). The resulting azimuth motion map is then used to refine the slave azimuth coordinates in the resampling lookup table.

Since external ice velocity mosaics are based on spatially and temporally averaged SAR and/or optical measurements [8–11], they could fail to account for temporal variations in the ice motion patterns and other dataset-specific sources of azimuth misregistration, such as ionospheric streak contributions [29]. These limitations could be avoided in principle by estimating the azimuth misregistration directly from the image pair at hand, using several available techniques. We investigated the use of offset tracking and MAI, as proposed respectively by [17,19], and of Burst-Overlap MAI (BO-MAI), the implementation of which is detailed in Appendix A. For Sentinel-1 data, however, we find that the measurement accuracy of MAI, and even more that of offset tracking, are too low to be beneficial and are influenced by a swath-dependent azimuth registration bias between the Sentinel-1A/B imagery, as detailed further in Appendix A. In contrast, an additional refinement based on BO-MAI, consisting of the steps within the dashed rectangle in Figure 2, was found to provide a slight improvement ($<\pm 0.1$ m/y) compared to using the external ice velocity mosaic alone.

An application example of the above-mentioned coregistration approaches is shown in Figure 3. The wrapped DInSAR phase is shown in Figure 3a in the case of a Stripmap-like coregistration, based only on a DEM and precise orbits. Substantial phase jumps occur at almost every burst overlap, often exceeding 0.5–1.5 rad as seen in Figure 4a, which shows the average unwrapped azimuth phase gradient for sub-swath IW3. Locally the phase discontinuities may exceed several radians. Figure 3b shows the results when MAI azimuth velocity measurements (Figure A1c in Appendix A) are used to refine the coregistration. Surprisingly this worsens the phase discontinuities in the slow-moving areas of the ice sheet, which show roughly the same magnitude at each burst boundary (Figure 4b). This is due to a bias in the MAI and azimuth offset tracking measurements, when applied to S1A/S1B pairs, as discussed further in Appendix A. The effects of measurement noise, due to decorrelation, are also

seen in the top-left area of Figure A1c, while compared to the non-refined coregistration, several phase jumps located on the fast-flowing ice stream are actually reduced. Figure 3c shows the case of a refined coregistration based on the PROMICE multi-year velocity mosaic described in Section 2.1. This approach almost completely eliminates the phase jumps seen in Figure 3a,b (as shown in Figure 4c). Applying an additional coregistration refinement based on BO-MAI azimuth velocity measurements (Figure A1d) results in only minor changes that are barely noticeable (Figures 3d and 4d), albeit for the very first burst overlap in IW3. The case in which the azimuth coregistration is refined with intensity offset tracking measurements is not shown, since this yields very similar, although slightly noisier, results to those based on MAI, due to the similar properties of the azimuth velocity measurements provided by these methods (compare Figures A1b,c).

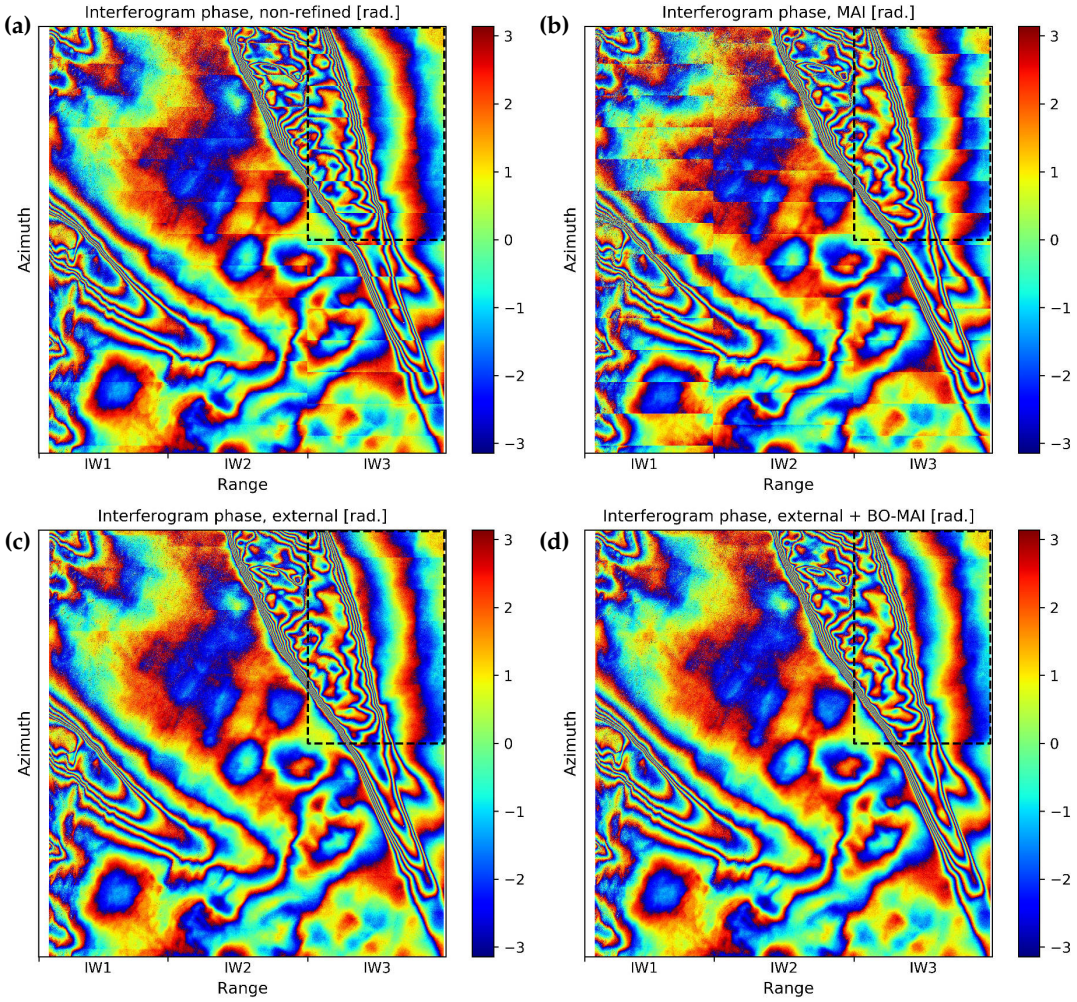

Figure 3. Wrapped DInSAR phase in radar geometry obtained using no azimuth coregistration refinement (**a**); a refinement based on Multi-Aperture Interferometry (MAI) (**b**); on the PROMICE multi-year velocity mosaic (**c**); and on the PROMICE multi-year velocity mosaic followed by Burst-Overlap (BO)-MAI (**d**). The dashed black rectangle indicates the region investigated in Figure 5. (Master/slave acquisitions: 22 December 2019 (S1A)/ 28 December 2019 (S1B), track: 112 descending)

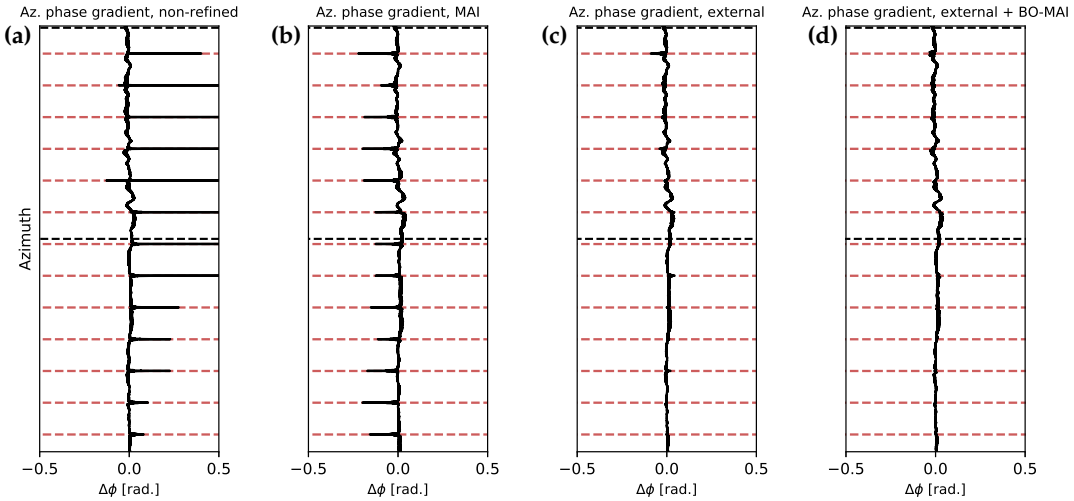

Figure 4. Average azimuth gradient of the unwrapped interferogram phase in sub-swath IW3 for each of the four processing approaches presented in Figure 3, i.e. using no azimuth coregistration refinement (**a**); a refinement based on Multi-Aperture Interferometry (MAI) (**b**); on the PROMICE multi-year velocity mosaic (**c**); and on the PROMICE multi-year velocity mosaic followed by Burst-Overlap (BO)-MAI (**d**) . The dashed red lines indicate the location of azimuth burst overlaps, while the dashed black lines indicate the region investigated in Figure 5.

To assess the impact of the wrapped phase discontinuities on the final DInSAR measurements, the phase of the interferograms shown in Figure 3 was unwrapped and scaled to obtain LoS velocities. Figure 5 shows a subset of the LoS velocity map obtained from each of the interferograms shown in Figure 3, omitting the poorly-performing MAI refinement case. The bottom plot of Figure 5 shows the line-of-sight velocity across the profile indicated by a dashed line in the three velocity maps. While the inclusion of the BO-MAI coregistration refinement yields a velocity profile that is indiscernible from solely applying the external ice velocity mosaic refinement, the non-refined case shows discontinuities up to 1.5 m/y near the azimuth burst overlaps. For an underlying v_a of 50 m/y, this is consistent with the discussion in Section 2.3.1. Note that in this case, the non-refined coregistration does not result in apparent phase unwrapping errors. In general, however, the unwrapping algorithm cannot be expected to reliably resolve phase ambiguities across the burst boundaries, and substantial unwrapping errors, leading to biases in the velocity measurements, may occur when applying the non-refined coregistration (see Figure S1 in the Supplementary Material).

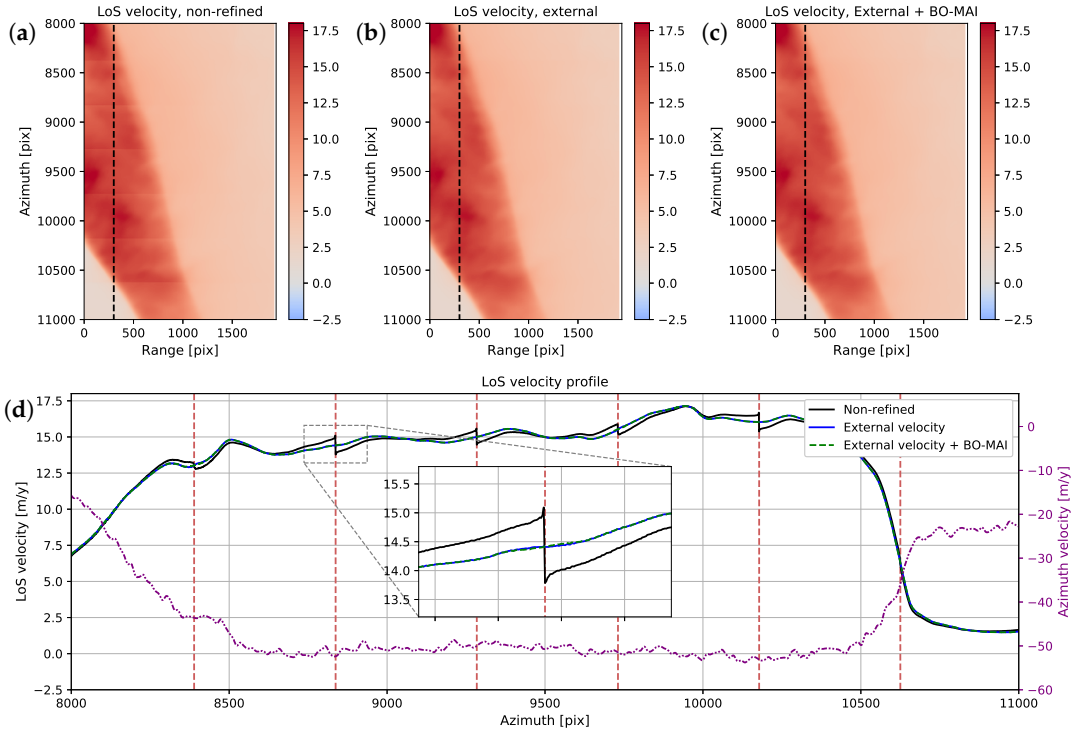

Figure 5. TOPS DInSAR line-of-sight velocity in radar geometry for the region within the dashed rectangle in Figure 3 obtained using no coregistration refinement (**a**), a refinement based on the PROMICE multi-year velocity mosaic (**b**), and on the PROMICE multi-year velocity followed by BO-MAI (**c**). Panel (**d**) shows line-of-sight and azimuth velocity (purple dashed line and right y-axis) along the profile indicated by the dashed line in (**a**–**c**). Azimuth velocities are based on the PROMICE multi-year mosaic.

2.4. Calibration and Error Estimation

Since DInSAR measures displacement relative to a reference point, namely the phase unwrapping seed, a calibration is required for each unwrapped interferogram in order to obtain absolute velocity estimates and to account for timing and orbit errors present in the radar data. The unknown absolute phase corresponds to a constant range offset, whereas orbit errors will result in slowly varying errors. In practice, it is difficult to separate the two effects, and we follow the approach in [30], modeling the unknown displacement as being due to a constant baseline error, and use GCPs to estimate the horizontal and vertical components of the error. Usually GCPs are selected in stationary areas (e.g., bedrock), but this approach has several problems with the present dataset. The region under consideration is an ice sheet bordered by steep mountainous terrain, with isolated bedrock areas separated by glaciers. The phase unwrapping algorithm is often not able to correctly unwrap across steep topography and ice/rock transitions, resulting in many of the stationary areas being prone to unwrapping errors. If GCPs are selected in such regions, the estimated velocity will be biased with respect to the ice-covered areas, affecting the overall calibration. Instead, we choose slow-moving GCPs on the ice sheet ($|v|$<18 m/y, corresponding to 0.05 m/d) from the PROMICE multi-year mosaic (Section 2.1), under the assumption that the velocity in such areas does not vary significantly with time. The error estimate of the calibrated displacement for each pixel is also carried out as described in [30], based on the interferometric coherence and the uncertainties of the GCP height and velocity estimates. The selected GCPs are shown in Figure 1a.

2.5. Fusion of Velocity Measurements

Both DInSAR and intensity offset tracking measure the radar components of ice velocity, DInSAR providing only the range (LoS) component, v_r, and offset tracking providing also the azimuth (along-track) component, v_a. In order to calculate the horizontal components of the Cartesian velocity vector, $\mathbf{v} = \left[v_x, v_y, v_z\right]^T$, we assume surface parallel flow, according to which $v_z = (\frac{\partial z}{\partial x} v_x + \frac{\partial z}{\partial y} v_y)$ [21], and use all available measurements (DInSAR, intensity offset tracking, or both) and Equation (4) to set up, for each output pixel, a weighted linear least squares problem, $\mathbf{u} = \mathbf{H}\mathbf{v} + \boldsymbol{\epsilon}$, which can be stated as:

$$\begin{bmatrix} v_{r1} \\ v_{a1} \\ \vdots \\ v_{rN} \\ v_{aN} \end{bmatrix} = \begin{bmatrix} \cos\theta_1 \cos\phi_1 + \sin\theta_1 \frac{\partial z}{\partial x} & \cos\theta_1 \sin\phi_1 + \sin\theta_1 \frac{\partial z}{\partial y} \\ -\sin\phi_1 & \cos\phi_1 \\ \vdots & \vdots \\ \cos\theta_N \cos\phi_N + \sin\theta_N \frac{\partial z}{\partial x} & \cos\theta_N \sin\phi_N + \sin\theta_N \frac{\partial z}{\partial y} \\ -\sin\phi_N & \cos\phi_N \end{bmatrix} \begin{bmatrix} v_x \\ v_y \end{bmatrix} + \boldsymbol{\epsilon} \tag{5}$$

where v_{rn} is the measured LoS velocity from pair number n and v_{an} is the corresponding azimuth velocity (not available for DInSAR measurements). The angles ϕ_n and θ_n describe the LoS vector for the master image of pair number n (cfr. Equation (4)). The local height gradient at the pixel under consideration, $(\frac{\partial z}{\partial x}, \frac{\partial z}{\partial y})$, is calculated numerically from the available DEM. The noise vector is assumed normally distributed with zero mean and diagonal covariance matrix Σ:

$$\Sigma = \begin{bmatrix} \sigma_{r1}^2 & 0 & \cdots & 0 \\ 0 & \sigma_{a1}^2 & \cdots & 0 \\ \vdots & \vdots & \ddots & \vdots \\ 0 & 0 & \cdots & \sigma_{aN}^2 \end{bmatrix} \tag{6}$$

with σ_{rn} and σ_{an} indicating the estimated standard deviations of the range and azimuth measurements for pair n. The weighted least squares solution to this system is:

$$\hat{\mathbf{v}} = (\mathbf{H}^T \boldsymbol{\Sigma}^{-1} \mathbf{H}) \mathbf{H}^T \boldsymbol{\Sigma}^{-1} \mathbf{u} \tag{7}$$

and the resulting covariance matrix of the estimate is $\mathbf{H}^T \boldsymbol{\Sigma}^{-1} \mathbf{H}$ from which the error estimates for $\hat{\mathbf{v}}$ can be retrieved as the diagonal elements.

The formulation above implies that for each pair, both range and azimuth measurements are available, but in case only DInSAR products are available, $\mathbf{u}$ and $\mathbf{H}$ will contain only rows with LoS measurements, and $\mathbf{H}$ may become ill-conditioned if the contributing DInSAR pairs are acquired from nearly parallel tracks. In the absence of azimuth velocity measurements, we thus require both ascending and descending LoS measurements to produce a valid output.

3. Results

3.1. SAR-Based Ice Velocity Mosaics

The intensity offset tracking method described in Section 2.2 was applied to all 12-day image pairs available in Table 1, which amount to three pairs per track. We found this to be the most favorable data selection for offset tracking, since the ice motion contribution in a six-day time span is often below the noise floor of offset tracking measurements, especially in the slow-moving regions, and also due to azimuth and range measurement biases affecting S1A/S1B pairs (cfr. Section 4 and Appendix A). The resulting horizontal ice velocity magnitude within the Zwally 2.1 drainage basin is shown in Figure 6a. Figure 6b shows also a different intensity offset tracking result, based solely on range intensity offset tracking. The two offset tracking results are quite similar, although the following differences can be noticed: (a) the range/azimuth map (Figure 6a) shows an improved coverage, since

a single ascending or descending track is sufficient to solve for the horizontal motion components in Equation (5), whereas an ascending/descending overlap is required for the range offset tracking case (Figure 6b); (b) the ionospheric streak contribution, for example, around (lat,lon)=(78N,42E), is absent in the range offset tracking mosaic (Figure 6b); (c) the latter shows a more prominent spatially-correlated noise pattern, particularly near the southern tip of the NEGIS, due to a known Level-1 processor block-processing effect affecting the range offsets, as discussed further in Section 4.

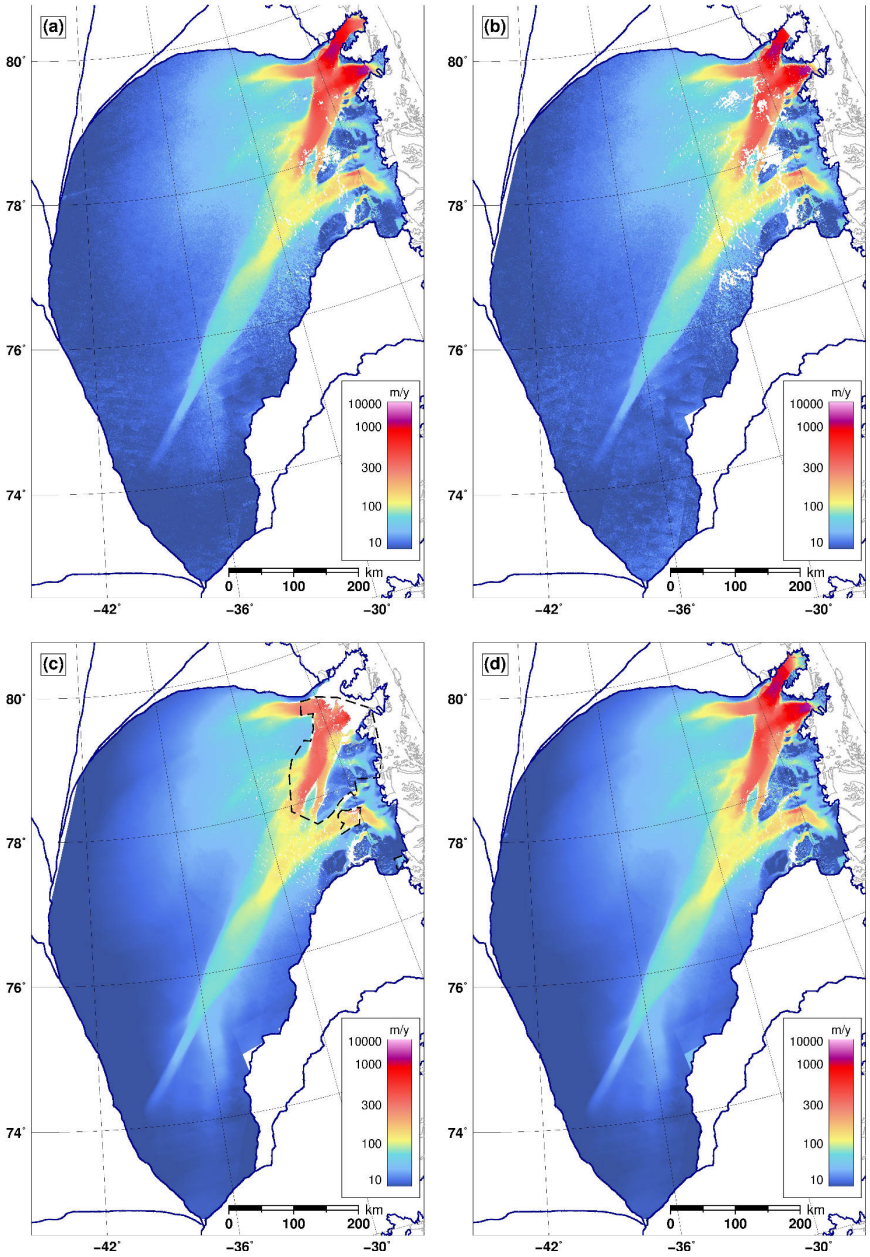

Figure 6. Horizontal velocity magnitude for Zwally drainage basin 2.1 [20] (dark blue polygons) based on (**a**) range/azimuth intensity offset tracking, (**b**) range intensity offset tracking, (**c**) the TOPS DInSAR approach presented in this paper, (**d**) the fusion (weighted average) of DInSAR and range/azimuth intensity offset tracking. The dashed polygons in panel (c) enclose DInSAR results that were discarded (cfr. Section 4) and not used in the generation of the fused result shown in panel (d).

Figure 6c shows the velocity magnitude obtained using the TOPS DInSAR approach outlined in Section 2.3, applied to all available six-day pairs in Table 1, which amount to five image pairs per track. This is the most favorable data selection for DInSAR, since it maximizes the temporal coherence and reduces the fringe rate in fast-flowing regions, improving the phase unwrapping results. The azimuth coregistration refinement (illustrated in Figure 2) was carried out using the PROMICE multi-year velocity mosaic as an external ice velocity mosaic, whereas the BO-MAI refinement was omitted since its contribution in this area of interest was found to be below 0.1 m/y. Compared to the offset tracking results one immediately notes the improvement in resolution, particularly in slow-moving regions where a much smoother pattern is observed. The DInSAR velocity product resolution is about 50×50 m on the ground, while the resolution of the offset tracking velocity products is, at best, the 560×560 m posting of the measurements. The velocity pattern at the upstream part of NEGIS appears much better resolved in the DInSAR product: the two sub-streams that merge into NEGIS and are barely visible in the offset tracking results are clearly resolved by DInSAR. Moving further downstream of NEGIS, one observes the main limitation of DInSAR, namely that velocity cannot be retrieved reliably on fast-flowing outlet glaciers. In Figure 7, we show the difference in velocity magnitude as obtained by DInSAR and range/azimuth offset tracking (Figure 6a) as well as the difference between DInSAR and the PROMICE multi-year velocity mosaic. Large spatially-correlated differences in velocity magnitude of >30 m/y are observed towards the outlet glacier fronts, and represent the typical signature of phase unwrapping errors [30]. In order to reduce the effect of phase unwrapping errors in the final velocity product, we discarded the DInSAR results within the regions indicated by the dashed polygons in Figure 6c. These polygons were generated manually, based on the comparison between DInSAR and the PROMICE multi-year velocity mosaic (Figure 7b).

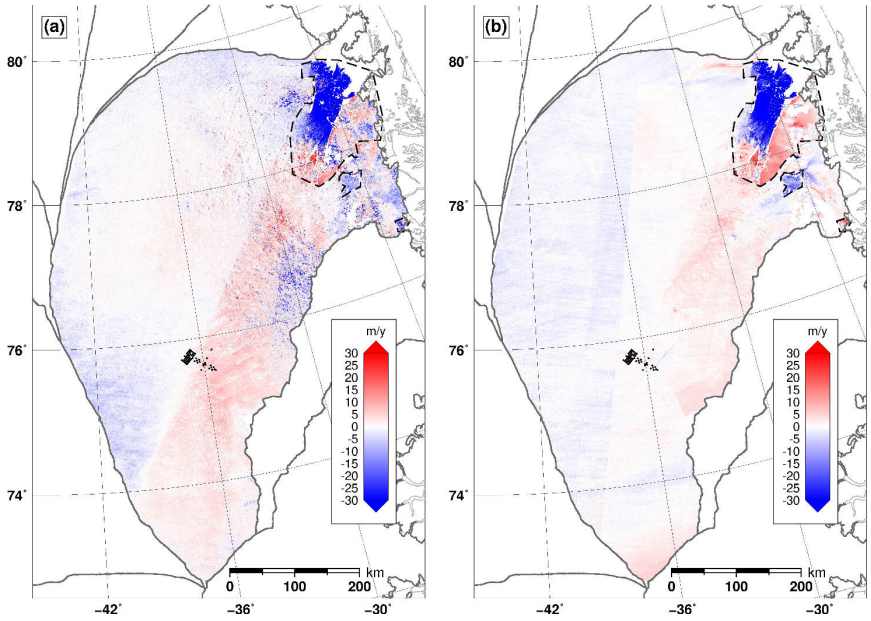

Figure 7. Velocity magnitude difference between: (**a**) DInSAR and range/azimuth offset tracking results (Figure 6a,c, respectively) (**b**) DInSAR and the PROMICE multi-year velocity mosaic (Figure 1a). The dashed polygons enclose DInSAR results that were discarded (cfr. Section 4). GPS measurements used for validation are shown as black dots. Zwally drainage basins [20] are traced in gray.

Figure 6d shows the final ice velocity magnitude mosaic obtained by the fusion of all DInSAR and range/azimuth intensity offset tracking measurements, as described in Section 2.5. In the interior parts, DInSAR dominates the fusion result, due to its lower standard deviation, and hence a velocity

pattern that is virtually identical to Figure 6c is observed. In faster flowing regions, such as some shear margins and the outer parts of the outlet glaciers, the fusion with offset tracking significantly improves the measurement coverage compared to DInSAR alone. The final spatial resolution and accuracy of the ice velocity mosaic is spatially variable, and the uncertainties provided by the framework of Section 2.5 account for variations in the data coverage, as well as for the difference in accuracy between DInSAR and offset tracking. Mosaics of the 1-σ uncertainties associated with the horizontal velocity components, σ_{v_x} and σ_{v_y}, are shown in Figure S2.

3.2. Validation

As validation, we compare the horizontal ice velocity measurements from each of the four SAR-based ice velocity mosaics in Figure 6 to available velocity measurements from EastGRIP GPS stakes (see Section 2.1). The GPS and radar data are in the same polar stereographic projection, and we compare the two horizontal components (v_x and v_y) separately. The results of the GPS comparison are shown in Figure 8 and a summary of error statistics (where the error is computed as $v_{SAR} - v_{GPS}$) is provided in Table 2. For the offset tracking cases we note a slightly better (i.e., lower) standard deviation of Δv_x when applying only range offsets, while the Δv_y standard deviation is lower when including azimuth offsets. This is not surprising, as the x and y directions are roughly aligned with the radar range and azimuth directions, respectively, at polar latitudes. Figure 8 shows the results for the DInSAR-only case, corresponding to Figure 6c, since the fused ice velocity mosaic in Figure 6d leads to a virtually identical comparison at the GPS locations, due to DInSAR measurements dominating the weighted fusion in Equation (5). This is also noted in Table 2, where the difference in error statistics between DInSAR and the DInSAR/offset tracking fusion is seen to be negligible. As expected, the DInSAR results show a substantially better agreement with GPS, compared to offset tracking. The standard deviation for Δv_x and Δv_y is 0.18 and 0.44 m/y—respectively, a factor four and factor five better than what was obtained with intensity offset tracking. In terms of bias, i.e., the mean of Δv_x and Δv_y, the DInSAR results show values of virtually zero for the v_x component and about -0.4 m/y for the v_y component, which is in the order of the error standard deviation. The low biases indicate that the DInSAR calibration procedure, utilizing GCPs in slow-moving areas of the ice sheet, has been successful, at least for the region in the vicinity of the GPS locations. For the offset tracking cases, biases of 2.8 m/y in range and $-5.2/-9.5$ m/y in azimuth are observed. The individual range and azimuth offsets were not calibrated, as we found a calibration based on a slowly-varying polynomial to generally introduce more errors than it resolves. The bias and standard deviation for Δv_y is higher for range-only offset tracking due to the reduced sensitivity to motion in the y direction, which is roughly aligned with azimuth.

Table 2. GPS comparison statistics. Columns show mean and standard deviation of Δv_x and Δv_y, which indicate the difference in velocity between SAR and GPS measurements, for each of the horizontal velocity components in m/y. 61 co-located GPS and SAR measurements were used in each case.

Method	Δv_x Mean	Δv_x Std.	Δv_y Mean	Δv_y Std.
PROMICE 2016–2019	−0.51	0.31	−0.83	0.74
OTR (range/azimuth)	2.80	0.80	−5.22	2.31
OTR (range only)	2.80	0.77	−9.53	2.64
DInSAR only	0.00	0.18	−0.41	0.44
DInSAR+OTR (range/azimuth)	0.02	0.18	−0.47	0.44

Figure 9 shows velocity magnitude profiles following the black and orange lines indicated in Figure 1b, for the range/azimuth offset tracking results (Figure 6a) and for DInSAR (Figure 6c) along with the PROMICE multi-year velocity mosaic. The profiles pass through several of the GPS locations and demonstrate the difference in terms of measurement bias between the DInSAR and offset tracking measurements (red and blue lines, respectively). Also, the difference in spatial resolution and error

variance between the different processing methods is apparent, with the offset tracking measurements varying several m/y over very short distances, while the DInSAR measurements generally show a smoother pattern. To verify the quality of the azimuth motion information used to refine the DInSAR coregistration, we also compare the PROMICE multi-year velocities with the GPS data. Although these are also based on intensity offset tracking, measurements have been averaged over several years, thus showing a smaller variance compared to the campaign offset tracking case. Compared to DInSAR however, the PROMICE multi-year mosaic shows a worse agreement with the GPS (see Table 2) and a worse spatial resolution, as seen in Figure 9.

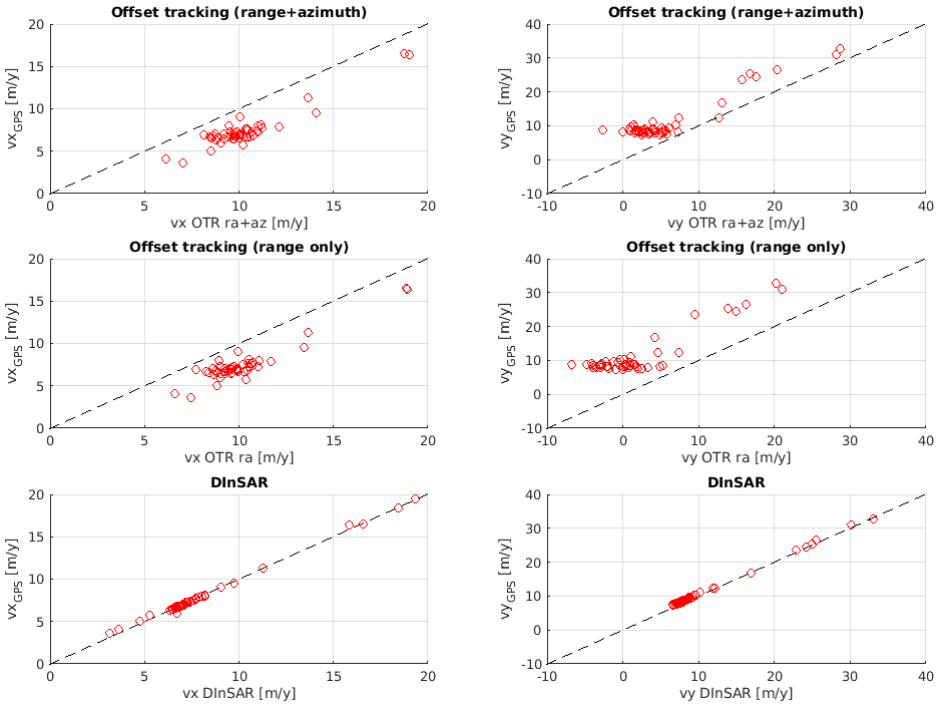

Figure 8. GPS comparison for the two horizontal velocity components v_x (**left column**) and v_y (**right column**) obtained via range/azimuth offset tracking (top row), range/range offset tracking (**middle row**), and DInSAR (**bottom row**). 61 GPS retrievals, acquired by EastGRIP, were used.

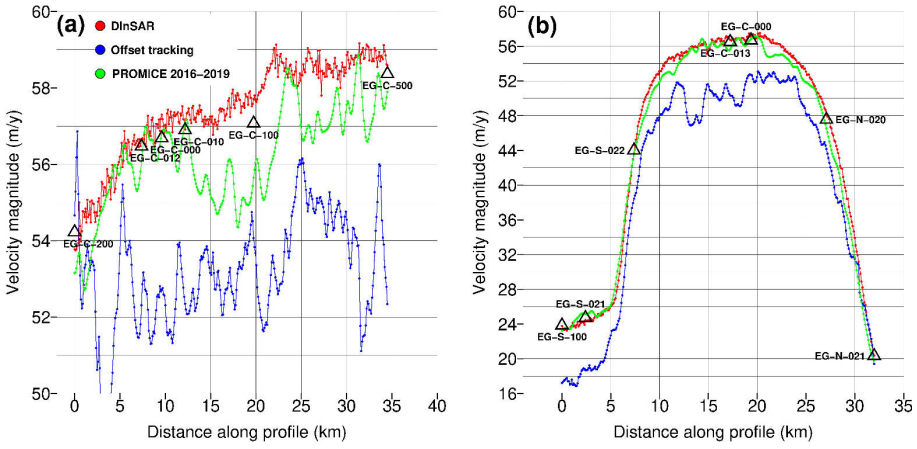

Figure 9. Velocity magnitude profiles for DInSAR (Figure 6c), range/azimuth offset tracking (Figure 6a), and the PROMICE multi-year mosaic (Figure 1a) along the black line (**a**) and the orange line (**b**) in Figure 1b.

4. Discussion

We have demonstrated a DInSAR processing scheme for Sentinel-1 TOPS ice velocity retrieval over a large drainage basin in Northeast Greenland. As expected, TOPS DInSAR provides accurate high resolution measurements in the slower-moving regions of the ice sheet, while offset tracking must still be used to obtain measurements over fast-flowing outlet glaciers. In general, refinement of the azimuth coregistration using the external PROMICE multi-year velocity mosaic was successful in reducing phase discontinuities at burst boundaries. For some image pairs we noted residual phase discontinuities even after applying such a refinement (e.g., Figure S3c), most likely due to ionospheric effects and to small biases in the PROMICE multi-year product towards the ice sheet interior (cfr. Figure 7b). The BO-MAI refinement often succeeded in reducing such residual discontinuities (e.g., Figure S3d), although the impact on the resulting velocity measurements was small ($\sim$0.1 m/y) in all the test cases we processed, which is why we denote BO-MAI as an optional step in our processing approach.

Aside from the improvement in spatial resolution and accuracy, the TOPS DInSAR velocity measurements also appear to be more immune to various data and/or processing artifacts affecting range and azimuth registration, but not the DInSAR phase. These include: (a) A sub-swath dependent bias (in the order of 15–30 m/y) affecting the MAI and azimuth offset tracking measurements from Sentinel-1A/1B or 1B/1A 6-day image pairs (see Appendix A); (b) An $\sim$10 m/y bias affecting range offset tracking measurements from Sentinel-1A/1B or 1B/1A 6-day image pairs (Figure S6c and Table S1, and Figure S8c and Table S3), which is consistent with the 15 cm average range misregistration observed between S1A and S1B SLC products in corner reflector experiments [31]; (c) An artifact observed in all range offset tracking measurements, presumably due to block-processing approximations of the Level-1 Sentinel-1 processor [32], which is the main cause of the "patchy" appearance of the slow-moving areas in the southern part of the Zwally 2.1 drainage basin in Figure 6a,b. Examples of the latter artifact are shown in Figures S6 and S8.

TOPS DInSAR velocity retrievals allow for improved analysis of ice dynamics and drainage. As the noise level in DInSAR retrievals is far lower than that obtained with offset tracking, it is generally not necessary to perform data stacking in order to achieve reliable velocity estimates. Hence, assuming frequent Sentinel-1 coverage, accurate velocity estimates can be generated on a sub-monthly time scale for the interior ice sheet, allowing for analysis with high spatial and temporal resolution, for example, monitoring intra-seasonal variations in ice dynamics. The improved ice velocity measurements also allow for improved estimates of strain rates in very high spatial and temporal resolution, thereby resolving the shear margins of fast flowing ice streams, where strain rates increase an order of magnitude over spatial scales of a few 100 m [23]. Ice velocity measurements are additionally applied in the evaluation of both surface mass balance (SMB) products and numerical ice sheet models. With more accurate estimates of the interior ice sheet velocity pattern, validation of SMB products and numerical ice sheet models becomes increasingly reliable [14,33,34].

The vast majority of the Greenland ice sheet moves with velocities <200 m/y and thus measurement accuracy and resolution could be greatly improved for ice sheet-wide velocity retrievals by routinely applying DInSAR along with intensity offset tracking. A pre-requisite to achieve DInSAR measurements of the quality described in this paper, is the availability of overlapping ascending and descending six-day acquisition pairs. In Greenland, this is currently limited to the winter acquisition campaigns and to areas of special interest, such as NEGIS, although the additional capacity provided by the forthcoming Sentinel-1C satellite could allow an increased availability of such data. From the processing point of view, the main challenges to be addressed in the design of an operational TOPS DInSAR/offset tracking processing scheme covering the entire Greenland ice sheet lie in (1) automatically discarding DInSAR measurements in areas prone to phase unwrapping errors; (2) consistently calibrating the DInSAR measurements; and (3) efficiently carrying out phase unwrapping of interferograms consisting of a large number of adjacent data slices, which can be challenging from the computational resource point of view, especially if network-based algorithms such as [27] are used.

A final note concerns the availability of external ice velocity mosaics to be used for the azimuth coregistration refinement in Figure 2. Although in this paper we relied on the PROMICE multi-year velocity mosaic, any Greenland-wide ice velocity mosaic of comparable accuracy could be used, such as those made available by [8–11]. If such a multi-year velocity mosaic is not available for a region of interest, one could in principle apply offset tracking (or MAI) to estimate the azimuth velocity prior to performing DInSAR. As mentioned in Section 2.3.2, however, the accuracy of offset tracking/MAI measurements based on only a single image pair was found to be too low to yield an adequate coregistration refinement. Hence, one would need to process an ensemble of acquisitions for the offset tracking/MAI azimuth velocity measurements to reach a noise level low enough to provide improvements over the simple geometric coregistration. Finally, since the fused DInSAR/offset tracking measurements show a better agreement with GPS compared to the PROMICE multi-year mosaic (cfr. Section 3.2), once the first ice sheet-wide velocity mosaics exploiting Sentinel-1 TOPS DInSAR are generated, these can be used as improved external ice velocity mosaics for the coregistration refinement within subsequent data processing.

5. Conclusions

Ice velocity measurements are frequently used for a host of different glaciological and climatological applications. With the launch of the Sentinel-1 satellites, the scientific community has been provided with an extensive SAR data coverage of the polar ice sheets. The contribution of this study is to demonstrate how the Sentinel-1 TOPS data archive can be further exploited by applying DInSAR processing in ice velocity retrieval. We present ice velocity measurements for the Zwally 2.1 Greenland drainage basin, applying TOPS DInSAR in the interior and intensity offset tracking over fast-flowing outlet glaciers. In comparison with available GPS measurements, the DInSAR ice velocity retrieval shows an accuracy that is four times better than that obtained by offset tracking, with standard deviations of 0.18 and 0.44 m/y in the x and y directions, respectively. Furthermore, the resolution of the DInSAR measurements are about 50 $\times$ 50 m on the ground, which is an order of magnitude better than what can be obtained with offset tracking.

In our DInSAR processing approach, image coregistration is refined by applying a correction in azimuth based on an external ice velocity mosaic and optionally an additional correction in burst overlaps using BO-MAI. With this refined coregistration approach, the TOPS-specific DInSAR challenges mainly related to phase discontinuities at the burst boundaries are overcome and the resulting DInSAR measurements are affected by the same coherence and phase unwrapping limitations that apply to Stripmap-mode DInSAR. Concerning the routine application of the method presented in this paper to the entire Greenland ice sheet, the main challenges lie in the integration of DInSAR and offset tracking measurements in areas which are more prone to phase unwrapping errors, and in the calibration of the DInSAR measurements. Also, these challenges, however, are well-known and are actually simplified compared to the Stripmap case, due to the wide coverage of the TOPS acquisition mode.

Supplementary Materials: The following are available online at http://www.mdpi.com/2072-4292/12/12/2014/s1, Figure S1: Line-of-sight velocity unwrapping error demonstration, Figure S2: 1σ uncertainties for the fused DInSAR and offset tracking mosaic, Figure S3: Wrapped interferograms demonstrating capabilities of BO-MAI coregistration refinement, Figure S4: Azimuth phase gradient for IW2 in S3, Figure S5: Azimuth velocity for descending image pair, Figure S6: Line-of-sight velocity for descending image pair, Figure S7: Azimuth velocity for ascending image pair, Figure S8: Line-of-sight velocity for ascending image pair, Table S1: GPS comparison for descending image pair, Table S2: Bias estimates for descending image pair, Table S3: GPS comparison for ascending image pair, Table S4: Bias estimates for ascending image pair.

Author Contributions: Conceptualization, J.P.M.B, J.K.A., and A.K.; methodology, J.K.A., J.P.M.B, and A.K.; software, A.K., and J.K.A.; validation, J.K.A., A.K, J.P.M.B, C.S.H, and A.G.; data curation, A.K., C.S.H., and A.G.; paper writing: J.K.A., J.P.M.B., A.K., and C.S.H. All authors have read and agreed to the published version of the manuscript.

Funding: This research was funded by DTU Space, Technical University of Denmark.

Acknowledgments: The PROMICE multi-year ice velocity mosaic was generated by Anne M. Solgaard, GEUS. Sentinel-1 data is provided by the EU Copernicus Programme, and processed by ESA. The GAMMA Remote Sensing and Consulting software [35,36] was used to build a prototype of the TOPS DInSAR processing scheme presented in Figure 2. This prototype processor was also used to generate the examples shown in Figures 3–5. The DTU Space inhouse interferometric processing software (IPP) was then used to build an operational TOPS DInSAR processor (currently omitting the additional BO-MAI refinement), which in turn was used to generate the results presented in Figures 6–9. All plots in geographic coordinates were created with the Generic Mapping Tools software Version 5.4.3 [37].

Conflicts of Interest: The authors declare no conflict of interest.

Appendix A. Azimuth Ice Velocity Measurements with Sentinel-1

The methods available to measure azimuth ground motion with Sentinel-1 TOPS data include: offset tracking, either based on coherence maximization [38] or on image amplitude as described in Section 2.2; Spectral Diversity, also known as MAI [39,40]; the method referred to in this paper as BO-MAI [41–43]. The latter two techniques exploit $\Delta\phi_a$ in Equation (1), by generating the following double-difference interferogram, the phase $\Delta\phi_{MAI}$ of which is given by:

$$\Delta\phi_{MAI} = \arg\{(M_u S_u^*)(M_l S_l^*)^*\} \tag{A1}$$

where $*$ denotes the complex conjugate, M and S denote master and slave SLC, and u and l denote forward- and backward-squinted acquisitions, respectively. An estimate of the azimuth misregistration $\Delta\eta$ in Equation (2) is given by:

$$\Delta\eta = \frac{\Delta\phi_{MAI}}{2\pi(f_u - f_l)} \tag{A2}$$

where f_u and f_l are the azimuth center frequencies of the forward- and backward-squinted SLCs, respectively. In MAI, the latter are generated via azimuth band-pass filtering of the master and slave acquisitions, exploiting the limited available azimuth bandwidth, which is about 325 Hz [16]. BO-MAI instead is applicable only within the azimuth burst overlap regions, where it exploits the large Doppler frequency separation created by the azimuth antenna steering. This varies between 4.4 kHz and 5.2 kHz depending on the image sub-swath [16], and thus provides a sensitivity to azimuth motion, which is an order of magnitude higher compared to MAI based on Equation (A2).

For the MAI implementation, the master and slave SLC images were deramped (i.e., basebanded), following the procedure described in [44], prior to band-pass filtering to generate forward- and backward-looking azimuth sub-bands. These were selected to have a bandwidth of 162 Hz (i.e., half the available azimuth bandwidth) each and a frequency separation of 162 Hz. The MAI processing approach described in [45] was then used, generating a full-resolution MAI interferogram and multi-looking with a factor of 20×5 in range and azimuth respectively, corresponding to 70×70 m on the ground. Finally, an adaptive phase filtering was carried out [46], with filter strength parameter $\alpha = 0.8$ and spectral estimation window size of 64×64 in range and azimuth, respectively. Phase unwrapping was not carried out since for Sentinel-1 6-day image pairs, azimuth velocities would have to be larger than ~ 1300 m/y in order to require phase unwrapping, and for such high displacements loss of coherence would hinder the retrieval of meaningful measurements anyway.

BO-MAI was implemented by forming the double-difference interferogram from the forward and backward squinted acquisitions for each azimuth burst overlap. A multi-looking of 12×3 in range/azimuth was applied (corresponding to about 50×50 m on the ground), followed by an adaptive filtering [46] with filter strength $\alpha = 0.8$ and spectral estimation window size of 8×8 in range/azimuth. The term $(f_u - f_l)$ in Equation (A2) was computed as the local difference in the instantaneous Doppler centroid frequencies within the burst overlap. Due to the much larger frequency separation in Equation (A2), ice motion of about 40 m/y is sufficient to cause the BO-MAI phase for a 6-day pair to exceed π rad, which would require phase unwrapping even for slow moving regions of the ice sheet. To avoid this delicate processing step, we generate the double-difference interferogram in Equation (A1) after applying the external ice-velocity mosaic to refine the coregistration lookup table,

as shown in Figure 2. This removes the bulk of the azimuth motion contribution, so that BO-MAI can be applied to the residual interferometric phase without the need for unwrapping. The final azimuth velocity estimate is obtained by adding back the motion contribution from the external ice velocity mosaic to the BO-MAI measurements.

Figure A1 presents azimuth velocity measurements for the scene shown in Figure 3, which have been derived from the azimuth projection of the PROMICE multi-year mosaic (a), intensity offset tracking (b), MAI (c), and BO-MAI (d). The BO-MAI measurements are spatially discontinuous, since they can only be carried out in the burst overlap regions, and clearly show the best agreement with the PROMICE multi-year mosaic. All measurements based on a single image pair, namely Figure A1b–d, are clearly affected by ionospheric streaks [29], which are instead significantly reduced in the PROMICE multi-year mosaic (Figure A1a) due to temporal and spatial averaging. A substantial part of the scene also shows significant loss of coherence for the MAI and offset tracking cases. Table A1 presents a comparison between each of the azimuth velocity retrievals shown in Figure A1 and the azimuth projection of the available GPS velocity measurements. The BO-MAI approach shows an accuracy that is comparable to the PROMICE multi-year mosaic, despite being based on only a single image pair (note also that only seven GPS measurements are co-located with burst overlaps for this image pair). Offset tracking and MAI are seen to yield substantially poorer accuracy, with standard deviations being in the order of 10 m/y.

Offset tracking and MAI also show an unexpected swath-dependent bias compared to BO-MAI and to the PROMICE multi-year mosaic, which is confirmed by the GPS comparison shown in Table A1. A similar azimuth bias was observed for all the processed 6-day pairs (Table 1), i.e., pairs consisting of one image from Sentinel-1A and one from Sentinel-1B, whereas it was never observed for 12-day pairs, i.e., S1A-S1A or S1B-S1B pairs (Figures S5 and S7). The magnitude of the bias depends on the sub-swath and was found to be between 15 and 30 m/y for 6-day image pairs, based on the average differences with respect to the PROMICE multi-year mosaic (see Table A2). The sign of the bias changes depending on whether the master image was acquired from Sentinel-1A or -1B (cfr. Figure S7, Tables S3 and S4), suggesting that it is caused by a relative azimuth misregistration between the S1A and S1B SLC products. Indeed our findings are consistent with the corner reflector experiment described in [31], which reports an average azimuth misregistration of 39 cm between S1A and S1B SLC products, based on reflectors located mainly within sub-swath IW1 and partly within IW2. This corresponds to an azimuth velocity bias of 23.7 m/y for a 6-day temporal baseline.

Concerning DInSAR, the use of the MAI measurements in Figure A1c within the coregistration refinement step in Figure 2 surprisingly increases the phase-discontinuities at the burst boundaries (Figure 3b) compared to a purely geometric coregistration approach (Figure 3a). Such discontinuities are instead reduced by using the azimuth-projected PROMICE multi-year mosaic (Figure A1a) and BO-MAI (Figure A1d), as shown in Figure 3c,d, respectively. A possible interpretation is that the S1A/S1B SLC azimuth misregistration bias concerns only the image amplitude, namely the observable in the corner reflector experiments and in intensity offset tracking, but not the image phase, which is the observable in BO-MAI and in DInSAR. The reason for observing this bias with MAI, which is also a phase-based technique, could be due to the effect of band-pass filtering, which creates a coupling between the existing amplitude misregistration and the interferometric phase.

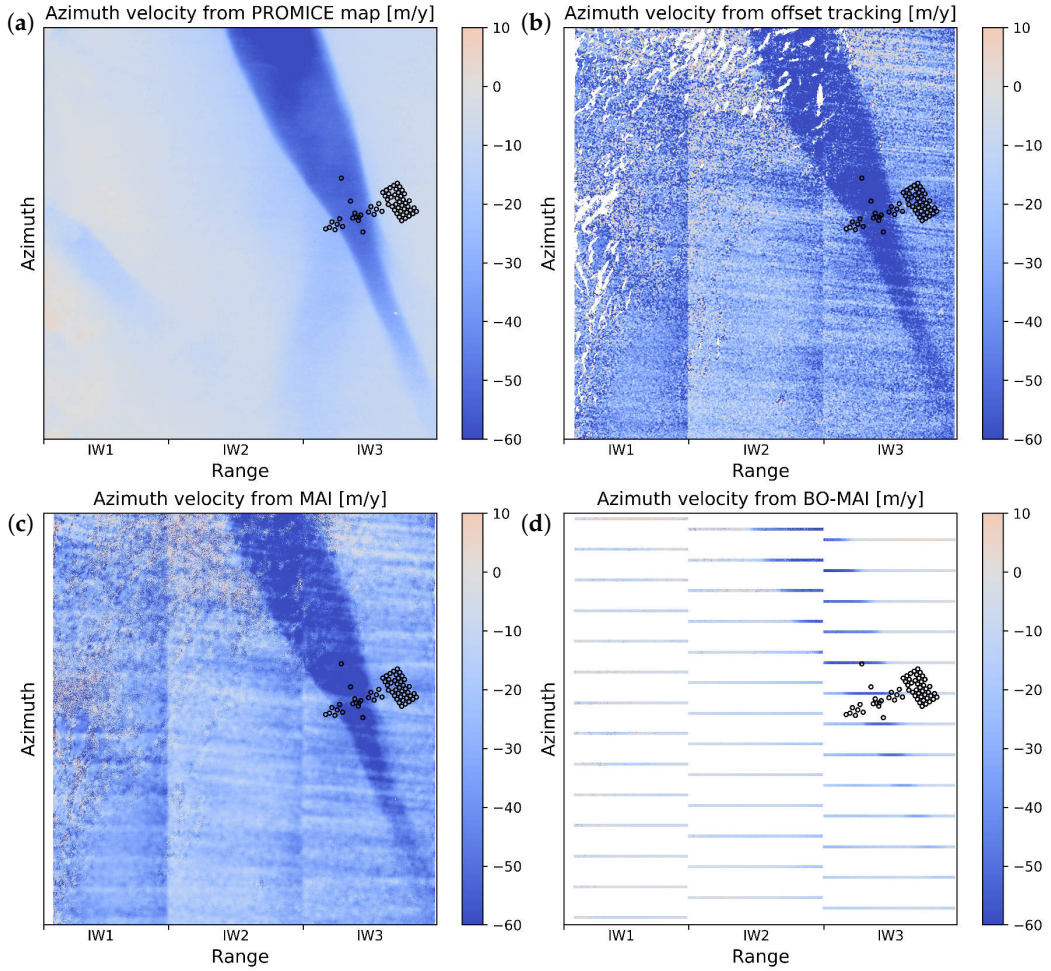

Figure A1. Azimuth velocity in radar geometry obtained from (**a**) re-projection of the PROMICE multi-year velocity mosaic; (**b**) azimuth intensity offset tracking on a single Sentinel-1 image pair; (**c**) Multi-Aperture Interferometry on a single Sentinel-1 image pair; and (**d**) Burst-Overlap Multi-Aperture Interferometry on a single Sentinel-1 image pair. The measurements in (**b**–**d**) are obtained from the same image pair shown in Figures 3–5. Black circles indicate GPS locations.

Table A1. GPS comparison statistics for the azimuth velocities shown in Figure A1. Columns show mean and standard deviation of Δv_{az}, which indicates the difference in velocity between SAR and GPS measurements in m/y. 61 co-located GPS and SAR measurements were used in each case, except for BO-MAI, as only 7 GPS measurements lay inside burst overlaps.

Method	Δv_{az} Mean	Δv_{az} Std.
PROMICE multi-year (offset tracking)	0.91	0.72
Azimuth offset tracking	−22.02	13.63
Multi-Aperture Interferometry (MAI)	−18.24	8.92
Burst-Overlap MAI (BO-MAI)	−0.79	1.10

Table A2. Mean difference in azimuth velocity for each sub-swath between the offset tracking, MAI, and BO-MAI results in Figure A1b–d and the PROMICE multi-year mosaic in Figure A1a. All values are in m/y.

	Δv_{az} Mean		
Method	**IW1**	**IW2**	**IW3**
Offset tracking (6-day)	−29.94	−16.80	−19.65
MAI (6-day)	−26.20	−13.63	−15.02
BO-MAI (6-day)	−1.13	1.11	0.73

References

1. Shepherd, A.; Ivins, E.; Rignot, E.; Smith, B.; van den Broeke, M.; Velicogna, I.; Whitehouse, P.; Briggs, K.; Joughin, I.; Krinner, G.; et al. Mass balance of the Greenland Ice Sheet from 1992 to 2018. *Nature* **2020**, *579*, 233–239. [CrossRef]
2. Box, J.E.; Colgan, W.T.; Wouters, B.; Burgess, D.O.; O'Neel, S.; Thomson, L.I.; Mernild, S.H. Global sea-level contribution from Arctic land ice: 1971–2017. *Environ. Res. Lett.* **2018**, *13*, 125012. [CrossRef]
3. Gray, A.; Mattar, K.; Vachon, P.; Bindschadler, R.; Jezek, K.; Forster, R.; Crawford, J. InSAR results from the RADARSAT Antarctic Mapping Mission data: Estimation of glacier motion using a simple registration procedure. In Proceedings of the IGARSS '98. Sensing and Managing the Environment, 1998 IEEE International Geoscience and Remote Sensing (Cat. No.98CH36174), Seattle, WA, USA, 6–10 July 1998; Volume 3, pp. 1638–1640. [CrossRef]
4. Strozzi, T.; Luckman, A.; Murray, T.; Wegmüller, U.; Werner, C.L. Glacier motion estimation using SAR offset-tracking procedures. *IEEE Trans. Geosci. Remote. Sens.* **2002**, *40*, 2384–2391. [CrossRef]
5. Goldstein, R.M.; Engelhardt, H.; Kamb, B.; Frolich, R.M. Satellite radar interferometry for monitoring ice sheet motion: Application to an Antarctic ice stream. *Science* **1993**, *262*, 1525–1530. [CrossRef] [PubMed]
6. Merryman Boncori, J.P.; Langer Andersen, M.; Dall, J.; Kusk, A.; Kamstra, M.; Bech Andersen, S.; Bechor, N.; Bevan, S.; Bignami, C.; Gourmelen, N.; et al. Intercomparison and Validation of SAR-Based Ice Velocity Measurement Techniques within the Greenland Ice Sheet CCI Project. *Remote Sens.* **2018**, *10*, 929. [CrossRef]
7. De Zan, F.; Guarnieri, A.M. TOPSAR: Terrain observation by progressive scans. *IEEE Trans. Geosci. Remote. Sens.* **2006**, *44*, 2352-2360. [CrossRef]
8. Nagler, T.; Rott, H.; Hetzenecker, M.; Wuite, J.; Potin, P. The Sentinel-1 mission: New opportunities for ice sheet observations. *Remote Sens.* **2015**, *7*, 9371-9389. [CrossRef]
9. PROMICE Scientific Data Portal: Sentinel-1 Greenland Ice Velocity, produced by GEUS and DTU Space. Available online: http://www.promice.org/PromiceDataPortal/ (accessed on 22 July 2020).
10. Joughin, I.; Smith, B.E.; Howat, I.M. A complete map of Greenland ice velocity derived from satellite data collected over 20 years. *J. Glaciol.* **2018**, *64*, 1–11. [CrossRef]
11. Mouginot, J.; Rignot, E.; Scheuchl, B.; Millan, R. Comprehensive annual ice sheet velocity mapping using Landsat-8, Sentinel-1, and RADARSAT-2 data. *Remote Sens.* **2017**, *9*, 364. [CrossRef]
12. Mouginot, J.; Rignot, E.; Scheuchl, B. Continent-wide, interferometric SAR phase, mapping of Antarctic ice velocity. *Geophys. Res. Lett.* **2019**, *46*, 9710–9718. [CrossRef]
13. Mouginot, J.; Rignot, E.; Bjørk, A.A.; van den Broeke, M.; Millan, R.; Morlighem, M.; Noël, B.; Scheuchl, B.; Wood, M. Forty-six years of Greenland Ice Sheet mass balance from 1972 to 2018. *PNAS* **2019**, *116*, 9239–9244. [CrossRef] [PubMed]
14. Smith-Johnsen, S.; De Fleurian, B.; Schlegel, N.; Seroussi, H.; Nisancioglu, K. Exceptionally high heat flux needed to sustain the Northeast Greenland Ice Stream. *Cryosphere* **2020**, *14*, 841–854. [CrossRef]
15. Prats-Iraola, P.; Scheiber, R.; Marotti, L.; Wollstadt, S.; Reigber, A. TOPS Interferometry with TerraSAR-X. *IEEE Trans. Geosci. Remote. Sens.* **2012**, *50*, 3179–3188. [CrossRef]
16. Yague-Martinez, N.; Prats-Iraola, P.; Gonzalez, F.R.; Brcic, R.; Shau, R.; Geudtner, D.; Eineder, M.; Bamler, R. Interferometric Processing of Sentinel-1 TOPS Data. *IEEE Trans. Geosci. Remote. Sens.* **2016**, *54*, 1–15. [CrossRef]

17. Scheiber, R.; Jager, M.; Prats-Iraola, P.; De Zan, F.; Geudtner, D. Speckle tracking and interferometric processing of TerraSAR-X TOPS sata for mapping nonstationary scenarios. *IEEE J. Sel. Top. Appl. Earth Obs. Remote. Sens.* **2014**, *8*, 1709–1720. [CrossRef]
18. Sánchez-Gámez, P.; Navarro, F.J. Glacier surface velocity retrieval using D-InSAR and offset tracking techniques applied to ascending and descending passes of sentinel-1 data for southern ellesmere ice caps, Canadian Arctic. *Remote Sens.* **2017**, *9*, 442. [CrossRef]
19. Scheuchl, B.; Mouginot, J.; Rignot, E.; Morlighem, M.; Khazendar, A. Grounding line retreat of Pope, Smith, and Kohler Glaciers, West Antarctica, measured with Sentinel-1a radar interferometry data. *Geophys. Res. Lett.* **2016**, *43*, 8572–8579. [CrossRef]
20. Antarctic and Greenland Drainage System. Zwally, J.H.; Giovinetto, M.B.; Beckley, M.A.; Saba, J.L. 2012. Available online: https://icesat4.gsfc.nasa.gov/cryo_data/ant_grn_drainage_systems.php (accessed on 22 July 2020)
21. Joughin, L.R.; Kwok, R.; Fahnestock, M.A. Interferometric estimation of three-dimensional ice-flow using ascending and descending passes. *IEEE Trans. Geosci. Remote. Sens.* **1998**, *36*, 25–37. [CrossRef]
22. Rizzoli, P.; Martone, M.; Gonzalez, C.; Wecklich, C.; Tridon, D.B.; Bräutigam, B.; Bachmann, M.; Schulze, D.; Fritz, T.; Huber, M.; Wessel, B.; Krieger, G.; Zink, M.; Moreira, A. Generation and performance assessment of the global TanDEM-X digital elevation model. *ISPRS J. Photogramm. Remote Sens.* **2017**, *132*, 119–139. [CrossRef]
23. Hvidberg, C.S.; Grinsted, A.; Dahl-Jensen, D.; Khan, S.A.; Kusk, A.; Andersen, J.K.; Neckel, N.; Solgaard, A.; Karlsson, N.B.; Kjær, H.A.; Vallelonga, P. Surface velocity of the Northeast Greenland Ice Stream (NEGIS): Assessment of interior velocities derived from satellite data by GPS. *Cryosphere Discuss.* **2020**, *2020*, 1–27. [CrossRef]
24. Kusk, A.; Boncori, J.; Dall, J. An automated system for ice velocity measurement from SAR. In Proceedings of the 12th European Conference on Synthetic Aperture Radar (EUSAR 2018), Aachen, Germany, June 4-7 2018; pp. 929–932.
25. Westerweel, J.; Scarano, F. Universal outlier detection for PIV data. *Exp. Fluids* **2005**, *39*, 1096–1100. [CrossRef]
26. Cumming, I.G.; Wong, F.H. *Digital Processing of Synthetic Aperture Radar Data: Algorithms and Implementation*; Artech House: Norwood, MA, USA, 2005.
27. Mario Costantini, T. A novel phase unwrapping method based on network programming. *IEEE Trans. Geosci. Remote. Sens.* **1998**, *36*, 813–821. [CrossRef]
28. Sansosti, E.; Berardino, P.; Manunta, M.; Serafino, F.; Fornaro, G. Geometrical SAR image registration. *IEEE Trans. Geosci. Remote. Sens.* **2006**, *44*, 2861–2870. [CrossRef]
29. Gray, A.L.; Mattar, K.E.; Sofko, G. Influence of Ionospheric Electron Density Fluctuations on Satellite Radar Interferometry. *Geophys. Res. Lett.* **2000**, *27*, 1451–1454. [CrossRef]
30. Mohr, J.J.; Boncori, J.P.M. An error prediction framework for interferometric SAR data. *IEEE Trans. Geosci. Remote. Sens.* **2008**, *46*, 1600–1613. [CrossRef]
31. Gisinger, C.; Balss, U.; Breit, H.; Schubert, A.; Garthwaite, M.; Small, D.; Gruber, T.; EinedeR, M.; Fritz, T.; Miranda, N. Recent Findings on the Sentinel-1 Geolocation Accuracy Using the Australian Corner Reflector Array. In Proceedings of the 2018 IEEE International Geoscience and Remote Sensing Symposium, Valencia, Spain, 22–27 July 2018, pp. 6356–6359.
32. De Zan, F. (German Aerospace Center, Oberpfaffenhofen, Germany). Personal Communication, 2019.
33. Hvidberg, C.S.; Keller, K.; Gundestrup, N.S.; Tscherning, C.C.; Forsberg, R. Mass balance and surface movement of the Greenland ice sheet at summit, Central Greenland. *Geophys. Res. Lett.* **1997**, *24*, 2307–2310. [CrossRef]
34. Mottram, R.; Simonsen, S.; Høyer Svendsen, S.; Barletta, V.; Sørensen, L.; Nagler, T.; Wuite, J.; Groh, A.; Horwath, M.; Rosier, J.; et al. An Integrated View of Greenland Ice Sheet Mass Changes Based on Models and Satellite Observations. *Remote Sens.* **2019**, *11*, 1407. [CrossRef]
35. Werner, C.; Wegmüller, U.; Strozzi, T.; Wiesmann, A. *GAMMA SAR and Interferometric Processing Software*; (Special Publication) ESA SP; European Space Agency: Frascati, Italy, 2000.
36. Wegmüller, U.; Werner, C.; Strozzi, T.; Wiesmann, A.; Frey, O.; Santoro, M. Sentinel-1 Support in the GAMMA Software. *Procedia Comput. Sci.* **2016**, *100*, 1305-1312. [CrossRef]

37. Wessel, P.; Smith, W.H.F.; Scharroo, R.; Luis, J.; Wobbe, F. Generic Mapping Tools: Improved Version Released. *Eos Trans. Am. Geophys. Union* **2013**, *94*, 409–410. [CrossRef]
38. Derauw, D. *DInSAR and Coherence Tracking Applied to Glaciology: The Example of Shirase Glacier*; (Special Publication) ESA SP; European Space Agency: Frascati, Italy 2000.
39. Scheiber, R.; Moreira, A. Coregistration of interferometric SAR images using spectral diversity. *IEEE Trans. Geosci. Remote. Sens.* **2000**, *38*, 2179–2191. [CrossRef]
40. Bechor, N.B.; Zebker, H.A. Measuring two-dimensional movements using a single InSAR pair. *Geophys. Res. Lett.* **2006**, *33*, L16311. [CrossRef]
41. Grandin, R.; Klein, E.; Métois, M.; Vigny, C. Three-dimensional displacement field of the 2015 Mw8.3 Illapel earthquake (Chile) from across- and along-track Sentinel-1 TOPS interferometry. *Geophys. Res. Lett.* **2016**, *43*, 2552–2561. [CrossRef]
42. Jiang, H.; Feng, G.; Wang, T.; Bürgmann, R. Toward full exploitation of coherent and incoherent information in Sentinel-1 TOPS data for retrieving surface displacement: Application to the 2016 Kumamoto (Japan) earthquake. *Geophys. Res. Lett.* **2017**, *44*, 1758–1767. [CrossRef]
43. Jiang, H.J.; Pei, Y.Y.; Li, J. Sentinel-1 TOPS interferometry for along-track displacement measurement. In Proceedings of the IOP Conference Series: Earth and Environmental Science, Beijing, China, 16–17 May 2017, p. 012019. [CrossRef]
44. Miranda, N. *Definition of the TOPS SLC Deramping Function for Products Generated by the S-1 IPF (Technical Note COPE-GSEG-EOPG-TN-14-0025, Issue 1, Rev. 3)*; Technical Report; European Space Agency: Frascati, Italy, 2017.
45. Merryman Boncori, J.P.; Pezzo, G. Measuring the north–south coseismic displacement component with high-resolution multi-aperture InSAR. *Terra Nova* **2015**, *27*, 28–35. [CrossRef]
46. Goldstein, R.M.; Werner, C.L. Radar interferogram filtering for geophysical applications. *Geophys. Res. Lett.* **1998**, *25*, 4035–4038. [CrossRef]

A.2 Burst overlap coregistration for Sentinel-1 TOPS DInSAR ice velocity measurements

This appendix provides the full manuscript:

A. Kusk, J. K. Andersen, and J. P. M. Boncori, Burst overlap coregistration for Sentinel-1 TOPS DInSAR ice velocity measurements, *IEEE Geoscience and Remote Sensing Letters*, vol. 19, pp. 1–5, 2021, doi:10.1109/LGRS.2021.3062905 (2021) [©2021 IEEE, reprinted with permission]

Burst Overlap Coregistration for Sentinel-1 TOPS DInSAR Ice Velocity Measurements

Anders Kusk, Jonas Kvist Andersen, and John Peter Merryman Boncori

***Abstract*— The application of Sentinel-1 interferometry to ice velocity measurements has until recently been limited by the significant horizontal scene motion associated with ice flow, which causes phase discontinuities (and associated unwrapping problems) at burst boundaries in Terrain Observation by Progressive Scans (TOPS) interferograms. Coregistering with a multiyear averaged external velocity mosaic based on offset-tracking can account for the bulk of the ice motion, but residual discontinuities sometimes remain, for example, due to seasonal variations in the ice velocity, or due to error sources such as azimuth shifts caused by ionospheric propagation. The presented method extends the external velocity coregistration with a local, spatially varying, coregistration in the burst overlap regions. This is based on the extended spectral diversity principle, which can only be applied in the overlap regions, but offers superior accuracy and resolution compared with traditional coregistration methods. The method considerably reduces phase discontinuities at burst boundaries, and potential new phase discontinuities at the overlap region edges are suppressed by an azimuth tapering of the applied coregistration shifts. An example scene is presented, and the phase discontinuities before and after application of the method are evaluated. The method is seen to remove phase discontinuities, with no adverse effects.**

***Index Terms*— Ice velocity, radar interferometry, Sentinel-1 (S1), synthetic aperture radar (SAR), Terrain Observation by Progressive Scans SAR (TOPSAR).**

I. Introduction

OPERATIONAL land ice velocity retrieval from Sentinel-1 (S1) Interferometric Wideswath (IW) radar data has until recently been limited to using amplitude-based methods such as offset-tracking [1]–[3]. This is due to the coupling between interferometric phase and azimuth misregistration, which is not negligible as in the Stripmap case. The Terrain Observation by Progressive Scans (TOPS) acquisition mode used by the Sentinel-1 synthetic aperture radar (SAR) instrument achieves a wide swath coverage by acquiring data in bursts, during which the antenna beam is electronically steered from aft to forward looking. This ensures that each target is imaged by the same part of the antenna pattern but leads to an azimuth-varying Doppler centroid. If, for some reason, an azimuth misregistration is present between the two images, this shift is projected on to the line-of-sight (LOS) vector and contributes to the observed interferometric phase by an amount φ_a [4]

$$\varphi_a = 2\pi f_{\mathrm{DC}}(\eta)\Delta\eta \tag{1}$$

where η is the azimuth time, $f_{\mathrm{DC}}(\eta)$ is the local Doppler centroid, and $\Delta\eta$ is the azimuth misregistration (in seconds). The local Doppler centroid includes both the effects of the TOPS beam steering and the physical antenna pointing, the latter contribution being close to zero due to the yaw steering implemented for Sentinel-1. This leads to phase variations within each burst and to jumps at burst boundaries, where the local Doppler centroid changes abruptly. An example of this is seen in Fig. 1(a). In turn, this introduces a phase bias in subsequent ice velocity measurements, both directly and indirectly, by inducing phase unwrapping errors, if the magnitude of such phase jumps approaches π rad. Azimuth misregistration can arise from orbit errors, ionospheric-induced azimuth shifts, and actual azimuth motion between the two SAR acquisitions, which are interfered. For ice sheets and glaciers, the motion contribution is nonnegligible and spatially varying and must be corrected [5]. In [6], speckle-tracking followed by spectral diversity (SD) was applied to TerraSAR-X data to estimate the spatially varying azimuth misregistration over each burst and refine the coregistration. For S1 IW data with a six-day baseline, this approach was found in [5] to be hampered by significant swath-dependent biases [7] in the geolocation of S1A and S1B products, and by the limited azimuth bandwidth available within an IW image burst. In [5], it was proposed to apply an external ice velocity mosaic, based on a multiyear average of offset-tracking measurements, to remove the bulk part of the misregistration due to ice motion. An example is shown in Fig. 1(b), where the external velocity has been used for range and azimuth coregistration, but not to flatten the phase. For many scenes, this is enough to reduce the burst boundary discontinuities to acceptable levels, but in some scenes, orbital errors, ionospheric shifts, or residual azimuth motion (due to trends or seasonal variations in the ice velocity) can still lead to discontinuities. It is proposed in [5] in these cases to reduce the residual phase jumps by applying a local SD coregistration in the burst overlap regions (burst overlap SD, or BO-SD), exploiting the large difference in the local Doppler centroid observed between the end of a burst and the start of the subsequent burst. This approach is further investigated and extended in this letter.

II. Methods

A. SD Coregistration

In the SD approach [8], the azimuth misregistration of two complex single look complex image (SLC) images, M and

Manuscript received November 17, 2020; revised January 8, 2021 and February 10, 2021; accepted February 24, 2021. Date of publication March 15, 2021; date of current version December 22, 2021. This work was supported in part by the European Space Agency (ESA) under Contract 4000129620/19/I-DT, awarded to the Phase-Based Sentinel-1 Ice Velocity (PHAB-IV) proposal in response to the ESA Earth Observation (EO) Science for Society Permanently Open Call. *(Corresponding author: Anders Kusk.)*

The authors are with the Danish National Space Institute, Technical University of Denmark, 2800 Kongens Lyngby, Denmark (e-mail: ak@space.dtu.dk).

Digital Object Identifier 10.1109/LGRS.2021.3062905

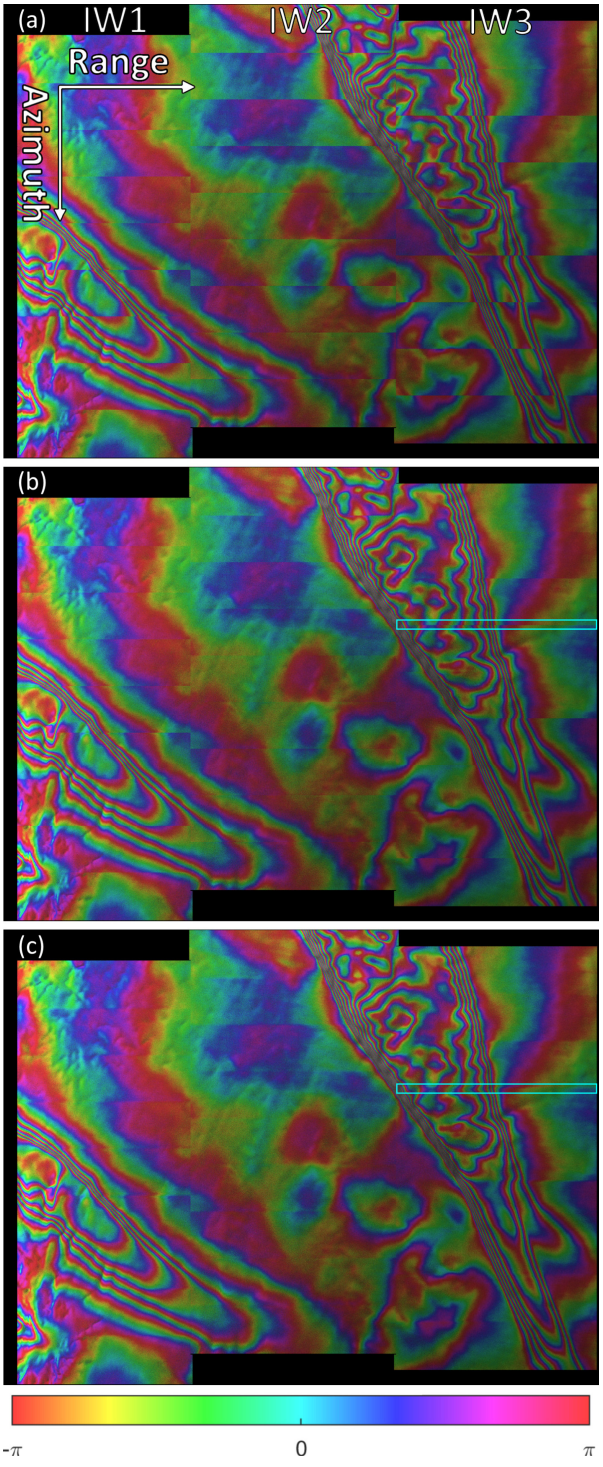

Fig. 1. Sentinel-1 interferograms (12 × 3 looks) of the NEGIS with various levels of refinement. (a) Interferogram coregistered only with orbits and digital elevation model (DEM). (b) Interferogram coregistered additionally with external velocity. (c) Interferogram coregistered with external velocity + BO-SD. The blue rectangles indicate the overlap region used for the plots in Fig. 3. The images were acquired from track 112 (descending) on January 14 and 20, 2019.

S, is estimated in three steps by: 1) bandpass filtering each image using two subbands centered about an upper and a lower center frequency, f_u and f_l; 2) generating upper and lower interferograms between the corresponding image subbands; and 3) forming the differential interferogram between the upper and lower subband interferograms with a phase, $\Delta\varphi_{\mathrm{SD}}$, given by

$$\Delta\varphi_{\mathrm{SD}} = \arg\left\{\left(M_u S_u^*\right)\left(M_l S_l^*\right)^*\right\}. \tag{2}$$

The azimuth misregistration estimate, $\Delta\hat{\eta}$ (in seconds), then becomes

$$\Delta\hat{\eta} = \frac{\Delta\varphi_{\mathrm{SD}}}{2\pi\left(f_u - f_l\right)}. \tag{3}$$

For S1 IW imagery, the available azimuth bandwidth B_a within each burst is around 325 Hz [4], thus limiting the optimal subband frequency difference to about 2/3 of this value [9]. In burst overlap regions, an enhanced SD (ESD) technique can be applied [10], which exploits the Doppler centroid difference between the adjacent bursts, yielding a bandwidth up to 5.2 kHz [4], with a corresponding increase in sensitivity relative to standard SD. The BO-SD approach described in this letter can be considered a spatially varying version of the ESD technique.

B. Motion Errors Due to Misregistration

When using the standard SD azimuth shift estimate to locally coregister the images, using the optimal frequency separation derived in [9], the uncertainty in the shift estimate translates into a phase bias uncertainty through (1) and (3), depending on the local Doppler centroid

$$\begin{aligned}\sigma_{\varphi_a,\mathrm{SD}} &= 2\pi\, f_{\mathrm{DC}}(\eta)\frac{\sigma_{\varphi_{\mathrm{SD}}}}{2\pi\,\frac{2}{3}B_a} \\ &= 2\cdot\frac{f_{\mathrm{DC}}(\eta)}{B_a}\cdot\sqrt{\frac{27}{16N_{\mathrm{eff}}}}\frac{\sqrt{1-\gamma^2}}{\gamma}\end{aligned} \tag{4}$$

where B_a is the processed azimuth bandwidth, N_{eff} is the number of independent looks averaged, γ is the interferometric coherence, and the expression for $\sigma_{\varphi_{\mathrm{SD}}}$ is based on (5) in [10]. The exact relation between the number of independent looks N_{eff} and the number of multilooked pixels depends on the spectral properties of the focused SAR imagery and on the implementation of the multilooking filter.

With BO-SD in the burst overlap region, the phase bias uncertainty becomes [10]

$$\begin{aligned}\sigma_{\varphi_a,\mathrm{BO-SD}} &= 2\pi\, f_{\mathrm{DC}}(\eta)\cdot\frac{\sigma_{\varphi_{\mathrm{BO-SD}}}}{2\pi\,\Delta f_{\mathrm{DC}}} \\ &= \frac{1}{2\sqrt{N_{\mathrm{eff}}}}\frac{\sqrt{1-\gamma^2}}{\gamma} \\ &= \frac{B_a}{3\,f_{\mathrm{DC}}(\eta)}\cdot\frac{\sigma_{\varphi_a,\mathrm{SD}}}{\sqrt{3}}\end{aligned} \tag{5}$$

where it is assumed that in the overlap region, $\Delta f_{\mathrm{DC}} \cong 2\,f_{\mathrm{DC}}(\eta)$. From (4) and (5), it can be seen that at the burst edges, the phase bias uncertainty of the BO-SD estimate is about 40 times smaller compared with the SD one.

If the phase contribution due to azimuth coregistration errors is interpreted as motion, the LOS velocity uncertainty is given by

$$\sigma_{v_{\mathrm{los}}} = \frac{1}{\Delta T}\cdot\frac{\lambda}{4\pi}\cdot\sigma_{\varphi_a} \tag{6}$$

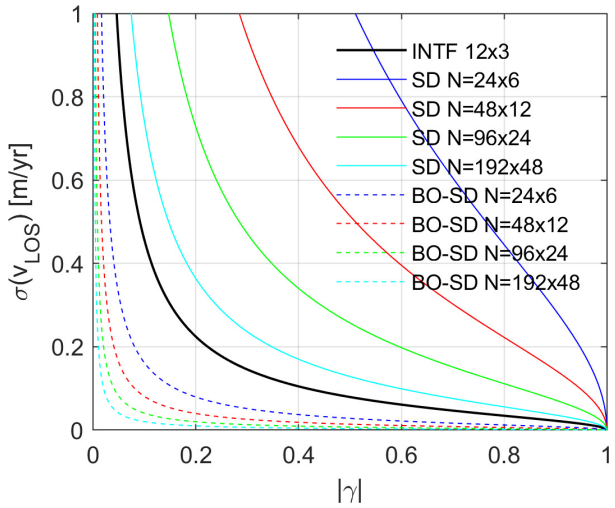

Fig. 2. Standard deviation of the LOS velocity bias estimate at the burst edge, from standard SD and BO-SD for various averaging window sizes. The parameters of IW2 have been used for local Doppler centroid and effective number of looks calculation, and a temporal baseline of six days is assumed. For reference, the black line indicates the noise of the interferogram LOS estimate multilooked with a 12×3 window.

where ΔT is the time difference between acquisitions (temporal baseline), and λ is the radar wavelength (5.55 cm for Sentinel-1).

In Fig. 2, the plots of the LOS velocity uncertainty (at burst edges, swath IW2) implied by (4)–(6), assuming a six-day temporal baseline, are shown for different multilooking window sizes. As a reference, the LOS uncertainty from the interferogram phase noise, corresponding to a 12×3 multilooking window, which was used to generate the interferograms in Fig. 1, is shown. To achieve a noise level just comparable with such an interferogram using the SD approach, a window larger than 192×48 in slant range and azimuth, respectively, corresponding to 670 m $\times$ 670 m on ground, is required at the burst edges. If BO-SD is used, significantly smaller averaging windows can be used and the LOS velocity errors can be reduced to less than 0.1 m/year using a 24×6 window, corresponding to about 85 m $\times$ 85 m on ground, even for quite low coherence levels. This increased spatial resolution is very welcome since it provides a sensitivity to the variations in the underlying ice motion and to spatially varying azimuth coregistration errors due to ionospheric propagation [11].

In addition, the BO-SD coregistration is not affected by the swath-dependent azimuth biases observed when applying standard SD to S1A-S1B or S1B-S1A image pairs, as detailed in [5, Appendix A]. These amount to azimuth misregistrations ranging between 37 and 75 μs in terms of azimuth time $\Delta\eta$, which lead to spatially varying interferometric phase errors through (1) and in turn to LOS velocity errors through (6). These values are consistent with geolocation biases measured in [7], but to the knowledge of the authors, the source of these biases has not been established at the time of writing.

C. Phase Unwrapping Requirements

The high sensitivity of the BO-SD phase to azimuth misregistration makes it susceptible to wrapping, since a shift of just 0.05 pixels, corresponding to 40 m/year for a six-day pair, will cause the BO-SD phase to exceed π radians at the burst edges. Although periodogram estimation methods could be applied to the wrapped phase, as suggested in [4] concerning ESD, their accuracy is insufficient for the application at hand, in which such estimates must be carried out locally, rather than on a burst- or image-wide basis. A more practical approach is to account for the bulk of the motion contribution to azimuth misregistration, using *a priori* information. For slow-moving regions in the interior of polar ice sheets, this can be provided by multiyear averaged external velocity products based on amplitude offset-tracking [5]. Of course, for regions with seasonal variations in the order of 40 m/year, such an approach would not be viable. However, such areas are likely to be fast-moving glaciers, which are not candidates for interferometric SAR (InSAR) anyway.

Azimuth shifts induced by ionospheric activity may in extreme cases exceed 0.05 pixels [11] and in principle require unwrapping. Such shifts are typically confined to narrow "streaks," which would lead to localized differential InSAR (DInSAR) phase errors both with and without the application of BO-SD.

III. Processing Algorithm

The TOPS InSAR processing chain used in the following is described in detail in [5]. The two SLCs are initially coregistered burst by burst using a resampling lookup table (LUT) based on precise orbits, a DEM, and an external ice velocity mosaic. The BO-SD procedure is then carried out in each burst overlap region, by forming interferograms for each burst, applying phase averaging (early multilooking, see [12]), and forming the differential interferogram (2) between the overlapping burst interferograms. The pixel-wise misregistration estimate is calculated by scaling the differential interferogram by the local Doppler centroid differences between the two bursts according to (3). This shift estimate is then used to update the resampling LUT and refine the coregistration in the overlap region.

Since the BO-SD refinement can only be carried out in the overlap region, this may cause discontinuities in the interferogram phase, at the edges of the overlap region, although these were in [5] generally seen to be smaller than the main discontinuity at the burst boundary. These residual discontinuities can be further suppressed by applying an azimuth tapering of the BO-SD shift estimate before it is used in the coregistration

$$w(n) = 0.5 - 0.5\cos\left(2\pi \frac{n}{N_o}\right) \tag{7}$$

where n is the azimuth line number counted from the overlap region start, and N_o is the number of azimuth lines in the overlap region. Following the refined coregistration, burst interferograms are formed as usual, followed by burst stitching (mosaicking) and multilooking.

IV. Results

The processing scheme described in Section III was applied to a Sentinel-1 A/B six-day image pair acquired over the North East Greenland Icestream (NEGIS) on January 14 and 20,

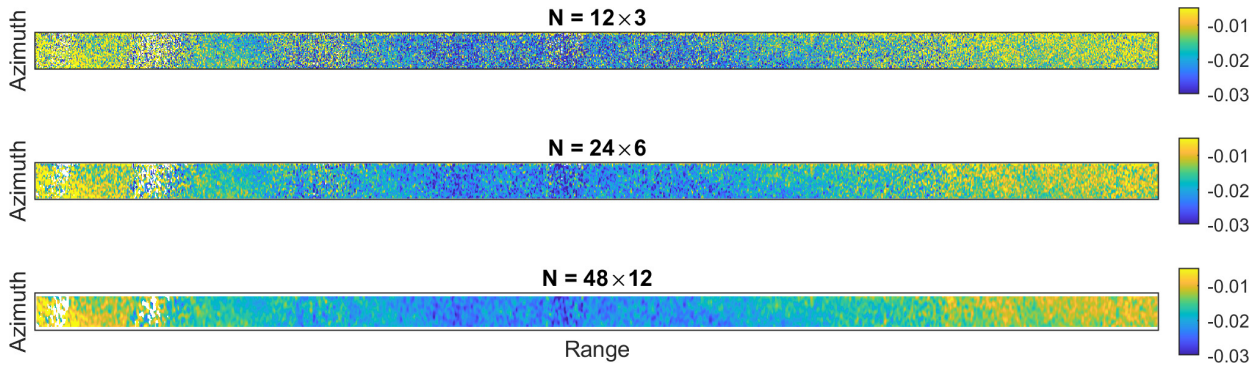

Fig. 3. Residual azimuth shift estimated with BO-SD for IW3 burst 3/4 overlap, in units of pixels. The azimuth tapering (7) is not applied here for illustration purposes.

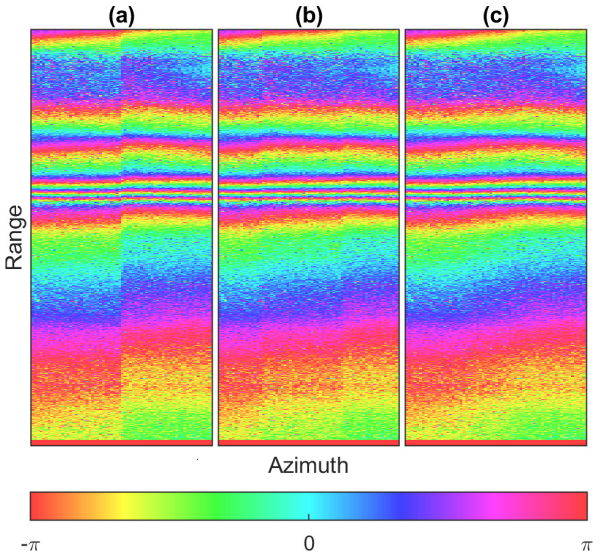

Fig. 4. Zoom on wrapped interferometric phase of the IW3 burst 3/4 overlap region. (a) External velocity coregistration. (b) External velocity + BO-SD, no tapering. (c) External velocity + BO-SD with azimuth tapering of the applied correction.

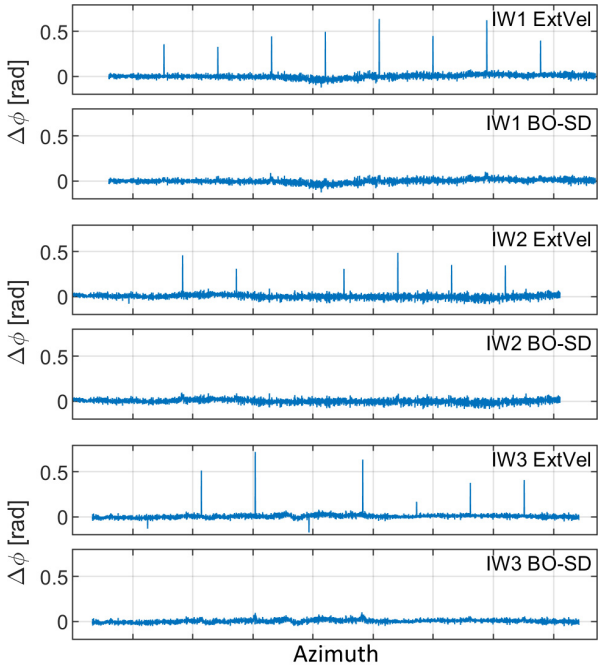

Fig. 5. Range-averaged azimuth phase gradient of unwrapped phase along each of the three swaths with and without BO-SD refinement.

2019, in an area with ice velocity magnitudes up to 60 m/year. Generating an interferogram (12 × 3 looks) by coregistering with only orbits and the TandemX 90-m DEM [13] yields the phase shown in Fig. 1(a), with clear discontinuities at all burst overlaps. Refining the coregistration with an external multiyear average ice velocity product based on offset-tracking [14] reduces the phase jumps in many parts of the scene, as shown in Fig. 1(b). Using the method described in Section III, the azimuth misregistration in the overlap region was then estimated using BO-SD. In Fig. 3, the estimated azimuth shift for a single overlap region (IW3 burst 3/4 overlap, indicated with a blue rectangle in Fig. 1) is illustrated for different averaging window sizes. Pixels with a coherence level below 0.2 were masked in all cases. For both 12 × 3 and 24 × 6 averaging, the noise level is seen to be significant compared with the actual signal in many regions. A 48 × 12 averaging factor was, therefore, selected, and the shift estimate was subsequently weighted with (6) and used to coregister locally the SLCs, resulting in the interferogram in Fig. 1(c). In the faster flowing regions, that is, in the bottom part of IW1 and within the ice stream, in IW3, the residual discontinuities are removed, with the fringes lining up seamlessly at the burst boundaries. In the slower flowing regions, for example, the upper half of IW2, the improvement is less visible, with the effect of the azimuth-induced shift biases still seen on either side of the overlap regions. However, the discontinuities are seen to be smoothed out over the overlap regions, and, crucially, in no case does the BO-SD coregistration seem to have a detrimental impact. Zooming in on the overlap region between bursts 3 and 4 in the IW3 swath (blue rectangles in Fig. 1), we show in Fig. 4(a) the phase with external velocity coregistration only [corresponding to Fig. 1(b)]; in Fig. 4(b) the phase with BO-SD coregistration but without the tapering (6) applied; and in Fig. 4(c) the phase with BO-SD coregistration and tapering applied [corresponding to Fig. 1(c)]. The phase discontinuity clearly disappears in Fig. 4(c), an effect that was observed for all burst boundaries in the interferogram.

To assess the residual discontinuities for the entire scene, the phases of the interferograms in Fig. 1(b) and (c) were unwrapped using a minimum cost flow algorithm [15], and the phase gradient along azimuth was estimated using the first-order differences. This phase gradient estimate was finally averaged in range, to produce the plots in Fig. 5, showing the average phase gradient along each swath, both for the coregistration using only the external velocity and for the proposed BO-SD coregistration. The latter is seen to consistently reduce the discontinuities from more than 0.5 rad to below 0.1 rad, with the residual discontinuities disappearing below the noise floor.

V. Conclusion

The method proposed above significantly reduces the phase discontinuities seen when applying TOPS interferometry to ice sheet scenes with horizontal motion. The main improvement comes from the introduction of an external velocity map in the coregistration, first proposed in [5]. This step removes the bulk of misregistration (and resulting phase discontinuities) due to ice motion and is a prerequisite for the method presented here, as it eliminates the need for phase unwrapping of the BO-SD estimate. As a potential added benefit, the BO-SD shift estimate can be saved and used on its own as an estimate of residual azimuth motion (i.e., relative to the external velocity map) in the burst overlap regions, as shown in [16].

The method described in this letter represents an incremental improvement, without detrimental effects, to the existing TOPS coregistration methods for nonstationary scenes such as ice sheets. It can be used to improve the quality of ice velocity products based on S1 interferometry, by reducing the discontinuities in the final velocity maps and the phase unwrapping errors these could potentially induce. The TOPS DInSAR algorithm described in this letter has been integrated in the Technical University of Denmark (DTU) in-house developed ice velocity processing system [1], and work is ongoing to include interferometric products in the Programme for Monitoring of the Greenland Ice Sheet (PROMICE) ice velocity product [14] produced by the Geologic Survey of Greenland and Denmark (GEUS) using this processor.

References

[1] A. Kusk, J. P. M. Boncori, and J. Dall, "An automated system for ice velocity measurement from SAR," in *Proc. 12th Eur. Conf. Synth. Aperture Radar (EUSAR)*, Aachen, Germany, 2018, pp. 929–932.

[2] T. Nagler, H. Rott, M. Hetzenecker, J. Wuite, and P. Potin, "The Sentinel-1 mission: New opportunities for ice sheet observations," *Remote Sens.*, vol. 7, no. 7, pp. 9371–9389, Jul. 2015, doi: 10.3390/rs70709371.

[3] I. Joughin, B. E. Smith, and I. Howat, "Greenland ice mapping project: Ice flow velocity variation at sub-monthly to decadal timescales," *Cryosphere*, vol. 12, no. 7, pp. 2211–2227, Jul. 2018, doi: 10.5194/tc-12-2211-2018.

[4] N. Yagüe-Martínez *et al.*, "Interferometric processing of Sentinel-1 TOPS data," *IEEE Trans. Geosci. Remote Sens.*, vol. 54, no. 4, pp. 2220–2234, Apr. 2016, doi: 10.1109/TGRS.2015.2497902.

[5] J. K. Andersen, A. Kusk, J. P. M. Boncori, C. S. Hvidberg, and A. Grinsted, "Improved ice velocity measurements with Sentinel-1 TOPS interferometry," *Remote Sens.*, vol. 12, no. 12, Jun. 2020, Art. no. 2014, doi: 10.3390/rs12122014.

[6] R. Scheiber, M. Jäger, P. Prats-Iraola, F. De Zan, and D. Geudtner, "Speckle tracking and interferometric processing of TerraSAR-X TOPS data for mapping nonstationary scenarios," *IEEE J. Sel. Topics Appl. Earth Observ. Remote Sens.*, vol. 8, no. 4, pp. 1709–1720, Apr. 2015, doi: 10.1109/JSTARS.2014.2360237.

[7] C. Gisinger *et al.*, "In-depth verification of Sentinel-1 and TerraSAR-X geolocation accuracy using the Australian corner reflector array," *IEEE Trans. Geosci. Remote Sens.*, vol. 59, no. 2, pp. 1154–1181, Feb. 2021, doi: 10.1109/TGRS.2019.2961248.

[8] R. Scheiber and A. Moreira, "Coregistration of interferometric SAR images using spectral diversity," *IEEE Trans. Geosci. Remote Sens.*, vol. 38, no. 5, pp. 2179–2191, Sep. 2000, doi: 10.1109/36.868876.

[9] R. Bamler and M. Eineder, "Accuracy of differential shift estimation by correlation and split-bandwidth interferometry for wideband and Delta-k SAR systems," *IEEE Geosci. Remote Sens. Lett.*, vol. 2, no. 2, pp. 151–155, Apr. 2005, doi: 10.1109/LGRS.2004.843203.

[10] P. Prats-Iraola, R. Scheiber, L. Marotti, S. Wollstadt, and A. Reigber, "TOPS interferometry with TerraSAR-X," *IEEE Trans. Geosci. Remote Sens.*, vol. 50, no. 8, pp. 3179–3188, Aug. 2012, doi: 10.1109/TGRS.2011.2178247.

[11] A. L. Gray, K. E. Mattar, and G. Sofko, "Influence of ionospheric electron density fluctuations on satellite radar interferometry," *Geophys. Res. Lett.*, vol. 27, no. 10, pp. 1451–1454, May 2000, doi: 10.1029/2000GL000016.

[12] F. De Zan, P. Prats-Iraola, and M. Rodriguez-Cassola, "On the dependence of Delta-k efficiency on multilooking," *IEEE Geosci. Remote Sens. Lett.*, vol. 12, no. 8, pp. 1745–1749, Aug. 2015, doi: 10.1109/LGRS.2015.2424272.

[13] P. Rizzoli *et al.*, "Generation and performance assessment of the global TanDEM-X digital elevation model," *ISPRS J. Photogramm. Remote Sens.*, vol. 132, pp. 119–139, Oct. 2017, doi: 10.1016/j.isprsjprs.2017.08.008.

[14] *PROMICE Sentinel-1 Greenland Ice Velocity Dataset*, Geol. Surv. Denmark Greenland (GEUS), Copenhagen, Denmark, 2021, doi: 10.22008/promice/data/sentinel1icevelocity/greenlandicesheet/v1.0.0.

[15] M. Costantini, "A novel phase unwrapping method based on network programming," *IEEE Trans. Geosci. Remote Sens.*, vol. 36, no. 3, pp. 813–821, May 1998, doi: 10.22008/PROMICE/DATA/SENTINEL1ICEVELOCITY/GREENLANDICESHEET/V1.0.0.

[16] R. Grandin, E. Klein, M. Métois, and C. Vigny, "Three-dimensional displacement field of the 2015Mw8.3 illapel Earthquake (Chile) from across- and along-track Sentinel-1 TOPS interferometry," *Geophys. Res. Lett.*, vol. 43, no. 6, pp. 2552–2561, Mar. 2016, doi: 10.1002/2016GL067954.

A.3 Connectivity approach for detecting unreliable DInSAR ice velocity measurements

This appendix provides the full manuscript:

J. K. Andersen, J. P. M. Boncori, and A. Kusk, Connectivity approach for detecting unreliable DInSAR ice velocity measurements, *IEEE Transactions on Geoscience and Remote Sensing*, vol. 60, pp. 1–12, 2022, doi:10.1109/TGRS.2022.3169722 (2022) [©2022 IEEE, reprinted with permission]

Supplementary material for the manuscript is provided in Appendix B.2.

Connectivity Approach for Detecting Unreliable DInSAR Ice Velocity Measurements

Jonas Kvist Andersen, John Peter Merryman Boncori, and Anders Kusk

***Abstract*— Differential synthetic aperture radar interferometry (DInSAR) allows for retrieval of ice velocity measurements of high resolution and accuracy. One of the main error sources in DInSAR is the phase unwrapping procedure. Unwrapping errors may be caused by several processes, including shear stresses associated with large motion gradients, which lead to loss of interferometric coherence. In many cases, unwrapping errors reach magnitudes corresponding to velocities of tens or even hundreds of meters per year. Traditional DInSAR implementations include pixel masking based on coherence thresholding; however, such a masking is not always sufficient. Consequently, the state-of-the-art for ice velocity retrievals involves either manual inspection of individual measurements or simply discarding measurements in regions where ice flow exceeds a predefined threshold. Here, we instead apply a masking based on thresholding of a pixel connectivity estimate with respect to a reference point, which aims to detect unwrapping errors based only on the estimated coherence pattern. The method is tested on both simulated and real data Sentinel-1 data from the Greenland Ice Sheet and effectively detects the majority of unwrapping errors (recall of 0.84 for the best performing threshold), although with a relatively low precision (0.52 for the best performing threshold). Importantly, higher magnitude unwrapping errors are associated with lower connectivity values, meaning that undetected errors have a significantly lower magnitude (median of 1.7 m/y, corresponding to a single phase cycle, compared with 40.5 m/y with no masking).**

***Index Terms*— Ice velocity, interferometry, phase unwrapping, Sentinel-1, synthetic aperture radar (SAR).**

I. Introduction

FOR several decades, synthetic aperture radar (SAR) satellite data have been applied in the measurement of ice velocity over glaciers and ice sheets. The technique of differential SAR interferometry (DInSAR) generally provides measurements of higher accuracy and resolution, compared with amplitude tracking techniques, although it cannot be applied where velocity gradients are high enough to yield phase ambiguities. In such regions, tracking-based techniques must be used. Hence, the optimal scheme for ice sheet-wide velocity retrieval uses DInSAR where possible, supplemented by tracking-based techniques (e.g., over fast-flowing glacier outlets). Such a scheme has previously been carried out using several SAR systems (e.g., Radarsat, Radarsat-2, and Advanced Land Observing Satellite Phased Array L-band Synthetic Aperture Radar (ALOS-PALSAR) [1], [2]). Since their launch in 2014 and 2016, respectively, the European Union (EU) Copernicus Sentinel-1 satellites have been extensively used to provide routine velocity measurements over polar regions, due to the extensive coverage and low revisit time provided by the terrain observation with progressive scans (TOPS) acquisition mode [3]. Sentinel-1 routine ice velocity retrievals, however, have so far been based solely on amplitude tracking, as the TOPS mode inherently leads to a coupling between differential phase and azimuth motion, which, if not accounted for, may result in intra-burst phase gradients and inter-burst phase discontinuities [1]–[4]. A resolution to this issue was presented in [5] and [6], where Sentinel-1 DInSAR and amplitude tracking measurements were combined to retrieve the ice velocity for a major Greenland drainage basin.

A remaining challenge concerning DInSAR ice velocity measurements, regardless of the SAR acquisition mode, is related to the phase unwrapping processing step. Most phase unwrapping algorithms seek to determine the correct number of 2π phase cycles to add/subtract to each pixel, so that the phase difference between any pair of image pixels is, in the absence of other contributions, proportional to the underlying motion gradient in the radar line-of-sight (LoS) direction. An unwrapping error then occurs when the algorithm assigns a wrong integer multiple of phase cycles. An error of N phase cycles translates to an LoS velocity error through

$$v_{\mathrm{LoS},\sigma} = 2\pi N \frac{\lambda}{4\pi \Delta T} = \frac{N\lambda}{2\Delta T} \tag{1}$$

where λ is the radar wavelength and ΔT is the temporal baseline of the interferogram. For a Sentinel-1 interferogram with a six-day baseline, an unwrapping error of a single phase cycle translates to a velocity error of about 1.7 m/y, which is already well above the achievable accuracy of DInSAR measurements [5]. Generally, however, unwrapping errors may reach magnitudes of tens of phase cycles, becoming the most significant error source in the resulting velocity measurements. Phase unwrapping errors arise due to phase differences between neighboring pixels being greater than π radians, which typically occur in and around areas exhibiting interferometric decorrelation (loss of coherence) [7]. Decorrelation may result from temporal changes between acquisitions (e.g., surface melt or precipitation), topographic effects (e.g., layover or shadow), spatial decorrelation, errors in geometrical coregistration, and from large spatial gradients in the velocity field, as are found over many outlet glaciers [7]–[10]. The

Manuscript received October 18, 2021; revised March 8, 2022; accepted April 18, 2022. Date of publication April 22, 2022; date of current version May 13, 2022. This work was supported by DTU Space, Technical University of Denmark. *(Corresponding author: Jonas Kvist Andersen.)*

The authors are with DTU Space, Technical University of Denmark, 2800 Kongens Lyngby, Denmark (e-mail: jkvand@space.dtu.dk).

This article has supplementary downloadable material available at https://doi.org/10.1109/TGRS.2022.3169722, provided by the authors.

Digital Object Identifier 10.1109/TGRS.2022.3169722

latter can lead to phase ambiguities and complete loss of coherence in areas of excessive shear stress [11]. Consequently, most phase unwrapping techniques apply a masking of the wrapped phase pixels based on some combination of coherence, phase residue density, intensity, topography, and other parameters [7], [12]. In general, however, unwrapping errors are not restricted to pixels with low coherence, high residue density, or radar shadow regions, but may propagate into neighboring regions. Hence, a pixel-wise masking based on such parameters will not always successfully prevent or discard all unwrapping errors.

Another common practice for preventing unreliable DInSAR measurements, due to the risk of unwrapping errors, in ice velocity retrievals is either to avoid carrying out DInSAR in areas where velocities above a certain threshold are expected [1] or to perform a visual inspection of each individual unwrapped interferogram to detect signs of unwrapping errors [2]. It is not, however, always possible to distinguish unwrapping errors from natural velocity variations. In addition, for ice sheet-wide monitoring applications, visual inspections would be excessively time-consuming. Finally, unwrapping errors are not always limited to regions of fast flow, as will be demonstrated in Section III.

The main objective of this work is to determine a procedure for discarding unreliable DInSAR measurements within a routine processing scheme, e.g., an ice sheet-wide velocity retrieval. Therefore, the procedure should be as automated as possible, requiring little input and manual inspection from the user. In this article, we present a masking approach based on the pixel connectivity measure, first proposed in [13]. In [13], a pixel-wise connectivity measure is presented, which measures how well a given pixel can be connected to a selected reference point through high coherence pixels. Unwrapping errors are often associated with low connectivity regions, as will also be demonstrated. The masking method is described in Sections II and III presents a validation on simulated data. Section IV presents an application of the method on real Sentinel-1 data. Section V provides a discussion of the results and the limitations of the masking approach. Finally, Section VI presents final conclusions on the findings.

II. Methodology

A. Interferometric Processing Chain

A typical DInSAR processing chain is shown in the gray blocks in Fig. 1. The specific approach used in this article for interferometric processing is that implemented in DTU's inhouse processing software (IPP) [14], which actually includes several processing steps prior to phase unwrapping to reduce the occurrence and extent of phase unwrapping errors [15]. For Sentinel-1 data, a refined coregistration is applied, which is described in [5] along with the full processing algorithm. Phase unwrapping is performed via a minimum cost flow (MCF) algorithm. Prior to unwrapping, weights are computed based on coherence and edge strength computed from the interferogram magnitude [16]. A mask is generated by discarding pixels with coherence below an adaptive threshold, depending on the selected number of range and azimuth looks, as well as pixels where layover or shadow effects are predicted, based on the input digital elevation model (DEM). Morphological erosion with a 5-pixel cross as the structure element [15], [17] is applied to the pixels above the threshold, thereby masking out areas bordering previously discarded pixels. A segmentation based on 4-point connectivity is then used to divide valid pixels into connected segments. Phase unwrapping is then carried out, with masked pixels being assigned a minimum weight, after which a baseline calibration is performed for the largest segment, followed by an absolute phase calibration of individual segments [15]. Unwrapped measurements are converted into displacement and calibrated through ground control points (GCPs) selected in slow-moving areas of the ice sheet [5], [15]. Although the coherence-based masking segmentation approach is effective at preventing some unwrapping errors, it is not always enough to prevent errors in particularly challenging regions. An example of this is shown in Fig. 2(a)–(c), where an unwrapping error is observed in a region of high coherence that is not isolated by the coherence-based segmentation approach. We propose the introduction of an additional processing step, following the phase unwrapping, which serves to improve the detection of unreliably unwrapped measurements, based on a pixel connectivity estimate, and mask them out.

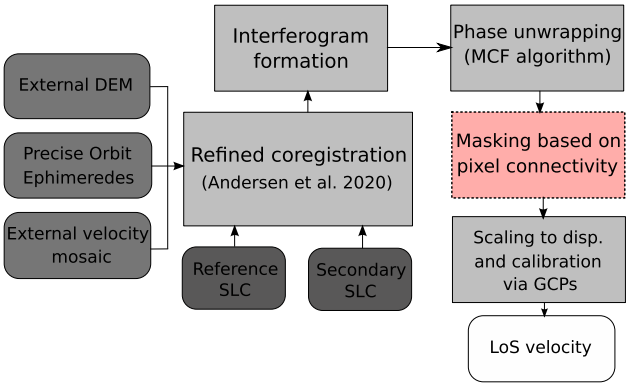

Fig. 1. Block diagram outlining the Sentinel-1 interferometric processing chain as presented in [5], with an added masking step based on pixel connectivity, described in Section II-B.

B. Masking Based on Pixel Connectivity

Unwrapping errors tend to occur in segments that are separated by areas of low coherence, which in the case of glaciers and ice sheets may be caused by excessive shear stress, surface melting, or precipitation. The segmentation process described in Section II-A allows for the detection of segments that are completely disconnected from the remainder of the scene by coherence pixels below a given threshold; however, regions that are only loosely connected may remain, such as the one in the top right of Fig. 2, and these are also prone to phase unwrapping errors. To detect such regions, we apply a masking procedure based on a measure of pixel connectivity, which was previously introduced in [13] in the context of topographic estimation. The connectivity defines how well each pixel is connected to a selected reference point based on a confidence map, i.e., a pixel-wise quality measure. An obvious choice for

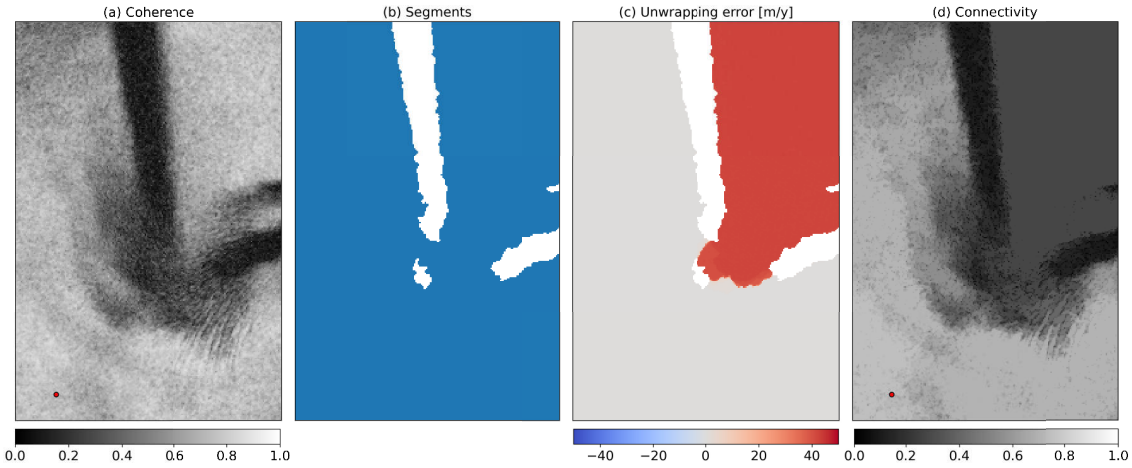

Fig. 2. Example showing (a) coherence, (b) segment map based on the coherence mask in the unwrapping algorithm, (c) detected unwrapping error (as described in Section II-A), and (d) connectivity image derived from the coherence (as described in Section II-B) with the reference point shown by the red dot. The example is a subset from a simulated interferogram (presented in Section III). Note that a large magnitude unwrapping error occurs in a region of high coherence, which is not isolated by the coherence-based mask segmentation, but where connectivity is low.

the confidence map is the interferometric coherence, as this is a general measure of phase quality, and, as previously mentioned, unwrapping errors are prevalent in areas that are disconnected by low coherence values. The connectivity at a specific pixel is then simply defined as the lowest coherence value encountered on the best available path to the reference point (i.e., the path with the highest minimum coherence value). Thus, the connectivity between a certain pixel and the reference point is high if they can be connected by a path of exclusively high coherence values. Conversely, a low connectivity is obtained if the two pixels can only be connected by paths which propagate through low coherence values.

Fig. 2(d) shows the connectivity map derived from the coherence with the reference point shown by the red dot. The coherence image contains a zone of low values, corresponding to a shear margin, and connectivity is observed to be low for pixels on the opposite side of the shear margin, with respect to the reference point. This region of low connectivity is seen to be associated with a large magnitude unwrapping error, which is not isolated by the coherence-based segmentation mask. Hence, such an error would not be corrected or discarded by the conventional unwrapping approach, but would be discarded by applying a masking of pixels with a connectivity below a certain threshold. In practice, the connectivity map is computed through Dijkstra's single-source shortest path algorithm [13], [18], implemented using a heap queue, which allows for relatively fast computation of the connectivity map (a fraction of the processing time needed for unwrapping).

Concerning the exploitation of the connectivity concept within a DInSAR processing chain, it is suggested (although not demonstrated) in [13] to correct large-scale unwrapping errors by computing connectivity maps based on several manually selected reference points followed by a calibration with GCPs in each region. The algorithm does not, however, provide a way of quantifying a connectivity threshold below which measurements are marked as unwrapping errors. Furthermore, for ice velocity applications, such a correction approach would require the availability of a dense network of GCPs where motion is known to within a single phase cycle (1.7 m/y for a Sentinel-1 six-day image pair), which is not realistic. The approach we propose consists of computation of the connectivity estimate based on a single reference point, followed by a masking of pixels below a connectivity threshold, ϵ_c, which are then deemed unreliable. For the pixel-wise confidence measure used to estimate the connectivity, we experimented with various weighting functions applied to the coherence (e.g., thresholding or sigmoidal weighting functions); however, the best results were found using the unweighted coherence. As the computation of connectivity requires only the coherence image, one could choose to apply the connectivity mask to the wrapped phase prior to phase unwrapping. In practice, however, we found that the MCF unwrapping algorithm performs better when applying the mask after unwrapping, as indicated by the red box in Fig. 1. In some instances, low coherence patches of a relatively small spatial extent, which are typically not observed to cause unwrapping errors, lead to low connectivity values in nearby pixels. To avoid masking out these generally unproblematic measurements, we apply a morphological closing to the binary connectivity mask before applying it. A simulated dataset is used to estimate the best performing connectivity threshold, as presented in Section III.

III. Validation on Simulated Data

In some cases, unwrapping errors may be easily recognizable in the LoS velocity estimate, e.g., in cases where the velocity field shows magnitudes or gradients that are unrealistic (based on *a priori* knowledge, e.g., an average velocity mosaic). In general, however, recognition may be complicated by seasonal variation in the velocity field. Furthermore, other potential error sources such as calibration errors are superimposed on any unwrapping errors. Therefore, to quantitatively examine the occurrence of unwrapping errors, and thus to allow for a validation of the connectivity masking

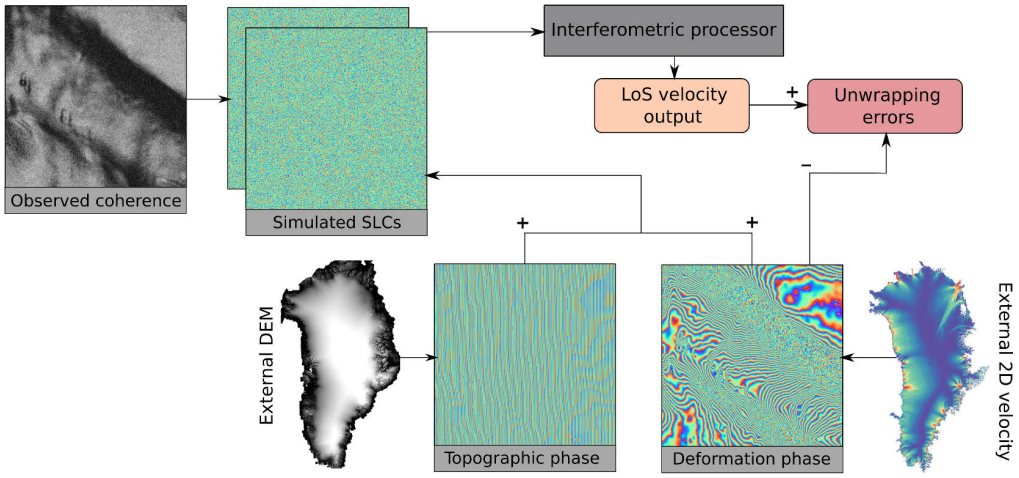

Fig. 3. Flowchart illustrating the process of interferogram simulation, which is further described in the Appendix. The two SLC images are simulated based on a coherence estimate from a real image pair, and a known velocity field is added to the differential phase, such that unwrapping errors can be detected through the difference between the input and output LoS velocity.

method, we generate simulated interferometric pairs of single look complex (SLC) SAR images based on realistic coherence estimates. The simulation procedure is described in the Appendix and outlined in Fig. 3. Each simulated interferogram contains phase contributions from speckle (estimated through the observed coherence of a real Sentinel-1 image pair), topography (computed through a DEM), and a known velocity field (an LoS projection of a multi-year average velocity mosaic derived with SAR offset tracking). While seasonal changes in surface properties are represented by the real coherence estimates used in simulating the interferograms, the motion input phase contribution does not include seasonal variations, as these are not expected to affect the general distribution of unwrapping errors. Furthermore, the simulations do not contain phase contributions from tropospheric and ionospheric effects. Although these are of course important error sources in DInSAR, they are not in general expected to cause phase unwrapping errors, due to the high degree of spatial correlation. Finally, the SLC simulation does not take into account the observed backscatter intensity, as variations associated with an increased likelihood of phase jumps (e.g., in layover or shadow areas) would also be characterized by the coherence.

The simulated SLCs are input to the processing chain in Fig. 1, using an amount of averaging corresponding to $L = 58$ independent looks and a coherence threshold of around 0.2. Phase unwrapping errors are then detected by computing the difference between the output LoS velocity from the simulated interferogram and the input (known) velocity field. The only phase contributions in this difference are unwrapping errors and phase noise. The estimated standard deviation of the phase noise for a coherence of 0.2 and $L = 58$ equivalent number of looks (corresponding to the applied multi-looking) is $\sigma_n(L) = 0.52$ rad. The coherence of 0.2 leads to an upper bound noise estimate, as lower coherence pixels are masked out in the unwrapping process. To account for phase noise, unwrapping errors are classified as pixels for which the difference between the resulting unwrapped phase, ϕ_{unw}, and the known motion contribution, ϕ_{def}, satisfies

$$|\phi_{\text{unw}} - \phi_{\text{def}}| > 2\pi - 3\sigma_n(L) = 4.71 \text{ rad}. \tag{2}$$

Note that the unwrapping errors detected in the simulation arising from the coherence estimate for a given image pair are not necessarily identical to those occurring in the unwrapping of the interferogram formed from the same imagery. This is due to the fact that the simulation generates, for each pixel, a single realization of the complex speckle affecting the reference and secondary images, based on the real coherence estimate. Therefore, the simulation results cannot directly be used to mask errors occurring in the corresponding real interferograms. The simulated interferograms allow for an evaluation of the phase unwrapping process, where unwrapping errors of any magnitude and spatial extent can be detected.

Unwrapping errors are more prone to occur further toward the ice sheet margin, where high shear stresses, caused by fast-flowing glaciers, and surface melt lead to loss of coherence. To evaluate the distribution of unwrapping errors and the performance of the masking method in such a setting, we selected a slice from an ascending Sentinel-1 track (relative orbit 74, interferometric wide (IW) swath mode, and HH-polarization) with 13 bursts in each of the three IW swaths, shown by the purple rectangle in Fig. 7. This slice covers an area downstream of the Northeast Greenland Ice Stream (NEGIS), near the outlets of the Zachariae and Nioghalvfjerdsfjorden glaciers. We then carried out the simulation procedure described in the Appendix for all possible six-day interferograms using all acquisitions from the year 2017, leading to a total of 60 simulated interferograms. The TanDEM-X 90 m Greenland DEM [19] and a 2016–2019 average velocity mosaic based on amplitude tracking measurements generated through Programme for Monitoring of the Greenland Ice Sheet (PROMICE) [20] were used in both image coregistration and interferogram simulations. Fig. 4(a) and (b) shows the multi-year PROMICE velocity projected to radar

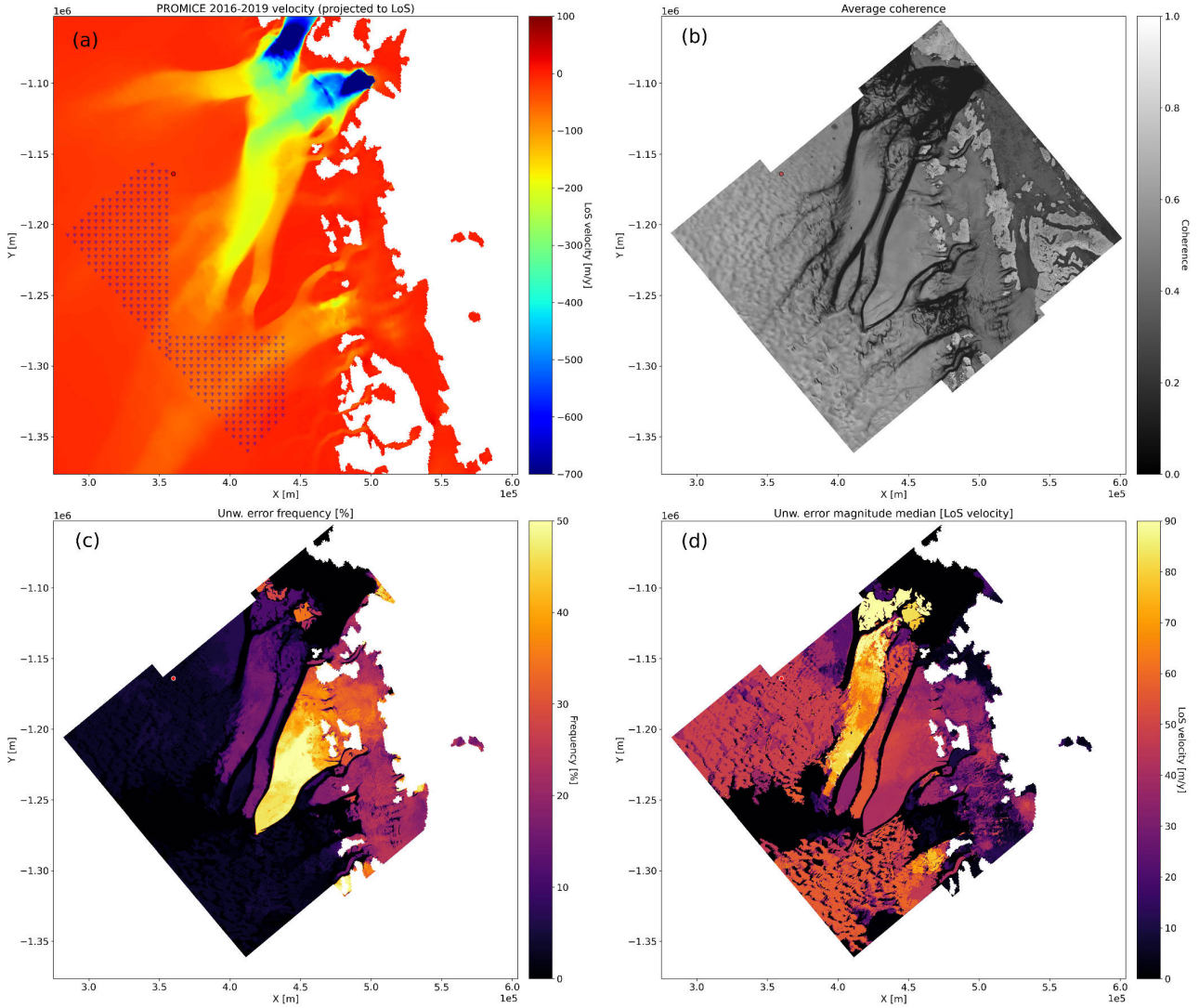

Fig. 4. (a) PROMICE 2016–2019 average velocity [20] projected to the scene LoS, (b) average coherence, (c) unwrapping error frequency, and (d) median unwrapping error magnitude for the simulated interferogram ensemble (60 image pairs in total) without applying connectivity-based masking. Transparent pixels indicate areas where data were discarded in all interferograms due to low coherence or areas where the PROMICE mosaic does not contain measurements (including pixels over ocean). The red dot indicates the connectivity reference point, used for all simulated interferograms, and blue triangles in (a) indicate GCPs used for 0th-order calibration of the output velocity measurements.

LoS and the average coherence level for the simulated interferograms. The coherence showed substantial scene-wide variations across the ensemble of interferograms, meaning that a range of different conditions are represented (see also Fig. S1 in the Supplementary Material). For each simulated interferogram, unwrapping errors were detected by comparing the obtained LoS velocity measurements with the input external velocity field, as described above. Fig. 4(c) and (d) shows the frequency of unwrapping errors and the median error magnitude for the 60-image pair ensemble observed when not applying the connectivity-based masking method. The figures illustrate how unwrapping errors tend to occur in areas that are confined by low coherence regions, generally caused by shear margins. Errors are thus observed within the downstream part of the ice stream and in the slow-moving region east of the stream. In the latter, unwrapping errors are more frequent; however, they also show a lower median magnitude, compared with the errors within the ice stream. Note that as part of the unwrapping algorithm, some pixels are masked out based on coherence level and the detection of layover/shadow, as described in Section II-A, leading to some areas being masked out in all interferograms.

For each of the simulated interferograms, a connectivity map was computed. The same connectivity reference point was selected for all interferograms (indicated by the red point in Fig. 4), in a region toward the interior ice sheet, where velocity is low, coherence is typically high, and unwrapping errors are not expected to occur. A range of connectivity thresholds were then used to generate a mask for each interferogram. Based on the results from a selection of test image pairs, the

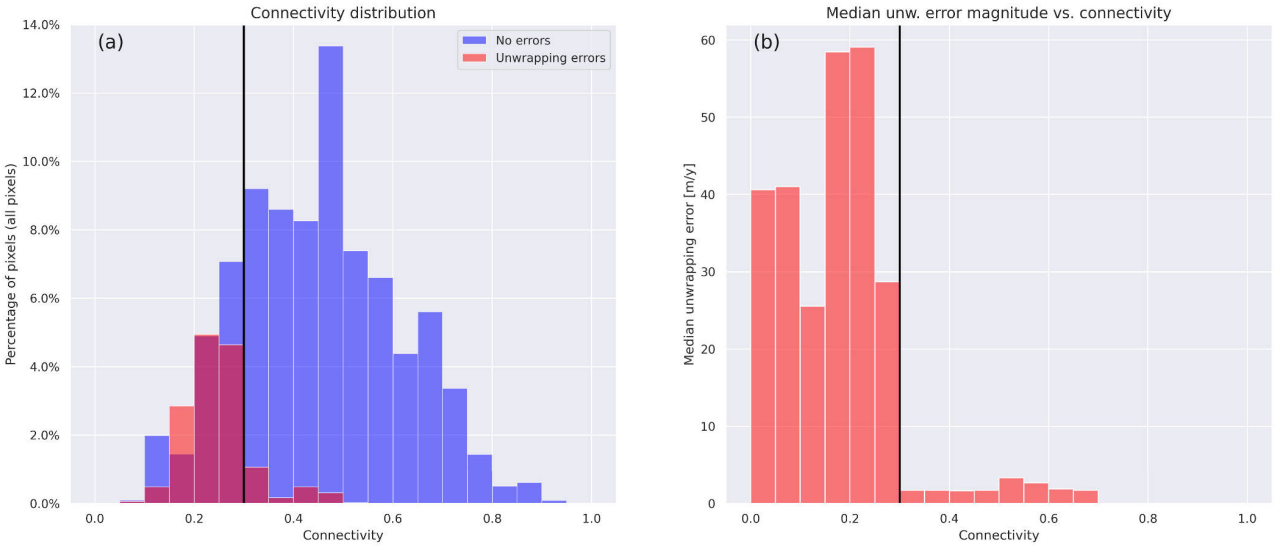

Fig. 5. (a) Histogram showing the distribution of connectivity values (distinguishing between pixels with and without detected unwrapping errors) for all pixels in the simulated interferogram ensemble and (b) bar plot showing median unwrapping error magnitude sorted by connectivity value (in bins with a width of 0.05) for all unwrapping error pixels in the simulated interferogram ensemble. In both the plots, the black line indicates connectivity equal to 0.30. Note that bars in (a) are semi-transparent, such that magenta indicates overlapping bars.

structuring element for morphological closing of the masks was selected as a 32×32 pixel diamond. As unwrapping errors can be detected at a pixel level, the performance of the connectivity masks can be quantitatively evaluated (Fig. S2 in the Supplementary Material shows examples of connectivity estimates and masking results for individual image pairs). To determine the best performing connectivity threshold, we compute the recall and precision measures obtained with connectivity thresholds in the range [0.20; 0.50], measured in increments of 0.05. Recall is defined as the number of true errors detected divided by all true errors in the ensemble, while precision is defined as the number of true errors detected divided by all detected errors. Hence, in this context, recall can be considered the estimated probability that a pixel affected by an unwrapping error actually gets masked out, whereas precision is the estimated probability that a pixel drawn from all the masked pixels is affected by an unwrapping error. The goal of the masking algorithm is to maximize both these measures. A high recall indicates that the masking algorithm is effective at detecting unwrapping errors, while a high precision means that few valid pixels are masked. Naturally, recall will increase with increasing connectivity thresholds, approaching 1 in the trivial case where all pixels are masked out, leading to 100% of errors being detected. Conversely, for very high connectivity thresholds, precision will decrease, since more and more valid pixels will be labeled as errors. To determine the connectivity threshold which achieves the best balance between recall and precision, the F_β-score can be applied. It is defined as

$$F_\beta = (1+\beta^2)\frac{\text{precision} \cdot \text{recall}}{\beta^2 \cdot \text{precision} + \text{recall}} \tag{3}$$

and is a measure of effectiveness of masking assuming β times as much importance is attached to recall as precision. In this case, we argue that a selection of $\beta > 1$ is sensible, meaning that a higher emphasis is put on minimizing the number of missed unwrapping errors (high recall), rather than minimizing the number of false detections (high precision). Here, we opt to use the F_2-score ($\beta = 2$) as a quality measure to be maximized. Table I shows the estimated recall, precision, and F_2-score, computed for all pixels in the 60-image pair ensemble and various connectivity thresholds. The table shows that recall increases substantially until $\epsilon_c = 0.30$, after which smaller improvements are observed. Precision is maximized at a threshold of 0.25–0.30 and then steadily drops, reflecting the increase in false detections for higher thresholds. The F_2-score reaches a maximum at $\epsilon_c = 0.30$, which is thus deemed the best performing connectivity threshold. For higher thresholds, the minor improvement in recall is canceled out by the decrease in precision, leading to an overall decrease in F_2-score. Note that the precision of 0.52 means that almost half of the discarded measurements actually do not contain errors. While arguably a high price to pay to detect the majority of unwrapping errors, a mitigating circumstance is that tracking-based methods may provide coverage where DInSAR measurements are discarded (although with a substantially lower accuracy). Recall and precision do not consider the magnitude of unwrapping errors. As seen in Table I, the median magnitude of remaining errors shows a substantial drop as the threshold is increased, suggesting that larger unwrapping errors are associated with lower connectivity levels.

Fig. 5 shows the distribution of connectivity, distinguishing between unwrapping errors and valid pixels, and median unwrapping error magnitude versus connectivity value for all pixels in the simulated interferogram ensemble. The majority of unwrapping errors are associated with a connectivity below 0.30, although a substantial amount of pixels below this

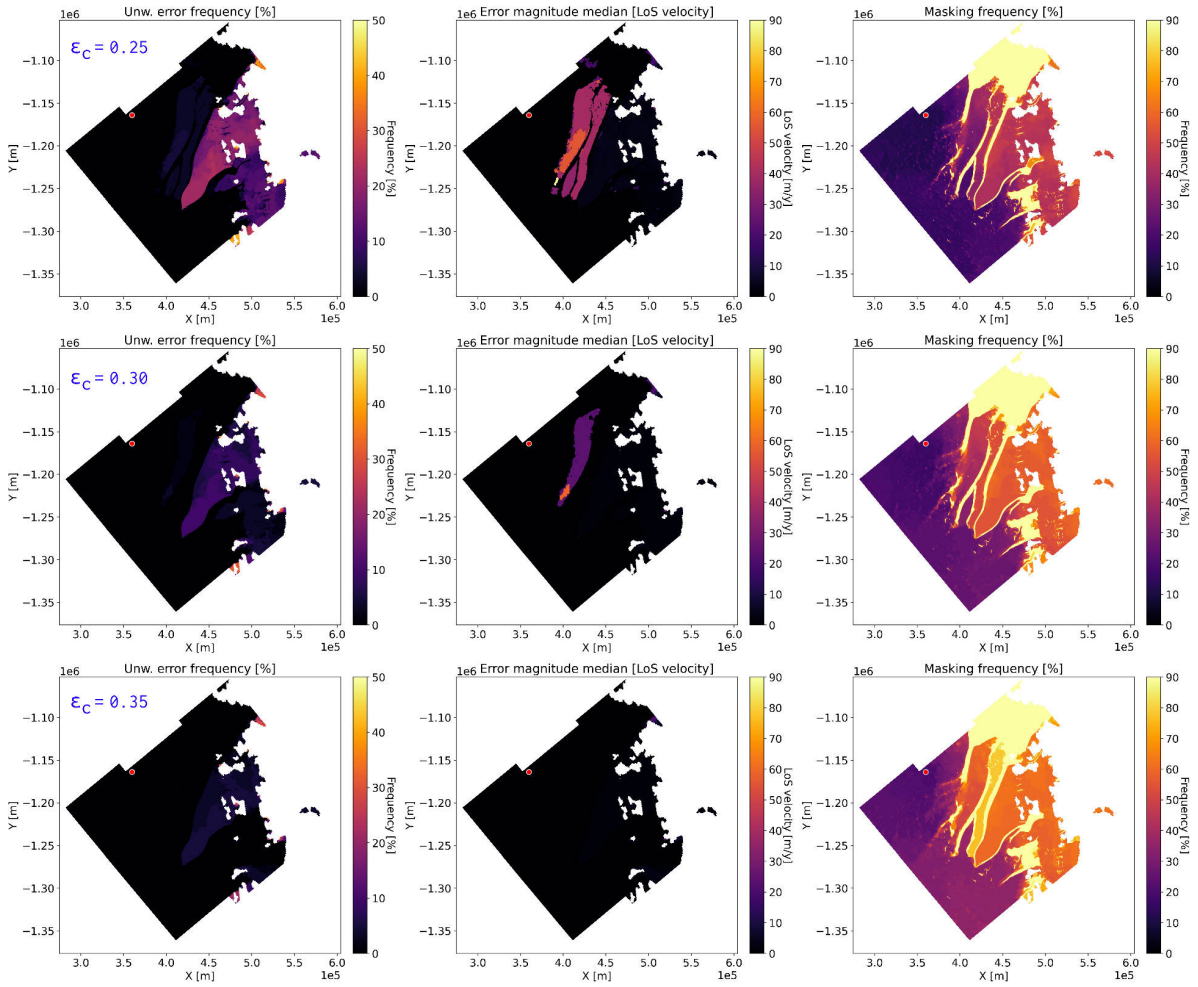

Fig. 6. Unwrapping error frequency (left column), average error (middle column), and masking frequency (right column) for the simulated interferogram ensemble after connectivity masking with a threshold of 0.25 (top row), 0.30 (middle row), and 0.35 (bottom row).

TABLE I

STATISTICS ILLUSTRATING THE PERFORMANCE OF CONNECTIVITY MASKING WITH DIFFERENT THRESHOLDS. THE STATISTICS ARE BASED ON ALL PIXELS FROM THE 60 SIMULATED INTERFEROGRAMS

Threshold	Recall	Precision	F2-score	Median error mag.
No masking	-	-	-	40.5 m/y
0.20	0.17	0.46	0.19	27.0 m/y
0.25	0.62	0.53	0.55	3.4 m/y
0.30	**0.84**	**0.52**	**0.75**	**1.7 m/y**
0.35	0.92	0.42	0.74	1.7 m/y
0.40	0.93	0.35	0.70	1.7 m/y
0.45	0.97	0.29	0.67	1.7 m/y
0.50	0.99	0.25	0.62	3.4 m/y

threshold do not contain errors, as also indicated by the precision and recall values in Table I. In addition, the median magnitude of unwrapping errors associated with a connectivity above 0.30 is 1.7 m/y (in fact, more than 90% of these unwrapping errors have a magnitude of either one or two phase cycles, corresponding to 1.7 and 3.4 m/y, respectively). Conversely, the median magnitude of unwrapping errors below 0.30 connectivity is 47.2 m/y. Finally, Fig. 6 shows the observed unwrapping error frequency and average magnitude obtained by applying connectivity masking with thresholds 0.25, 0.30, and 0.35. Comparing the results with Fig. 4 demonstrates a substantial reduction in unwrapping error frequency scene-wide in all three cases. Increasing the threshold from 0.25 to 0.30 provides a noticeable improvement in terms of error frequency, whereas further increasing the threshold to 0.35 leads to an increased masking frequency but only a relatively small reduction in error frequency, as also indicated by the observed values in Table I.

IV. APPLICATION EXAMPLE: NORTHEAST GREENLAND ICE STREAM

The connectivity masking approach was also applied to real image pairs. To this end, we acquired Sentinel-1 IW data in HH-polarization from two ascending and three descending tracks over the downstream portion of NEGIS spanning the period December 1, 2019–January 27, 2020 (see Fig. 7 and

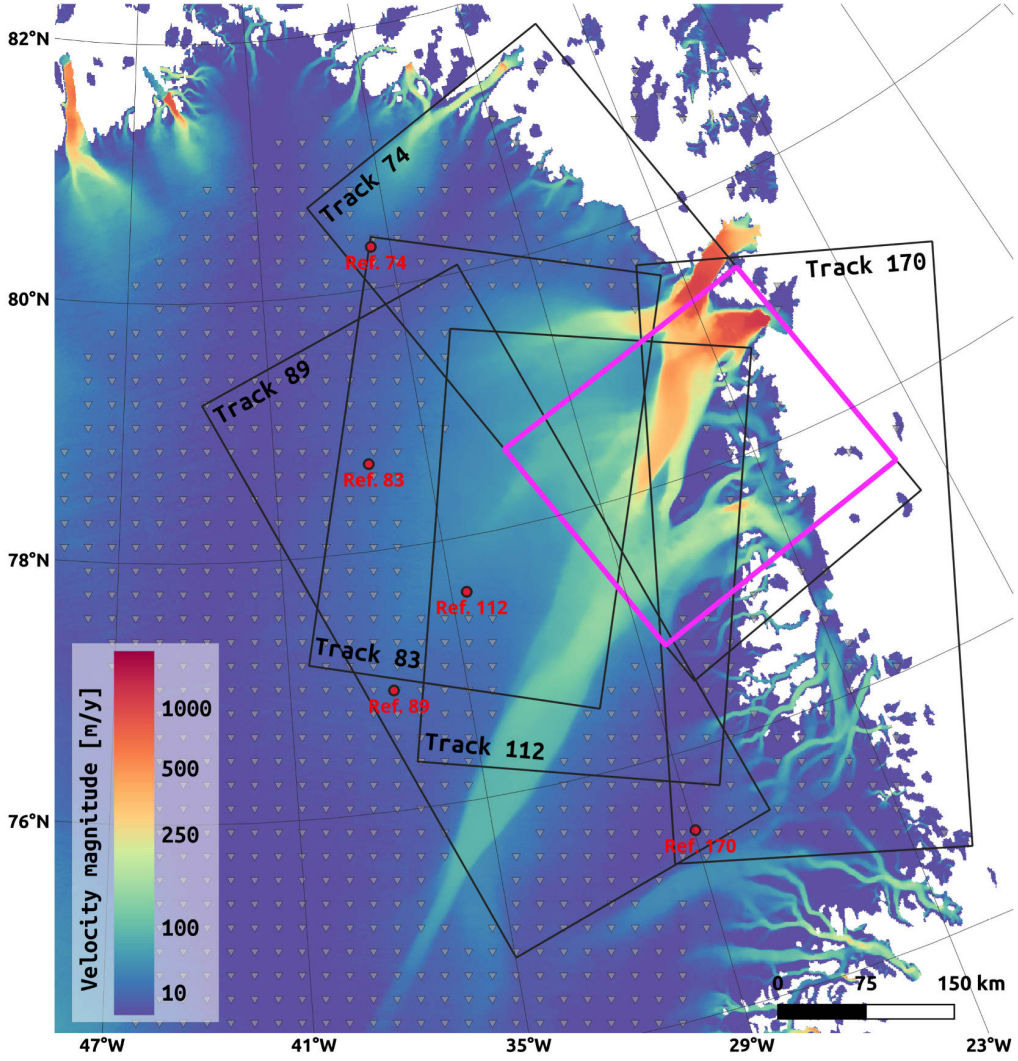

Fig. 7. Overview of the Sentinel-1 data processed in this study (shown in map projection EPSG:3413). Black rectangles indicate Sentinel-1 tracks used to estimate 2-D velocity over part of the Northeast Greenland Ice Stream (presented in Section IV), whereas the magenta rectangle indicates the subset processed for the simulated interferograms (presented in Section III). GCPs used for calibration are shown as gray triangles and red points indicate connectivity reference points. The color scale indicates velocity magnitude from the Programme for Monitoring of the Greenland Ice Sheet (PROMICE) 2016–2019 average mosaic.

Table II), allowing for the retrieval of the average horizontal velocity field with application of the surface-parallel flow assumption [21]. For each of the image pairs, interferometric processing was carried out as outlined in Section II-A with multi-looking corresponding to $L = 58$ independent looks. Connectivity was then estimated, with the reference point for each track indicated in Fig. 7, and the same threshold was applied in the masking of all image pairs. The reference points were selected based on the same rationale as in Section III, namely, that they are in regions toward the interior parts of the ice sheet where coherence tends to be high and velocity is low. Based on the results from the simulated data (see Section III), we chose to test the following subset of connectivity thresholds, $\epsilon_c = \{0.25, 0.30, 0.35\}$. A diamond-shaped structuring element of 32×32 pixels was once again used in the morphological closing of each mask.

TABLE II

OVERVIEW OF SENTINEL-1 DATA PRESENTED IN SECTION IV. ALL IMAGES ARE IN IW MODE AND HH-POLARIZATION. THE SPATIAL EXTENT OF EACH TRACK IS SHOWN IN FIG. 7

Track	Cycles	Acquisition dates
74 (asc.)	A: 187-191, B: 116-121	1 Dec. 2019 - 24 Jan. 2020
83 (desc.)	A: 188-191, B: 118-120	20 Dec. 2019 - 25 Jan. 2020
89 (asc.)	A: 188-191, B: 116-120	2 Dec. 2019 - 25 Jan. 2020
112 (desc.)	A: 187-191, B: 116-121	4 Dec. 2019 - 27 Jan. 2020
170 (desc.)	A: 186-191, B: 116-120	8 Dec. 2019 - 27 Jan. 2020

Fig. 8 shows the magnitude of the horizontal velocity field inferred from all processed tracks (following the same inversion approach outlined in [5]), both with and without connectivity masking. Also shown is the difference between the velocity magnitude from the obtained measurements and

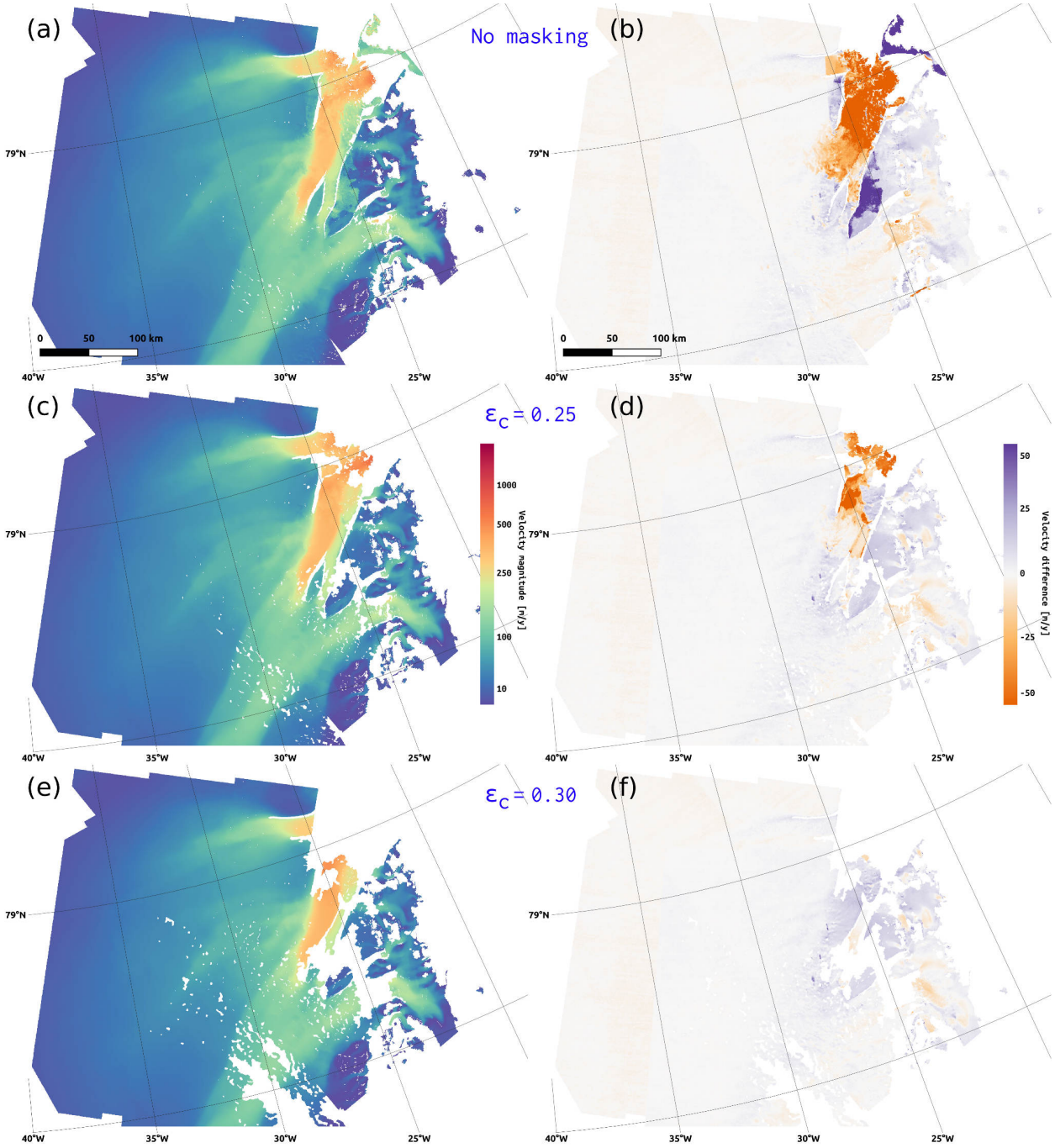

Fig. 8. Horizontal velocity magnitude for the period December 1, 2019–January 27, 2020 obtained from the NEGIS Sentinel-1 image pairs shown in Table II and Fig. 7(a), (c), and (e) and difference in horizontal velocity magnitude with respect to the PROMICE multi-year mosaic (b), (d), and (f) in the case of no masking (a) and (b) and connectivity masking with a threshold of 0.25 (c) and (d) and 0.30 (e) and (f), respectively. In both masking cases, a morphological closing with a 32 × 32 pixel diamond-shaped structuring element was applied.

the multi-year average PROMICE map, based on amplitude offset tracking. Differences between these velocity fields may be caused by unwrapping errors, temporal variations in the velocity field, atmospheric effects, and calibration errors. Inspecting Fig. 8(b) reveals several contiguous areas of high magnitude differences, most of which are in regions that, based on the simulation experiments, are expected to be prone to unwrapping errors. The sharp gradients surrounding these areas suggest that they are likely caused by unwrapping errors, rather than, e.g., seasonal velocity variations or calibration errors. Fig. 8(d) and (f) shows how some of the suspected unwrapping errors are eliminated with a connectivity threshold of 0.25, while setting $\epsilon_c = 0.30$ appears to eliminate all the major (suspected) unwrapping errors. Note that some measurements, which based on the velocity difference measure are not expected to be unwrapping errors, are also

discarded by the connectivity masking in both the cases (for instance in the upstream part of NEGIS). This is also in line with the expectations based on the simulation experiments, where a precision on the order of 0.5 was estimated for the presented connectivity thresholds. Although coherence is generally expected to be higher in winter months, many of the six-day interferograms in this dataset show moderately low coherence levels toward the interior ice sheet (see Fig. S3 in the Supplementary Material). While these coherence levels seemingly do not lead to unwrapping errors, they do lead to low connectivity levels and consequently to the discarding of valid measurements and a lowered precision. The case of $\epsilon_c = 0.35$ is not shown, as the 0.30 threshold already seems to detect the vast majority of errors.

V. Discussion

An advantage of the connectivity masking approach is that it allows for an automated masking of each individual interferogram, independent of external datasets. Hence, instead of discarding all measurements from a region that is expected to be prone to unwrapping errors (as would be common practice), one can apply connectivity masking and achieve DInSAR velocity measurements with high reliability. We tested the method in the downstream part of NEGIS, an area where features often associated with unwrapping errors (such as high levels of shear, ice–bedrock transitions, and frequent loss of coherence) are well-represented. Although the ensemble of simulated interferograms all cover the same region, a wide variety of coherence (and hence unwrapping error) realizations are observed, allowing evaluation of the connectivity masking approach under different conditions. It is possible that the masking performance and the optimal connectivity threshold might show some variation for a different distribution of coherence realizations or for different geographical regions.

The connectivity measure generally captures unwrapping errors well, with most error pixels in the simulated dataset being associated with lower connectivity values. As indicated by Table I and Fig. 5(b), when applying a 0.30 connectivity threshold, a majority of missed detections have an error magnitude of a single phase cycle (1.7 m/y). Fig. S2 in the Supplementary Material shows the connectivity and unwrapping error occurrences for some of the simulated interferograms. For one of these interferograms, an error of a single phase cycle occurs in a large region where connectivity is moderately high, meaning that it remains undetected by connectivity masking. Based on our observations, the connectivity masking approach is generally more effective at detecting unwrapping errors of large spatial scales and large magnitudes. The morphological closing, which is applied to reduce the number of valid measurements discarded, may lead to missed detections of unwrapping errors at a scale smaller than the structuring element.

As mentioned in Section II-B, several coherence weighting functions were tested in the generation of a confidence measure for connectivity estimation, although we found unweighted coherence to perform the best. It is, of course, also possible to combine different parameters or external datasets in the confidence measure, as long as the final measure is normalized to an interval of [0; 1]; however, this was not thoroughly investigated in this study.

In the evaluation of the best performing connectivity thresholds, we weighted recall higher than precision, arguing that missing the detection of unwrapping errors comes at a higher price than discarding valid measurements. Consequently, the threshold of 0.30, which we deemed optimal for both the simulated and real data, has an estimated precision of 0.52, meaning that nearly half of the discarded measurements are valid. Since amplitude tracking either way must be carried out to cover fast-flowing parts of glaciers, these measurements can be used to provide coverage in regions where DInSAR measurements are discarded, albeit at a lower resolution and accuracy. However, if DInSAR and tracking-based measurements are combined using weights that are inversely proportional to the estimated accuracy, as in, e.g., [5], DInSAR measurements will dominate the resulting velocity field wherever they are available. Hence, measurements containing unwrapping errors will not be averaged out by the combination with amplitude tracking measurements but will propagate to the final product, highlighting the importance of detecting as many unwrapping errors as possible, especially those of high magnitudes, even at the cost of low precision. Fortunately, the simulations suggest that generally, unwrapping errors of higher magnitudes are associated with lower connectivity levels (see Table I and Fig. 5), increasing the likelihood of detecting larger errors.

In the cases presented here, the reference point for connectivity estimation was selected manually as a point toward the interior part of the ice sheet, where coherence is typically higher and unwrapping errors are not generally expected. The reference point selection could be automated by selecting the point of maximum coherence within the largest interferogram segment (following the segmentation process mentioned in Section II-A). Figs. S4 and S5 in the Supplementary Material show the connectivity maps and unwrapping error distributions obtained for two of the simulated image pairs when using different reference points, including the reference point defined by the automated approach. Nearly identical masking results are obtained for the various reference points, suggesting a limited sensitivity to the reference point selection. For very large scenes (e.g., Sentinel-1 tracks extending across the Greenland Ice Sheet), reference point selection may in some cases be somewhat complicated, e.g., in case a large region of low coherence forms a divide between two coherent regions. In such a case, it may be beneficial to divide the scene in smaller subsets and process these separately. Automation of such a process should be further investigated before the connectivity masking approach is applied in a fully ice sheet-wide operational manner.

VI. Conclusion

The occurrence of unwrapping errors is one of the most significant sources of error in DInSAR ice velocity retrieval, specifically affecting measurements toward the ice sheet margin, near glacier outlets. As demonstrated here, conventional methods such as coherence-based masking and segmentation alone are not sufficient to fully prevent unwrapping errors.

We propose a masking approach based on pixel connectivity estimation, adapted from the work of [13], to improve detection of unreliable DInSAR measurements. In this approach, a mask is generated for each individual interferogram by masking out pixels with a connectivity below a certain threshold, specified by the user. The connectivity estimate is based solely on the interferometric coherence and a single reference point and hence does not require a full DInSAR time series to be processed, nor does it rely on external datasets. For the examples presented here, the connectivity reference point selection was done manually; however, we argue that this process can be automated by selecting the point of maximum coherence in the largest interferogram segment. The results obtained for both the simulated and real data suggest that a reasonable connectivity threshold is on the order of 0.30. With such a threshold, we estimate a recall of 0.84 and a precision of 0.52, indicating that the majority of unwrapping errors are detected, although nearly half of the discarded measurements are not actually affected by unwrapping errors. In ice sheet-wide routine retrievals, DInSAR measurements are, ideally, combined with tracking-based measurements. As the coverage of the tracking-based methods is better than that obtained by DInSAR, coverage may still be achieved in areas that are flagged by connectivity-based masking. Therefore, we prioritize masking the majority of unwrapping errors even at the cost of discarding some valid DInSAR measurements. Finally, we observe a tendency for unwrapping errors of higher magnitudes to be associated with pixels of lower connectivity values, with the simulated interferogram ensemble showing a median error of only 1.7 m/y for pixels with connectivity above 0.30. Hence, larger unwrapping errors are more likely to be detected, even when masking with relatively low connectivity thresholds.

APPENDIX
INTERFEROGRAM SIMULATION

For each interferogram, the simulation procedure is as follows.

1) Carry out a refined coregistration of a real Sentinel-1 data pair, as described in [5] and [6].
2) Estimate interferometric coherence, applying multi-looking with a factor of 18 × 4 in range × azimuth. The coherence estimate is then interpolated (using inverse distance weighting) to full resolution in the geometry of the first SLC.
3) Simulate two complex SLCs, u_1 and u_2, in the same geometry and with the same coherence as the real data pair, according to [22]
$$u_1 = \sqrt{1-\gamma}\,a + \sqrt{\gamma}\,c \tag{4}$$
$$u_2 = \sqrt{1-\gamma}\,b + \sqrt{\gamma}\,c \tag{5}$$
where a, b, and c are uncorrelated stationary white complex Gaussian processes of equal (unit) variance, and γ is the estimated coherence.
4) Add deterministic phase contributions representing the flat-earth term, the topography, and the deformation to the first SLC image
$$u_1^{\text{det}} = u_1 e^{j(\phi_{\text{flat}}+\phi_{\text{topo}}+\phi_{\text{def}})}. \tag{6}$$
The flat-earth and topographic contributions, ϕ_{flat} and ϕ_{topo}, are estimated through precise orbits and an external DEM, whereas the deformation phase term is computed as
$$\phi_{\text{def}} = -\frac{4\pi}{\lambda} v_{\text{LoS}}\,\Delta T \tag{7}$$
where λ is the radar wavelength, v_{LoS} is the LoS velocity component, and ΔT is the temporal baseline, which is equal to six days for all the interferograms presented here. The LoS velocity is computed by projecting an external ice velocity mosaic, e.g., a multi-year velocity average, on the radar LoS. Atmospheric phase contributions are neglected, as these generally do not lead to unwrapping errors.
5) Finally, the simulated SLCs enter a usual DInSAR processing scheme (omitting coregistration, as this has already been done prior to coherence estimation). The interferogram is formed as
$$I^{\text{sim}} = u_1^{\text{det}} u_2^{*} \tag{8}$$
and once flattening is carried out, based on the same orbit files and DEM applied in the simulations, the only remaining phase contributions are the deformation term, which is known, and the phase noise corresponding to the coherence estimate.

ACKNOWLEDGMENT

The PROMICE multi-year average ice velocity mosaic was generated by Anne M. Solgaard, Geological Survery of Denmark and Greenland (GEUS). Sentinel-1 data are provided by the European Union (EU) Copernicus Programmre. Interferometric processing was carried out using the DTU Space inhouse processing software (IPP).

REFERENCES

[1] I. Joughin, B. E. Smith, and I. M. Howat, "A complete map of Greenland ice velocity derived from satellite data collected over 20 years," *J. Glaciol.*, vol. 64, no. 243, pp. 1–11, Feb. 2018.
[2] J. Mouginot, E. Rignot, and B. Scheuchl, "Continent-wide, interferometric SAR phase, mapping of Antarctic ice velocity," *Geophys. Res. Lett.*, vol. 46, no. 16, pp. 9710–9718, Aug. 2019.
[3] T. Nagler, H. Rott, M. Hetzenecker, J. Wuite, and P. Potin, "The Sentinel-1 mission: New opportunities for ice sheet observations," *Remote Sens.*, vol. 7, no. 7, pp. 9371–9389, 2015.
[4] F. De Zan, P. Prats-Iraola, R. Scheiber, and A. Rucci, "Interferometry with TOPS: Coregistration and azimuth shifts," in *Proc. EUSAR*, Jun. 2014, pp. 949–952.
[5] J. K. Andersen, A. Kusk, J. P. M. Boncori, C. S. Hvidberg, and A. Grinsted, "Improved ice velocity measurements with Sentinel-1 Tops interferometry," *Remote Sens.*, vol. 12, no. 12, p. 2014, Jun. 2020.
[6] A. Kusk, J. K. Andersen, and J. P. M. Boncori, "Burst overlap coregistration for Sentinel-1 Tops DInSAR ice velocity measurements," *IEEE Geosci. Remote Sens. Lett.*, vol. 19, pp. 1–5, 2022.
[7] C. Werner, U. Wegmüller, and T. Strozzi, "Processing strategies for phase unwrapping for INSAR applications," in *Proc. EUSAR*, Jun. 2002, pp. 353–355.
[8] M. Eineder, "Efficient simulation of SAR interferograms of large areas and of rugged terrain," *IEEE Trans. Geosci. Remote Sens.*, vol. 41, no. 6, pp. 1415–1427, Jun. 2003.
[9] E. W. Hoen and H. Zebker, "Penetration depths inferred from interferometric vol. decorrelation, observed over the Greenland ice sheet," *IEEE Trans. Geosci. Remote Sens.*, vol. 38, no. 6, pp. 2571–2583, 2000.
[10] O. Hellwich, "SAR phase unwrapping: Implications of terrain shape and smoothing," in *Proc. EUSAR*, 1998, pp. 51–56.

[11] R. M. Goldstein, H. Engelhardt, B. Kamb, and R. M. Frolich, "Satellite radar interferometry for monitoring ice sheet motion: Application to an Antarctic ice stream," *Science*, vol. 262, no. 5139, pp. 1525–1530, 1993.
[12] H. A. Zebker and J. Villasenor, "Decorrelation in interferometric radar echoes," *IEEE Trans. Geosci. Remote Sens.*, vol. 30, no. 5, pp. 950–959, Sep. 1992.
[13] L. Galli, "A new approach based on network theory to locate phase unwrapping unreliable results," in *Proc. IEEE Int. Geosci. Remote Sens. Symp. (IGARSS)*, Jul. 2001, pp. 118–120.
[14] A. Kusk, J. Boncori, and J. Dall, "An automated system for ice velocity measurement from SAR," in *Proc. EUSAR*, 2018, pp. 929–932.
[15] J. J. Mohr and J. P. M. Boncori, "An error prediction framework for interferometric SAR data," *IEEE Trans. Geosci. Remote Sens.*, vol. 46, no. 6, pp. 1600–1613, Jun. 2008.
[16] M. Costantini, "A novel phase unwrapping method based on network programming," *IEEE Trans. Geosci. Remote Sens.*, vol. 36, no. 3, pp. 813–821, May 1998.
[17] M. Hubig, S. Suchandt, and M. Eineder, "Automatic correction of baseline and phase unwrapping errors in SAR interferograms," in *Proc. EUSAR*, 2000, pp. 131–134.
[18] E. W. Dijkstra, "A note on two problems in connexion with graphs," *Numer. Math.*, vol. 1, no. 1, pp. 269–271, Dec. 1959.
[19] P. Rizzoli *et al.*, "Generation and performance assessment of the global TanDEM-X digital elevation model," *ISPRS J. Photogramm. Remote Sens.*, vol. 132, pp. 119–139, Oct. 2017.
[20] A. Solgaard *et al.*, "Greenland ice velocity maps from the PROMICE project," *Earth Syst. Sci. Data*, vol. 13, no. 7, pp. 3491–3512, Jul. 2021.
[21] I. R. Joughin, R. Kwok, and M. A. Fahnestock, "Interferometric estimation of three-dimensional ice-flow using ascending and descending passes," *IEEE Trans. Geosci. Remote Sens.*, vol. 36, no. 1, pp. 25–37, Jan. 1998.
[22] R. Bamler, "Interferometric stereo radargrammetry: Absolute height determination from ERS-ENVISAT interferograms," in *Proc. IEEE Int. Geosci. Remote Sens. Symp. (IGARSS)*, vol. 2, Jul. 2000, pp. 742–745.

Jonas Kvist Andersen received the M.Sc.Eng. degree in earth and space physics and engineering from the Technical University of Denmark, Kongens Lyngby, Denmark, in 2019, where he is currently pursuing the Ph.D. degree with the Microwaves and Remote Sensing Division, DTU Space, working on applying synthetic aperture radar (SAR) interferometric techniques for Sentinel-1 TOPS-mode ice velocity retrieval.

He has contributed to research collaborations with, e.g., the European Space Agency and the Geological Survey of Denmark and Greenland.

John Peter Merryman Boncori received the Laurea degree *(summa cum laude)* in communications engineering and the Ph.D. degree in geoinformation from the University of Rome "Tor Vergata," Rome, Italy, in 2003 and 2007, respectively.

Since then, he has worked as a Researcher at the Technical University of Denmark, Kongens Lyngby, Denmark, and the National Institute of Geophysics and Volcanology, Rome. Since 2017, he has been an Associate Professor at the Microwaves and Remote Sensing Division, DTU Space, Technical University of Denmark, Kongens Lyngby, Denmark, where he has been the Head of Division since 2020. He has worked on a range of international research projects related to SAR data processing and interferometric synthetic aperture radar (SAR) techniques and their application in measurements of, e.g., seismic deformation and ice flow.

Anders Kusk received the M.Sc. degree in electrical engineering and the Ph.D. degree in synthetic aperture radar (SAR) processing techniques from the Technical University of Denmark, Kongens Lyngby, Denmark, in 2002 and 2006, respectively.

He was a Post-Doctoral Researcher at the Technical University of Denmark. Since 2009, he has been at the Microwaves and Remote Sensing Division, DTU Space, Technical University of Denmark, as a Research Engineer. His research interests include ice flow mapping from SAR data within the European Space Agency (ESA) Icesheets Climate Change Initiative (CCI) Project and the National Danish PROMICE Project (Programme for Monitoring of the Greenland Ice Sheet). He also participates in system development, processor development, and campaign activities for ESA's P-band Polarimetric Airborne Radar Ice Sounder (POLARIS).

A.4 Simplistic machine learning approaches for pixel-level unwrapping error detection

This appendix provides a short, unpublished manuscript, which builds upon the work documented in Appendix A.3 and was submitted for the DTU PhD Course *02910 Computational Data Analysis*, taken as part of the PhD degree.

J. K. Andersen, Simplistic machine learning approaches for pixel-level unwrapping error detection, *unpublished* (2021)

Abstract

In this study, three supervised binary classification models are applied for the detection of phase unwrapping errors in Differential Interferometric Synthetic Aperture Radar ice velocity measurements. The models are trained and evaluated on a data set consisting of simulated interferograms, covering a region of the Northeast Greenland ice sheet margin. Performance on the simulated data is impressive, with the Random Forest and AdaBoost Decision Tree models showing accuracies on the order of 0.9. Further work should be carried out, however, to assess how well this performance translates to real data sets from various regions on the ice sheet.

1. Introduction

Ice velocity is an essential parameter in the monitoring of contributions to sea level rise by glaciers and ice sheets. Additionally, accurate knowledge on ice dynamics allows glaciologists to better understand the nature and evolution of the major ice sheets. Since the 1990s, Synthetic Aperture Radar (SAR) satellites (a particular type of imaging radars) have proved an invaluable source of ice velocity measurements [1–3]. Contrary to optical instruments, radars do not rely on sunlight and may even measure through cloud covers - benefits that are especially relevant in polar regions. Differential SAR Interferometry (DInSAR) is a method in which the phase difference between two subsequent acquisitions (from two subsequent satellite passes, typically separated by a few days) is exploited to measure ground deformation in the radar line-of-sight direction, through the relation:

$$d_{LoS} = \frac{4\pi}{\lambda}\Delta\phi \tag{1}$$

where d_{LoS} is the line-of-sight deformation (which can be scaled to a velocity estimate), λ is the radar wavelength, and $\Delta\phi$ is the measured 2D phase difference map, also known as an interferogram. The theoretical accuracy of DInSAR deformation measurements is a fraction of the radar wavelength (which is typically in the range of 5-25 cm).

The main limitation in DInSAR is that the measured phase differences are wrapped in an interval of $[0; 2\pi]$. Hence, a phase unwrapping procedure is required in order to determine the absolute phase difference at each pixel, i.e. an algorithm that determines the correct integer number of phase cycles (2π radians) to add/subtract from each phase difference. Several approaches have been applied to address this problem, e.g. [4, 5]. In this study we assume the use of a Minimum Cost Flow unwrapping algorithm, as described in [6], and a DInSAR processing algorithm as described in [7]. Phase unwrapping errors occur when the unwrapping algorithm assigns a wrong integer of phase cycles to a given pixel. In this study we work with interferograms with a 6-day temporal separation and a 5.4 GHz SAR system, meaning that a phase error of 2π radians translates to a velocity estimation error of 1.7 m/y, however, in general, unwrapping errors may have magnitudes of many phase cycles, leading to velocity errors of tens or even hundreds of m/y. In some cases, unwrapping errors lead to physically infeasible output velocity measurements and hence a manual inspection may allow for error detection. In general, however, as the true velocity field is unknown, the exact extent of unwrapping errors cannot be determined. Therefore, for the study of unwrapping error propagation, I have generated a set of simulated interferograms based on coherence estimates from real image pairs and a known velocity field. In such a case, the true velocity is known at every pixel and any deviations of one or more phase cycles between the input and output velocity fields will be caused by unwrapping errors. The simulated data set will be further described in Section 2.

Phase unwrapping errors are often induced in and around regions of low interferometric coherence, meaning regions where the radar scattering properties of the surface undergoes change during the time between the two acquisitions. A coherence of zero implies that the retrieved phase is pure noise, while a coherence equal to one implies no noise. Most unwrapping algorithms apply a masking in which pixels with coherence below a certain threshold are discarded. Such an approach, however, is not enough to prevent all types of erroneous measurements, as unwrapping errors may propagate into regions with high coherence levels. In order to improve the detection of such errors, I have recently investigated the performance of using pixel connectivity, first defined in [8], to apply an additional masking of the DInSAR output. The connectivity measure is derived from the coherence and a selected reference pixel. The connectivity for a given pixel is high if there exists a path

connecting it to the reference point which passes through only high coherence values. Conversely, if the given pixel can only be connected to the reference by passing through low coherence values, the resulting connectivity is low. An example of a coherence image and a resulting connectivity measure is seen in Fig. 2. Note that the reference point is selected towards the interior ice sheet, where coherence is generally high and unwrapping errors are rarely observed. The resulting connectivity is low for image segments that are separated by zones of low coherence (these zones are primarily caused by shear margins, i.e. high velocity gradients, which cause the ice fabric to rotate and hence to alter its radar scattering properties).

It turns out that the connectivity measure is a relatively good indicator of unwrapping errors - the majority of observed unwrapping errors occur in pixels with low connectivity values, as observed in Fig. 1. Hence, simply masking pixels with a connectivity below some threshold (e.g. 0.3) performs quite well in terms of detecting unwrapping errors. However, as also indicated by Fig. 1, this method leads to a substantial amount of false positives (represented by the blue bars to the left of the vertical black line).

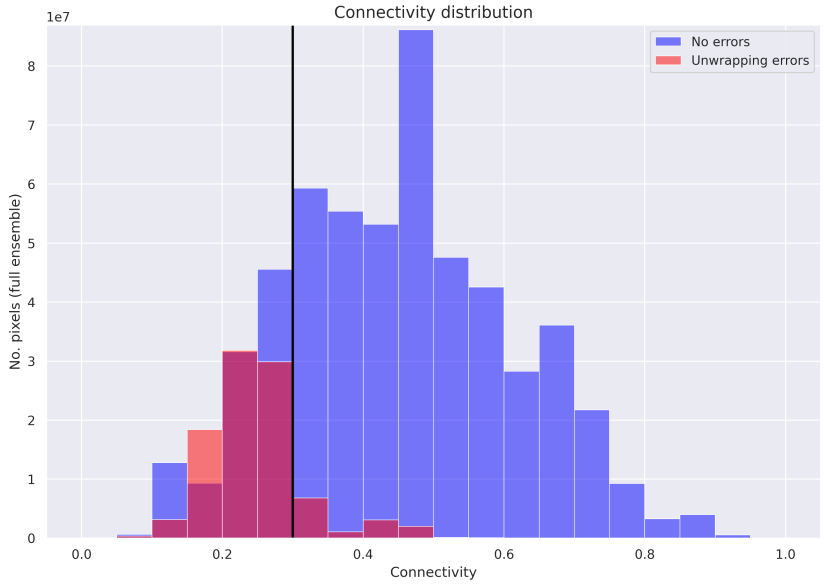

Figure 1: Histogram showing the distribution of pixel connectivity for the simulated data set presented in Section 2. Note that a majority of unwrapping errors occur in pixels with connectivity below 0.3 (indicated by the black line), although a substantial amount of valid pixels are also below this threshold.

The goal of this study is to improve the detection of DInSAR unwrapping errors through machine learning methods introduced in the course, incorporating both the connectivity measure as well as other available input features. As the simulated data set is available, we use this to construct a binary classification problem, classifying between pixels with unwrapping errors and error-free pixels. Several methods from the course are viable candidates in solving such a problem. Here, we investigate the performance of Logistic Regression, as well as two ensemble methods based on Decision Trees, namely Random Forest and AdaBoost.

2. Data description

In this study we use data from the EU Copernicus Sentinel-1 satellites, which both carry a C-band SAR system. The two satellites are in a polar orbit with a 12-day repeat cycle and are separated by 180°, meaning that the minimum revisit time is 6 days. As previously mentioned, a set of simulated interferograms was generated, such that the true unwrapping error distribution is known. A total of 60 simulated interferograms were generated based on the observed coherence in real Sentinel-1 6-day interferograms from a region in the downstream part of the Northeast Greenland Ice Stream. Fig. 2 shows the five input features used in this study for one of the simulated interferograms. Also shown is the obtained map of unwrapping error occurrence for the given interferogram. Although the exact magnitude of each unwrapping error is known (and could be used to formulate a regression problem), in this study we simply generate a binary class, where an error of any

magnitude is assigned a value of 1, while error-free (also called valid) pixels are assigned a value of 0. This binary class is then used as the output in the formulation of a supervised binary classification problem. Note that some pixels are discarded in the unwrapping process (based on coherence and intensity levels), and those pixels are of course excluded, since an output is not available.

The five input features are the interferometric coherence, the pixel connectivity, the radar backscatter intensity, the scene topography, and an a priori estimate of the radar line-of-sight velocity field (a multi-annual average velocity mosaic, re-projected to line-of-sight). Note that the topography and a priori velocity fields are identical for all 60 simulated interferograms. The other three input features vary between interferograms.

As the scene under investigation has a wide extent (roughly 250×250 km) and the features are on a 50×50 m grid, training models on the entire data set is infeasible. Instead, the data must be heavily sub-sampled. The sampling process also allows us to deal with the inherent class imbalance - there are many more valid pixels than error pixels, which, if unaccounted for, may lead to poor generalization of the trained models. The sampling process therefore consists of extracting an equal amount of valid and error pixels. The samples are drawn at random from the entire data set (except for 4 interferograms, which are reserved for additional validation purposes), such that different conditions are represented in the data used for model training. To keep computation times at a reasonable level, a total of $N = 20.000$ pixels were selected for the final data set for model training and evaluation. Note that this comprises a tiny fraction of the original data set, which contains $>10^9$ samples.

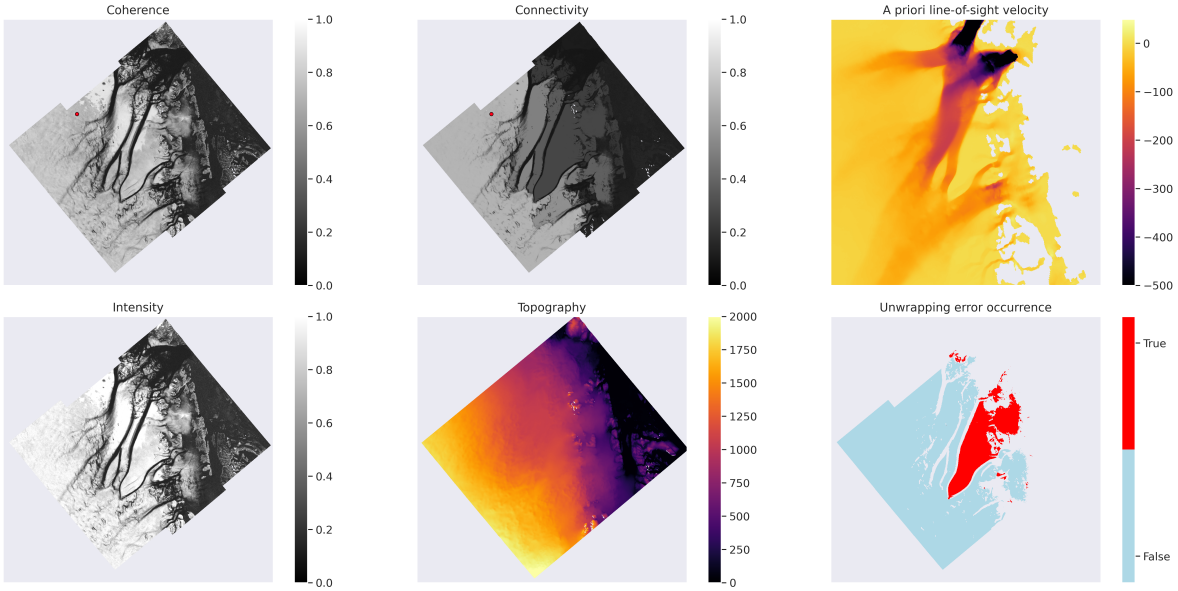

Figure 2: Examples of each of the variables in the input data set, here shown for a single interferogram. The full data set consists of 60 simulated interferograms, based on the estimated coherence from 60 real Sentinel-1 interferograms covering the same region in Northeast Greenland (Sentinel-1 track ID: 74, ascending). The unwrapping error occurrence is a binary class, used as an output in the classification problem, with the remaining variables used as input features. A red dot marks the reference point for the connectivity estimate.

3. Methodology

We investigate the performance of three supervised binary classification models. Logistic Regression is included, as it is a relatively simple and easily implemented model, which does not require prior knowledge on variable distributions or covariances. While different forms of regularization can be introduced to Logistic Regression, in this case we choose to omit regularization, based on the fact that we have many observations and few input features. The other two models under investigation stem from ensemble methods, both based on Decision Trees (DTs), namely Random Forest and AdaBoost DTs. Random Forest (RF) applies the bagging principle to DTs, where random samples are drawn in a bootstrap fashion, building multiple DTs in an effort to decrease prediction

variance by averaging out noise. A further refinement is done by picking a random subset of input features to determine each of the DTs splits - this decreases the correlation of the generated DTs, further lowering the total ensemble variance. Conversely, AdaBoost DTs applies the boosting principle, where each DT in the ensemble is built adaptively, emphasizing samples that lead to miss-classifications by giving these samples higher weights. While bagging leads to a reduction in variance, boosting allows for a reduction of both variance and bias.

Model selection for the Random Forest and AdaBoost models is done through a cross-validation setup, in which all possible combinations of the hyper-parameters listed in Table 1 are trained and tested through 5-fold cross-validation. In all cases, the input features are standardized. The model with the highest mean test score, which is equivalent to the mean accuracy, is then selected (for Random Forest, the out-of-bag score is used). A total of 80% of the sampled data set is used for the model selection cross-validation, while the remaining 20% is reserved as a validation set for the final models. While different ranges of of the listed parameters were experimented with, it should be noted that there are additional hyper-parameters, which could be tuned for each of the methods. Hence, it is likely that an even better model could be obtained with the applied methods.

Logistic Regression	**Random Forest**	**AdaBoost Decision Trees**
No regularization (penalty: 'none')	criterion: {'gini', 'entropy'} max_depth: $\{1; 20\}$ max_features: $\{1; 5\}$ n_estimators: $\{1; 100\}$	criterion: {'gini', 'entropy'} max_depth: $\{1; 20\}$ max_features: $\{1; 5\}$ n_estimators: $\{1; 150\}$

Table 1: Overview of the various hyper-parameters investigated for each of the implemented models. Model selection was based on 5-fold cross-validation, implemented through the `GridSearchCV` function in `sklearn`, allowing testing of all combinations of parameters.

Once the best performing model parameters have been determined, the final Random Forest and AdaBoost models are trained on the entire 80% data set. Note that we do not carry out any regularization steps to select a simpler model (e.g. through the one-standard-error rule), meaning that there is a chance that our models will be somewhat overfitting the sampled data set and hence not achieve optimal generalization. As no parameter search is performed for Logistic Regression, this model is simply trained on the 80% data set to begin with. Then, performance of the models is estimated by comparing their predictions on the remaining 20% of the data set (not used for model selection or training) with the ground truth.

4. Results

Table 2 shows an overview of the performance of the final models, trained on 80% of the sampled data set and tested on the remaining 20%, along with their hyper-parameters. Aside from the accuracy, also the recall (number of true positive detections divided by all positive samples, where 'positive' means an unwrapping error) and precision (number of true positives divided by all positive detections) are reported. Additionally, the F_β-score is defined as:

$$F_\beta = (1 + \beta^2) \cdot \frac{\text{precision} \cdot \text{recall}}{\beta^2 \cdot \text{precision} + \text{recall}} \tag{2}$$

and is a measure of detection performance when considering recall β times as important as precision. In Table 2, we report the F_2-score of the models, arguing that detecting as many unwrapping errors as possible is more important than limiting the number of false positives.

Table 2 shows the Logistic Regression model performing quite well, with a recall just above 0.9, meaning that 90% of unwrapping errors in the validation set are correctly detected (the precision being somewhat lower, due to false positives). The two ensemble methods show an even better performance: The Random Forest and AdaBoost DTs both achieve F_2-scores above 0.93, with Random Forest slightly outperforming AdaBoost in terms of both recall, precision, and accuracy.

Model	Accuracy	Recall	Precision	F_2-score
Logistic Regression (no regularization)	0.880	0.904	0.864	0.896
Random Forest (criterion='entropy', max depth=15, max features=5, no. estimators=79)	0.947	0.950	0.944	0.949
AdaBoost DTs (criterion='entropy', max depth=11, max features=5, no. estimators=143)	0.929	0.931	0.929	0.931

Table 2: Overview of performance of the final models (best performing parameters, based on model selection). The models were trained on 80% of the sampled data set and tested on the remaining 20%.

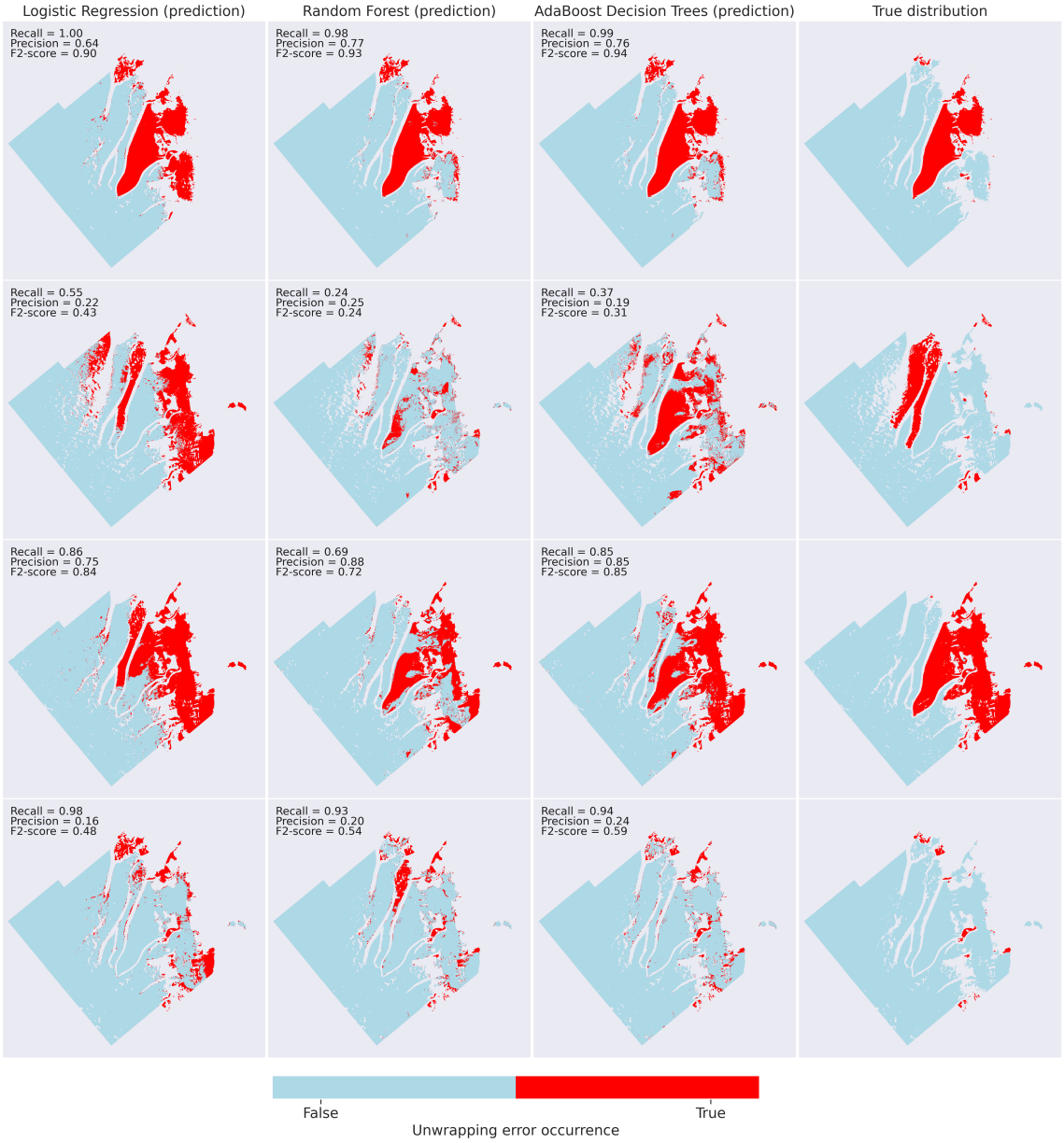

Figure 3: Predictions of the three final models along with ground truth (columns) on four of the full simulated interferograms, reserved from the original data set (one interferogram per row).

It is interesting to investigate how well the final models can predict unwrapping errors in an entire interferogram. To facilitate this, four of the original 60 simulated interferograms were reserved (meaning they were excluded from the training data set). Fig. 3 shows the model predictions of all three models for the four reserved interferograms, along with the ground truth (i.e. the true distribution of unwrapping errors). For the interferograms in the first and third rows, all three models perform impressively well, detecting the vast majority of errors (recall higher than 0.85 in all but on case), although also including some false positives. The ensemble methods show a somewhat higher precision than Logistic Regression. The second row interferogram, where unwrapping errors occur within the fast-flowing ice stream, is not captured well by any of the models. A possible explanation could be that the training samples included few instances of errors in this region. Finally, the fourth row interferogram, which shows only local errors of small extents, leads to good results in terms of recall, although also including a substantial amount of false positives, which drives the precision down.

5. Discussion

The greatest limitation of this study is the fact that the models are trained and evaluated on measurements from only a single region of the Greenland ice sheet. Although the preliminary results presented here look promising, I doubt that the models trained here would generalize well to all other ice sheet regions. Still, considering the small amount of training data included, the results certainly motivate further investigations, particularly into applying ensemble classification methods to the unwrapping error detection problem. A natural next step would be to investigate the performance of the models on simulated data from different regions (perhaps even without including samples from the new data set in the training). Eventually, a qualitative evaluation of the model performance on real data would also be of interest.

The Random Forest model implementation automatically computes the importance of each of the input features. The feature importance estimates obtained for the final Random Forest model are shown in Table 3. Unsurprisingly, connectivity is by far the most important feature in the unwrapping error detection. Coherence and backscatter intensity are the least important features. This perhaps makes sense, seeing as the lowest coherence pixels are already masked out by the unwrapping algorithm, and the intensity image is often similar to the coherence. Finally, both the a priori (i.e. multi-year average) velocity and topography fields show a relatively high importance. This, presumably, reflects how the model learns to associate regions with certain altitudes and flow speeds with a higher risk of unwrapping errors. This tendency may be problematic for a small training data set, however as long as a wide range of unwrapping errors (i.e. errors occurring in different regions) is represented, this behavior may be desirable. Note that other input parameters are available, such as the pixel weights computed by the unwrapping algorithm or the unwrapped phase values - also, the effect of omitting the less important features (such as coherence and intensity) should also be investigated.

	Coherence	**Connectivity**	**A priori velocity**	**Intensity**	**Topography**
Random Forest	0.05	0.62	0.18	0.03	0.12

Table 3: Overview of estimated feature importance (rounded to two decimals) for the final Random Forest model (hyper-parameters listed in Table 2).

Recently, I have applied a simple masking based on thresholding of the connectivity estimate. As can be deduced from the histogram in Fig. 1, this approach is relatively effective at detecting unwrapping errors (since the vast majority of errors are associated with low connectivity), however a significant amount of false positives are also detected - for the full data set presented here, a connectivity threshold of 0.30 leads to a recall of 0.86 and a precision of 0.52. The work presented here suggests to me that better results may be obtainable with either of the three investigated models, although further work must be done to investigate the response of the models to training data from different regions and different interferogram realizations. Also, introducing some form of regularization in the model selection step might be beneficial and should be looked into.

Other ideas for future investigations could be applications of a semantic segmentation method through Convolutional Neural Networks, e.g. using the UNet architecture [9], or unsupervised approaches (applied to real data, instead of simulations), e.g. various clustering methods.

References

[1] R. Goldstein, H. Engelhardt, B. Kamb, and R. Frolich, "Satellite radar interferometry for monitoring ice sheet motion: Application to an antarctic ice stream," *Science*, vol. 262, no. 5139, pp. 1525–1530, 1993.

[2] I. Joughin, B. E. Smith, and I. M. Howat, "A complete map of Greenland ice velocity derived from satellite data collected over 20 years," *Journal of Glaciology*, vol. 64, no. 243, pp. 1–11, 2018.

[3] J. Mouginot, E. Rignot, and B. Scheuchl, "Continent-wide, interferometric SAR phase, mapping of Antarctic ice velocity," *Geophysical Research Letters*, vol. 46, pp. 9710–9718, 16 2019.

[4] R. M. Goldstein and C. L. Werner, "Radar interferogram filtering for geophysical applications," *Geophysical Research Letters*, vol. 25, no. 21, pp. 4035–4038, Nov. 1998.

[5] M. Costantini, "A novel phase unwrapping method based on network programming," *IEEE Transactions on Geoscience and Remote Sensing*, vol. 36, no. 3, pp. 813–821, 1998.

[6] J. J. Mohr and J. P. M. Boncori, "An error prediction framework for interferometric SAR data," *IEEE Transactions on Geoscience and Remote Sensing*, vol. 46, no. 6, pp. 1600–1613, 2008.

[7] J. Andersen, A. Kusk, J. Boncori, C. Hvidberg, and A. Grinsted, "Improved ice velocity measurements with Sentinel-1 TOPS interferometry," *Remote Sensing*, vol. 12, no. 12, 2020.

[8] L. Galli, "A New Approach Based on Network Theory to Locate Phase Unwrapping Unreliable Results," in *Proceedings of IGARSS 2001*, 118–120.

[9] O. Ronneberger, P. Fischer, and T. Brox, "U-net: Convolutional networks for biomedical image segmentation," in *Medical Image Computing and Computer-Assisted Intervention - MICCAI 2015*, 2015, pp. 234–241.

A.5 Wintertime lake drainage cascade triggers large-scale ice flow response in Greenland

This appendix provides the full manuscript:

N. Maier, J. K. Andersen, J. Mouginot, F. Gimbert, and O. Gagliardini, Wintertime lake drainage cascade triggers large-scale ice flow response in Greenland, *Science*, [in review] (2022)

Supplementary material for the manuscript is provided in Appendix B.3.

Title:

Wintertime lake drainage cascade triggers large-scale ice flow response in Greenland

Authors:

Nathan Maier[1*], Jonas Kvist Andersen[2], Jeremie Mouginot[1,3], Florent Gimbert[1] and Olivier Gagliardini[1]

Affiliations:

[1]Univ. Grenoble Alpes, CNRS, IRD, Grenoble INP, IGE, 38000 Grenoble, France

[2]DTU Space, Tech. Univ. of Denmark, 2800 Kgs. Lyngby, Denmark

[3]Depart. of Earth System Science, Univ. of California- Irvine, Irvine CA 92697, USA

[*]Corresponding Author Email: ntmaier@gmail.com

One sentence summary:

We show large changes in dynamics due to surface melt occur during winter in Greenland.

Abstract:

Surface melt forces summertime ice flow accelerations on glaciers and ice sheets. Here, we show that large melt-forced accelerations also occur in winter in Greenland. We document supraglacial lakes (SGLs) draining in cascades at unusually high elevation, causing an expansive flow acceleration over a ~5200 km^2 region during winter. The three-component interferometric surface velocity field reveals the underlying flood propagation with unprecedented detail, providing novel constraints on hydrology-dynamic forcing. The triggering SGLs continuously grew over 40 years and suddenly released decades of stored meltwater into regions of the bed never previously forced, demonstrating surface melt can impact dynamics well beyond its production. We show these events are common and linked to changing climate, and thus will likely impact ice sheet evolution into the future.

Main text:

The annual velocity cycle along the margins of Greenland is closely linked to meltwater availability (*1–10*). In early summer, the ice sheet accelerates as surface meltwater is delivered to the bed and is routed through an inefficient subglacial drainage system favoring high basal water pressures (*1–7*, *10*). In late summer, drainage efficiency gains cause water pressures to decrease, decelerating the ice sheet back to or below the previous winter values (*1–7*, *10*). In the absence of surface melt during the winter period, flow speed typically follows a monotonic increase (*5*, *7*, *11*), which is attributed to decreasing ice-bed coupling from in situ production of basal melt (*7*, *11*). This cycle is the basis of current understanding of hydrology-dynamic coupling and how increased melt will influence flow speeds and mass loss in the future (*12*).

Large transient changes in surface velocities are typically not expected during winter due to the absence of surface melt. Yet, perennial water storage of the previous summer's meltwater can occur within supraglacial lakes (SGLs) that remain partially unfrozen through winter (*13–17*). Recent work indicates isolated lakes can drain during winter (*13*, *17*), but it is thought these drainages do not have a significant impact on flow speeds (*13*). This contrasts to many observations made during summer, where SGL drainages drive multi-day accelerations across large areas due to the high water influx rates from the drainage reducing friction and enhancing bed velocities while propagating downgradient (*1*, *18–20*). This phenomenon is more prominent

for clusters of lakes that drain successively over short time periods as a result of acceleration-driven stress transients that promote hydrofracturing of multiple lakes (*19*, *21*).

Here, we document a cascading lake drainage event that causes an expansive glacier acceleration over approximately ~5200 km^2 of the ice sheet during winter in western Greenland (*Fig. 1*). On approximately March 9th 2018, two SGLs drained in a land terminating sector just south of Jakobshavn Isbræ 142 km inland from the westernmost ice margin and at high elevations (~1600 m) (*Fig. 1, S1*). This altitude corresponds to multi-year snowline (*22*), which approximates the transition between the accumulation and ablation zones. Before the event, no observable acceleration is detected in Sentinel-1 DInSAR line-of-sight (LoS) velocities, which are sensitive to centimeter scale surface displacements (vertical and horizontal) over the six-day acquisition period (*Fig. 1C*, *Methods*). These incipient drainages trigger an acceleration in the direct vicinity of the draining lakes marking the initiation of a marginally propagating velocity wave.

Between March 9th and 12th, eight additional lakes drained ~40 km downstream and ~20 km north of the original drainage cluster (*Fig. 1D, Fig. S1*). During this period, LoS velocities increase up to 160% of pre-drainage values. The wave exhibits a complex structure and bifurcates into two main paths. The wave heading west propagates towards Nordenskiöld Glacier, a relatively slow-moving outlet glacier (~200 m yr^{-1}) terminating on a sediment delta (*Fig. S2*). This western path shows multiple branches emanating from the northern and southern part of the original drainage cluster that coalesce downglacier later on. The wave heading north propagates towards Jakobshavn Isbræ, the fastest marine-terminating outlet glacier in Greenland (>10 km yr^{-1}), along a single branch (*Fig. 1*). All of these branches closely follow the troughs in the bed topography and SGL drainage always falls in their vicinity.

As the event continues, the westward wave front continues to move downglacier and shows again a complex multi-branched structure following bed depressions. The northernmost wave front is no longer clearly visible, extending beyond the usable DInSAR observations. The westward branches eventually coalesce ~80 km downglacier from the original drainage site. LoS velocities within the main wave remain 160% their background value. Between March 18th and 24th, the westward wave front enters the main Nordenskiöld trough, and velocities increase to ~250% background. Between March 24th and 30th, three more SGLs are observed to drain about 60 km upglacier of the wave front. This drainage causes an additional acceleration following an angular bed trough to the north and rejoins the main wave path before entering the Nordenskiöld bed trough. The wave front reaches the terminus of Nordenskiöld between March 30th and April 4th, about 25 days after its initiation. This timing coincides with the proglacial release of water from Nordenskiöld proglacial delta observed in optical imagery on April 2nd and 9th (*Fig. S2*).

By combining different lines-of-sight obtained using ascending and descending Sentinel-1 passes and assuming that the displacements recorded over the different passes are similar and that horizontal flow direction remains unchanged (*Methods*), we invert for horizontal motion (relative to pre-drainage velocities) and the vertical displacement and find they exhibit strikingly distinct patterns (*Fig. 2*). The horizontal velocity field is smooth and spatially extends over tens up to a hundred of kilometers, while the uplift is concentrated in a bead and thread structure of characteristic width on the order or less than ten kilometers, where high uplift patches (~25 cm) are linked together through thinner uplift connectors of lower amplitude. Synthetic modeling validates our decomposition assumptions and the interpretation that the decomposed fields mainly represent horizontal and vertical motion (*Fig. 2*; *Methods*).

We interpret the uplift which produces the complex structure in *Fig. 1* as changes in bed separation and likely flow pathways (*Fig. 2, S3*, *Methods*) as the ~0.18 km^3 of meltwater (*Methods*) injected into the ice-bed interface drains towards the margin. This is based on the following evidences: (i) neither vertical motion resulting from vertical strain or bed tangential motion are likely to produce such a pattern (*Fig. S4*); (ii) the uplifted branches correspond to hydropotential lows within the bed troughs, which is the expected pathway of subglacially draining water (*Fig. 1A, S5*); (iii) regions of highest uplift correspond to depressions in the hydropotential (subglacial sinks) (*Fig. S6*). The bead and thread uplift structure suggests a fill and spill drainage style that is similar to the drainage of subglacial lakes (*23*, *24*), with water captured by each sink along the flow path and released when the pressure reaches the hydropotential lip of each depression.

Drainage through these regions requires overpressure, which can physically cause bed separation either due to the detachment of the ice base via floatation or upward cavity formation via ice creep (*1*, *2*, *4*, *25–28*), and is thus consistent with the beads of high uplift (*Fig. 2, S6*). The comparatively smooth and large spatial extent of the horizontal field indicates much of the horizontal acceleration is not directly related to bed separation. This suggests changes in bed friction are linked to bed separation as conceptualized by (*25*, *29*, *30*) and much larger changes in dynamics occur through stress transmission within the ice - a behavior inferred previously from scarce subglacial measurement and modeling (*8*, *10*, *31–33*) but never confirmed observationally. Alternatively, changes in bed friction could also be set by water pressure increases beyond the uplifted region, however subglacial observations suggest limited pressure communication across short distances (*31*, *34*).

We estimate the speed of the velocity wave that propagates along the interpreted Nordenskiöld drainage pathways (*Methods, Fig. S3*) to be between 0.03-0.17 m s^{-1} (*Fig. 3, Methods*). Repeat dye tracer experiments in Greenland have shown seasonally evolving drainage velocities, where drainage velocities of ~0.1 m s^{-1} were observed early in the melt season and increased to drainage velocities of ~1 m s^{-1} as the melt season progressed (*35*, *36*). This change was inferred to reflect the transition from inefficient drainage to more efficient and channelized drainage pathways. Our event-averaged drainage velocity of ~0.1 m s^{-1} and 1-10 km scale of the uplifted regions would imply drainage through inefficient and distributed subglacial drainage pathways. The inferred drainage speed slows to about 0.05 m s^{-1} as the water enters the Nordenskiöld final trough while horizontal velocities increase by 250%. This occurs even though modeled hydropotential gradients are higher than upgradient regions and no modeled subglacial sinks are present *(Fig. 3*) and implies other factors primarily control drainage speeds. One possibility is that the drainage system conductivity is lower within the trough, leading to lower drainage velocities even with higher hydropotential gradients. This could be due to the accumulation of sediments, where water drains mainly via Darcian flow, or to differences in the pre-existing drainage system geometry.

In the absence of surface melting, which can cause SGL overspill, the drainages likely occur due to hydrofracture to the ice base, which occurs when water pressure within a surface crevasse exceeds the ice pressure (*37–41*). The initial formation of crevasses necessary for hydrofracture requires precursor events that generate tensile stress transients (*19*, *39*). Here, no precursor is observed (*Fig. 1*), however it is possible that a short duration event would not be detected in our six-day velocity maps. Yet, the initially draining lakes are located near the snowline (*Fig. 1*) and are far inland from the terminus of any outlet glacier which would be the most plausible source of transient behavior during winter (*42*). Given no precursor is detected, we suggest it is plausible that initial fracturing occurred locally due to expansion and contraction of the ice surface due to large air temperature fluctuations (*43*, *44*). The event occurred during a period of rapid cooling observed at nearby weather stations (*Fig. S7*) (*45*) after a well-documented arctic heatwave event (*46*), indicating that the event coincided with favorable conditions for thermal fracturing. Colocated near-surface ice temperatures also indicate an increase during this cooling, suggesting refreezing (*Fig. S7*), which could also potentially cause surface fracture via expansion.

Once the initial lake drainage has started, the ice displacements generate stress transients that can trigger hydrofracture within nearby lakes (*38–41*), thus initiating a cascade of SGL drainages near the original drainage location (*19*). Interestingly, many drainages occur more than 40 km away from the initial drainage, and up to 14 days after the original drainage. This would indicate that their drainage is unrelated to stress transients related to ice-tectonic deformations around the incipient drainages and are tapped after the velocity wave passes and tensile stress conditions are favorable for hydrofracture.

Prior to this event, spatially expansive winter transients due to surface melt forcing have not been previously observed (*13*, *17*). Comparing the flow velocities before and after the flood wave passes shows that the influence on dynamics persists beyond the event. Regions along and around the drainage pathway have slowed in the regions upstream of the Nordenskiöld bed trough by 5-10% while within the Nordenskiöld bed trough velocities have increased by 10-20% (*Fig. 1J*). This implies that the passing of the subglacial flood ultimately decreases subglacial pressures and basal water storage in the inland regions and increases it near the margin. A lasting influence on hydrology-dynamics is also observed after lake drainages during summer,

where friction (*1*, *18*) and water storage at the base (*20*) have been observed to change as a result of large influxes of water into the drainage system. Due to the winter timing of the lake drainages, this lingering impact might precondition the drainage system for the following summer, impacting other aspects of the annual hydrology-dynamic cycle.

The horizontal speed-up during the event increases annual marginal ice discharge (~0.5 - 5 m) by 1-4% (*Fig. S8*) compared to a year with no winter transients. This variability is small but on the same order as the annual velocity variability linked to extreme melt years in Greenland (6%) (*47*). However, unlike annual melt variability, where large-scale atmospheric patterns can produce anomalous melt rates over large areas of the margin (*48–50*), the spatial impact of the lake drainage is constrained to a region around the SGLs and drainage pathways. Thus, in order to have an impact on interannual variability comparable to anomalous melt years, melt-forced winter transients would need to occur frequently and in other locations. Undertaking a precursory search in the vicinity of Nordenskiöld glacier during the following years, we identified two additional winter drainage events with associated dynamic changes (*Fig. S9*), suggesting these events are likely a common part of hydrology-dynamics along the margins of the ice sheet.

Tracking the evolution of the SGLs since 1972 to estimate the changes in their area through time (*Fig. 4, S10*, *Methods*) reveals that increasing air temperatures due to climate warming precondition the region for winter drainages. The SGLs that first drain occur at high elevations near the long-term equilibrium-line (*22*). We note that many of these lakes formed and grew for decades before initially draining, and for the two highest lakes, this was the first observed instance of drainage after a half century of growth (*Fig. 4, S10*). This suggests that events like these, where high-elevation SGLs drain and trigger an expansive acceleration downgradient of the drainage site, are fundamentally linked to changes in melt production, which promote the formation of high elevation lakes and increase the availability of liquid water during winter. This is reflected in the historical lake evolution record. The lakes above 1570 m in altitude started to drain after 2007, those between 1500 and 1570 m have been draining since 2002, while those below have been draining regularly since the beginning of our observations (*Fig. 4*).

Our finding clearly links dynamic changes during winter to melt-forcing, demonstrating surface melt can have a prolonged influence on dynamics that persists beyond the period when it is produced. Moreover, we demonstrate this lag can be up to decades, meaning the hydrology-dynamic cycle which is usually considered on an annual and seasonal basis can operate on fundamentally different timescales. With the current climate warming, both melt production and liquid water persistence during winter will increase as temperatures rise and the ELA migrates to higher elevations (*51*). We also find that once initial drainage occurs, they occur more frequently thereafter (*Fig. 4*). Thus, these high elevation drainages, which as we document here can initially occur during winter, might be a critical component of widening of the zone where melt-forced dynamics occur. Future work should set out to establish the frequency of large, melt-forced winter transients, and identify whether they result from extreme winter temperature changes or another trigger mechanism. The latter will ultimately determine the overall impact of melt-forced winter transients in a warmer world.

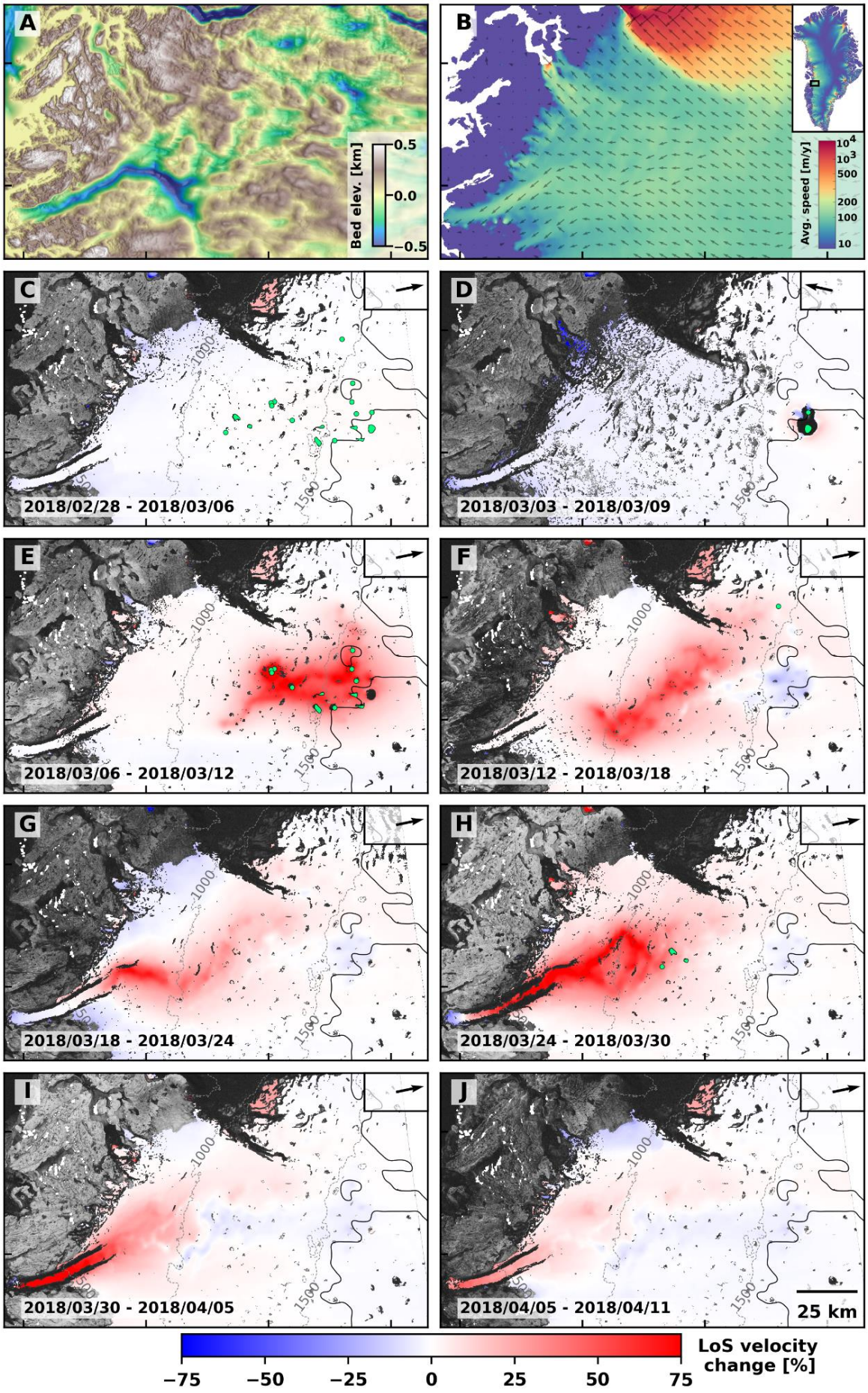
A
Bed elev. [km]
0.5
0.0
−0.5
B
Avg. speed [m/y]
10^4
10^3
500
200
100
10
C
2018/02/28 - 2018/03/06
D
2018/03/03 - 2018/03/09
E
2018/03/06 - 2018/03/12
F
2018/03/12 - 2018/03/18
G
2018/03/18 - 2018/03/24
H
2018/03/24 - 2018/03/30
I
2018/03/30 - 2018/04/05
J
2018/04/05 - 2018/04/11
1000
1500
25 km
LoS velocity change [%]
−75
−50
−25
0
25
50
75

Figure 1 – Winter drainage cascade and dynamic response – Panels (**A**) and (**B**) show bed elevation (*52*, *53*) and 1995-2016 average velocity (*54*). Remaining panels show the change in line-of-sight velocity (relative to a pre-event acquisition) for Sentinel-1 interferometric (DInSAR) measurements (*Methods*). Panel (**C**) shows the location of all lakes inferred to have completely or partially drained (green polygons, or dots for lakes smaller than 2 km^2) along with the velocity anomaly field pre-drainage. The following panels show the sequence of lake drainages and the propagation of the resulting velocity wave. Lakes appear when they are inferred to drain, coincident with the period of the velocity acquisition. Velocity changes are measured from Sentinel-1 tracks 90 (panels (**C**) and (**E**)-(**J**)) and 127 (panel (**D**)). The black arrow indicates ground-projected line-of-sight, dashed lines indicate surface elevation contours, and the solid line indicates the time-averaged snow line (*22*).

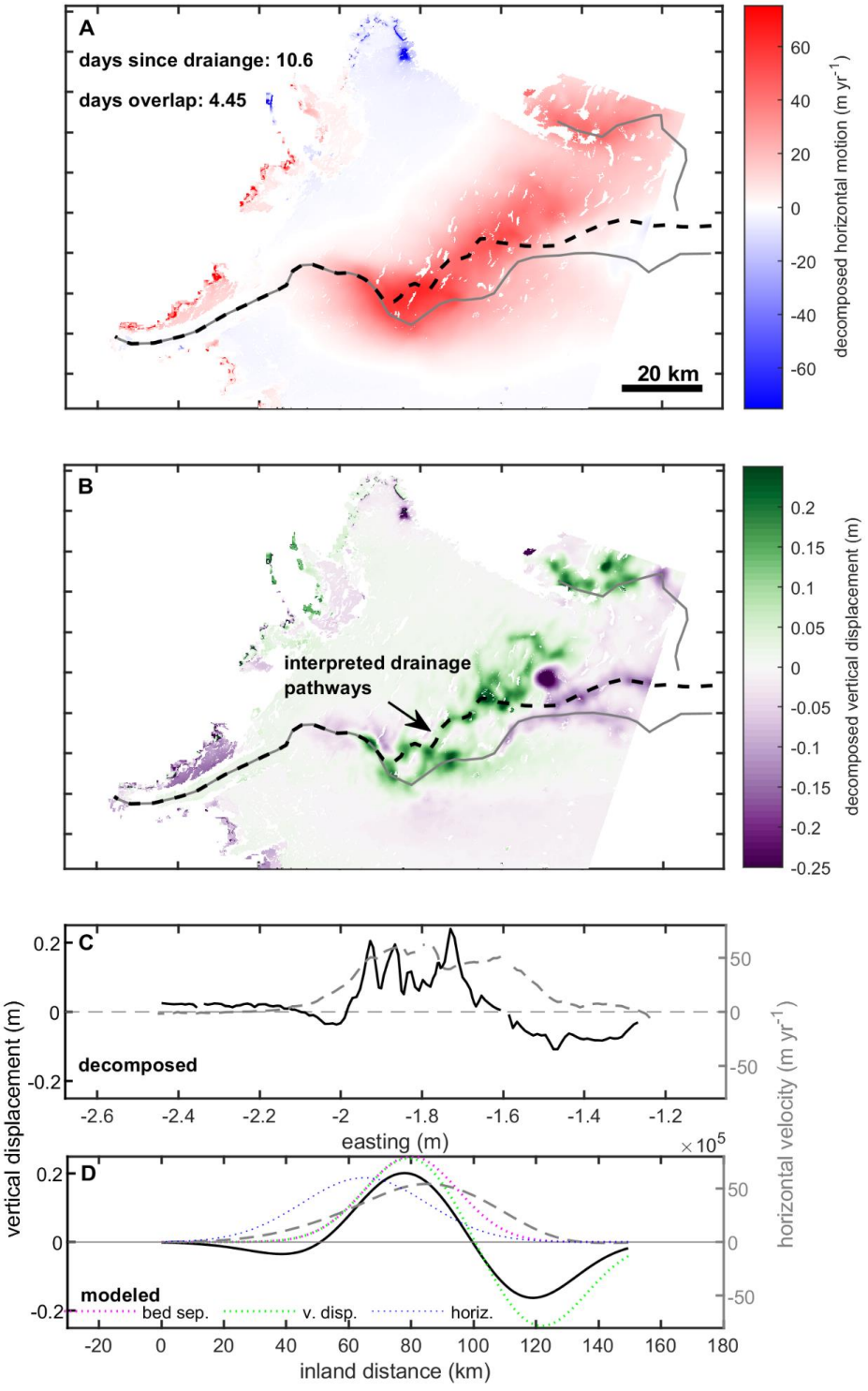

Figure 2 – Decomposed motion – Snapshot of decomposed horizontal motion (relative to pre-drainage velocities) (**A**) and vertical surface displacement (**B**) during drainage event (centered around 10.6 days after drainage). The three interpreted flow pathways are shown with solid gray and black dashed lines. **C.** Decomposed horizontal (gray dashed) and vertical (solid black) motion along the center flowline (dashed black line panel **C**). **D**. Decomposition (horizontal motion - gray dashed, vertical displacement - solid black) of synthetic velocity wave (dotted blue) and uplift wave (dotted pink, vertical displacement (i.e. change in uplift over 6-day window) - dotted green) with characteristics constrained by the data (*Methods*).

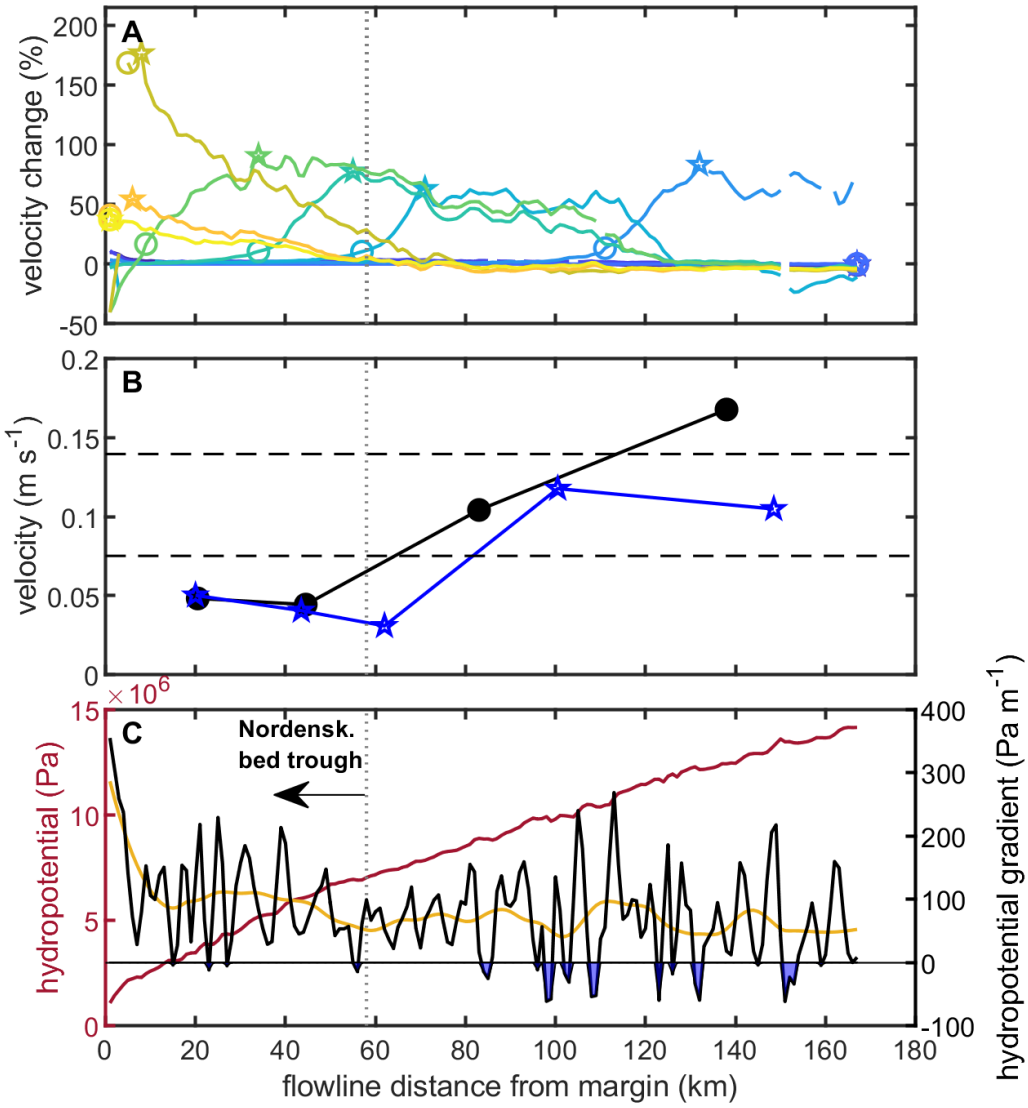

Figure 3 – Subglacial drainage characteristics – (**A**) Percent velocity changes along one of the inferred Nordenskiöld drainage pathways (black dashed line in *Fig. 2*) as the velocity wave propagates to the margin (right to left). Stars show tracked wave peaks and circles show tracked wave fronts (*Methods*). (**B**) Estimated wave velocity using the tracked peaks (stars) and fronts (circles). Velocity marker is shown at the mid-point between the two tracked peaks or fronts used to estimate the speed. Dashed bounds show event integrated drainage velocity inferred from optical imagery (*Fig. S2*). (**C**) Left axis shows hydropotential (maroon line) assuming ice-overburden pressure, right-axis shows hydropotential gradients (black line), and smoothed hydropotential gradients (orange line) along flowline. Blue shading shows location of hydropotential depressions.

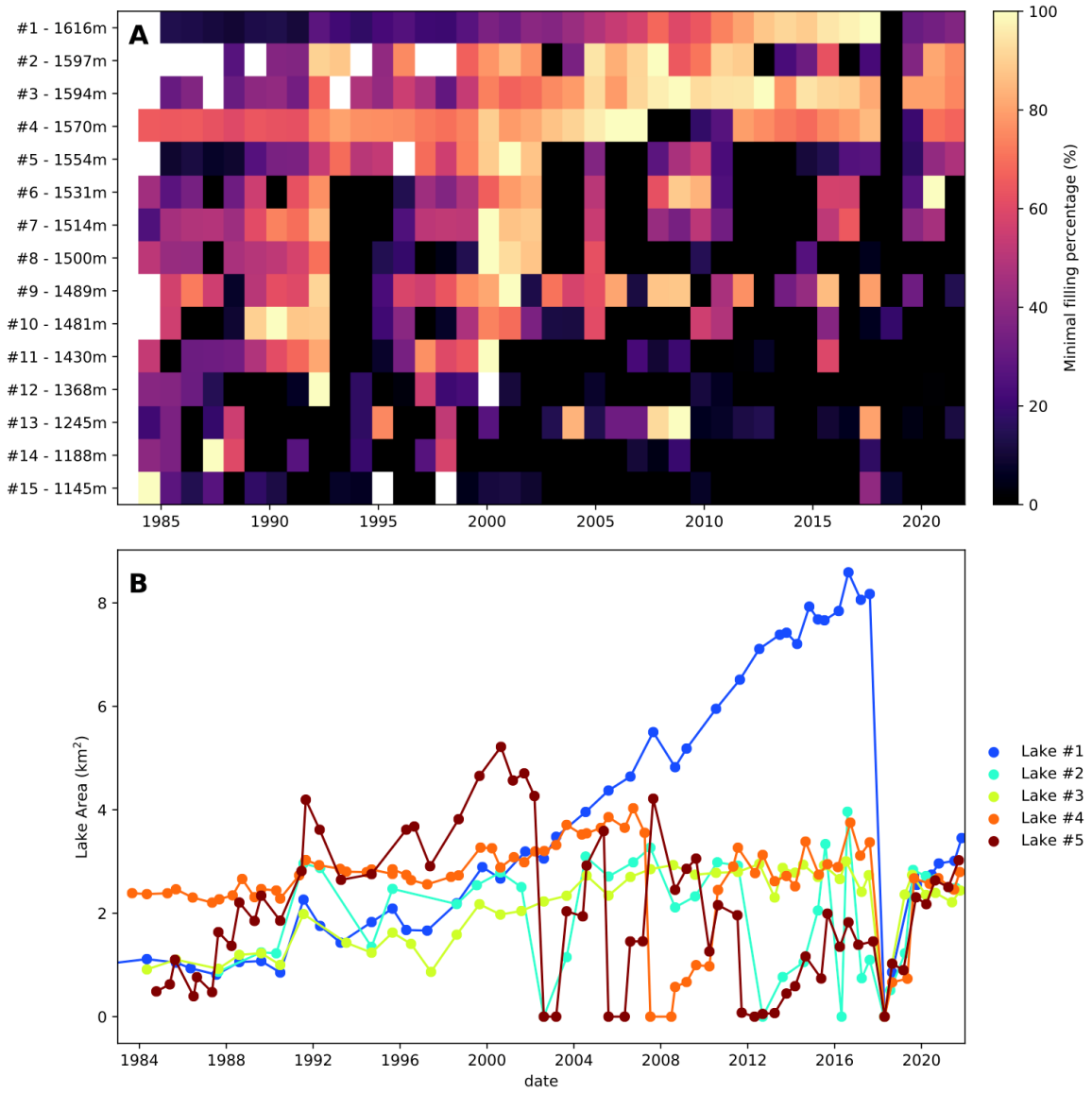

Figure 4 – Multi-decadal supraglacial lake evolution - (**A**) The percent fill of the lakes since 1983 relative to the largest area observed over the 1983-2022 period is shown. Where multiple areas are estimated for a year, the minimum value is shown, which generally indicates that the lake emptied in that year. The lake contours used to calculate the area are digitized from the Landsat archive (*Methods*). The altitude of each lake is indicated next to the lake number. (**B**) The area in km^2 of the five highest lakes in elevation as a function of time is plotted (all lakes are shown in *Fig. S10*). We note Lake 1 could be identified all the way back to 1972, but the data is trimmed to the timespan where all SGLs had data.

References and Notes:

1. L. C. Andrews, M. J. Hoffman, T. A. Neumann, G. A. Catania, M. P. Lüthi, R. L. Hawley, K. M. Schild, C. Ryser, B. F. Morriss, Seasonal evolution of the subglacial hydrologic system modified by supraglacial lake drainage in western Greenland. *Journal of Geophysical Research: Earth Surface*. 123, 1479–1496 (2018).
2. I. Bartholomew, P. Nienow, D. Mair, A. Hubbard, M. A. King, A. Sole, Seasonal evolution of subglacial drainage and acceleration in a Greenland outlet glacier. *Nature Geoscience*. 3, 408–411 (2010).
3. I. Bartholomew, P. Nienow, A. Sole, D. Mair, T. Cowton, M. King, S. Palmer, Seasonal variations in Greenland Ice Sheet motion: Inland extent and behaviour at higher elevations. *Earth and Planetary Science Letters*. 307, 271–278 (2011).
4. M. Hoffman, G. A. Catania, T. Neumann, L. Andrews, J. Rumrill, Links between acceleration, melting, and supraglacial lake drainage of the western Greenland Ice Sheet. *Journal of Geophysical Research: Earth Surface*. 116 (2011).
5. A. Sole, P. Nienow, I. Bartholomew, D. Mair, T. Cowton, A. Tedstone, M. A. King, Winter motion mediates dynamic response of the Greenland Ice Sheet to warmer summers. *Geophysical Research Letters*. 40, 3940–3944 (2013).
6. R. S. van de Wal, W. Boot, M. Van den Broeke, C. Smeets, C. Reijmer, J. Donker, J. Oerlemans, Large and rapid melt-induced velocity changes in the ablation zone of the Greenland Ice Sheet. *science*. 321, 111–113 (2008).
7. R. Van de Wal, C. Smeets, W. Boot, M. Stoffelen, R. Van Kampen, S. H. Doyle, F. Wilhelms, M. R. van den Broeke, C. Reijmer, J. Oerlemans, Self-regulation of ice flow varies across the ablation area in south-west Greenland. *Cryosphere*. 9, 603–611 (2015).
8. N. Maier, N. Humphrey, T. Meierbachtol, J. Harper, Deformation motion tracks sliding changes through summer, western Greenland. *Journal of Glaciology*, 1–10 (2021).
9. L. A. Stevens, M. D. Behn, S. B. Das, I. Joughin, B. P. Noël, M. R. van den Broeke, T. Herring, Greenland Ice Sheet flow response to runoff variability. *Geophysical Research Letters*. 43, 11–295 (2016).
10. A. Derkacheva, F. Gillet-Chaulet, J. Mouginot, E. Jager, N. Maier, S. Cook, Seasonal evolution of basal environment conditions of Russell sector, West Greenland, inverted from satellite observation of surface flow. *The Cryosphere*. 15, 5675–5704 (2021).
11. J. Harper, T. Meierbachtol, N. Humphrey, J. Saito, A. Stansberry, Generation and fate of basal meltwater during winter, western Greenland Ice Sheet. *The Cryosphere*. 15, 5409–5421 (2021).
12. B. J. Davison, A. J. Sole, S. J. Livingstone, T. R. Cowton, P. W. Nienow, The influence of hydrology on the dynamics of land-terminating sectors of the Greenland Ice Sheet. *Frontiers in Earth Science*. 7, 10 (2019).
13. C. L. Benedek, I. C. Willis, Winter drainage of surface lakes on the Greenland Ice Sheet from Sentinel-1 SAR imagery. *The Cryosphere*. 15, 1587–1606 (2021).
14. L. S. Koenig, D. Lampkin, L. Montgomery, S. Hamilton, J. Turrin, C. Joseph, S. Moutsafa, B. Panzer, K. Casey, J. D. Paden, Wintertime storage of water in buried supraglacial lakes across the Greenland Ice Sheet. *The Cryosphere*. 9, 1333–1342 (2015).
15. D. J. Lampkin, L. Koenig, C. Joseph, J. E. Box, Investigating controls on the formation and distribution of wintertime storage of water in supraglacial lakes. *Frontiers in Earth Science*, 370 (2020).
16. R. Law, N. Arnold, C. Benedek, M. Tedesco, A. Banwell, I. Willis, Over-winter persistence of supraglacial lakes on the Greenland Ice Sheet: Results and insights from a new model. *Journal of Glaciology*. 66, 362–372 (2020).
17. L. Schröder, N. Neckel, R. Zindler, A. Humbert, Perennial supraglacial lakes in Northeast Greenland observed by polarimetric SAR. *Remote Sensing*. 12, 2798 (2020).
18. M. J. Hoffman, M. Perego, L. C. Andrews, S. F. Price, T. A. Neumann, J. V. Johnson, G. Catania, M. P. Lüthi, Widespread moulin formation during supraglacial lake drainages in Greenland. *Geophysical Research Letters*. 45, 778–788 (2018).
19. P. Christoffersen, M. Bougamont, A. Hubbard, S. H. Doyle, S. Grigsby, R. Pettersson, Cascading lake drainage on the Greenland Ice Sheet triggered by tensile shock and fracture. *Nature communications*. 9, 1–12 (2018).
20. J. Mejía, J. Gulley, C. Trunz, M. Covington, T. Bartholomaus, S. Xie, T. Dixon, Isolated cavities dominate Greenland ice sheet dynamic response to lake drainage. *Geophysical Research Letters*, 48, 19 (2021)
21. A. A. W. Fitzpatrick, A. L. Hubbard, J. Box, D. J. Quincey, D. Van As, A. Mikkelsen, S. H. Doyle, C. Dow,

B. Hasholt, G. A. Jones, A decade (2002–2012) of supraglacial lake volume estimates across Russell Glacier, West Greenland. *The Cryosphere*. 8, 107–121 (2014).
22. B. Vandecrux, M. MacFerrin, H. Machguth, W. T. Colgan, D. van As, A. Heilig, C. M. Stevens, C. Charalampidis, R. S. Fausto, E. M. Morris, Firn data compilation reveals widespread decrease of firn air content in western Greenland. *The Cryosphere*. 13, 845–859 (2019).
23. C. F. Dow, M. A. Werder, S. Nowicki, R. T. Walker, Modeling Antarctic subglacial lake filling and drainage cycles. *The Cryosphere*. 10, 1381–1393 (2016).
24. S. J. Livingstone, D. J. Utting, A. Ruffell, C. D. Clark, S. Pawley, N. Atkinson, A. C. Fowler, Discovery of relict subglacial lakes and their geometry and mechanism of drainage. *Nature communications*. 7, 1–9 (2016).
25. O. Gagliardini, D. Cohen, P. Råback, T. Zwinger, Finite-element modeling of subglacial cavities and related friction law. *Journal of Geophysical Research: Earth Surface*. 112 (2007)
26. C. Helanow, N. R. Iverson, J. B. Woodard, L. K. Zoet, A slip law for hard-bedded glaciers derived from observed bed topography. *Science Advances*. 7, eabe7798 (2021).
27. T. C. Bartholomaus, R. S. Anderson, S. P. Anderson, Response of glacier basal motion to transient water storage. *Nature Geoscience*. 1, 33–37 (2008).
28. T. Cowton, P. Nienow, A. Sole, I. Bartholomew, D. Mair, Variability in ice motion at a land-terminating Greenlandic outlet glacier: the role of channelized and distributed drainage systems. *Journal of Glaciology*. 62, 451–466 (2016).
29. C. Schoof, The effect of cavitation on glacier sliding. *Proceedings of the Royal Society A: Mathematical, Physical and Engineering Sciences*. 461, 609–627 (2005).
30. V. C. Tsai, L. C. Smith, A. S. Gardner, H. Seroussi, A unified model for transient subglacial water pressure and basal sliding. *Journal of Glaciology*. 68, 390–400 (2022).
31. L. C. Andrews, G. A. Catania, M. J. Hoffman, J. D. Gulley, M. P. Lüthi, C. Ryser, R. L. Hawley, T. A. Neumann, Direct observations of evolving subglacial drainage beneath the Greenland Ice Sheet. *Nature*. 514, 80 (2014).
32. M. J. Hoffman, L. C. Andrews, S. F. Price, G. A. Catania, T. A. Neumann, M. P. Lüthi, J. Gulley, C. Ryser, R. L. Hawley, B. Morriss, Greenland subglacial drainage evolution regulated by weakly connected regions of the bed. *Nature communications*. 7, 13903 (2016).
33. C. Ryser, M. P. Lüthi, L. C. Andrews, G. A. Catania, M. Funk, R. Hawley, M. Hoffman, T. A. Neumann, Caterpillar-like ice motion in the ablation zone of the Greenland ice sheet. *Journal of Geophysical Research: Earth Surface*. 119, 2258–2271 (2014).
34. C. Rada, C. Schoof, Channelized, distributed, and disconnected: subglacial drainage under a valley glacier in the Yukon. *Cryosphere*. 12 (2018).
35. D. Chandler, J. Wadham, G. Lis, T. Cowton, A. Sole, I. Bartholomew, J. Telling, P. Nienow, E. Bagshaw, D. Mair, Evolution of the subglacial drainage system beneath the Greenland Ice Sheet revealed by tracers. *Nature Geoscience*. 6, 195–198 (2013).
36. D. M. Chandler, J. L. Wadham, P. W. Nienow, S. H. Doyle, A. J. Tedstone, J. Telling, J. Hawkings, J. D. Alcock, B. Linhoff, A. Hubbard, Rapid development and persistence of efficient subglacial drainage under 900 m-thick ice in Greenland. *Earth and Planetary Science Letters*. 566, 116982 (2021).
37. T. R. Chudley, P. Christoffersen, S. H. Doyle, M. Bougamont, C. M. Schoonman, B. Hubbard, M. R. James, Supraglacial lake drainage at a fast-flowing Greenlandic outlet glacier. *Proceedings of the National Academy of Sciences*. 116, 25468–25477 (2019).
38. S. B. Das, I. Joughin, M. D. Behn, I. M. Howat, M. A. King, D. Lizarralde, M. P. Bhatia, Fracture propagation to the base of the Greenland Ice Sheet during supraglacial lake drainage. *Science*. 320, 778–781 (2008).
39. L. A. Stevens, M. D. Behn, J. J. McGuire, S. B. Das, I. Joughin, T. Herring, D. E. Shean, M. A. King, Greenland supraglacial lake drainages triggered by hydrologically induced basal slip. *Nature*. 522, 73–76 (2015).
40. S. H. Doyle, A. L. Hubbard, C. F. Dow, G. A. Jones, A. A. W. Fitzpatrick, A. Gusmeroli, B. Kulessa, K. Lindback, R. Pettersson, J. E. Box, Ice tectonic deformation during the rapid in situ drainage of a supraglacial lake on the Greenland Ice Sheet. *Cryosphere*. 7, 129–140 (2013).
41. M. Tedesco, I. C. Willis, M. J. Hoffman, A. F. Banwell, P. Alexander, N. S. Arnold, Ice dynamic response to two modes of surface lake drainage on the Greenland ice sheet. *Environmental Research Letters*. 8, 034007 (2013).
42. T. Moon, I. Joughin, B. Smith, M. R. Van Den Broeke, W. J. Van De Berg, B. Noël, M. Usher, Distinct

patterns of seasonal Greenland glacier velocity. *Geophysical research letters*. 41, 7209–7216 (2014).
43. E. A. Podolskiy, K. Fujita, S. Sunako, Y. Sato, Viscoelastic Modeling of Nocturnal Thermal Fracturing in a Himalayan Debris-Covered Glacier. *Journal of Geophysical Research: Earth Surface*. 124, 1485–1515 (2019).
44. T. Sanderson, Thermal stresses near the surface of a glacier. *Journal of glaciology*. 20, 257–283 (1978).
45. R. S. Fausto, D. van As, K. D. Mankoff, B. Vandecrux, M. Citterio, A. P. Ahlstrøm, S. B. Andersen, W. Colgan, N. B. Karlsson, K. K. Kjeldsen, Programme for Monitoring of the Greenland Ice Sheet (PROMICE) automatic weather station data. *Earth System Science Data*. 13, 3819–3845 (2021).
46. J. E. Overland, Rare events in the Arctic. *Climatic Change*. 168, 1–13 (2021).
47. A. J. Tedstone, P. W. Nienow, A. J. Sole, D. W. F. Mair, T. R. Cowton, I. D. Bartholomew, M. A. King, Greenland ice sheet motion insensitive to exceptional meltwater forcing. *PNAS*. 110, 19719–19724 (2013).
48. S. H. Doyle, A. Hubbard, R. S. Van De Wal, J. E. Box, D. Van As, K. Scharrer, T. W. Meierbachtol, P. C. Smeets, J. T. Harper, E. Johansson, Amplified melt and flow of the Greenland ice sheet driven by late-summer cyclonic rainfall. *Nature Geoscience*. 8, 647–653 (2015).
49. E. Hanna, X. Fettweis, S. H. Mernild, J. Cappelen, M. H. Ribergaard, C. A. Shuman, K. Steffen, L. Wood, T. L. Mote, Atmospheric and oceanic climate forcing of the exceptional Greenland ice sheet surface melt in summer 2012. *International Journal of Climatology*. 34, 1022–1037 (2014).
50. M. Tedesco, X. Fettweis, Unprecedented atmospheric conditions (1948–2019) drive the 2019 exceptional melting season over the Greenland ice sheet. *The Cryosphere*. 14, 1209–1223 (2020).
51. B. Noël, W. J. van de Berg, S. Lhermitte, M. R. van den Broeke, Rapid ablation zone expansion amplifies north Greenland mass loss. *Science advances*. 5, eaaw0123 (2019).
52. M. Morlighem, C. N. Williams, E. Rignot, L. An, J. E. Arndt, J. L. Bamber, G. Catania, N. Chauché, J. A. Dowdeswell, B. Dorschel, BedMachine v3: Complete bed topography and ocean bathymetry mapping of Greenland from multibeam echo sounding combined with mass conservation. *Geophysical Research Letters*. 44, 11–051 (2017).
53. M. Morlighem, IceBridge BedMachine Greenland, Version 3. *Boulder, Colorado USA. NASA National Snow and Ice Data Center Distributed Active Archive Center* (2018), doi:https://doi.org/10.5067/2CIX82HUV88Y.
54. J. Mouginot, E. Rignot, A. A. Bjørk, M. Van Den Broeke, R. Millan, M. Morlighem, B. Noël, B. Scheuchl, M. Wood, Forty-six years of Greenland Ice Sheet mass balance from 1972 to 2018. *Proceedings of the National Academy of Sciences*. 116, 9239–9244 (2019).
55. J. K. Andersen, A. Kusk, J. P. M. Boncori, C. S. Hvidberg, A. Grinsted, Improved ice velocity measurements with Sentinel-1 TOPS interferometry. *Remote Sensing*. 12, 2014 (2020).
56. A. Solgaard, A. Kusk, J. P. Merryman Boncori, J. Dall, K. D. Mankoff, A. P. Ahlstrøm, S. B. Andersen, M. Citterio, N. B. Karlsson, K. K. Kjeldsen, Greenland ice velocity maps from the PROMICE project. *Earth System Science Data*. 13, 3491–3512 (2021).
57. A. Kusk, J. K. Andersen, J. M. Boncori, (VDE, 2021), pp. 1–5.
58. P. Rizzoli, M. Martone, C. Gonzalez, C. Wecklich, D. B. Tridon, B. Bräutigam, M. Bachmann, D. Schulze, T. Fritz, M. Huber, Generation and performance assessment of the global TanDEM-X digital elevation model. *ISPRS Journal of Photogrammetry and Remote Sensing*. 132, 119–139 (2017).
59. A. Kusk, J. P. M. Boncori, J. Dall, (VDE, 2018), pp. 1–4.
60. C. Legleiter, M. Tedesco, L. Smith, A. Behar, B. Overstreet, Mapping the bathymetry of supraglacial lakes and streams on the Greenland ice sheet using field measurements and high-resolution satellite images. *The Cryosphere*. 8, 215–228 (2014).
61. A. Pope, T. A. Scambos, M. Moussavi, M. Tedesco, M. Willis, D. Shean, S. Grigsby, Estimating supraglacial lake depth in West Greenland using Landsat 8 and comparison with other multispectral methods. *The Cryosphere*. 10, 15–27 (2016).
62. P. Morin, C. Porter, M. Cloutier, I. Howat, M.-J. Noh, M. Willis, B. Bates, C. Willamson, K. Peterman, (2016), pp. EPSC2016-8396.
63. B. H. Hills, J. T. Harper, T. W. Meierbachtol, J. V. Johnson, N. F. Humphrey, P. J. Wright, Processes influencing heat transfer in the near-surface ice of Greenland's ablation zone. *The Cryosphere*. 12, 3215–3227 (2018).

Data Availability: All data used to generate this manuscript is currently archived and publicly available for download. Ice surface elevation: doi.org/10.5067/H0KUYVF53Q8M, Land/Ice classification: doi.org/10.5067/B8X58MQBFUPA, Bed topography: doi.org/10.5067/2CIX82HUV88Y, Snowline elevation: doi:10.18739/A2V40JZ6C. Sentinel-1 and Sentinel-2: https://scihub.copernicus.eu/, Landsat: https://earthexplorer.usgs.gov/, ArcticDEM: doi.org/10.7910/DVN/OHHUKH.

Acknowledgments: We acknowledge the U.S. Geological Survey for the use of Landsat products. Sentinel-1 & -2 data is provided by the European Space Agency (ESA) through the EU Copernicus program. We thank Poul Christoffersen for discussions which improved this work. **Funding**: This work was funded by the French National Research Agency grants ANR-19-CE01-0011-01 and ANR-17-CE01-0008 and the French space agency (CNES). JKA acknowledges support from DTU Space. **Author Contributions:** NM analyzed the data, identified the SGL drainages, and is the primary author of the manuscript. JKA produced the DInSAR time series and contributed to the writing of the manuscript. JM produced the historical SGL record and contributed to the data analysis and writing of the manuscript. FG contributed to the data analysis and writing of the manuscript. OG contributed to the writing of the manuscript. **Competing Interests:** The authors declare they have no competing interests.

List of Supplementary Materials:

Figure S1 - Lake surface before and after drainage
Figure S2 - Changes at Nordenskiöld ice tongue
Figure S3 - Interpreted drainage pathways
Figure S4 - Vertical surface displacement components
Figure S5 - Hydropotential field near SGLs
Figure S6 - Bead and thread structure in relation to subglacial sinks
Figure S7 - Drainage event in relation to temperature variability
Figure S8 - Percent increase in annual velocity
Figure S9 - Other identified drainages and dynamic response
Figure S10 - Historical SGL area changes
Figure S11 - Spline lake-bottom interpolation
Figure S12 - Map view of spline lake-bottom interpolation

Chapter B | Supplementary material for manuscripts

B.1 Supplementary material for "Improved ice velocity measurements with Sentinel-1 TOPS interferometry"

This appendix provides supplementary material for the manuscript in Appendix A.1 (presented in chapter 3.3).

The supplementary material contains the following Figures and Tables:

Figure S1 - Line-of-sight velocity transect plot (unwrapping error case)
Figure S2 - Uncertainty estimates for horizontal velocity components in DInSAR/OTR mosaic
Figure S3 - Additional example of coregistration refinements
Figure S4 - Azimuth phase gradients corresponding to Fig. S3
Figure S5 - Azimuth velocity measurements corresponding to image pair from Fig. 3-5
Figure S6 - Line-of-sight velocity measurements corresponding to image pair from Fig. 3-5
Table S1 - GPS comparison for measurements shown in Figs. S5-S6
Table S2 - Estimated offsets for measurements shown in Figs. S5-S6
Figure S7 - Azimuth velocity measurements corresponding to image pair from Fig. S3
Figure S8 - Line-of-sight velocity measurements corresponding to image pair from Fig. S3
Table S3 - GPS comparison for measurements shown in Figs. S7-S8
Table S4 - Estimated offsets for measurements shown in Figs. S7-S8

Supplementary Material for "Improved Ice Velocity Measurements with Sentinel-1 TOPS Interferometry"

Jonas Kvist Andersen[1,*], Anders Kusk[1], John Peter Merryman Boncori[1], Christine Schøtt Hvidberg[2], and Aslak Grinsted[2]

[1] DTU Space Institute, Technical University of Denmark (DTU), DK-2800 Kongens Lyngby, Denmark; jkvand@space.dtu.dk (J.K.A.); jme@space.dtu.dk (J.P.M.B.); ak@space.dtu.dk (A.K.)

[2] Niels Bohr Institute, University of Copenhagen, DK-2100 Copenhagen, Denmark; ch@nbi.ku.dk (C.S.H.), aslak@nbi.ku.dk (A.G.)

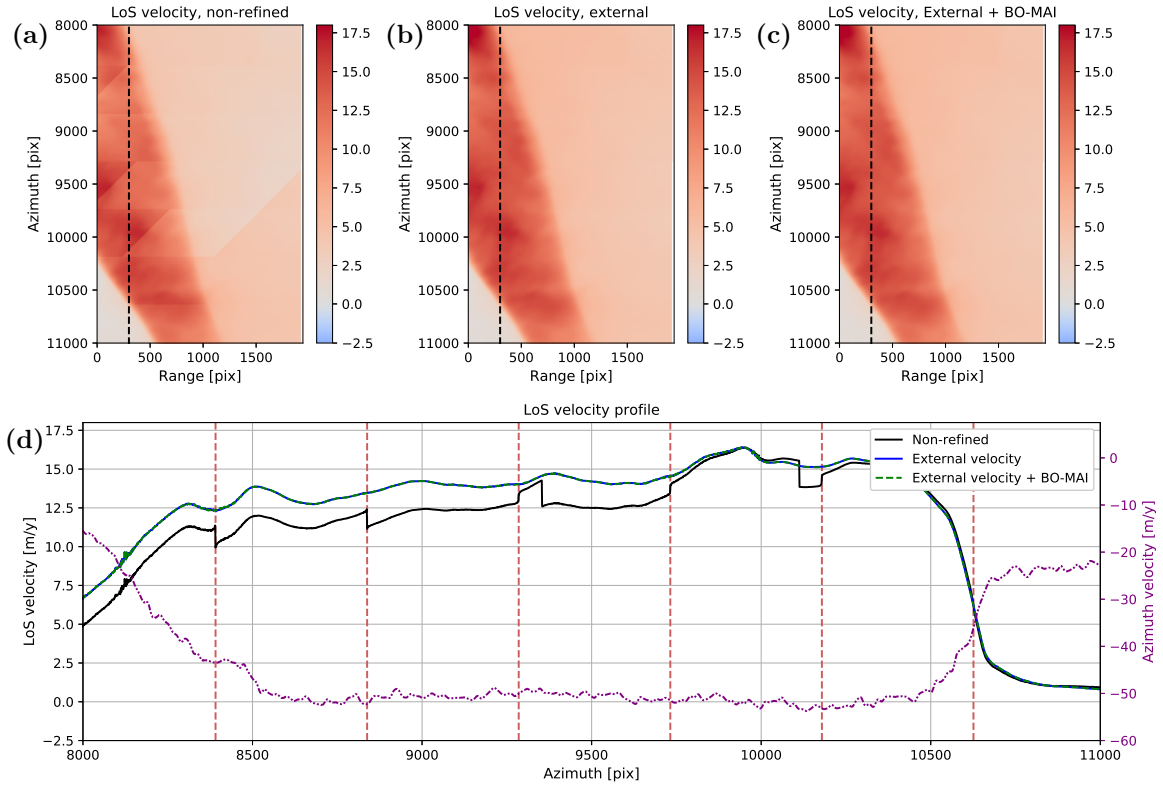

Figure S1: TOPS DInSAR line-of-sight velocity obtained using no coregistration refinement (**a**), a refinement based on the PROMICE multi-year velocity mosaic (**b**), and on the PROMICE multi-year velocity followed by BO-MAI (**c**). Panel (**d**) shows line-of-sight versus azimuth velocity (purple dashed line and right y-axis) along the profile indicated by the dashed line in (a)-(c). Azimuth velocities are based on the PROMICE multi-year mosaic. The plots cover the same region indicated by the dashed rectangle in Figure 5 in the main text, however for an interferogram generated from two different acquisitions (master/slave acquisitions: 2019-12-28 (S1B)/2020-01-03 (S1A), track: 112, descending).

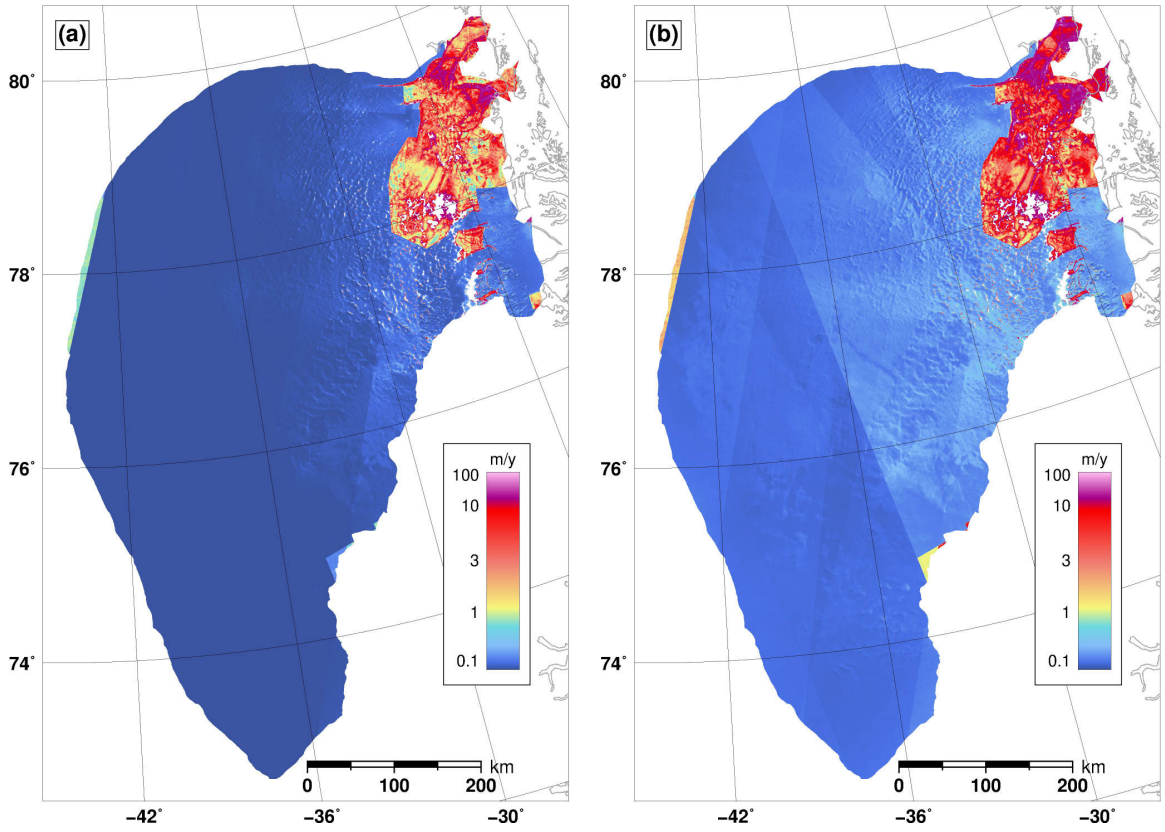

Figure S2: Horizontal velocity component 1σ uncertainties σ_{v_x} (**a**) and σ_{v_y} (**b**) for the fused DInSAR and offset tracking mosaic in Figure 6d in the main text.

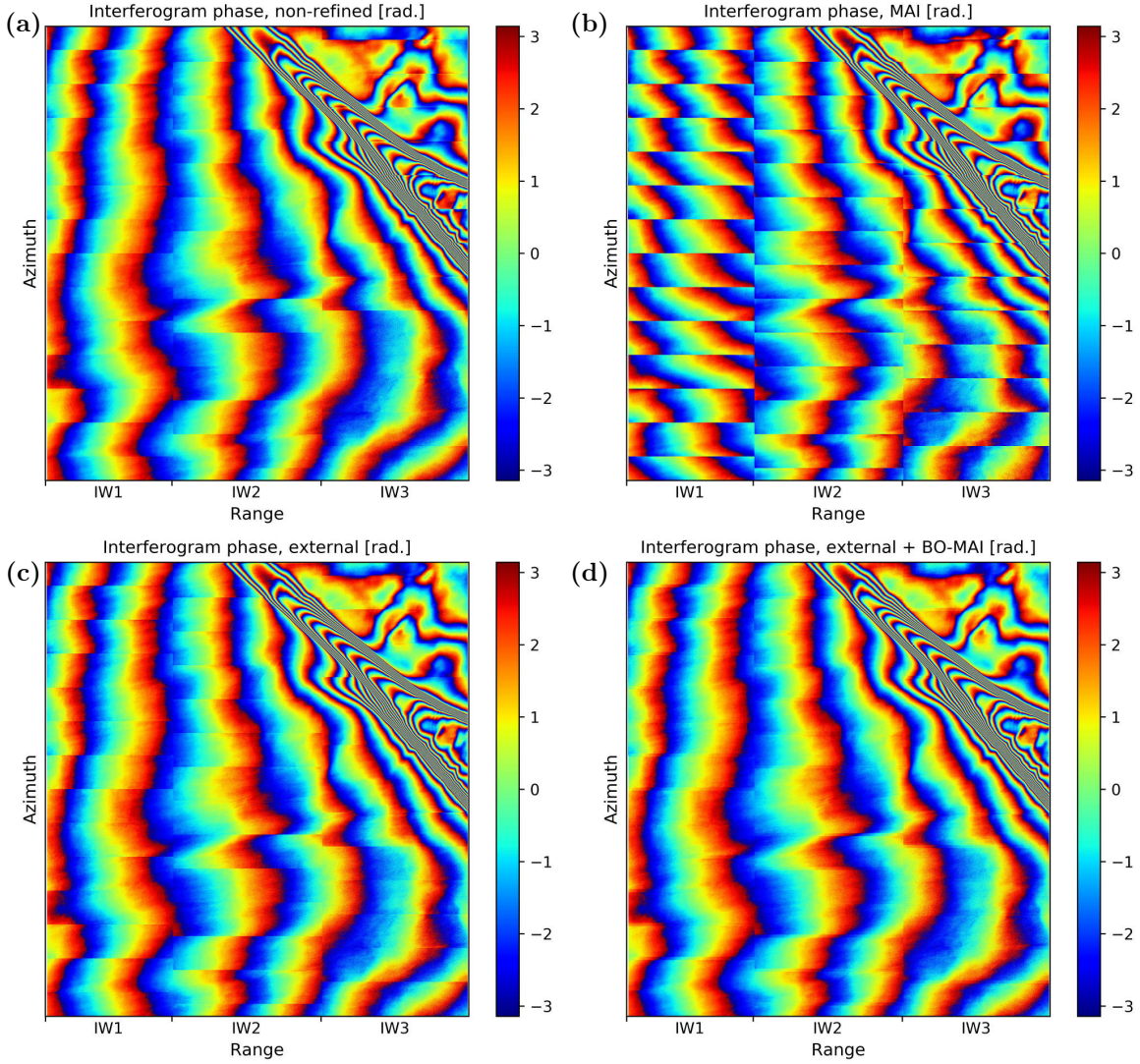

Figure S3: Wrapped interferogram phase obtained for a single Sentinel-1 image pair processed with (**a**) no coregistration refinement, (**b**) MAI coregistration refinement, (**c**) external multi-year velocity coregistration refinement, and (**d**) external multi-year refinement + BO-MAI coregistration refinement in burst overlaps. (Master/slave acquisitions: 2019-12-22 (S1B)/2019-12-28 (S1A), track: 31 ascending).

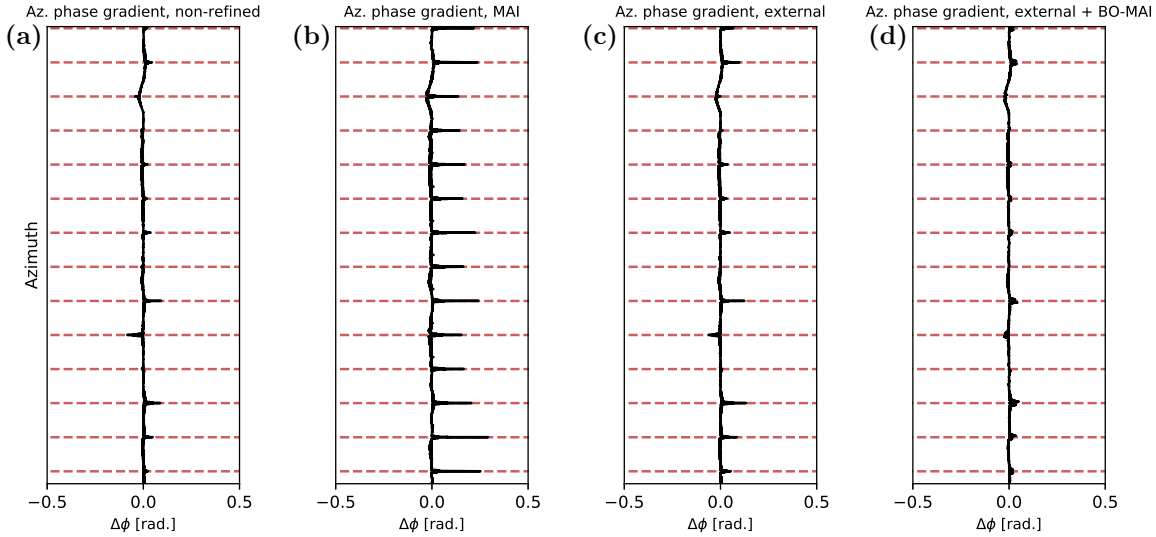

Figure S4: Plots showing the average azimuth gradient of the unwrapped interferogram phase in sub-swath IW2 for each of the four processing approaches presented in Figure **S3**. The dashed red lines indicate the location of azimuth burst overlaps.

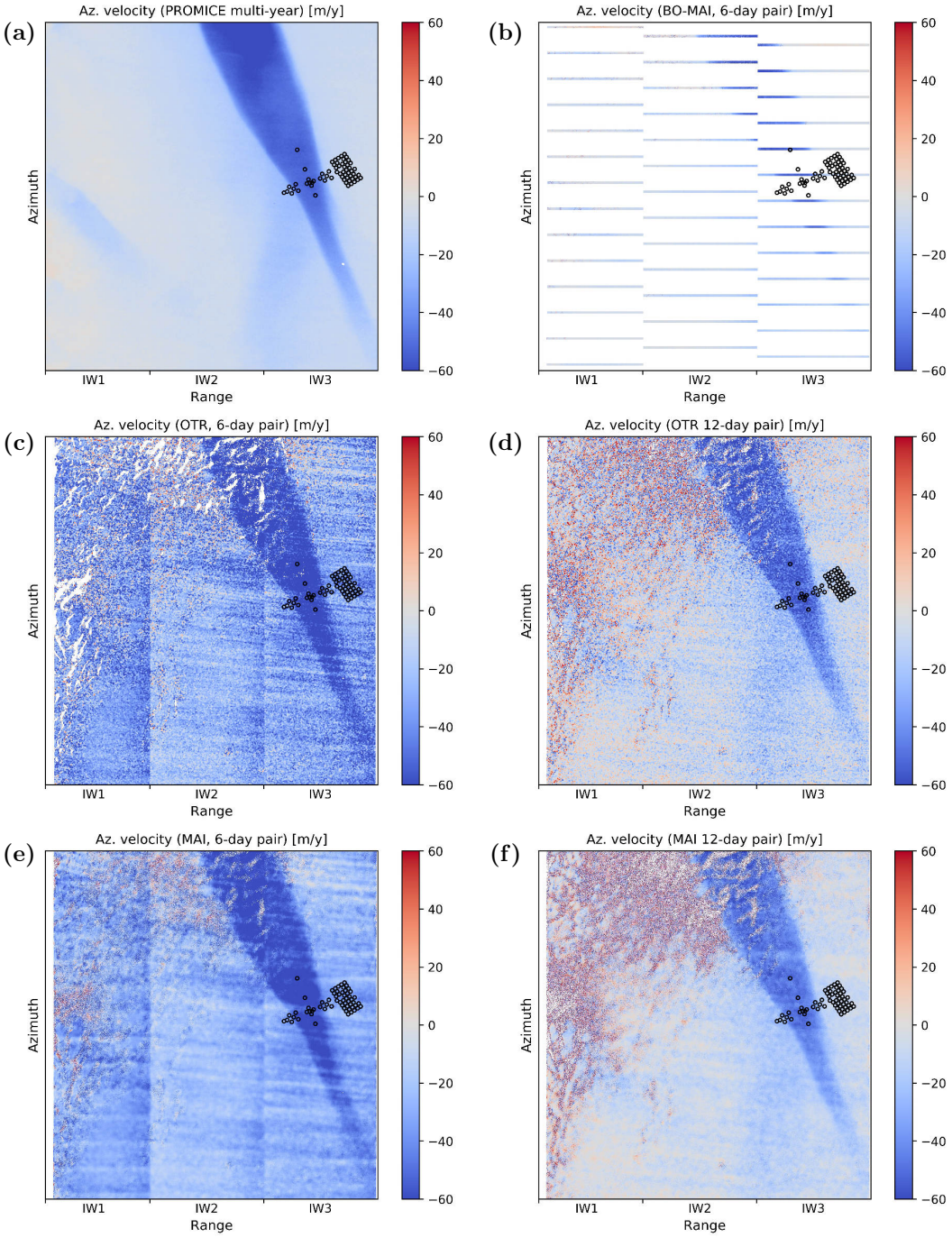

Figure S5: Azimuth velocity for the image pair presented in Figures 3-5 in the main text (Master/slave acquisitions: 2019-12-22 (S1A)/2019-12-28 (S1B), track: 112 descending) as measured by (**a**) a re-projection of the PROMICE multi-year mosaic, (**b**) BO-MAI, (**c**) intensity offset tracking, (**e**) MAI (same as Figure A1 in the main text). Additionally, (**d**) and (**f**) show azimuth velocity obtained for a 12-day pair (2019-12-22 (S1A)/2020-01-03 (S1A)), using intensity offset tracking and MAI, respectively.

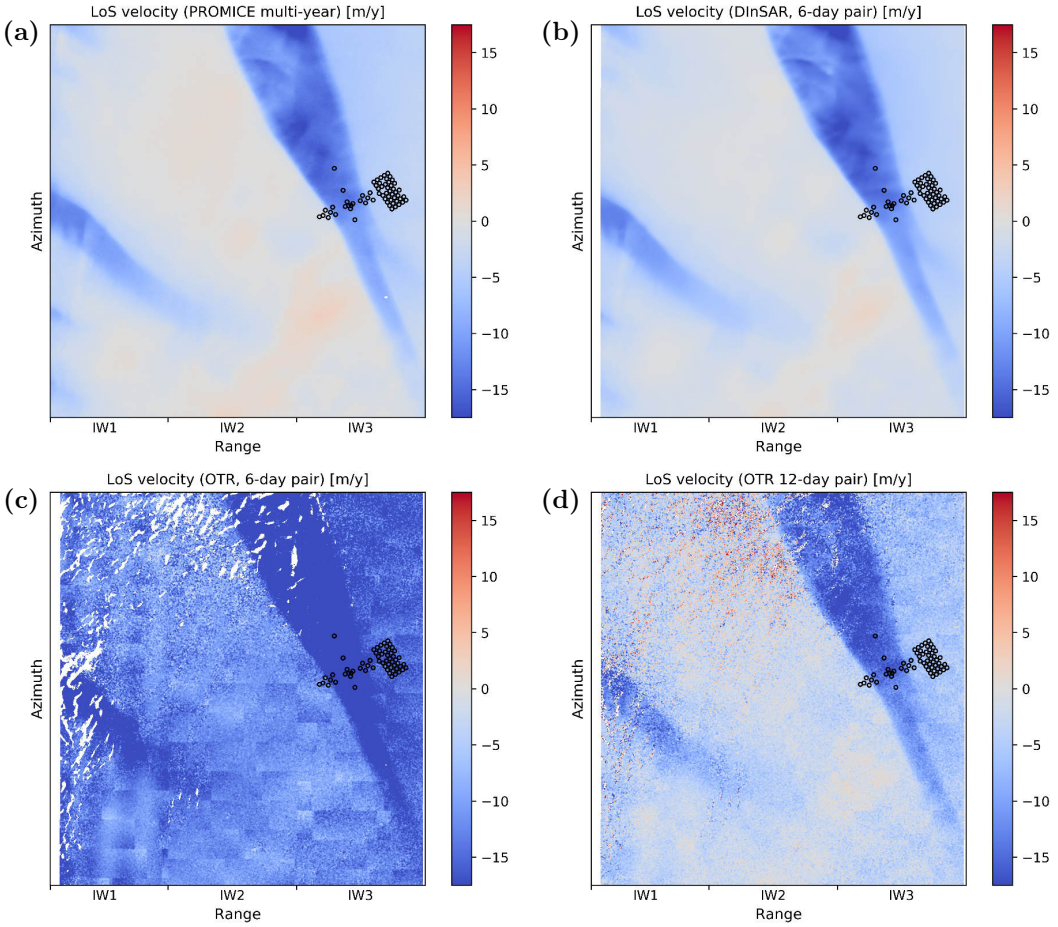

Figure S6: Line-of-sight velocity for the image pair presented in Figures 3-5 and A1 in the main text (master/slave acquisitions: 2019-12-22 (S1A)/2019-12-28 (S1B), track: 112 descending) as measured by (**a**) a re-projection of the PROMICE multi-year mosaic, (**b**) the TOPS DInSAR approach described in the main text (calibrated based on GCPs from the PROMICE multi-year mosaic), (**c**) intensity offset tracking. (**d**) Line-of-sight velocity obtained for a 12-day pair (2019-12-22 (S1A)/ 2020-01-03 (S1A)). Panel c shows an example of the "patch-like" artefact in the range offset tracking measurements, which is not found in the DInSAR measurements (panel b). It is most easily seen in the 6-day results, although it is also present in 12-day pairs, as seen in panel d.

Table S1: GPS comparison statistics for the azimuth and line-of-sight velocities shown in Figures **S5** and **S6**. Columns show mean and standard deviation of Δv_{az} and Δv_{LoS}, which indicate the difference in azimuth and line-of-sight velocity, respectively, between SAR and GPS measurements in m/y. 61 co-located GPS and SAR measurements were used in each case, except for BO-MAI, as only 7 GPS measurements lay inside burst overlaps.

	Δv_{az}		Δv_{LoS}	
Method	**mean**	**std.**	**mean**	**std.**
PROMICE multi-year mosaic	0.91	0.72	-0.32	0.21
Offset tracking (12-day)	-0.35	8.52	1.87	1.49
Offset tracking (6-day)	-22.02	13.63	10.99	1.70
DInSAR (6-day)	-	-	0.05	0.15
MAI (12-day)	1.46	3.66	-	-
MAI (6-day)	-18.24	8.92	-	-
BO-MAI (6-day)	-0.79	1.10	-	-

Table S2: Mean difference in azimuth/line-of-sight velocity between the offset tracking, MAI, DInSAR, and BO-MAI results presented in Figures **S5** and **S6** with respect to the PROMICE multi-year mosaic. All results are in m/y.

	Δv_{az} **mean**			Δv_{LoS} **mean**		
Method	**IW1**	**IW2**	**IW3**	**IW1**	**IW2**	**IW3**
Offset tracking (6-day)	-29.94	-16.80	-19.65	11.26	11.15	11.55
Offset tracking (12-day)	-0.75	-0.10	-0.05	1.99	1.55	2.17
DInSAR (6-day)	-	-	-	0.66	0.76	0.38
MAI (6-day)	-26.20	-13.63	-15.02	-	-	-
MAI (12-day)	0.49	1.69	1.99	-	-	-
BO-MAI (6-day)	-1.13	1.11	0.73	-	-	-

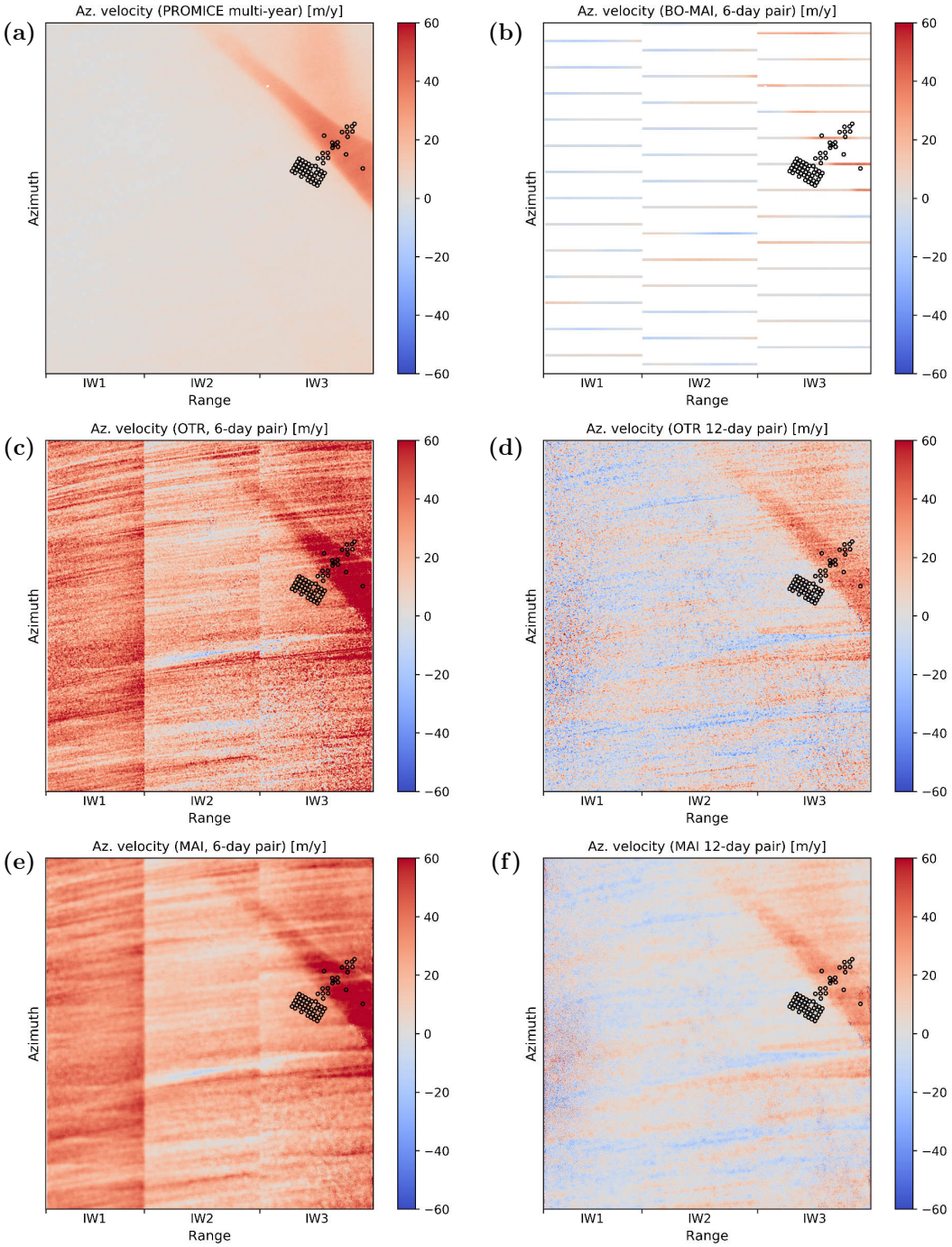

Figure S7: Azimuth velocity for the 6-day image pair shown in Figure **S3** (master/slave acquisitions: 2019-12-22 (S1B)/2019-12-28 (S1A), track: 31 ascending) as measured by (**a**) a re-projection of the PROMICE multi-year mosaic, (**b**) BO-MAI, (**c**) intensity offset tracking, (**e**) MAI. Panels (**d**) and (**f**) show the azimuth velocity obtained for a 12-day pair (2019-12-22 (S1B)/2020-01-03 (S1B)), using intensity offset tracking and MAI, respectively.

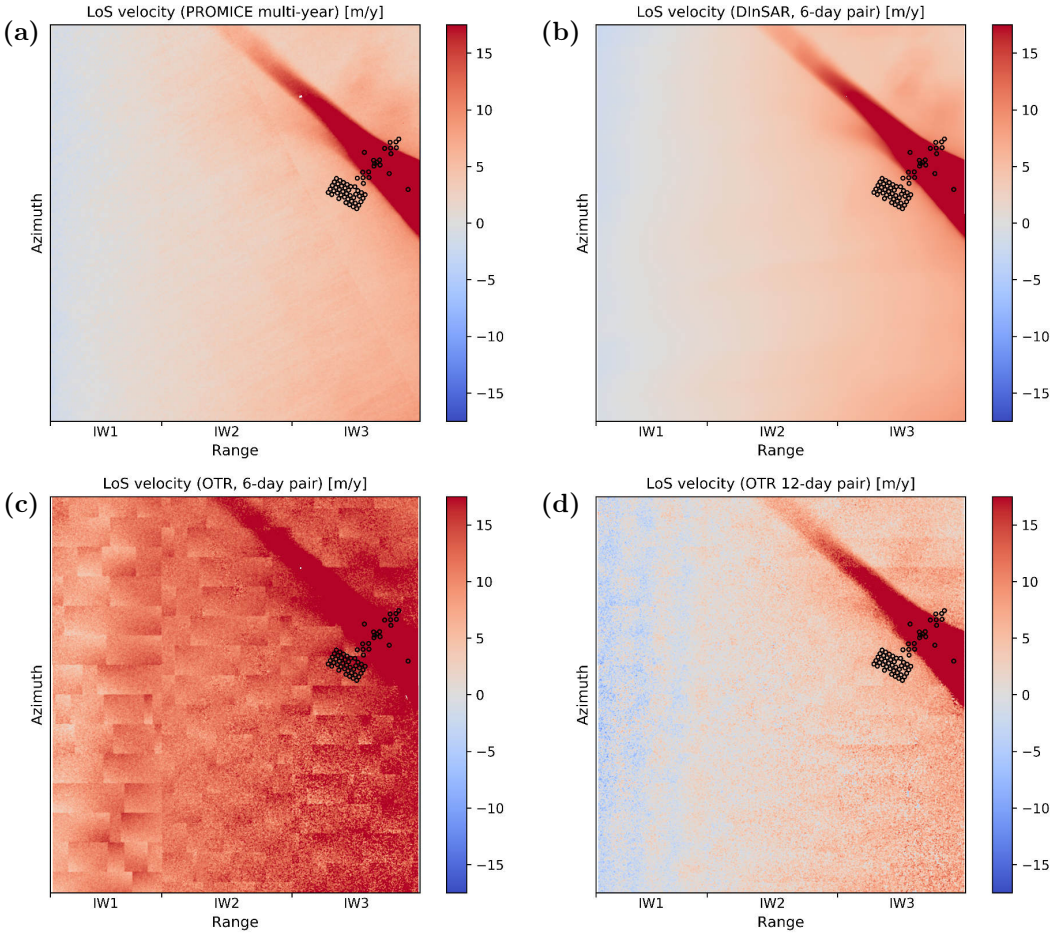

Figure S8: Line-of-sight velocity for the 6-day image pair shown in Figure **S3** (master/slave acquisitions: 2019-12-22 (S1B)/2019-12-28 (S1A), track: 31 ascending) as measured by (**a**) a re-projection of the PROMICE multi-year mosaic, (**b**) the TOPS DInSAR approach described in the main text (calibrated based on GCPs from the PROMICE multi-year mosaic), (**c**) intensity offset tracking. (**d**) Line-of-sight velocity obtained for a 12-day pair (2019-12-22 (S1B)/2020-01-03 (S1B)), using intensity offset tracking. Panel c shows an example of the "patch-like" artefact in the range offset tracking measurements, which is not found in the DInSAR measurements (panel b). It is most easily seen in the 6-day results, although it is also present in 12-day pairs, as seen in panel d.

Table S3: GPS comparison statistics for the azimuth and line-of-sight velocities shown in Figures **S7** and **S8**. Columns show mean and standard deviation of Δv_{az} and Δv_{LoS}, which indicate the difference in azimuth and line-of-sight velocity, respectively, between SAR and GPS measurements in m/y. 61 co-located GPS and SAR measurements were used in each case, except for BO-MAI, as only 5 GPS measurements lay inside burst overlaps.

	Δv_{az}		Δv_{LoS}	
Method	**mean**	**std.**	**mean**	**std.**
PROMICE multi-year mosaic	-0.63	0.64	0.57	0.37
Offset tracking (12-day)	-2.68	9.01	0.49	1.45
Offset tracking (6-day)	24.62	9.42	-9.13	1.81
DInSAR (6-day)	-	-	-0.23	0.19
MAI (12-day)	-4.91	5.60	-	-
MAI (6-day)	21.18	5.01	-	-
BO-MAI (6-day)	-3.49	2.36	-	-

Table S4: Mean difference in azimuth/line-of-sight velocity between the offset tracking, MAI, DInSAR, and BO-MAI results in Figures **S7** and **S8** with respect to the PROMICE multi-year mosaic. All results are in m/y.

	Δv_{az} **mean**			Δv_{LoS} **mean**		
Method	**IW1**	**IW2**	**IW3**	**IW1**	**IW2**	**IW3**
Offset tracking (12-day)	-2.34	-2.59	-2.01	0.83	0.53	0.13
Offset tracking (6-day)	32.44	15.86	23.27	-9.26	-9.53	-9.60
DInSAR (6-day)	-	-	-	0.11	0.03	-0.31
MAI (12-day)	-2.90	-3.03	-2.83	-	-	-
MAI (6-day)	32.78	14.56	20.15	-	-	-
BO-MAI (6-day)	-4.95	-5.55	-3.09	-	-	-

B.2 Supplementary material for "Connectivity approach for detecting unreliable DInSAR ice velocity measurements"

This appendix provides supplementary material for the manuscript in Appendix A.3 (presented in chapter 4.2).

The supplementary material contains the following Figures:

Figure S1 - Examples of coherence images used in simulations
Figure S2 - Examples of coherence, connectivity, and connectivity masks for simulated data
Figure S3 - Examples of observed coherence for image pairs processed in Section IV
Figure S4 - Connectivity reference point sensitivity analysis (example image pair 1)
Figure S5 - Connectivity reference point sensitivity analysis (example image pair 2)

Supplementary Material for "Connectivity Approach for Detecting Unreliable DInSAR Ice Velocity Measurements"

Jonas Kvist Andersen[1,*], **John Peter Merryman Boncori**[1], **and Anders Kusk**[1]

[1]DTU Space Institute, Technical University of Denmark (DTU), DK-2800 Kongens Lyngby, Denmark; jkvand@space.dtu.dk (J.K.A.); jme@space.dtu.dk (J.P.M.B.); ak@space.dtu.dk (A.K.)

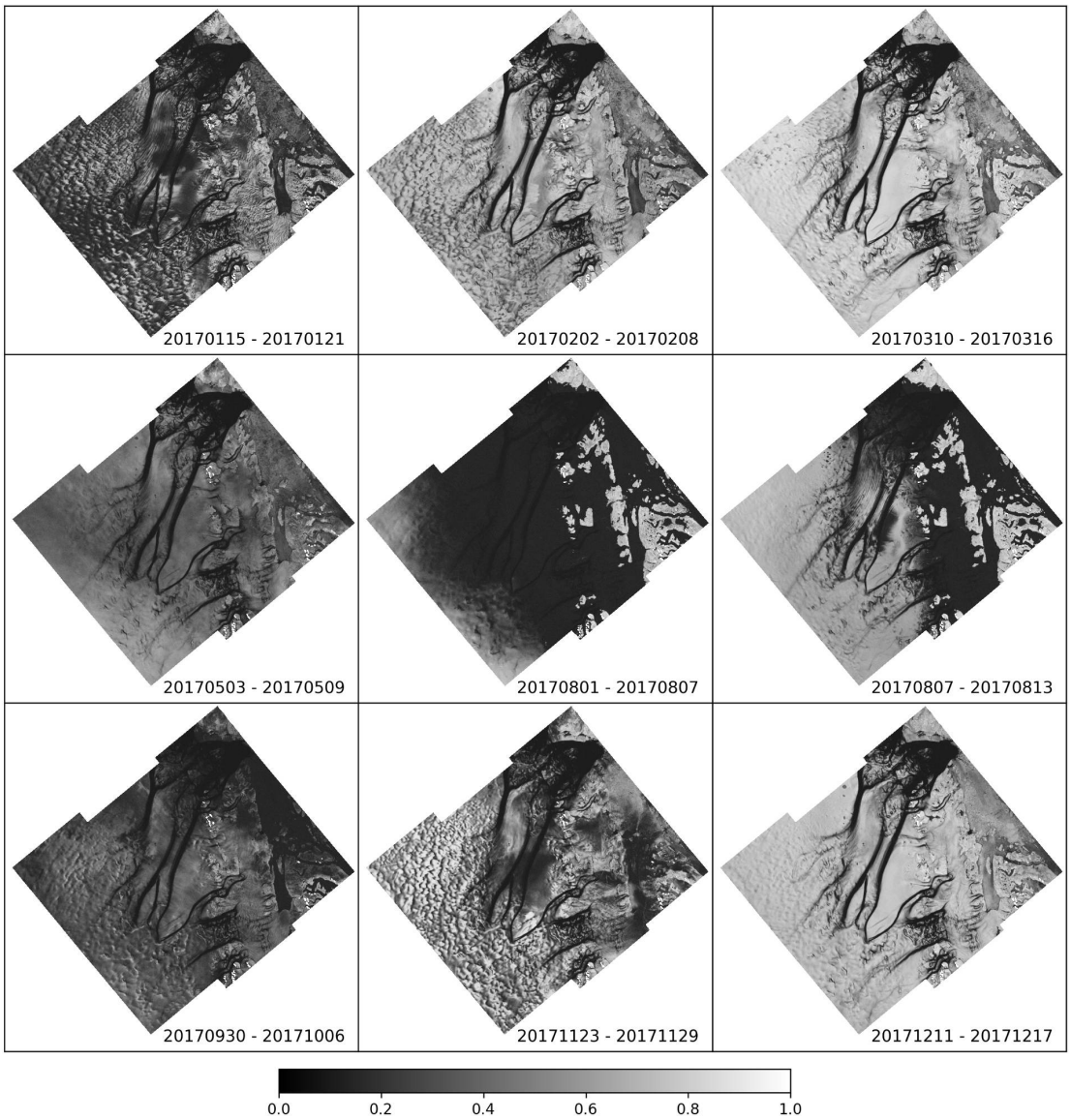

*Figure **S1**: Examples of observed coherence for 9 of the Sentinel-1 image pairs used as input for interferogram simulations (presented in Section III in the main text). The overall coherence level varies substantially, even between subsequent 6-day image pairs (e.g. the two shown image pairs from August). The highest average coherence levels were observed in March-April and December, while the lowest levels were observed in July-August and January.*

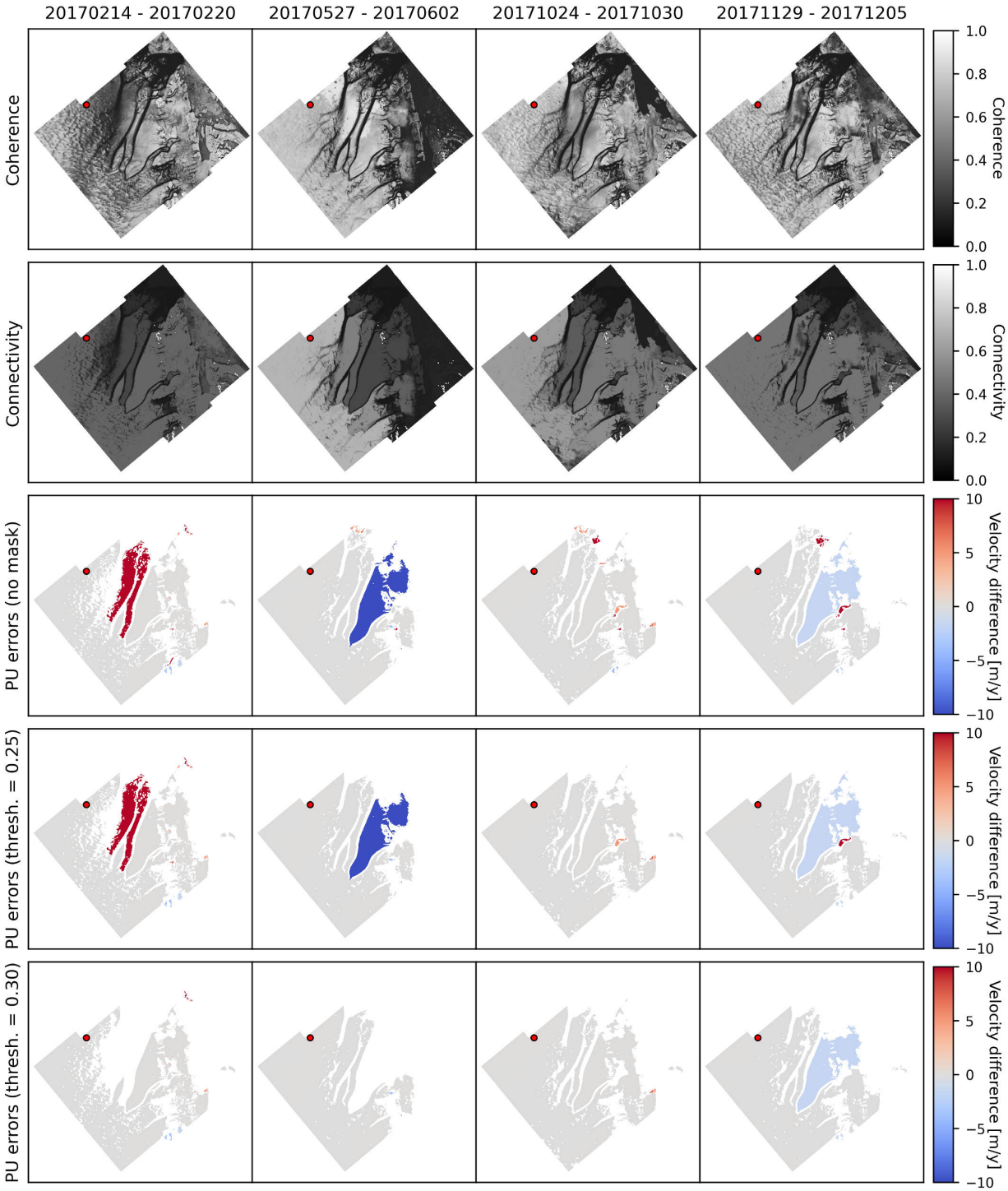

*Figure **S2**: Examples showing coherence, connectivity, and observed unwrapping errors (i.e. difference between input and output LoS velocity) with and without connectivity-based masking for three of the simulated interferograms presented in Section III in the main text. The two bottom rows show unwrapping error occurrences after masking with a connectivity threshold of 0.25 and 0.30, respectively. The connectivity reference point is indicated by a red dot. The dates of each image pair are indicated in the top of each column. For the two interferograms to the left, unwrapping errors of a large scale and magnitude are successfully masked out. The third column shows a case where only small-scale unwrapping errors are present - most of these are masked out, along with with some error-free pixels, leading to a decreased precision. Finally, the fourth column shows a case where a single phase cycle unwrapping error occurs in a large region where connectivity is relatively high, meaning that the error is undetected by connectivity masking (even with a threshold of 0.40).*

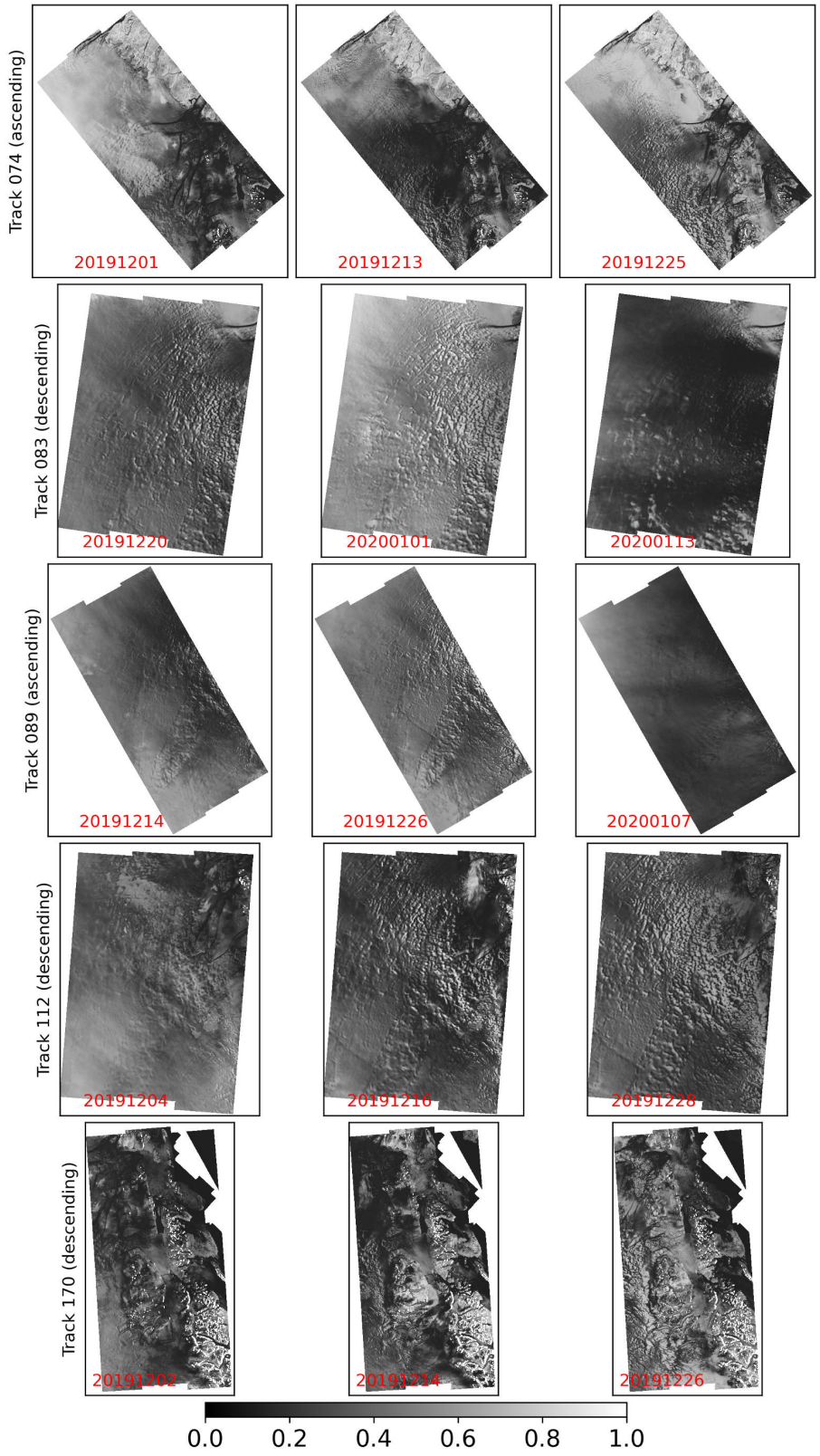

*Figure **S3**: Observed coherence for 3 of the image pairs in each of the Sentinel-1 tracks processed in the Northeast Greenland Ice Stream (NEGIS) data set, presented in Section IV in the main text. The red text indicates the acquisition date of the reference image (and all the interferograms have a temporal baseline of 6 days). Note that many of the interferograms show moderately low coherence levels, even towards the ice sheet interior.*

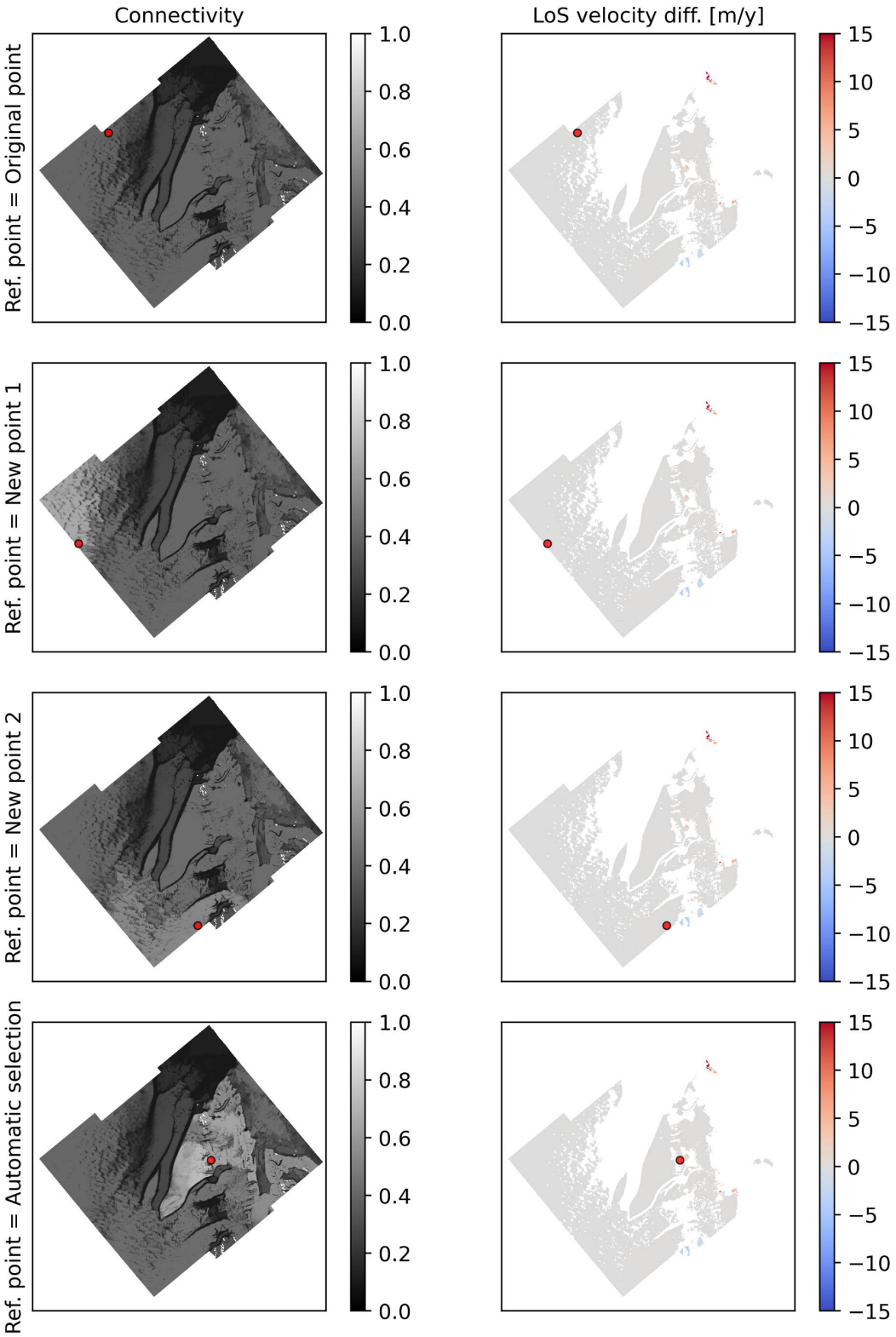

*Figure **S4**: Connectivity (left column) and LoS velocity difference obtained after masking with a connectivity threshold of 0.30. Each row shows the results obtained with a different reference point (indicated by a red dot) for the simulated interferogram with acquisition dates 20170214 and 20170220. The top row corresponds to the reference point presented in the manuscript (and in Figure S2) and the bottom row represents an automatically selected reference point (selected as the point of maximum coherence within the largest segment in the scene).*

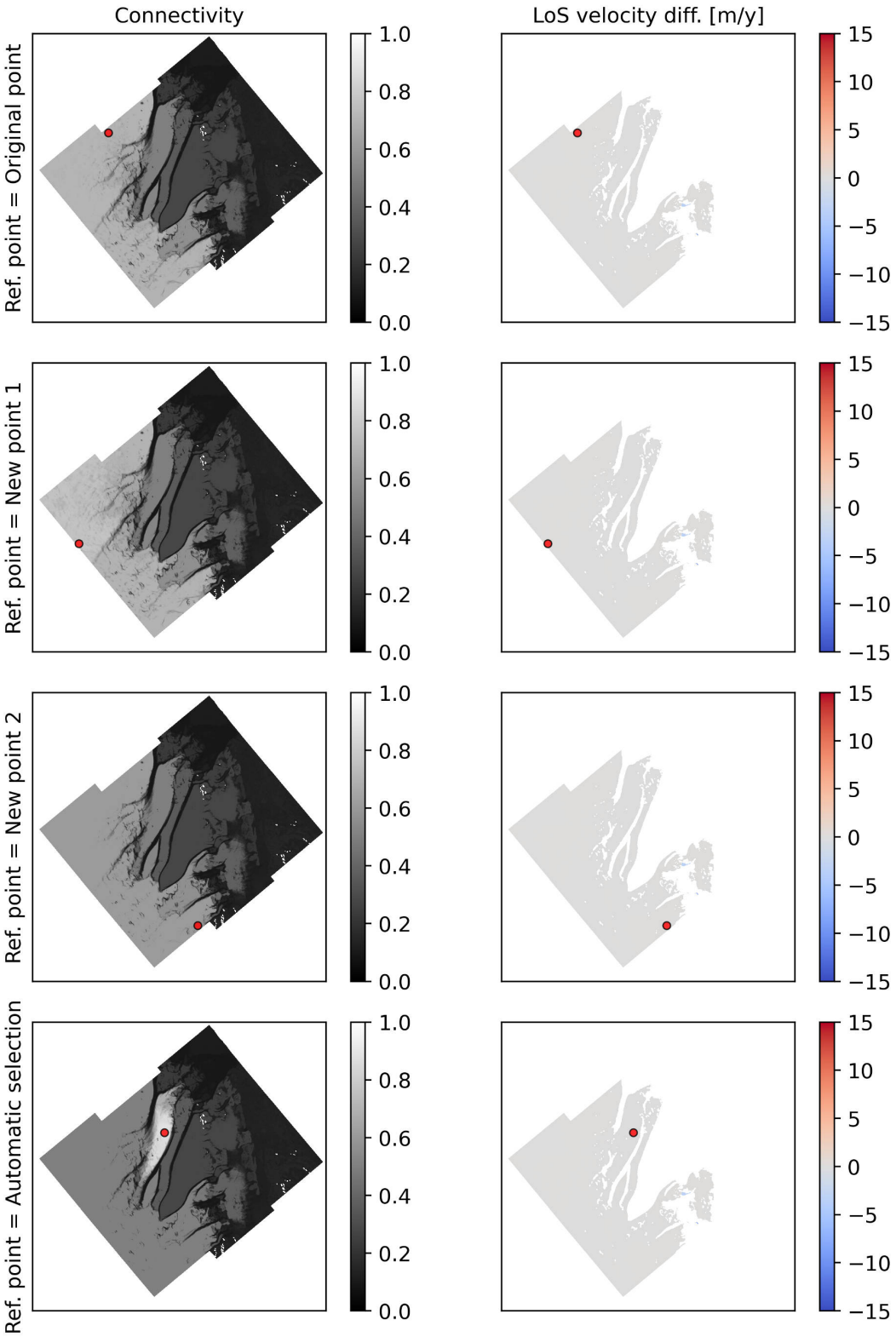

*Figure **S5**: Connectivity (left column) and LoS velocity difference obtained after masking with a connectivity threshold of 0.30. Each row shows the results obtained with a different reference point (indicated by a red dot) for the simulated interferogram with acquisition dates 20170527 and 20170602. The top row corresponds to the reference point presented in the manuscript (and in Figure S2) and the bottom row represents an automatically selected reference point (selected as the point of maximum coherence within the largest segment in the scene).*

B.3 Supplementary material for "Wintertime lake drainage cascade triggers large-scale ice flow response in Greenland"

This appendix provides supplementary material for the manuscript in Appendix A.5 (presented in chapter 5.3).

The supplementary material contains the following:

Section - Materials and Methods
Figure S1 - Lake surface before and after drainage
Figure S2 - Changes at Nordenskiöld ice tongue
Figure S3 - Interpreted drainage pathways
Figure S4 - Vertical surface displacement components
Figure S5 - Hydropotential field near SGLs
Figure S6 - Bead and thread structure in relation to subglacial sinks
Figure S7 - Drainage event in relation to temperature variability
Figure S8 - Percent increase in annual velocity
Figure S9 - Other identified drainages and dynamic response
Figure S10 - Historical SGL area changes
Figure S11 - Spline lake-bottom interpolation
Figure S12 - Map view of spline lake-bottom interpolation

NOTE: Please note that θ in eqs. (1)-(2) refers to the SAR look vector elevation angle (also referred to as the grazing angle), as indicated in Figure 2.8 in Chapter 2.6.

Science
AAAS

Supplementary Materials for

Wintertime lake drainage cascade triggers large-scale ice flow response in Greenland

Nathan Maier[1], Jonas Kvist Andersen[2], Jeremie Mouginot[1,3], Florent Gimbert[1] and Olivier Gagliardini[1]

[1]Univ. Grenoble Alpes, CNRS, IRD, Grenoble INP, IGE, 38000 Grenoble, France
[2]DTU Space, Tech. Univ. of Denmark, 2800 Kgs. Lyngby, Denmark
[3]Depart. of Earth System Science, Univ. of California- Irvine, Irvine CA 92697, USA
*

Correspondence to: ntmaier@gmail.com

This PDF file includes:

Materials and Methods

DInSAR Velocities

Differential SAR Interferometry (DInSAR) exploits the difference in phase signal between subsequent acquisitions, which, once unwrapped, is proportional to displacement in the radar line-of-sight (LoS). Although DInSAR only retrieves a single component of the velocity vector and is limited to regions in which interferometric coherence is retained, the measurement accuracy is significantly higher than that obtained in tracking-based measurements (~0.5 m/y vs. tens of m/y)(*54–56*), as the sensitivity is limited by the radar wavelength (several centimeters) rather than the sensor resolution (several meters). Furthermore, the achievable spatial resolution is about an order of magnitude better than that obtained with tracking.

We use Sentinel-1 image pairs with a 6-day temporal baseline (the shortest possible) from three tracks (T90, T25, and T127) to map displacements before, during, and after the lake drainages. LoS velocity measurements are generated following the approach outlined in (*55*) and (*57*), using a 2016-2019 multi-year average velocity map generated through PROMICE (*56*) and the TanDEM-X Digital Elevation Model (*58*) for image coregistration and phase flattening. Interferograms are multi-looked with a factor of 15 x 3 in range/azimuth and unwrapped using a Minimum Cost Flow algorithm. The resulting 6-day LoS velocity maps have a pixel spacing of 50 m x 50 m and measurements from all tracks are resampled to the same (50 m x 50 m) grid. The DTU IPP software (*59*) is used for all interferometric processing steps.

In some cases, we use flow-projected velocities where LoS (Fig. S7) are rotated into the flow direction obtained by the 2016-2019 multi-year average velocity map (*56*), making the assumption that all motion is horizontally derived. This is used to compare the increased displacement resulting from the winter drainage to the multi-year average velocity (*Fig. S8*). Because the flood wave (described in more detail below) causes uplift and downlift as it moves into a region and then passes, the integrated displacement will mostly reflect horizontal motion.

Identifying winter lake drainages

We manually identified 15 winter supraglacial lake drainages during March of 2018 using all Sentinel-2 (ESA) and Landsat 8 (USGS) optical imagery acquired for the region between February 15th and April 29th, 2018. Freezing of the lake surface during winter provides a visually recognizable, near-roughness-free surface which is readily identified from the surrounding regions (*Fig. S1*). Optical imagery from the previous summer visually confirms these surfaces reflect locations of supraglacial lakes. Lake drainages are identified via the abrupt change from smooth surfaces to collapse basins from scene to scene, where the smooth frozen surfaces are observed to change to a highly fractured and depressed configuration. We interpret the fracture and depression to be the result from the loss of mechanical support provided by the underlying water, indicating drainage or partial drainage of the lake below the ice lid via hydrofracture. In the other instances, lakes were identified by the appearance of a new surface fracture observed

to intersect the lake, resulting in the roughness-free surface to entirely disappear or become greatly reduced in area from between two image scenes (*Fig. S1*). Similar surface features were also used to confirm winter drainage detection using other methods (*13*, *17*). In some of the identified drainages, thermally incised sinuous drainage pathways towards the fractures are also observed, indicating water flow towards the fracture (*Fig. S1*). The acceleration resulting from the lake drainages was identified first, thus the search window in time and space for finding the lakes was well constrained prior to the systematic image search. We also identify three smaller water features (supraglacial pots) that were inferred to drain in a region of high uplift. These were identified via changes in backscatter from Sentinel-1 (*13*, *17*). We interpret these features to be relic moulins.

Decomposing vertical and horizontal motion

We exploit the fact that the DInSAR measurements are sensitive to both horizontal and vertical motion to decompose the velocity into vertical and horizontal components using data from two ascending and descending overlapping Sentinel-1 tracks. Estimating the three-dimensional vector requires three spatio-temporally overlapping tracks with different viewing geometries. Here we estimate two components of the velocity: horizontal speed in the flow direction, u_{FD}, and vertical speed, u_v, using a priori constraints on the flow direction, enabling us to use only two spatio-temporally overlapping tracks. We use the horizontal flow direction from the PROMICE average velocity map (2016-2019) (*56*) and assume that this flow direction is the same throughout the drainage event. The measured LoS motion from each track can then be decomposed as:

$$u_{LoS} = cos\ \alpha\ cos\ \theta\ u_{FD} + sin\ \theta\ u_v \quad (1)$$

where $\alpha = \beta - \phi$ is the angle between the horizontal flow angle, β, and the ground-projected radar LoS (described by the angle φ). We use measurements from one ascending and one descending track to solve for the two unknowns, u_{FD} and u_v. The temporal overlap between the two tracks is 4.5 days, meaning that some uncertainty is added by the fact that the two measurement periods do not perfectly overlap. However, given the nature of the event, where the increased displacement is caused by a horizontally propagating velocity wave, we expect the displacement to be similar. We test this assumption and our inference of uplift by decomposing a synthetic wave model constrained by the observations (described in next section).

To reduce the noise from spatially correlated errors specific to each track, we estimate the change in, rather than absolute dynamics resulting from the drainage event. Hence, eq. (1) becomes:

$$du_{LoS} = cos\ \alpha\ cos\ \theta\ du_{FD} + sin\ \theta\ du_v \quad (2)$$

where du_{LoS} is the difference between the measured LoS velocity field and a reference field (taken as a DInSAR LoS measurement from the same track, prior to any of the drainages).

Decomposed Synthetic Wave Model

We decompose a synthetic coupled horizontal and vertical displacement wave using the same procedure as for the observed data to determine how the assumptions made to decompose the line-of-sight-velocities distort the retrieved fields. We model a coupled horizontal and vertical flowline velocity wave, which mimics a horizontal flow increase driven by bed separation, as gaussian kernels propagating across a 160 km flowline at a wave speed constrained by our data (0.03 – 0.17 m s^{-1}) (see *Calculating Drainage Velocities*). The width (σ between 10 and 30 km, width between 20 and 60 km) and amplitude (45 – 80 m yr^{-1} horizontal velocity increase, 0.1 - 0.25 m vertical displacement) of the waves were chosen to approximate those observed in the data. We then calculate the accumulated horizontal displacement and change in uplift that would occur between the two 6-day windows that overlap by 4.5 days to match the interval between the T90 and T25 orbital tracks. Finally, we decompose the signal using the mean orbital parameters from the T90 and T25 tracks.

Given the model parameters and assumptions, we find the best fit for the data retrieved fields is a horizontal (amplitude = 60 m yr^{-1}) and vertical uplift/bed separation wave (amplitude = 0.25 m) propagating at a velocity of 0.08 m s^{-1}. The best fit indicates the horizontal velocity wave is wider (σ = 15 km) and precedes (by 15 km) the uplift wave (σ = 10 km). These parameters capture the phase relationship between the peaks as well as the pre- and post-wave dips in vertical displacement observed in the decomposed fields. The phase difference between the decomposed and synthetic waves, as well as the pre-wave dip in vertical displacement indicates the fields are somewhat distorted compared to the original values due to the mismatch in temporal overlap. However, we still find we can clearly identify distinction between horizontal motion and vertical displacement, allowing us to infer vertical and horizontal fields from the decomposed data.

Estimating approximate SGL volumes

Depth retrieval based on empirical (*60*) or physical (*61*) multi-spectral methods cannot be applied to estimate SGL volumes due to the presence of an ice lid during winter. Examining the near 50-year time series (described below) also shows that many of the high elevation lakes never become ice-free even during summer. To circumvent these limitations and roughly estimate total SGL volume prior to drainage we interpolate the sub-lake bathymetry from 2 m resolution ArcticDEMs (*62*). We start by manually digitizing each lake-outline along the visible edge of the ice lid and remove this area from a corresponding ArcticDEM strip collected between 2013 and 2017 during times where the lake volume is inferred to be lower or similar to that during the 2018 winter. We then interpolate a lake bathymetry using a spline (MATLAB curve fitting toolbox, smoothing parameter 0.9) over seven SGL cross sections (*Fig. S11*). The fit relies on the local slope adjacent to the ice basin to estimate the lake depth (*Fig. S12*). The maximum lake depths agree well with those found by other methods (~4-10 m) (*60*, *61*). The ice lid elevation is estimated using the median of the intersecting points between the lake outline and the DEM. We can then estimate the lake volume by assuming a lid thickness of ~2 m which has been observed (*15*) and

modeled (*16*) at the end of winter and then integrate the volume at each DEM grid cell. We note that even though the method has high uncertainty, it overcomes the limitations of winter imagery while still being empirically based. We test the sensitivity of the volume estimates by repeating the procedure using 8 different DEMs for Lake 2, and show a consistency of +/- 11%. We note most of the lakes are identified with collapsed ice lids, such that actual volume of water that makes it to the bed cannot be confidently estimated, as some of the lakes may have only partially drained. Thus, we interpret these estimates as volume maximums which could have drained to the bed.

Interpreting drainage pathways

The decomposed velocity components demonstrate that the complex structure is a result of vertical uplift (*Fig. 2*) which were interpreted to represent primary drainage pathways. Using this interpretation, we manually delineate the major flow pathways using a map of the maximum LoS velocities recorded during the event, which retains the complex structure from the drainage site to the margin (*Fig. S3*). We identify two major westward pathways and one major northward drainage pathway, a secondary drainage pathway from the lake drainages that occur just upgradient of the Nordenskiöld trough, and a connector between the secondary and primary westward drainage pathways.

Calculating drainage velocities

We track the wave front and peaks for consecutive DInSAR velocity maps (using T90) to determine the position of the velocity wave through time along inferred drainage pathways. The wave front is defined as the first location on the ascending limb of the wave where LoS velocities are 10% higher than pre-drainage velocities. The wave peak is taken as the flowline maximum. We then differentiate the wave fronts or peaks between two consecutive flowline velocity profiles to get the distance traveled which is converted to velocity using the 6-day repeat period (*Fig. 3*).

Long-term SGL evolution

We document the evolution of the surface area for the 15 supraglacial lakes identified to drain during the event over the last 50 years. We downloaded 1275 optical images from the Landsat satellite record that began in 1972 (only 1983 onward is shown in *Fig. 4*), built a stack of sub-images for each lake and manually digitized their outline twice a year when possible, before May/June when the melt season begins and a second time between August and November at the end of the melt season. We then calculated the evolution of the area of the lakes (*Fig. 4*) through time to establish the historical context of the SGL evolution preceding the winter drainage event.

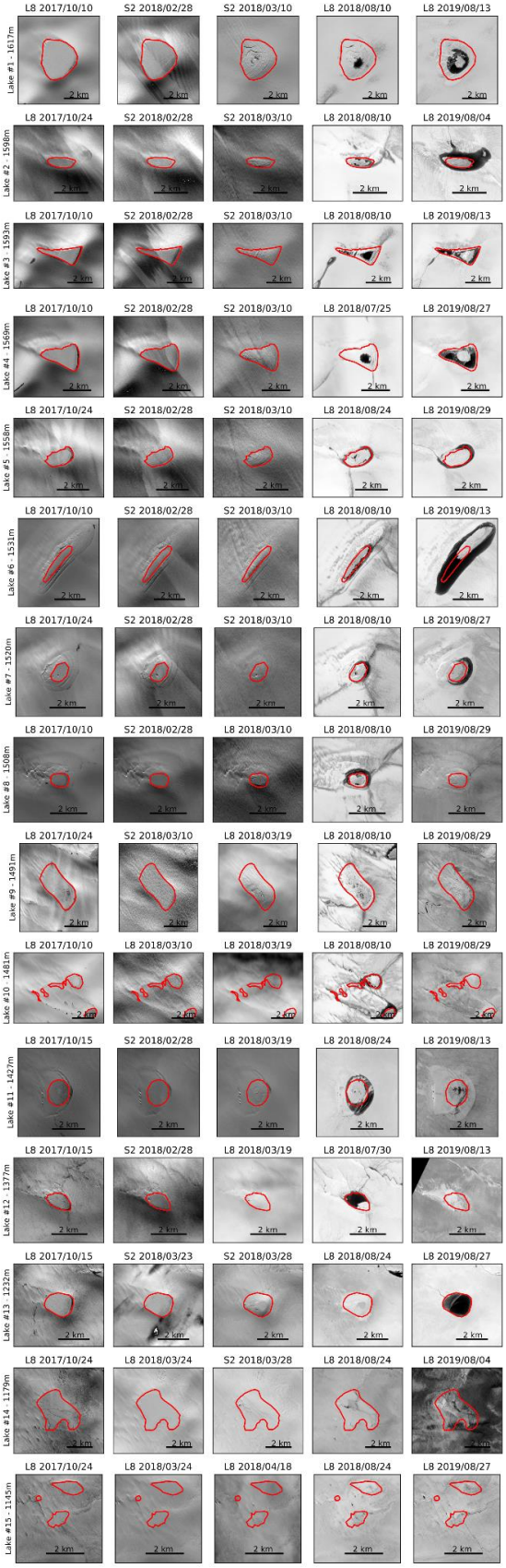
L8 2017/10/10
S2 2018/02/28
S2 2018/03/10
L8 2018/08/10
L8 2019/08/13
Lake #1 - 1617m
L8 2017/10/24
S2 2018/02/28
S2 2018/03/10
L8 2018/08/10
L8 2019/08/04
Lake #2 - 1598m
L8 2017/10/10
S2 2018/02/28
S2 2018/03/10
L8 2018/08/10
L8 2019/08/13
Lake #3 - 1593m
L8 2017/10/10
S2 2018/02/28
S2 2018/03/10
L8 2018/07/25
L8 2019/08/27
Lake #4 - 1569m
L8 2017/10/24
S2 2018/02/28
S2 2018/03/10
L8 2018/08/24
L8 2019/08/29
Lake #5 - 1558m
L8 2017/10/10
S2 2018/02/28
S2 2018/03/10
L8 2018/08/10
L8 2019/08/13
Lake #6 - 1531m
L8 2017/10/24
S2 2018/02/28
S2 2018/03/10
L8 2018/08/10
L8 2019/08/27
Lake #7 - 1520m
L8 2017/10/10
S2 2018/02/28
L8 2018/03/10
L8 2018/08/10
L8 2019/08/29
Lake #8 - 1508m
L8 2017/10/24
S2 2018/03/10
L8 2018/03/19
L8 2018/08/10
L8 2019/08/29
Lake #9 - 1491m
L8 2017/10/10
L8 2018/03/10
L8 2018/03/19
L8 2018/08/10
L8 2019/08/29
Lake #10 - 1481m
L8 2017/10/15
S2 2018/02/28
L8 2018/03/19
L8 2018/08/24
L8 2019/08/13
Lake #11 - 1427m
L8 2017/10/15
S2 2018/02/28
L8 2018/03/19
L8 2018/07/30
L8 2019/08/13
Lake #12 - 1377m
L8 2017/10/15
S2 2018/03/23
S2 2018/03/28
L8 2018/08/24
L8 2019/08/27
Lake #13 - 1232m
L8 2017/10/24
L8 2018/03/24
S2 2018/03/28
L8 2018/08/24
L8 2019/08/04
Lake #14 - 1179m
L8 2017/10/24
L8 2018/03/24
L8 2018/04/18
L8 2018/08/24
L8 2019/08/27
Lake #15 - 1145m
2 km

6

Figure S1 - Lake evolution before and after the drainage from Landsat (L8) and Sentinel-2 (S2) optical images. The red outlines indicate the lake perimeters in fall 2017 prior to the event.

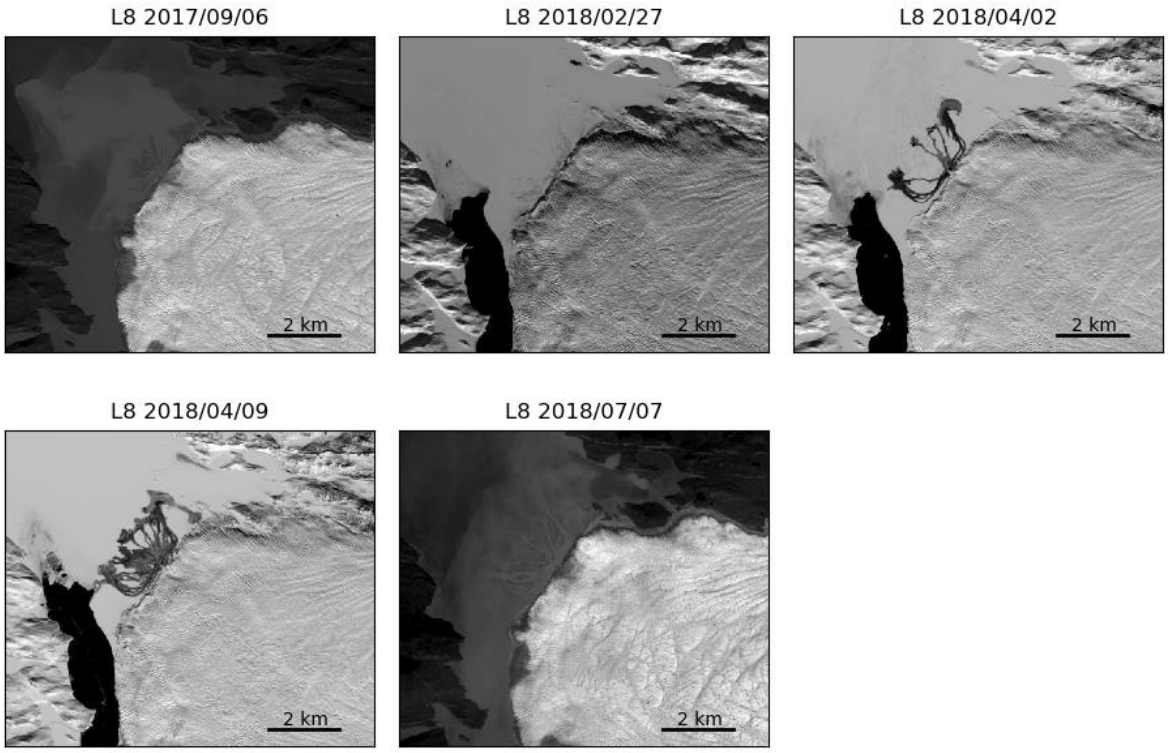

Figure S2 – Landsat images of the Nordenskiöld ice tongue showing the outwash in early April 2018 following supraglacial lake drainages. At this time of the year the surface of the sedimentary delta in front of Nordenskiöld is covered with snow, making it possible to clearly identify the areas swept by the flow.

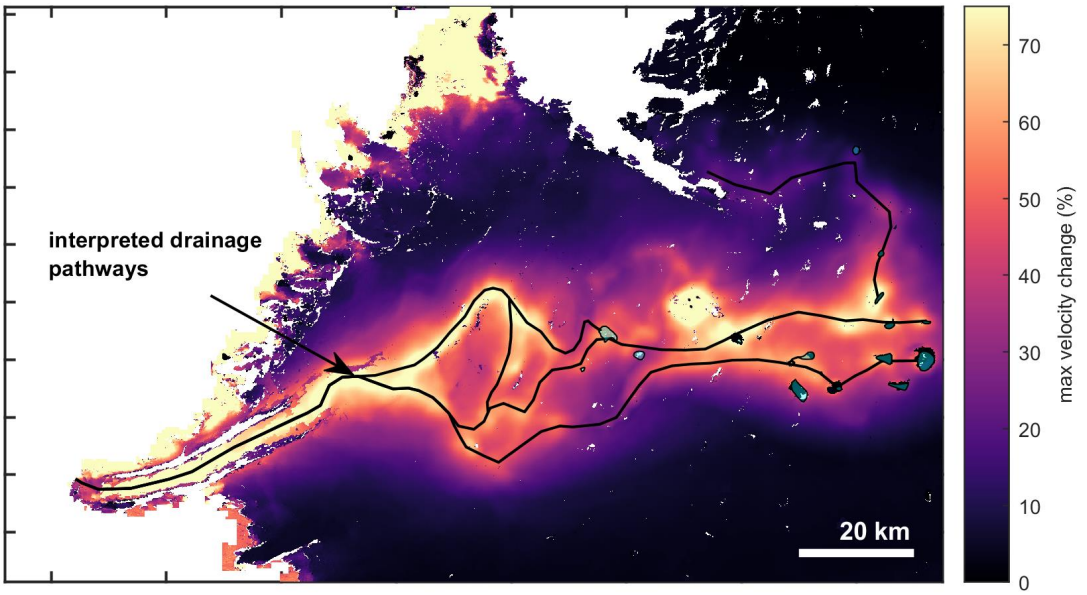

Figure S3 – Interpreted Drainage Pathways – Complex structure from max flow projected velocities during drainage event (track 90) were used to visually interpret inferred drainage pathways (black lines). Cyan fill shows drained lake locations.

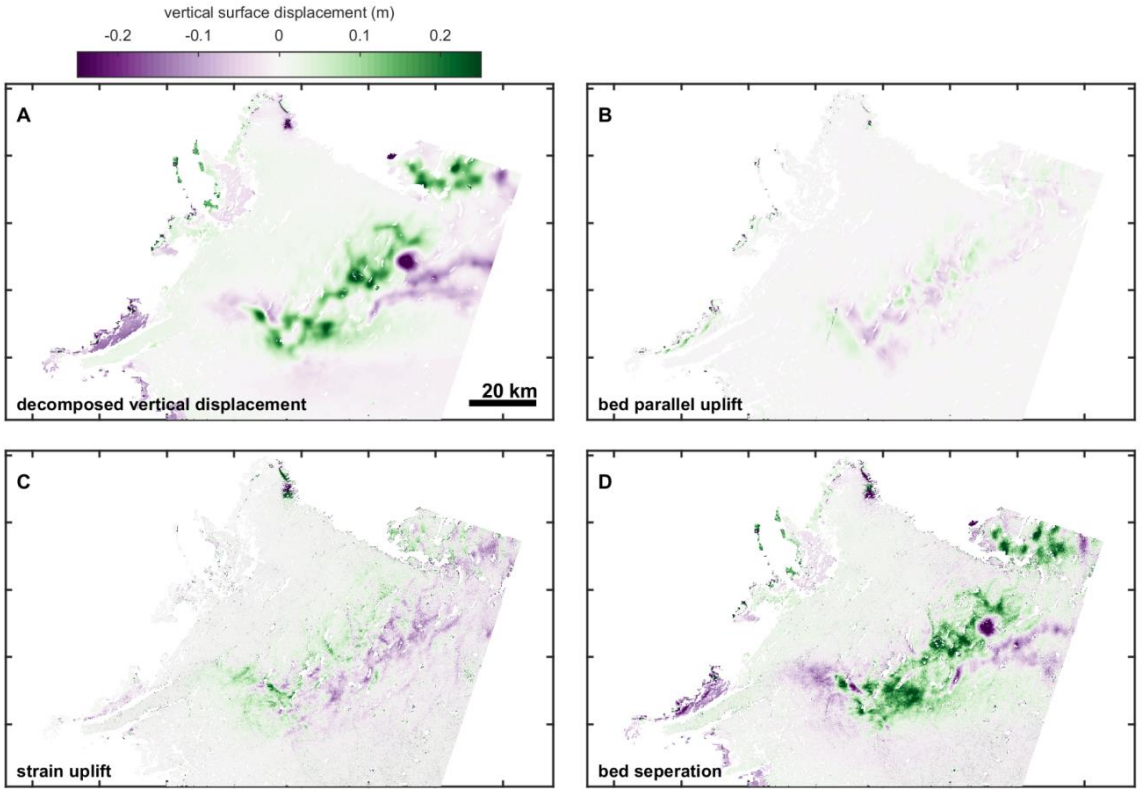

Figure S4 – Vertical surface displacement components – Decomposed vertical motion (**A**), bed parallel uplift (**B**), vertical displacement due to vertical strain (**C**), and bed separation (**D**). Vertical strain and bed separation were estimated with the decomposed horizontal velocity assuming changes in motion are derived from sliding. Bed separation is taken as the residual between the decomposed vertical motion and the bed parallel and vertical strain uplift.

10

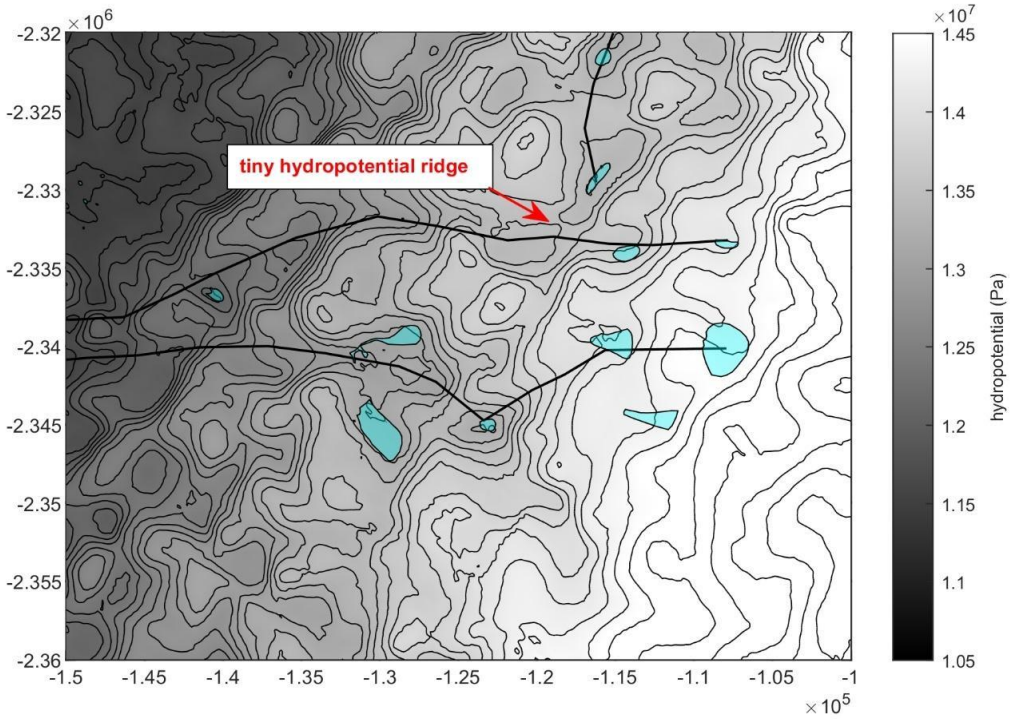

Figure S5 – Zoom of hydropotential for a region that incorporates the start of three major inferred drainage pathways. The two westward propagating drainage pathways are separated from the northernmost hydropotential pathway by a small ridge of high pressure (arrow). Hydropotential gradients were calculated assuming ice overburden pressure. Cyan regions show locations of supraglacial lakes that drained during the event.

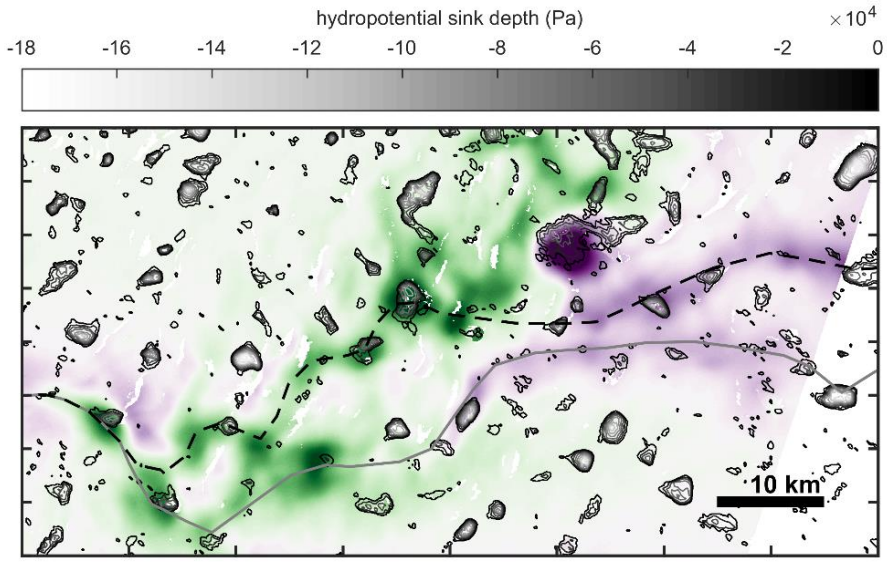

Figure S6 – Bead and thread uplift structure in relation to subglacial sinks and interpreted flowlines (same as shown on Fig. 2). Subglacial sinks are delineated with hydropotential contours.

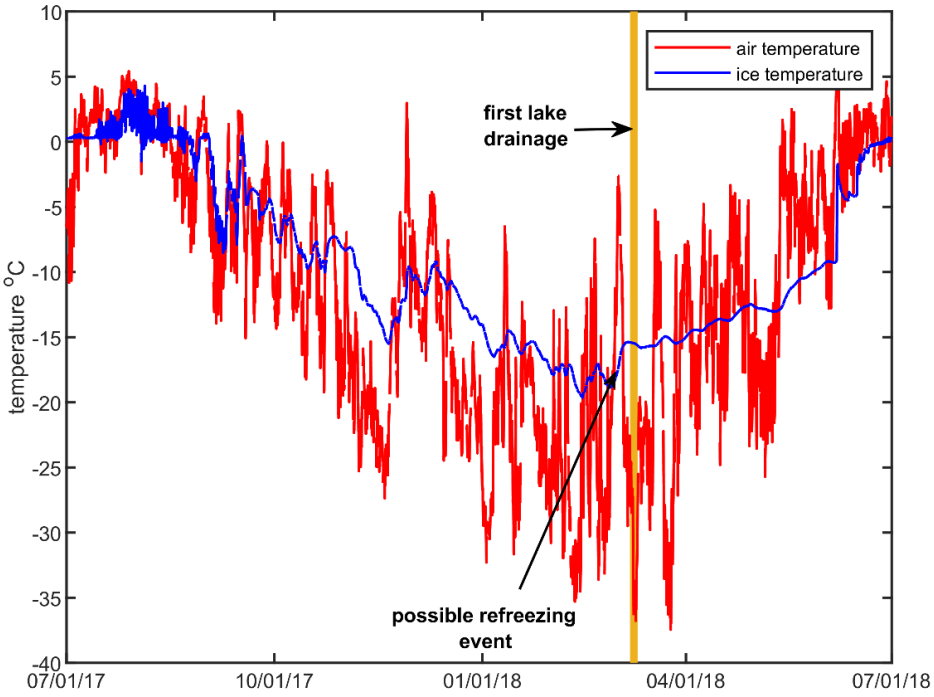

Figure S7 – Drainage event in relationship to observed temperature variability – Measured air temperature (2 meter) and ice temperature (1 meter) from the PROMICE UPE-U AWS station located ~200 km north of the drainage site at a similar elevation (*45*). Time series records 2018 winter heat wave and rapid cooling directly prior to first lake drainage. Ice temperature record (blue line) shows an increase in ice temperature as air temperatures drop, suggesting latent heat release from refreezing (*63*).

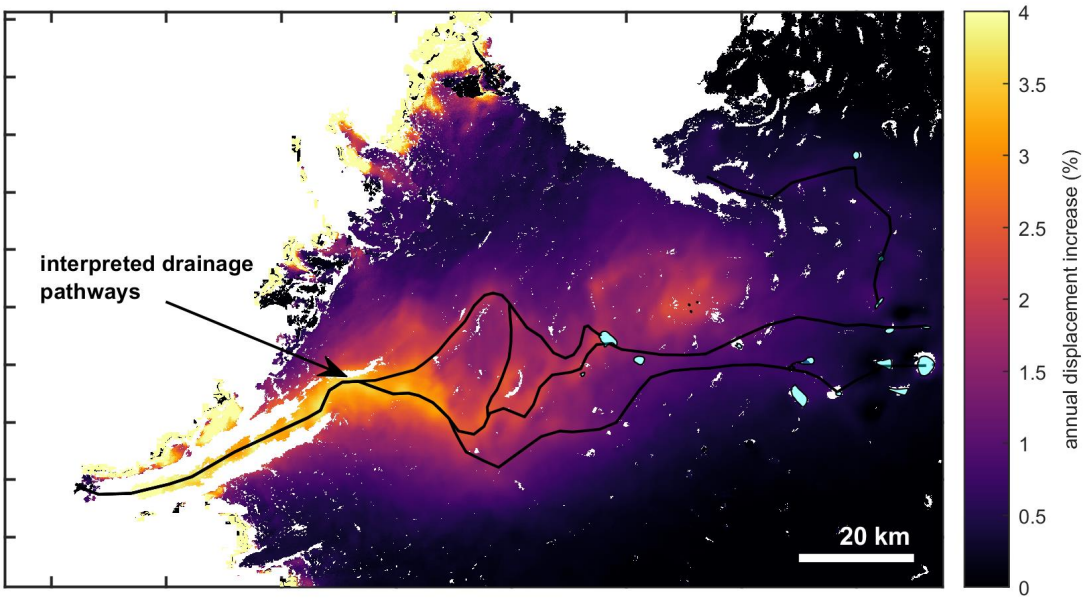

Figure S8 – Percent increase in annual velocity due to elevated velocities during the event. Black lines show inferred flow pathways. Increase was calculated using multi-year average annual displacement from 2016-2019 (*56*) and flow projected velocities (*Methods*).

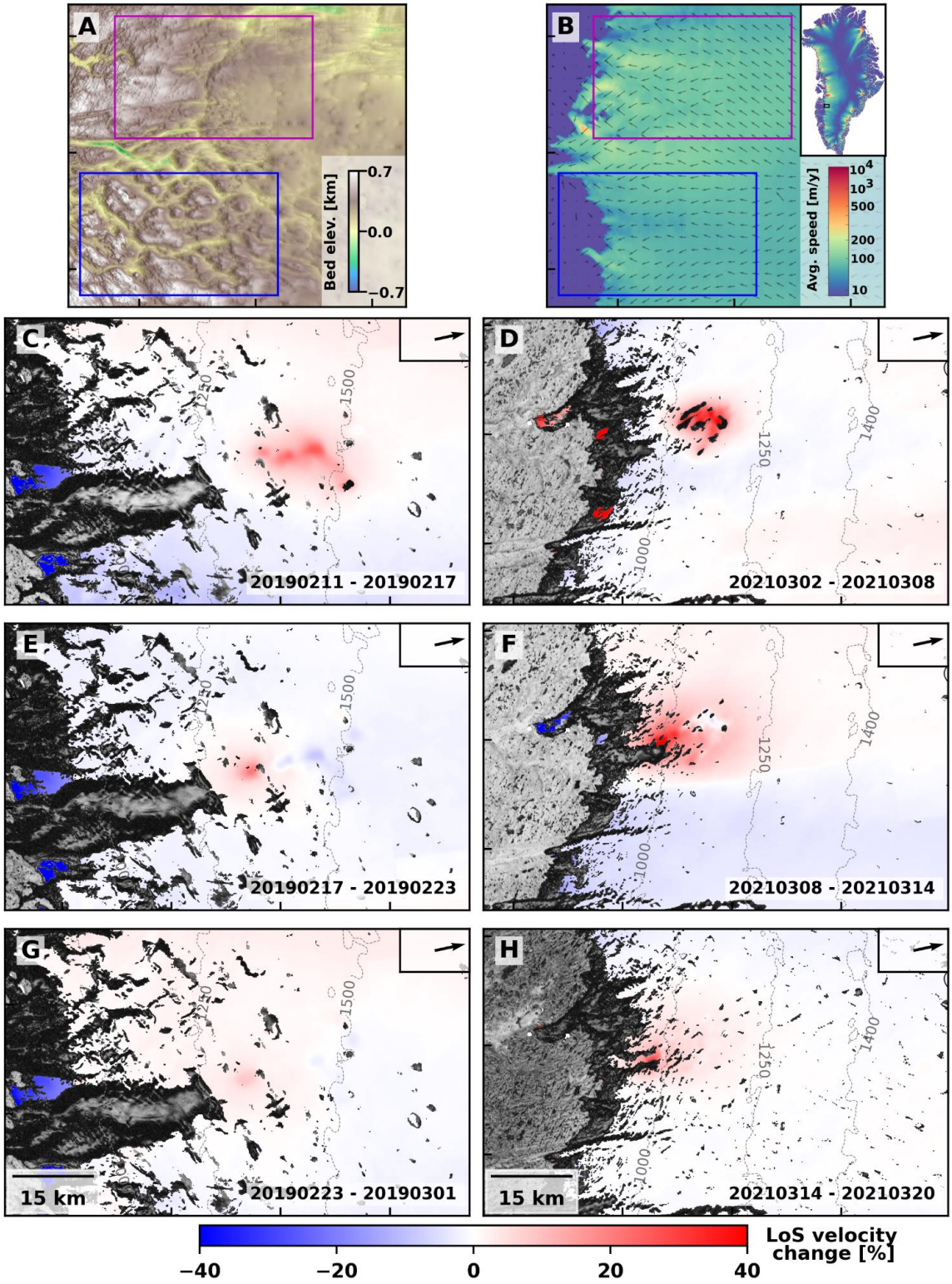
A
Bed elev. [km]
0.7
0.0
−0.7
B
Avg. speed [m/y]
10^4
10^3
500
200
100
10
C
20190211 - 20190217
D
20210302 - 20210308
E
20190217 - 20190223
F
20210308 - 20210314
G
15 km
20190223 - 20190301
H
15 km
20210314 - 20210320
1000
1250
1400
1500
LoS velocity change [%]
−40
−20
0
20
40

Figure S9 – Dynamic response to lake drainages identified during February 2019 40 km south of Russell Glacier (**C**,**E**,**G**) and March 2021 50 km north of Russell Glacier (**D**,**F**,**H**) measured with Sentinel-1 DInSAR (track 90) consecutive 6-day pairs. Panels (**C**)-(**H**) show the relative change in line-of-sight velocity (in percent) with respect to a pre-event acquisition overlayed on the coherence for the respective image pair. Panels (**A**) and (**B**) show bed elevation and 1995-2016 average velocity in the region of the 2019 event (blue rectangle) and the 2021 event (magenta rectangle).

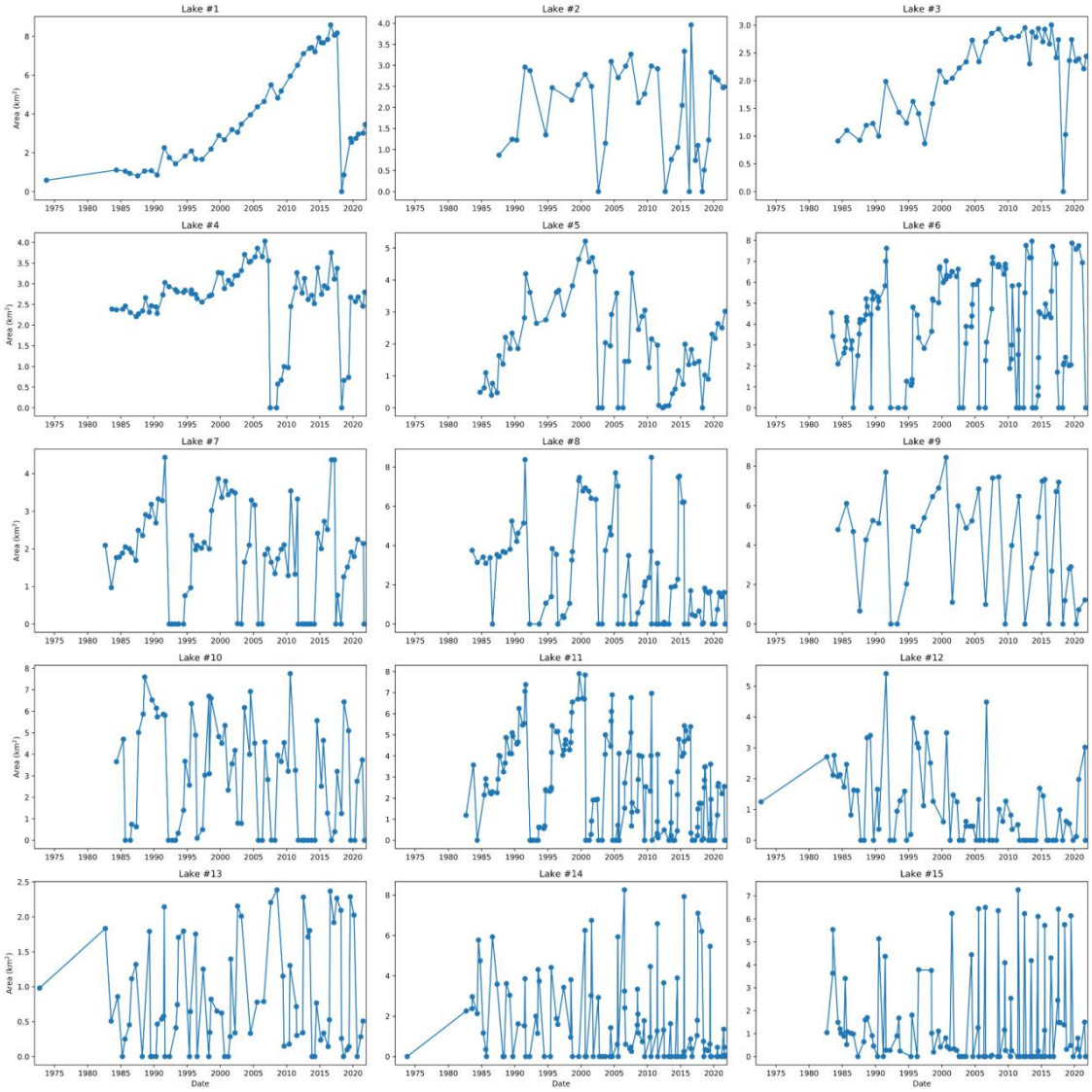

Figure S10 – The area in km^2 of lakes that drained during the event is plotted as a function of time.

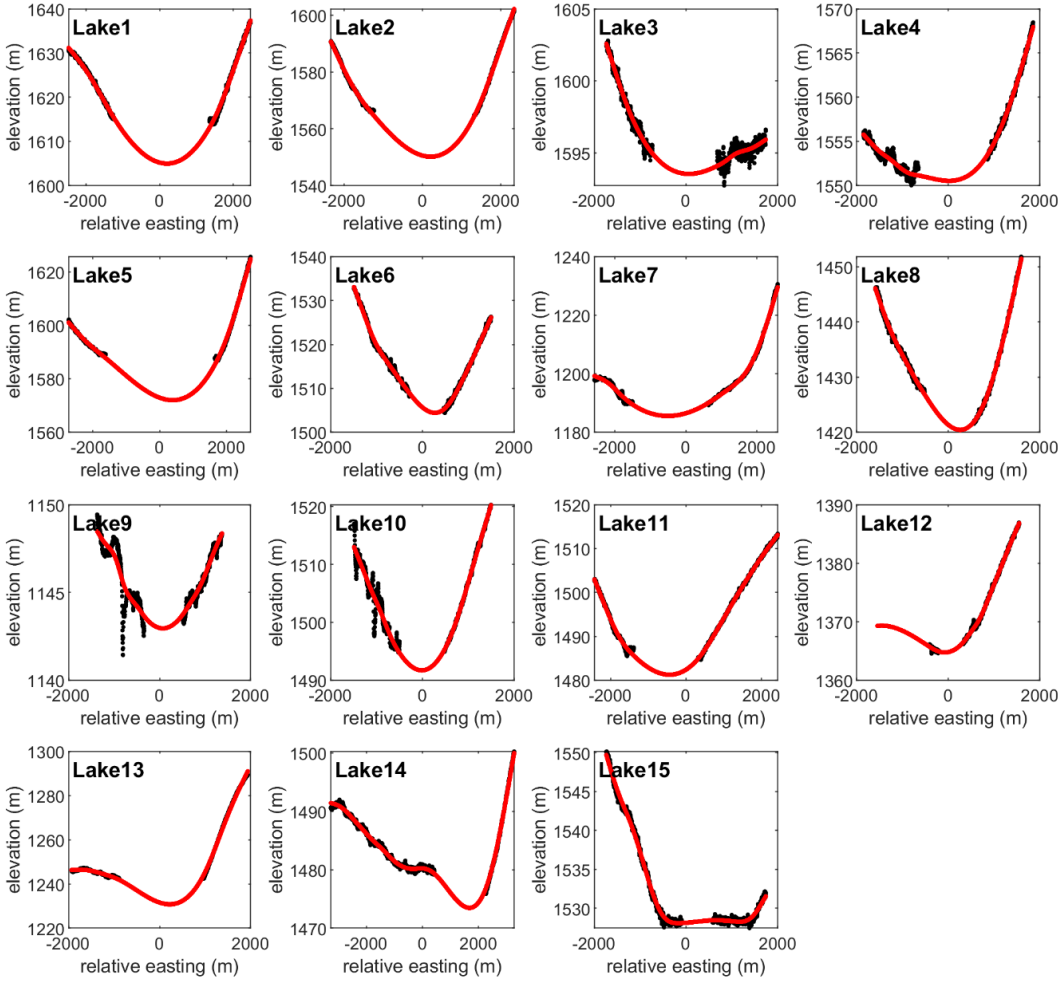

Figure S11 – Spline lake-bottom interpolation. Two-dimensional cross section of smoothing spline (red line, smoothing parameter = 0.9) fit through ArcticDEM (*62*) elevation data (black line) for all 15 lakes.

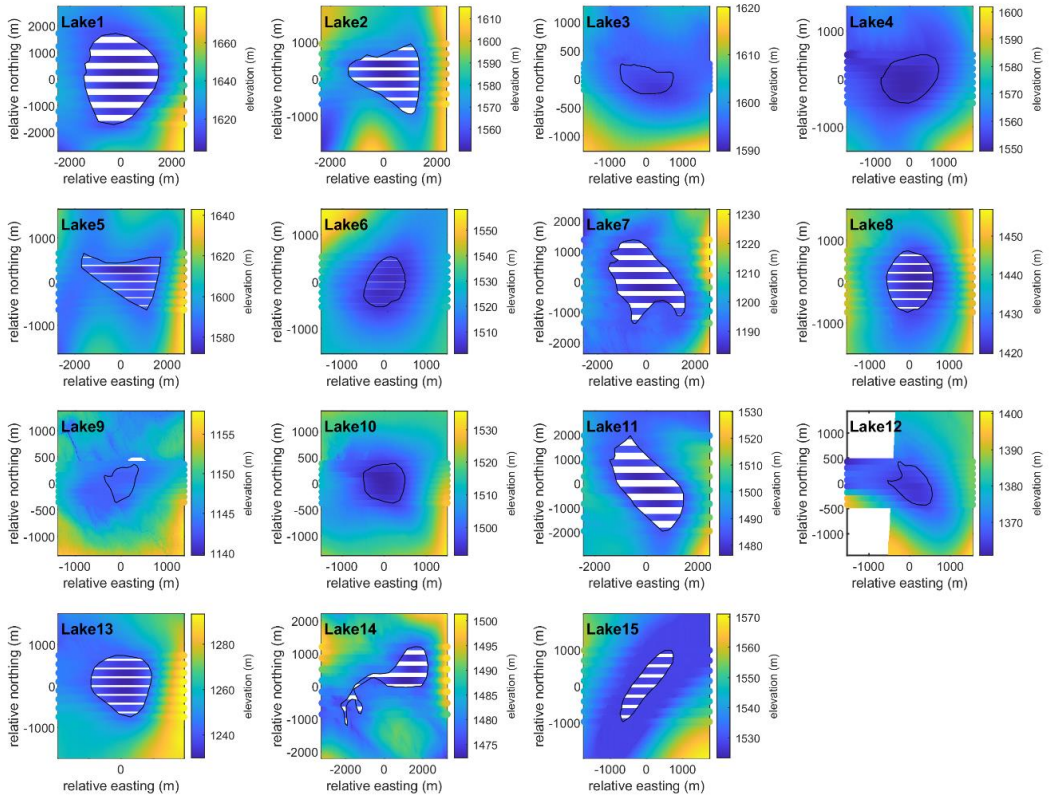

Figure S12– Map view of spline lake-bottom interpolation. Map view of smoothing splines (horizontal lines, smoothing parameter = 0.9) fit through ArcticDEM (*62*) elevation data (background data) for all 15 lakes.

Technical
University of
Denmark

Ørsted Plads, Building 348
2800 Kgs. Lyngby

www.space.dtu.dk